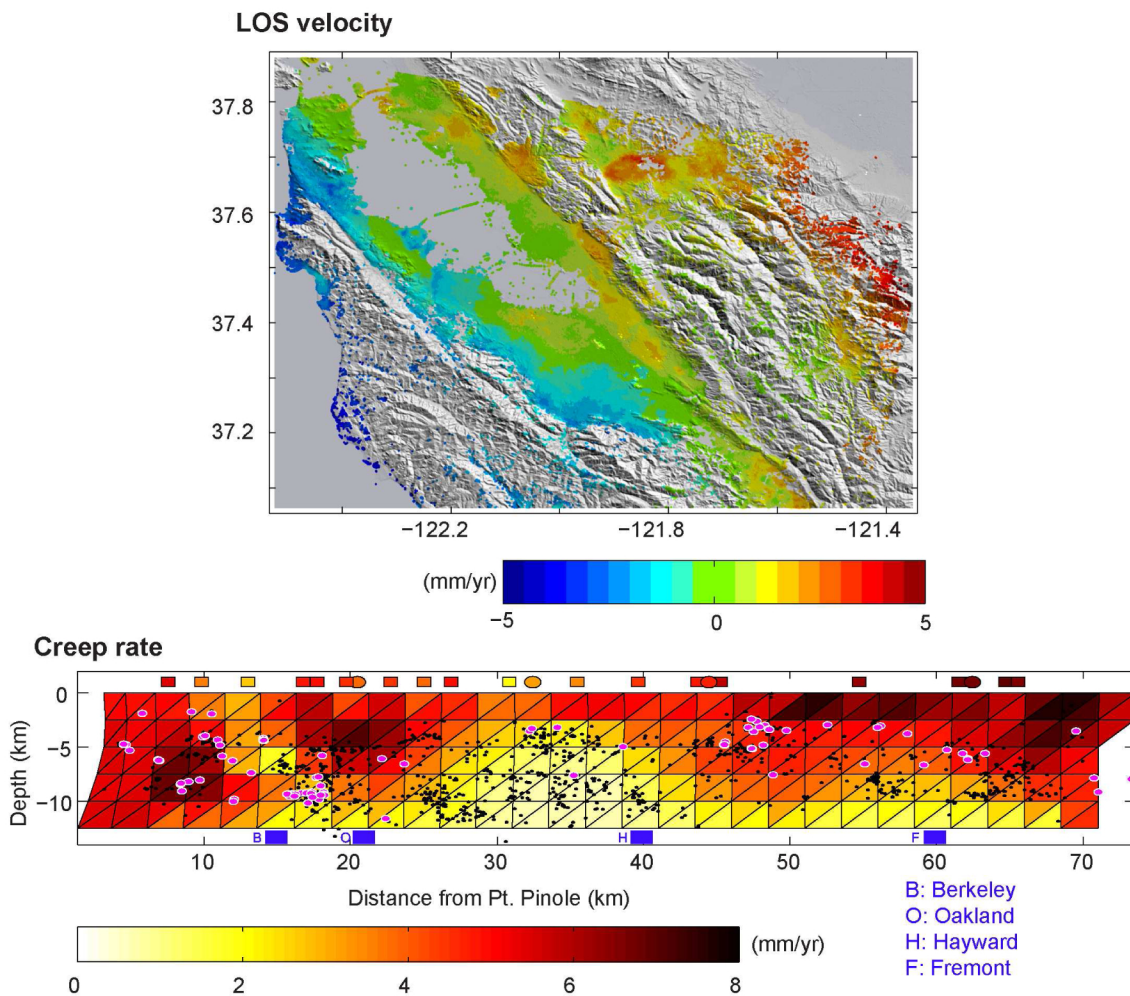


# Berkeley Seismological Laboratory



**Annual Report**  
**July 2011 - June 2012**



**Berkeley Seismological Laboratory**  
**Annual Report**  
**July 2011 - June 2012**

### Cover Picture

From Research Section 4: This model of creep, movement on the Hayward Fault with no accompanying earthquake, suggests that the creep rate near the surface is faster along the southern section of the fault. At greater depth, the situation is reversed, with higher rates in the north than in the south. Given the fact that most of the Hayward fault has accumulated a deficit of 30%-90% of its long-term slip budget, we estimate that seismic moment for a  $M_w$  ~6.3-6.8 has accumulated since the last big event in 1868.

# Contents

<b>1</b>	<b>Director's Report</b>	<b>1</b>
1	Highlights	1
2	Facilities Review	2
3	BSL Personnel News	4
4	Acknowledgements	4
<b>2</b>	<b>Research Studies</b>	<b>5</b>
1	Episodic Tremors Highlight Slow Slip Events in Central California	6
2	Searching for Small Deformation Signals in Laser Strainmeter Data Associated with Seismic Tremor in Parkfield	8
3	TremorScope: Imaging the Deep Workings of the San Andreas Fault	10
4	Time-dependent Model of Creep on the Hayward Fault from Joint Inversion of 18 Years of InSAR and Surface Creep Data	12
5	Landslide Risk Assessment (LSRA): GPS Instrumentation and Remote Sensing Study of Slope Movement in the Berkeley Hills, California.	14
6	Investigating Fault Slip and Rheology Along the San Andreas Fault in the San Juan Bautista Region	16
7	Aseismic Slip and Fault Interaction from Repeating Earthquakes in the Loma Prieta Aftershock Zone	18
8	Surface Slip during Large Owens Valley Earthquakes from EarthScope Lidar	20
9	Testing the Temporal Persistence of Slip Rate Along the Little Lake Fault, Eastern California Shear Zone	22
10	Examining the Mechanical Behavior and Evolution of the Southern San Andreas Fault System through Determination of Late Quaternary Slip Rates and Distinct Element Simulations	24
11	Investigating Fault Slip Budget in the Mendocino Triple Junction	26
12	Incipient Faulting near Lake Pillsbury, CA	28
13	Measurements of PBO Borehole Seismometer Orientations	30
14	Spatiotemporal Behaviors in Earthquake Multiplets at the Geysers Geothermal Field, CA	32
15	A systematic analysis of seismic moment tensor for seismicity at The Geysers Geothermal Field, California	34
16	Joint Inversion of Seismic and Geodetic Data for the Source of the 4th March 2010 $M_w$ 6.3 Jia-Shian, SW Taiwan, Earthquake	36
17	Deciphering the Mystery of the Great Indian Ocean Earthquakes	38
18	Source Spectral Variation and Yield Estimation Derived from High Frequency P and S Coda	40
19	Regional Moment Tensor Inversion for Shallow Sources: the Effects of Free-Surface Vanishing Traction	42
20	ShakeAlert: A Unified EEW System for California	44
21	ElarmS Earthquake Early Warning	46
22	Earthquake Early Warning with GPS Data	48
23	GPS Rapid Response to Moderate Earthquakes: A Case Study of the Alum Rock Earthquake	50
24	Using Smartphones to Detect Earthquakes	52
25	Probing the Deep Rheology of Tibet: Constraints from 2008 $M_w$ 7.9 Wenchuan, China Earthquake	54
26	Global Waveform Tomography with the Spectral Element Method: A Second-Generation Upper-Mantle Model	56
27	The DNA12 Seismic Velocity Model	58
28	Trust but Verify: a spot check for the new stratified model of upper mantle anisotropy beneath North America	60
29	3-D Seismic Velocity Structure of the Hawaii Hotspot from Joint Inversion of Body Wave and Surface Wave Data	62

30	Azimuthal anisotropy in the Pacific upper mantle . . . . .	64
31	Anisotropic Upper Mantle Shear-wave Structure of East Asia from Waveform Inversion . . . . .	66
32	An Exceptionally Large ULVZ at the Base of the Mantle near Hawaii . . . . .	68
33	Do "double SS precursors" mean double discontinuities? . . . . .	70
34	Inversion of Receiver Functions without Deconvolution . . . . .	72
35	Surface-Wave Methods for Monitoring Subsurface Properties in Permafrost Soils . . . . .	74
<b>3</b>	<b>BSL Operations</b>	<b>76</b>
1	Berkeley Digital Seismic Network . . . . .	78
2	California Integrated Seismic Network . . . . .	88
3	Northern Hayward Fault Network . . . . .	94
4	Parkfield Borehole Network (HRSN) . . . . .	103
5	Bay Area Regional Deformation Network . . . . .	114
6	Northern California Earthquake Data Center . . . . .	120
7	Data Acquisition and Quality Control . . . . .	130
8	Northern California Earthquake Monitoring . . . . .	136
9	Outreach and Educational Activities . . . . .	142
	<b>Glossary</b>	<b>144</b>
	<b>Appendix I Publications, Presentations, Awards, and Panels 2011-2012</b>	<b>146</b>
	<b>Appendix II Seminar Speakers 2011-2012</b>	<b>156</b>
	<b>Appendix III Organization Chart 2011-2012</b>	<b>159</b>

# Chapter 1

## Director's Report

### 1 Highlights

It is a great pleasure to present this year's Berkeley Seismological Laboratory (BSL) Annual Report. This is my first report as Director of the lab and it is exhilarating to see the wide range of BSL activities captured in these pages. The BSL today fosters both an active solid Earth research program and a cutting-edge geophysical observing facility. Spanning both of these realms, BSL provides an environment in which the extramural research program is strengthened and broadened by the facility, and the facility continues to push the boundaries of terrestrial observations in response to research needs. The contributions to this report are divided along these two lines. The research accomplishments are covered in Chapter 2, and progress in the development of our facilities is contained in Chapter 3. But first, I would like to highlight some of this year's activities.

The beginning of a new directorship provides an opportunity to reaffirm the BSL mission. After a review of the BSL's goals, priorities, and activities, we have developed the following mission statement consisting of four central tenets.

#### **BSL's Mission: Sound science, serving society**

**Fundamental research:** *Support fundamental research into all aspects of earthquakes, solid earth processes and their effects on society through the collection, archival and delivery of high quality geophysical data and through fostering a dynamic research environment that connects researchers across disciplines to geophysical observation systems.*

**Hazard information:** *Provide robust and reliable real-time data and information on Northern California earthquakes to government, public and private institutions, and to the public, in partnership with the US Geological Survey, CalEMA and other collaborating institutions.*

**Broad education:** *Enable the broad consumption of earthquake information and solid earth science through education and outreach to all sectors of society. Educate and train students at all levels through classes and research opportunities.*

**Professional operation:** *Create a productive professional working environment to enable efficient and robust operation and management of the geophysical facilities and career development of the staff and students.*

The basic research covered in Chapter 2 spans many topics in geophysics, seismology and tectonics. There are a total of 35 two-page summaries that range from micro-earthquake studies along the well-established San Andreas Fault to incipient faulting elsewhere; from aseismic slip on faults to great earthquake studies; from the structure of the deepest mantle to the properties of permafrost; from global seismic velocity structure to regional rheology. In addition to the two-page summaries, you will also find a list of publications and presentations about this research in Appendix I.

One of the exciting new developments during 2011-12 was a two-pronged effort to design and build a full prototype earthquake early warning system for California. This is being done thanks to generous funding by the Gordon and Betty Moore Foundation. In partnership with Caltech, the University of Washington and the USGS, we are now developing new algorithms to rapidly characterize the extent of faulting during large magnitude earthquakes. This will complement the current point-source methodologies that are the basis of the demonstration warning system that is running today. The second prong is the creation of BSL Earthquake Research Affiliates Program. It is designed to nurture partnerships between the BSL and the users of earthquake information. The program allows us to develop hazard products, including early warning, that are designed to fulfill the specific needs of private and public institutions and companies. The program currently has four members who are receiving earthquake alerts from the demonstration system. They are evaluating how their institution would respond to earthquake alerts in the future to reduce the impacts of earthquakes. You can find more information on the early warning effort in Chapter 2, Sections 20, 21, 22, 23, and 24.

The Gordon and Betty Moore Foundation has also funded our Tremorscope project. This project will in-

stall and operate a network of eight high-quality stations in the Cholame region south of Parkfield, CA, where seismic tremor has been found in the deep roots of the San Andreas fault zone. The network will be made up of four surface stations with broadband seismometers and accelerometers, and four borehole installations with geophones downhole, as well as digital broadband sensors and accelerometers. By the end of June 2012, all but two of the 8 stations were permitted, and the first two surface stations were installed and sending data. We evaluated data from these two sites to develop improvements to installation procedures before installing the other two surface sites. Over the next year, we expect to install and begin operating the remaining surface stations, as well as the borehole sites.

The BSL received significant funding from the USGS, in the framework of the American Recovery and Reinvestment Act (ARRA), to upgrade the recording systems at many of the Berkeley Digital Seismic Network (BDSN) broadband and borehole stations over the past three years. These upgrades are now completed at both our broadband and borehole stations. With the exception of two borehole sites installed under the auspices of Caltrans and several locations where we digitize other geophysical parameters such as electric and magnetic field strength, we now have new data loggers at all stations. All the broadband/strong motion sites now have some model of the Quanterra Q330 data logger, and the borehole sites have the 8-channel Basalt data logger.

In the last year, the BSL also completed work under the ARRA program to upgrade the Bay Area Regional Deformation (BARD) network's infrastructure, processing flow, and website. This included upgrading equipment at nearly half of the BARD GPS stations and installing six new stations (GASB, JRSC, MCCM, MNRC, PTRO, and WDCB), all co-located with BDSN seismometers. All BARD stations are now streaming data at 1 Hz. The upgraded receivers allowed us to make our real-time GPS data streams available more easily to the wider community. The real-time data streams also facilitate our in-house, real-time, high-rate processing of GPS data to produce station displacement estimates that can be used to inform real-time earthquake products, including Earthquake Early Warning systems. Daily processing and time-series generation for BARD backbone stations was re-established and the BARD webpage upgraded to provide more information (<http://earthquakes.berkeley.edu/bard>). More information about BARD can be found in Chapter 3, Section 5.

## 2 Facilities Review

The Berkeley Seismological Laboratory (BSL) is an Organized Research Unit (ORU) on the UC Berkeley cam-

pus. Its mission is unique in that, in addition to research and education in seismology, geophysics, and earthquake-related science, it is responsible for providing timely information on earthquakes to the UC Berkeley constituency, to the general public, and to various local and state governments, and private organizations. The BSL is therefore both a research center and a facility/data resource, which sets it apart from most other ORUs. A major component of our activities is focused on developing and maintaining several regional observational networks, and participating, along with other agencies, in various aspects of the collection, analysis, archival, and distribution of data pertaining to earthquakes, while maintaining a vigorous research program on earthquake processes and Earth structure. In addition, the BSL staff spends considerable time on public relations activities, including tours, talks to public groups, response to public inquiries about earthquakes, and an informational web presence (<http://earthquakes.berkeley.edu/>).

UC Berkeley installed the first seismograph in the Western Hemisphere at Mount Hamilton (MHC) in 1887. Since then, it has played a leading role in the operation of state-of-the-art seismic instruments and in the development of advanced methods for seismic data analysis and interpretation. Notably, the installation, starting in 1927, of Wood-Anderson seismographs at four locations in Northern California (BKS, ARC, MIN, and MHC) allowed the accurate determination of local earthquake magnitude from which a unique historical catalog of regional earthquakes has been maintained to this day, providing crucial input to earthquake probabilities studies.

Over the years, the then Berkeley Seismographic Stations (BSS) continued to keep pace of technological improvements. The first centrally telemetered network using phone lines in an active seismic region was installed by BSS in 1960. The BSS was the first institution in California to operate a 3-component "broadband system" (1963). It played a major role in the early characterization of earthquake sources using "moment tensors" and source-time functions. The BSS also made important contributions to the early definitions of detection/discrimination of underground nuclear tests and, jointly with UCB Engineering, to earthquake hazards work.

Starting in 1986, the BSS acquired four state-of-the-art broadband instruments (STS-1), while simultaneously developing PC-based digital telemetry. These two developments laid the groundwork for the modern networks we operate today. As telecommunication and computer technologies made rapid progress, in parallel with broadband instrument development, paper record reading was abandoned in favor of automated analysis of digital data. One paper-based helicorder does remain operational, primarily for the press and visitors to view.

Today, the BSL's networks can be divided into three

groups of instrumentation that are deployed at a total of 70 sites across central and northern California. The instrumentation types predominantly consist of broadband plus strong motion seismic, borehole seismic, and GPS, and are often co-located when appropriate. Data from all instrumentation streams continuously into the BSL's real-time monitoring system providing for earthquake notification and characterization, and also into the archive where it can be accessed immediately by researchers around the world for scientific study.

The Berkeley Digital Seismic Network (BDSN) is our regional seismic network of about 40 sites where both broadband and strong motion seismic instrumentation is installed. This network is the backbone of the BSL's operations, feeding the necessary data for real-time estimation of location, size and rupture parameters for earthquakes in central and northern California. This network has been steadily growing since the 1990's and consists of very high quality, low noise sites, making the data ideal for a range of research efforts. The array can be used to study local or global earthquake sources, and provides data for investigation of 3D crustal structure in California and its effects on regional waveform propagation, which in turn affect the intensity of ground shaking in larger earthquakes. Recent additions to the network include an ocean bottom seismometer in the Monterey Bay (MOBB) providing real-time data via an undersea cable (operated in collaboration with MBARI), and also the Tremorscope stations along the Cholame section of the San Andreas Fault just south of Parkfield.

The real-time data is also Berkeley's contribution to the California Integrated Seismic Network (CISN), which is a federation of networks that jointly provide all real-time earthquake information in the state. Since 1996, the BSL and the USGS in Menlo Park have closely cooperated to provide the joint earthquake notification program for Northern California. This program capitalizes on the complementary capabilities of the networks operated by each institution to provide rapid and reliable information on the location, size and other relevant source parameters of regional earthquakes. The real-time earthquake information is made available through the BSL's website (<http://earthquakes.berkeley.edu>).

The BSL's borehole networks represent the second grouping of instrumentation. The High Resolution Seismic Network (HRSN) was installed in 1987 and now consists of 12 operating sites. Additional borehole sites will soon be added as part of the Tremorscope project. These instruments have led to wide-ranging research into earthquake processes due to their high sensitivity, low noise, and proximity to micro-earthquakes, clusters and tremor sources along the highly studied Parkfield section of the San Andreas Fault. In the Bay Area, the Hayward Fault Network also includes 15 borehole instruments that have been installed progressively since the 1990s. Again, the

goal of this network is to collect high signal-to-noise data for micro-earthquakes along the Hayward Fault to gain insight into the physics that govern fault rupture and its nucleation.

The third instrumentation type is GPS. The BSL operates the Bay Area Regional Deformational (BARD) Network consisting of 32 primary sites, 18 collocated with BDSN seismometers. All sites record with a 1 Hz sample rate and telemeter the data to BSL in real-time. Continuous GPS data tracks the motion of the tectonic plates and allows us to assess the strain buildup along faults as well as its release either through creeping episodes or through earthquakes. The application of GPS data feeds to real-time earthquake information is also a relatively new development. Very rapid processing now generates displacement waveforms that in turn support the development of improved real-time earthquake analysis methods for significant earthquakes.

The BSL's IT group is active in the development of new software for the collection, archival and real-time analysis of the various geophysical data streams that we collect. In 2009, the new AQMS seismic network software package was rolled out following a multi-year development effort by the BSL in collaboration with other CISN partners. This software provides all the real-time processing components needed by regional seismic networks and is now being rolled-out across the US. The development of real-time GPS processing software is a current area of focus for the lab along with development and implementation of earthquake early warning algorithms that can process the data quickly enough to provide alerts to people a few seconds to tens of seconds before shaking is felt.

Archival and distribution of data from the BSL and other regional geophysical networks is performed at the Northern California Earthquake Data Center (NCEDC), operated at the BSL in collaboration with USGS Menlo Park. The data reside on a mass-storage device (current holdings ~60 TB), and are accessible online (<http://www.ncedc.org>). In addition to BSL network data, data from the USGS Northern California Seismic Network (NCSN), and other Northern California networks, are archived and distributed through the NCEDC. The NCEDC also maintains, archives and distributes various earthquake catalogs.

Finally, the field engineering team is responsible for maintaining our existing ~70 geophysical observatories across Northern California, and designing and installing new sites. Of particular note is the completion in 2011 of the ARRA-funded upgrades. These urgently needed equipment upgrades replaced aging dataloggers at almost all BSL observatories, providing for more robust and more rapid transmission of data from the sites to the BSL real-time system. The group is now focused on the design and installation of the new Tremorscope borehole and surface stations just south of Parkfield along the

Cholame section of the San Andreas Fault.

All of these operations are supported by an operations and research staff of 10, an IT staff of 7, an engineering staff of 5, and an administrative support group shared with the Department of Earth and Planetary Science consisting of 7. In addition, there are currently 5 Postdoctoral Scholars and 14 PhD graduate students associated with the lab, along with 10 affiliated faculty.

Core University funding to our ORU provides salary support for one staff scientist (shared by three researchers), one IT staff member, one engineer, our operations manager, and two administrative assistants, and represents about one fifth of the total infrastructure support budget. The remaining support comes from extramural grants and contracts, primarily from the USGS, DOE, NSF, and the State of California, through its Emergency Management Agency (CalEMA). Currently, grants from the Gordon and Betty Moore Foundation contribute significantly to our operations as do the contributions from the members of our Earthquake Research Affiliates Program.

### 3 BSL Personnel News

Four new PhD graduate students joined the lab in the fall of 2011: Sierra Boyd, Cheng Cheng, Brent Delbridge, and Qingkai Kong. Also, Thomas Bodin, a new Miller Postdoctoral Fellow, and H. Serdar Kuyuk, a Postdoctoral Fellow, joined the lab. One PhD student, Aurelie Guilhem, graduated in December 2011. Her dissertation was titled “Analysis of unusual earthquake and tremor seismicity at the Mendocino Triple Junction and Parkfield, California.” Postdoctoral Fellow Colin Amos also departed from the lab.

As usual, a stream of visitors spent various lengths of time at the lab. Jamie Barron, Morgan Guinois, Matthias Meschede, and Sergei Ventosa all visited from Institut de Physique du Globe de Paris, France, at various times. Simona Colombelli from the University of Naples spent 8 months at the lab working on earthquake early warning, and Jiajun Chong from the University of Science and Technology of China spent a summer working on waveform inversion in the Tibetan region.

The BSL staff remained mostly stable during this year following the significant changes of the previous few years. Administrative support continues to be provided through a shared services model with the Department of Earth and Planetary Science under the leadership of manager Judith Coyote. The IT and research staff also remained mostly stable. Tom Weldon left the research staff and we are pleased to welcome Clay Miller who joined the BSL as a Staff Research Associate.

Finally, in June 2012, Bill Karavas left the BSL. Bill was the lead engineer for the BSL networks for almost 20 years. During that time Bill led the effort to build

the BDSN and much of the BARD network. He was also involved in supporting the borehole networks for the last few years. The quality of the BSL data, used by researchers around the world, would not be what it is without Bill’s careful oversight of all engineering operations for the last two decades and we are very grateful to Bill for his efforts during that time.

### 4 Acknowledgements

I would like to thank our technical and administrative staff, scientists and students for their efforts throughout the year and their contributions to this annual report. Individual contributions to activities and report preparation are mentioned in the corresponding sections, except for the appendix sections, which were prepared by Jennifer Taggart.

I also wish to especially thank the individuals who have regularly contributed to the smooth operation of the BSL facilities: Mario Aranha, Doug Dreger, Aaron Enright, John Friday, Peggy Hellweg, Ivan Henson, Ingrid Johanson, Bill Karavas, Clay Miller, Josh Miller, Pete Lombard, Bob Nadeau, Doug Neuhauser, Charley Paffenbarger, Jennifer Taggart, Taka’aki Taira, Stephen Thompson, Bob Uhrhammer, Tom Weldon, and Stephane Zuzlewski, and, in the administrative office, Marion Banks, Matt Carli, Judith Coyote, Dawn Geddes, and Gretchen vonDuering. I also wish to thank our undergraduate assistants, Cora Bernard, Jennifer Taing and David Tang, for their contributions to our research and operations activities.

I am particularly grateful to Jennifer Taggart and Peggy Hellweg for their help in putting together this annual report and bringing it to completion.

The Annual Report of the Berkeley Seismological Laboratory is available on the web at [http://earthquakes.berkeley.edu/annual\\_report](http://earthquakes.berkeley.edu/annual_report).

# Chapter 2

## Research Studies

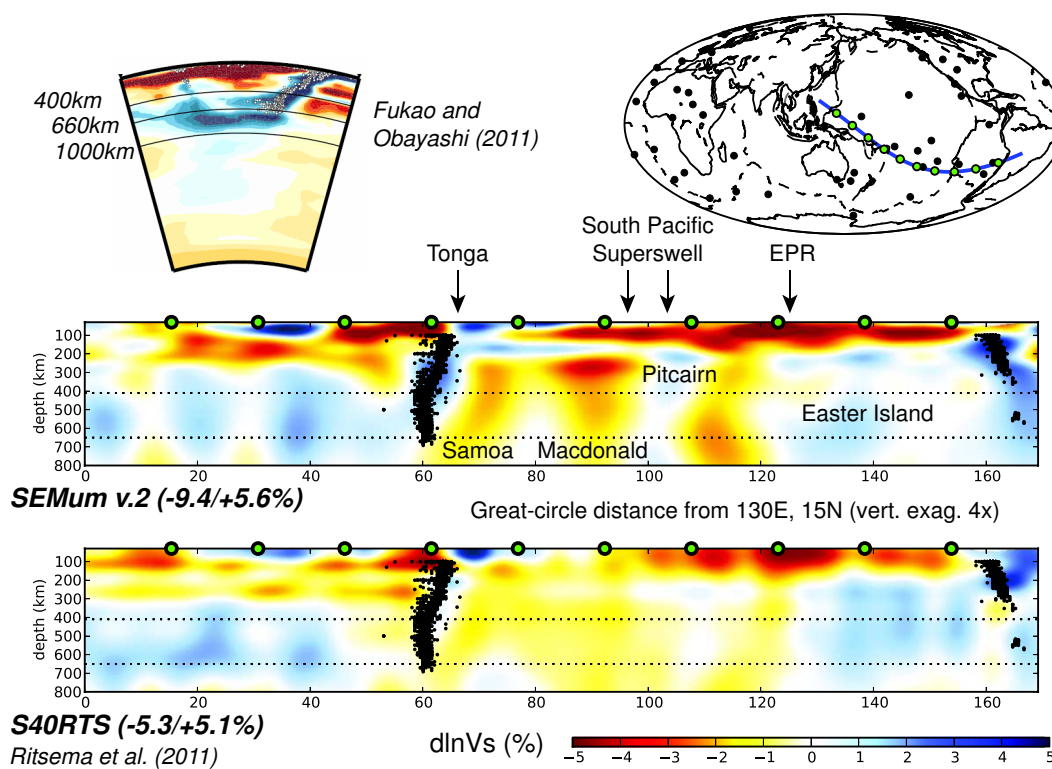


Figure 2.1: Upper mantle Earth structure beneath the South Pacific, imaged using seismic waves. Deep seismicity highlights subducted slabs, the remains of tectonic plates. The authors' second-generation, global upper-mantle model has been refined to improve interpretation of shallow upper-mantle structure under the oceans. From Research Section 26.

# 1 Episodic Tremors Highlight Slow Slip Events in Central California

Aurélie Guilhem and Robert M. Nadeau

## 1.1 Introduction

We present evidence that recurring episodes of non-volcanic tremors (NVT) along the San Andreas fault (SAF) near Parkfield, California are reminiscent of seismic events associated with episodic tremor and slip (ETS) and slow slip events (SSE) observed in subduction zones. They show systematic differences between aperiodic and periodic recurrences that are related to the 2004 M6.0 Parkfield (PKD) earthquake and the long-term SAF slip rate. After constraining their locations, duration, and response compared to repeating earthquake activity along the SAF, we propose a simple SSE model for the 52 PKD episodes observed in almost 10 years. We suggest that  $\sim 10$ -day period SSEs correspond to slips of  $\sim 7.8$  mm, occurring on a SAF parallel patch that is  $\sim 25$  km long and between 15 km and 30 km depth.

## 1.2 Recurrence and size of the episodes

Figure 2.2 shows the updated catalog of NVT detections occurring along the SAF near PKD between 27 July 2001 and 21 March 2011. 2791 tremor bursts are reported, corresponding to continuously elevated signals of 3 to 21 minutes. During this time period, we automatically identified 52 episodes of tremors (Figure 2.2) lasting on average 10 days. The episodes' recurrence times, which range between 30 and 130 days, vary during the nearly 10 years of detection with periodic and aperiodic patterns (Figure 2.2). Before the 2004 PKD earthquake the episode recurrence is irregular. Between the 2004 PKD earthquake and 2009, recurrence intervals progressively lengthen at a rate of  $\sim 17.5$  days/year (Figure 2.2). Since 2009, however, the irregularity in recurrence has returned.

The episode sizes also change after the PKD earthquake. We find that before the fore-tremor, there was in average about 68 minutes of tremors per episode. Episode size increased to about 120 minutes between the PKD mainshock and 2009. But, similarly to what is observed with the recurrence times, after 2009 the episodes sizes returned to levels more comparable to those seen before the fore-tremor, with an average of about 86 minutes of tremors per episode.

## 1.3 Location of the episodes

NVTs near PKD concentrate in two regions along the SAF: Monarch Peak and Cholame. By comparing their spatio-temporal activity in the two regions we find that the NVTs that compose the episodes are located near

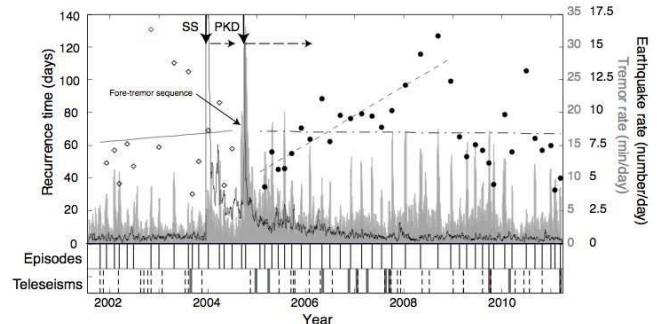


Figure 2.2: Tremor activity (gray) between 2001 and 2011 and recurrence times of episodes before (diamond) and after (dot) the 2004 Parkfield (PKD) earthquake. The overlying line shows the M1.4+ earthquake activity within 100 km of Parkfield. Times of the episodes are indicated by the vertical, continuous lines. Bottom: times of M7.5+ earthquakes.

Cholame, between 15 and 30 km depth, and on the western side of the SAF (Figure 2.3), along an  $\sim 25$  km segment.

We also use the locations of 88 low-frequency earthquake (LFE) families reported by *Shelly and Hardebeck* (2010) to help provide additional constraints on the location of the NVT episodes. Because of the strong association between NVT and LFE activities, we make the assumption that the LFEs that are consistent in activity with NVT episodes occur within the source region of the NVT episodes. To identify them, we compare the timing of the NVT and LFE episodes between 2005 and 2010, using a measure of correlated episodicity, beta, for each of the 88 LFE families. Figure 2.3 shows that the LFE families that mimic the NVT episodes are also located along the same 25-km segment of the SAF (high beta values).

## 1.4 Source characteristics of the SSEs

It is possible to try to estimate the size of these SSEs. We compare the cumulative duration of the tremor activity to the cumulative slips inferred from groups of repeating earthquakes observed along the SAF in the creeping section, in the PKD coseismic zone, and in an intermediate region NW of the PKD rupture. We find that this last group better mimics the tremor activity both before and after the PKD earthquake. From their corresponding cumulative slip, we infer that the SSEs would correspond

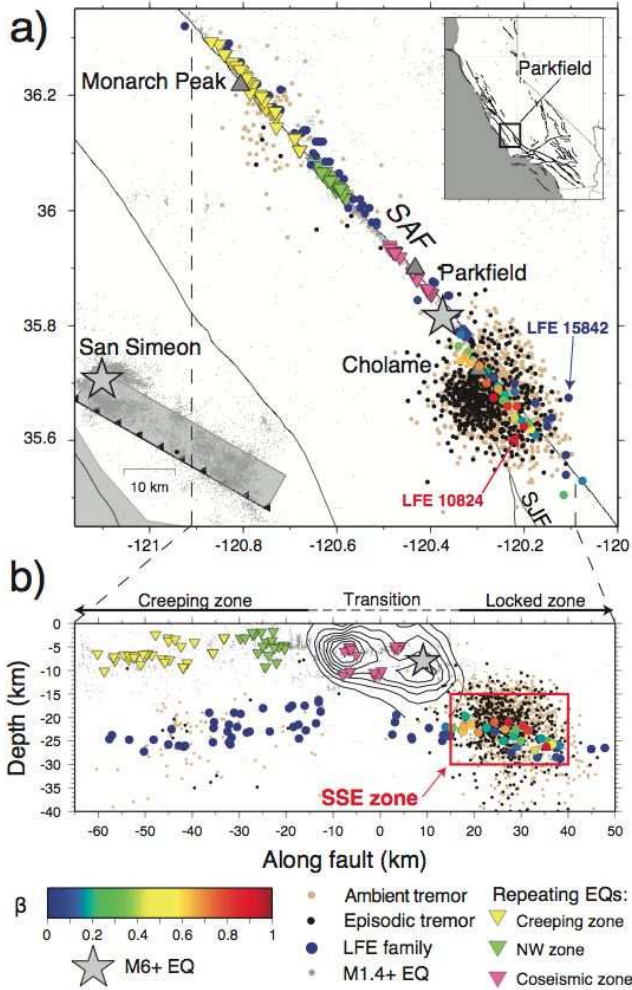


Figure 2.3: Location of well-located NVT activity (black dots: episodic, brown: non-episodic), LFEs (colored dots), and REQs (inverted triangles) in central California. The LFE families (circles) are color-coded by their beta coefficient (warm color: similar behavior, cold color: different). a) Map view. b) Cross-section view.

to slips of  $\sim 8$  mm during 10 day periods. Combined with the estimates of the size of their source region, they correspond to  $M_w 5.2$  events on average.

We also use an empirical linear relationship from *Aguiar et al.* (2009) that links the moment release of geodetically observed Cascadia SSEs to the cumulative duration of tremors during ETS events. From  $\sim 89.5$  hours of SAF NVT activity recorded between 2001 and 2011, this gives a cumulative moment magnitude of 6.4. And each individual 10-day NVT/SSE episode ranges between  $M_w 5.0$  and 5.4, with an average at  $M_w 5.2$ . Assuming correct area and displacement estimates, our results also suggest very little bias between the NVT duration determinations of *Aguiar et al.* (2009) and this study.

Furthermore, it is possible to explore parameters linked to strain release and stress drop that are important for inversion of the SSE deformation. We find that the strain release is on the order of  $4e-7$ , over 24 times smaller than those that have been used in previous unsuccessful searches for geodetic signals associated with tremors in the region (*Smidth and Gomberg*, 2009). Finally, this implies an average stress drop of  $\sim 12$  kPa for the SAF SSEs. This is 2 to 3 orders of magnitude smaller than for regular earthquakes, but this is consistent with NVT observations in the region and in other tremor regions.

## 1.5 Discussion

Our results open perspectives for further study of SSEs, and changes in the behavior of the SAF episodic tremors can give information on variations in the state of stress in the deep fault zone. This study emphasizes the importance of studying the SAF NVTs with the goal of estimating the fault stress regime and its changes through time. SAF NVTs provide information on small changes in the properties of the fault that other geophysical techniques have yet to successfully illuminate.

## 1.6 Acknowledgements

Supported by the U.S. Geological Survey through award G10AC00093 and by the National Science Foundation through awards EAR0738342 and EAR0910322.

## 1.7 References

- Aguiar, A.C., T.I. Melbourne, Scrivner, C.W., Moment release rate of Cascadia tremor constrained by GPS, *J. Geophys. Res.*, 114, B00A05, 2009.
- Shelly, D. R., Hardebeck, J. L., Precise tremor source locations and amplitude variations along the lower-crustal central San Andreas fault, *Geophys. Res. Lett.*, doi:10.1029/2010GL043672, 2010.
- Smith, E.F., Gomberg, J., A search in strainmeter data for slow slip associated with triggered and ambient tremor near Parkfield, California, *J. Geophys. Res.*, 114, B00A14, 2009.

## 2 Searching for Small Deformation Signals in Laser Strainmeter Data Associated with Seismic Tremor in Parkfield

Brent Delbridge and Roland Bürgmann

### 2.1 Introduction

It has been hypothesized that shear dislocation on the plate interface accompanies deep tremor and low frequency earthquakes (LFE's) (e.g. *Wech and Creager, 2007; Ide et al, 2007; Shelly, 2007*). We hope to test this claim on tremor and LFE's on the San Andreas fault (SAF) through rigorous statistical examination of the laser strainmeter data from two long baseline instruments near Chalome, CA . It has also been shown that slow slip accompanies tremor in several subduction zones, however, there has not been an observation of deformation associated with the observed tremor in a transform fault setting such as the SAF, despite the ubiquitous presence of tremor and low frequency earthquakes (*Shelly et al, 2007; Nadeau et al, 2005*). It is believed that the strain rate is too small to be detectable by GPS, and previous studies attempting to use borehole strainmeters in Park-

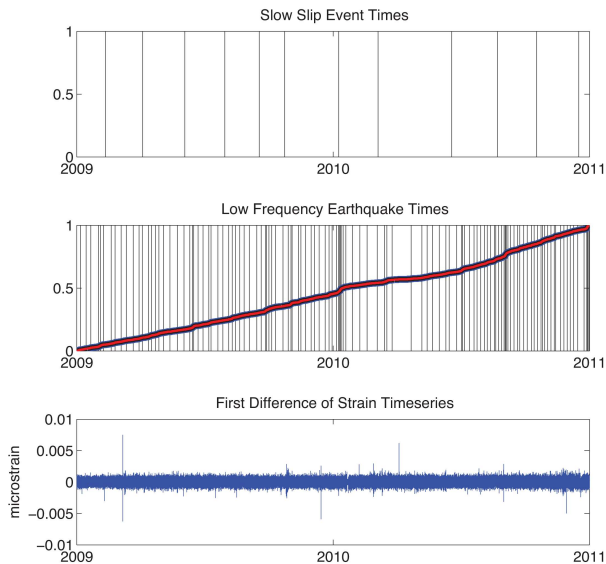


Figure 2.4: The top panel plots vertical lines to represent the times of peak correlation within large tremor bursts, which have been interpreted as slow slip events by Guilhem and Nadeau. The second panel shows the times of every thousandth LFE event as a vertical line, while the continuous curve represents a normalized cumulative count of all LFE events in the selected time period. In the bottom panel we show the first difference of processed data where non-tectonic signals have been removed using the barometric pressure, tides, and optical anchors.

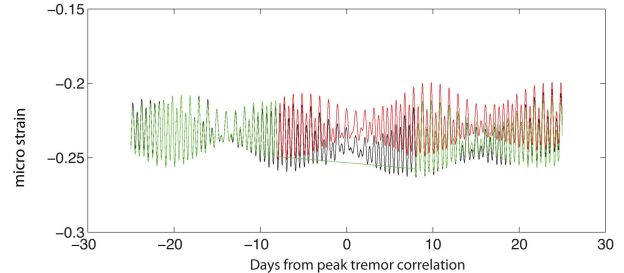


Figure 2.5: The black curve is the raw strainmeter data, the green curve is the fit to the data excluding the window about the peak correlation time, and the red curve is the model that is removed from the data.

field have failed to detect any observable strain associated with tremor swarms triggered by passing surface waves (*Smith et al, 2009*). This study hopes to go beyond that work and take advantage of the large number of LFE observations to lower drastically the signal to noise ratio. Additionally, we hope to observe strain associated with newly identified large tremor swarms that are inferred to as slow slip events (SSE's) with moment magnitudes exceeding 5 (*Guilhem et al, in press*). These slow slip events have durations of  $\sim 5$ -10 days, far too long to be observed with traditional seismometers, and the deformation is far below the detection level of GPS. However we believe that Laser strainmeter (LSM) is particularly well suited to observe these signals, due to the relatively low detection level at periods of  $10^5$  to  $10^6$  seconds (*Agnew, 2003*).

### 2.2 Data

We have three different types of datasets to utilize in this analysis: high rate time series, a dense point process series, and a sparse quasi-periodic point process. These correspond to the laser strainmeter records, locations and times of low frequency earthquakes, and recently identified clusters of tremor which are believed denote otherwise aseismic slow slip events respectively. We do not believe these data to be independent. Below we show the times of the inferred SSE events, a normalized cumulative count of LFE events, and the first difference of a sample strainmeter record. The strain timeseries is not raw data, but derived data. We have taken the calibrated signal and removed known physical signals such as tides, barometric effects, corrections due to the vac-

uum pressure, and local corrections calculated from the instrument’s optical anchors. This derived data is what we will view as a signal plus noise and a seasonal component.

## Methodology

In order to observe the small offsets and temporal correlation of LFE deformation in the straindata we employ an empirical correction to the data. The corrections we use are intended to facilitate stacking of the data. We first select 25 days on either side of each time shown in the top panel of 2.4. Since we suppose that there is deformation happening around this time, we do not use the 5 days surrounding the selection times. From the remaining 40 days we perform a least squares inversion to fit the diurnal and semidiurnal tides, simultaneously with a linear trend and step function. The step function here is not used to estimate an offset but rather to prevent any bias in the linear fitting. The coefficients for the tidal amplitudes and linear fit are then used to create a model of the tides and drift over the entire 50 day window and are removed from the data. An example this procedure is show in Figure 2.5.

## 2.3 Problem Formulation

Let the strain timeseries be denoted by  $Y(t)$ , the slow slip point process times by  $\tau_i^{SSE}$ , and the low frequency earthquake times by  $\tau_j^{LFE}$ . We will denote the response in the strain timeseries due to a tectonic point processes as  $F(\tau_i^{SSE})$  and  $G(\tau_j^{LFE})$  respectively.

$$Y(t) = \sum_i F(\tau_i^{SSE}) + \sum_j G(\tau_j^{LFE}) + trend + seasonal + noise \quad (2.1)$$

Though since the signal associated with the LFE process is *a priori* believed to be below our level of detection, we most likely believe the data to be

$$Y(t) = \sum_i D^{SSE}(\tau_i^{SSE}) + trend + seasonal + noise. \quad (2.2)$$

The goal of this study is to find the deformation associated with each point process. Or in other words, is the signal we derive from the strainmeter after accounting for the seasonal signal and trend correlated with either of our candidate point processes.

## 2.4 References

Agnew D, Wyatt F, Long-Base Laser Strainmeters: A Review, *Scripps Institution of Oceanography Technical Report*, 2003

Guilhem A, and Robert N, Episodic tremors and deep slow-slip events in Central California, *Earth and Planetary Science Letters*, under review.

Ide S, Shelly D, Beroza G, Mechanism of deep low frequency earthquakes: Further evidence that deep non-volcanic tremor is generated by shear slip on the plate interface, *Geophys. J. Int.*, 34, 3, 2007.

Nadeau R, Dolenc D, Nonvolcanic tremors deep beneath the San Andreas fault, *Science*, 307, 5708, 2005.

Shelly D, Beroza G, Ide S, Non-volcanic tremor and low-frequency earthquake swarms, *Nature*, 446, 7140, 2007.

Wech AG, Creager KC, Cascadia tremor polarization evidence for plate interface slip, *Geophys. Res. Lett.*, 31, 22, 2007.

## 3 TremorScope: Imaging the Deep Workings of the San Andreas Fault

Roland Bürgmann, Richard Allen, Pascal Audet, Douglas Dreger, Robert Nadeau, Barbara Romanowicz, Taka'aki Taira, Margaret Hellweg

### 3.1 Introduction

Until recently, active fault zones were thought to deform via seismic earthquake slip in the upper, brittle section of the crust, and by steady, aseismic shear below. However, in the last few years, this view has been shaken by seismological observations of seismic tremor deep in the roots of active fault zones. First recognized on subduction zones in Japan and the Pacific Northwest, tremor has also been found to be very active on a short section of the San Andreas to the southeast of one of the most densely monitored fault segments in the world, near Parkfield (*Nadeau and Dolenc, 2005*). This deep ( $\sim 20\text{-}30$  km) zone of activity is located right below the nucleation zone of the great 1857 Fort Tejon earthquake. Thus, understanding the temporally and spatially complex faulting process in this zone may help us better understand the conditions that lead to such large ruptures.

### 3.2 The Project Plan

The tremor source region is south-east of existing seismic networks around Parkfield, along the San Andreas Fault. We are adding eight seismic stations, the TremorScope (TS) network, in this area to complement existing instrumentation.



Figure 2.6: Installation of seismic vault at TremorScope station THIS.

Six of eight planned sites for the TS network have been permitted and the first two two surface stations installed. Figure 2.6 shows installation of the seismometer vault at station THIS. Surface installations have a broadband seismometer, an accelerometer and a digitizer. The borehole sites, with a hole about 300 m deep will have an accelerometer at the surface. Downhole will be a cemented, three-component set of gimbaled, 2 Hz geophones. Three boreholes will be equipped with a Guralp downhole sensor package, consisting of a three-component broadband seismometer, a three-component accelerometer and a digitizer. At all locations, data will be logged onsite and forwarded to Berkeley for real-time processing. The data will be used in real-time earthquake monitoring (see Operational Section 8), as well as for tremor studies. The first data are in. Figure 2.7 shows triggered tremor from the M8.6 earthquake of April 11, 2012, in the recording of station TSCN. This tremor was also apparent at HRSN stations.

### 3.3 Perspectives

Data from the TremorScope project will improve earthquake monitoring in the region south of Parkfield. Insights from the project will also contribute to understanding tremor and slip in other regions of the world where such phenomena have been observed, but are not nearly as accessible. Should a great San Andreas earthquake occur during this experiment, the network would also provide unprecedented and exciting insights into the seismic rupture process.

### 3.4 Acknowledgements

This work is funded by grant 2754 from the Gordon and Betty Moore Foundation.

### 3.5 References

Nadeau, R., and D. Dolenc (2005), Nonvolcanic tremors deep beneath the San Andreas fault, *Science*, 307, 389, doi:10.1126/science.1107142.

### Mw8.6 Off the West Coast of Northern Sumatra 2012 April 11

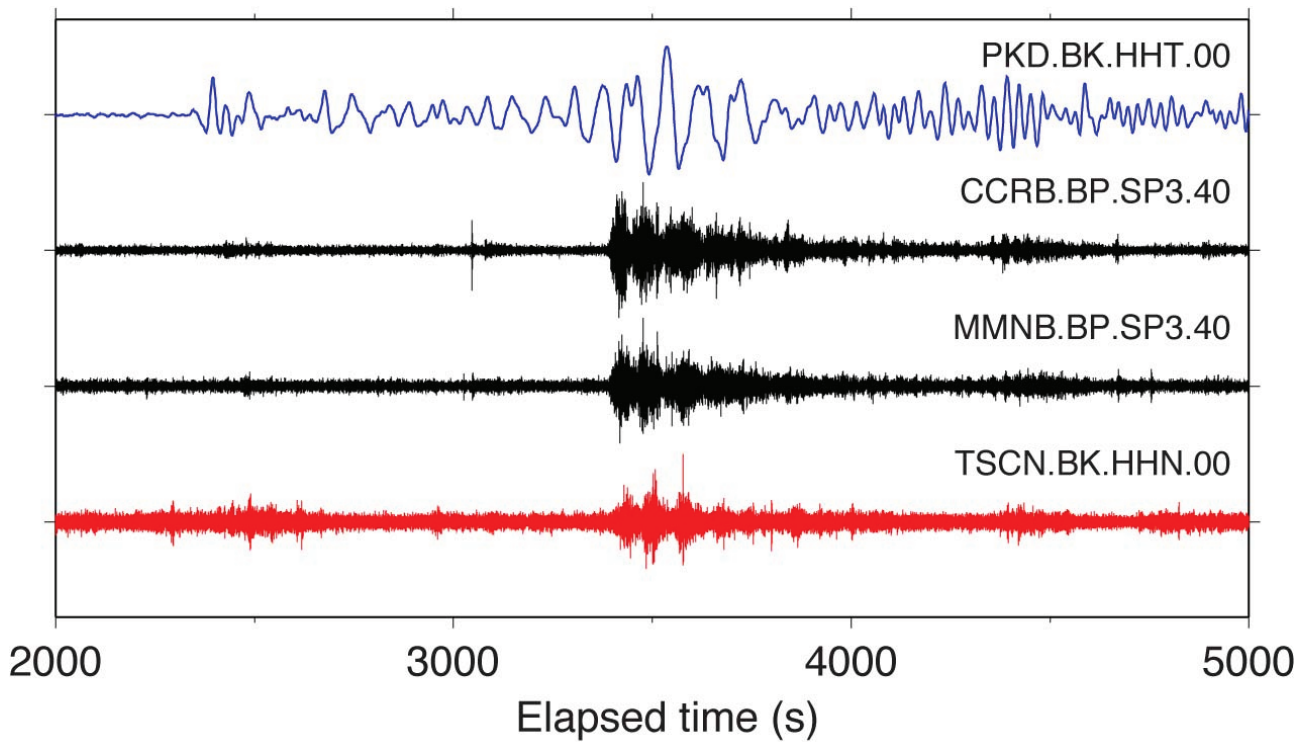


Figure 2.7: Triggered tremor in the surface waves of the April 11, 2012, M8.6 earthquake which occurred off the West Coast of Northern Sumatra. Tremor is apparent in the records of HRSN stations CCRB and MMNB as well as at TremorScope station TSCN.

# 4 Time-dependent Model of Creep on the Hayward Fault from Joint Inversion of 18 Years of InSAR and Surface Creep Data

Manoochehr Shirzaei, Roland Bürgmann

## 4.1 Introduction

Spatial and temporal variations of aseismic fault creep represent important factors in realistic estimation of seismic hazard due to their influence on the size and recurrence interval of large earthquakes along partially coupled faults. To solve for a time-dependent model of creep on the Hayward fault, we invert 18 years of surface deformation data (1992 - 2010), obtained by interferometric processing of 52 and 50 synthetic aperture radar (SAR) images acquired by the ERS1/2 and ENVISAT satellites, respectively, and surface creep data obtained at more than 25 alignment and creepmeter stations. To jointly invert the residual InSAR displacement time series and the surface creep data and to obtain a time-dependent model of creep on the Hayward fault, we use an iterative re-weighted L2-norm minimization approach combined with a linear Kalman filter. The time-dependent model constrains a zone of high slip deficit (low creep rate) that may represent the locked rupture asperity of past and future  $M \approx 7$  earthquakes.

## 4.2 Approach

In this research, we include 18 years of InSAR data collected by the ERS-1, ERS-2 and Envisat satellites. A total of 831 interferograms are processed from 102 images collected between 1992 and 2011. These are processed into a time series of surface range change and used as input in the time-variable modeling. The time history of the creep on Hayward fault is obtained by time-dependent joint inversion of the InSAR time series and surface creep data. To this aim, we employ a method consisting two main operators: (i) a L1-norm minimization operator and (ii) a recursive filter, Kalman Filter (KF), to generate time series of the creep. These two operators are combined in an iterative manner (*Shirzaei and Walter, 2010*). The InSAR data are complemented by observation of surface creep obtained from alignment array measurements (*Lienkaemper, et al., 1991; Lienkaemper and Galehouse, 1997*) and creepmeter data (*Bilham and Whitehead, 1997*) along the Hayward fault.

## 4.3 Observations and Results

Figure 2.8a shows a map of the LOS velocities of the obtained InSAR time series. Major components of the resolved signal include displacement due to plate motions and elastic strain accumulation across the San Andreas fault system, and non-tectonic land subsidence and re-

bound. Here, we focus on the discontinuity along the Hayward fault that is an indicator for shallow fault creep and comprises shorter wavelength features compared to the long term interseismic deformation components (e.g., [*Schmidt, et al., 2005*]). The time-dependent creep rate model of the Hayward fault for 1992-2010 is shown in Figure 2.8b. The darker colors indicate more right-lateral creep. In Figure 2.8b, the location of the creepmeters and alignment arrays and their associated observations of actual surface creep are shown for comparison with the creep model. There is very good agreement between the model and surface creep observations. Our results show that the upper 3-4 km of the Hayward fault from 45 to 70 km distance, creeps faster than the northern section (km 0 - 30). In the north, the faster creep occurs at a depth of 5 - 10 km. A large locked patch that creeps at  $< 1$  mm/yr is constrained at 25 - 45 km, in agreement with earlier works (*Simpson, et al., 2001; Malservisi, et al., 2003; Funning, et al., 2005; Schmidt, et al., 2005*) but not with the model result of *Evans, et al. (2012)*.

## 4.4 Conclusion

We present a spatiotemporal model of creep on the Hayward fault. To this end we explored an 18-year-long time series of InSAR deformation and surface creep data. Our time-dependent creep model reveals a persistent accumulation of slip deficit (more than 90% of the geologic slip rate) along a buried  $\sim 25$ -km-long and  $\sim 7$ -km-wide section of the fault. These results suggest that the creep rate is faster at shallow depths along the southern Hayward fault compared to the northern fault section, which has higher rates at depth. This variation may reflect changes in the regional stress field and/or material heterogeneities along the Hayward fault. Given the fact that most of the Hayward fault accumulates a slip deficit of 30%-90% of its long-term slip budget, we estimate a seismic moment accumulation of  $M_w \sim 6.3$ -6.8, respectively, due to rupturing only the large central locked zone or rupture propagation to the entire 70 km of the Hayward fault including the area of low deficit, since the last big event in 1868.

## 4.5 References

- Bilham, R., and S. Whitehead (1997), Subsurface creep on the Hayward fault, Fremont, California, *Geophys. Res. Lett.*, 24, 11, 1307-1310.
- Evans, E. L., J. P. Loveless, and B. J. Meade (2012), Geodetic constraints on San Francisco Bay Area fault slip rates and

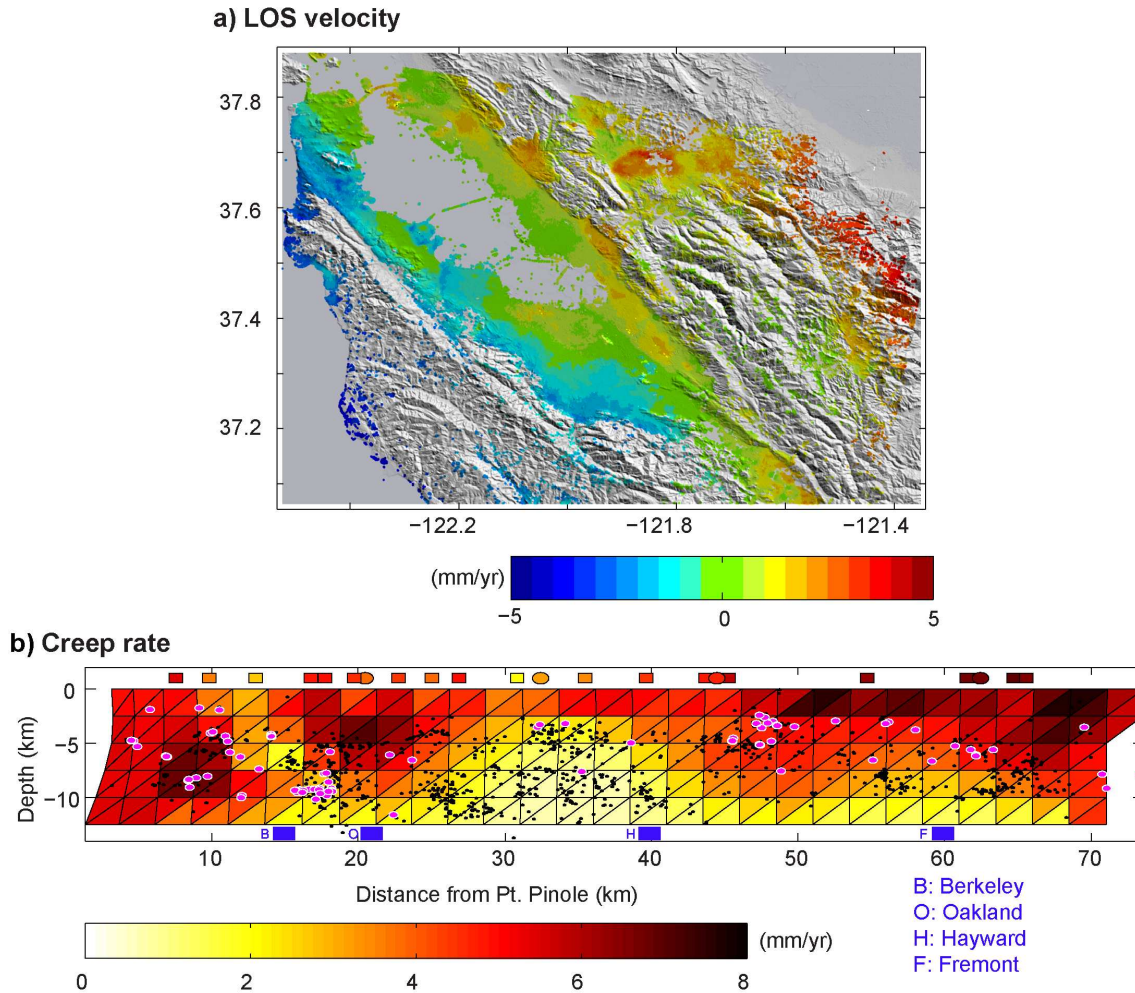


Figure 2.8: a) The LOS velocity from 1992-2010 InSAR time series. Red and blue colors indicate movement toward and away from the satellite, respectively. The satellite incidence angle and heading angles are  $23^\circ$  and  $188^\circ$ . b) Average right-lateral creep rate along the Hayward fault. In addition to microseismicity shown by black dots, the magenta circles show the location of repeating events. Average 1992-2010 rates from surface measurements are shown by symbols on top with same color scale. (See color figure on cover.)

potential seismogenic asperities on the partially creeping Hayward fault, *Journal of Geophysical Research-Solid Earth*, 117.

Funning, G., R. Bürgmann, A. Ferretti, F. Novali, and D. A. Schmidt (2005), Kinematics, asperities and seismic potential of the Hayward fault, California from ERS and RADARSAT PS-InSAR, *EOS, Transactions American Geophysical Union*, 86, 52.

Lienkaemper, J. J., G. Borchardt, and M. Lisowski (1991), Historic creep rate and potential for seismic slip along the Hayward fault, California, *J. Geophys. Res.*, 96, 18261-18283.

Lienkaemper, J. J., and J. S. Galehouse (1997), Revised long-term creep rates on the Hayward fault, Alameda and Contra Costa counties, California, Open-File Rept. 97-690, 618 pp, U.S. Geol. Surv.

Malservisi, R., C. Gans, and K. P. Furlong (2003), Numerical modeling of strike-slip creeping faults and implications for the Hayward fault, California, *Tectonophysics*, 361, 1-2, 121-137.

Schmidt, D. A., R. Bürgmann, R. M. Nadeau, and M. d'Alessio (2005), Distribution of aseismic slip rate on the Hay-

ward fault inferred from seismic and geodetic data, *J. Geophys. Res.*, 110, B8.

Shirzaei, M., and T. R. Walter (2010), Time-dependent volcano source monitoring using interferometric synthetic aperture radar time series: A combined genetic algorithm and Kalman filter approach, *J. Geophys. Res.*, 115, B10421, doi:10.1029/2010JB007476.

Simpson, R. W., J. J. Lienkaemper, and J. S. Galehouse (2001), Variations in creep rate along the Hayward fault, California, interpreted as changes in depth of creep, *Geophysical Research Letters*, 28, 11, 2269-2272.

## 5 Landslide Risk Assessment (LSRA): GPS Instrumentation and Remote Sensing Study of Slope Movement in the Berkeley Hills, California.

Julien Cohen-Waeber (Civil and Environmental Engineering), Roland Bürgmann, Nicholas Sitar (Civil and Environmental Engineering)

### 5.1 Introduction

The objective of this study is to characterize slope deformation as a result of static and dynamic forces, using the most current geodetic technologies that measure active ground surface displacement. New and improved methods for geodetic and remote data collection, such as continuous GPS, and Interferometric Synthetic Aperture Radar (InSAR) allow for a level of primary site characterization and eventual landslide risk assessment that was previously not possible. These technologies need to be incorporated into current practice and tested. Active landsliding across the Lawrence Berkeley National Laboratory (LBNL) site and the greater Berkeley Hills region, California, has been the object of many investigations over recent decades, though the mechanisms of currently mobile, slow moving slides are still poorly understood. Previous studies suggest that a trend in landslide mobility is associated with regional climate and active tectonic conditions in addition to the local geologic setting. A first focus of this project is therefore to study the spatial and temporal distribution of active Berkeley Hills landsliding in relation to local precipitation and ground shaking events by a careful observational program. This program includes the instrumentation of individual landslides with permanent continuously streaming GPS stations, and regional monitoring of slope surface deformation by InSAR time series analysis. Subsequently, the mechanisms of some of these slow moving landslides will be modeled, integrating our surface observations with previous subsurface investigations and monitoring.

### 5.2 Setting

As part of the northwest trending California Coast Range geomorphic province, the Berkeley Hills are an uplifted block of Jurassic to Tertiary sedimentary, volcanic and metamorphic rock formed during regional transpression related to the active plate margin 1-2 million years ago. Now largely overlain by Quaternary colluvial and alluvial deposits, this generally highly fractured, intensely weathered, moderately soft rock is prone to landsliding. In addition to the geologic setting, studies suggest a trend in Berkeley Hills landslide mobility associated with regional climate and active tectonic conditions (*Alan Kropp and Associates*, 2002; *Hilley et al.*, 2004; *Quigley et al.*, 2010). Today, over 500 landslide-related geologic and geotechnical investigation reports are available for LBNL

and the Berkeley Hills alone, and form a solid background to this project.

### 5.3 Methodology

Two state of the art geodetic sensing technologies form the primary modes of data acquisition in this project: high rate, continuously streaming, Global Positioning Systems (GPS) and space-borne Interferometric Synthetic Aperture Radar (InSAR). These methods are complementary in that GPS provides discrete ground surface displacement measurements with millimeter scale accuracy and precision, while InSAR time series analysis produces spatial averages at decameter resolution with sub-centimeter precision. Combining these methods allows for spatial and temporal distribution analysis of ground surface displacements due to landsliding in relation to local precipitation and ground shaking events. By incorporating these surface observations with previous investigations and monitoring, the landslide mechanisms can then be modeled.

### 5.4 Project Status

The first phase of this project has been to instrument individual landslides with autonomous, continuously streaming GPS stations, collecting readings at 1Hz for average daily solutions and a 5Hz buffer in the case of seismic activity. Each device has been specifically designed for permanent installation as a stand-alone station and made to capture actual landslide displacement at depth. Anchored on deep-seated reinforced concrete foundations to avoid the effects of surficial disturbance, the stations are solar powered and equipped with a wireless antenna for remote access. Since January 2012, five such stations have been successfully installed at LBNL and one at the University of California Blake Garden on the Blakemont Landslide. Four additional sites in the Berkeley Hills are in the process of being developed. With the concurrent development of this GPS network, InSAR time series analysis has also begun. Satellite-based Radar images for InSAR time series analysis are available for the Berkeley Hills region dating back to 1992 and have already been the object of several studies as shown in *Hilley et al.* (2004) and *Quigley et al.* (2010).

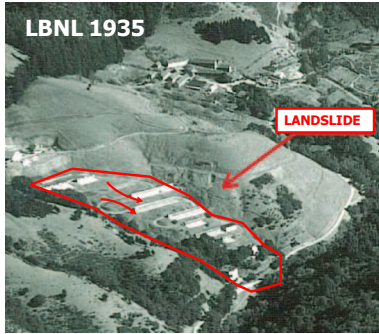


Figure 2.9: 1935 air photo depicting LBNL landslide.

### 5.5 Preliminary Results

Since January 2012, the first 6 continuously streaming GPS stations (LRA 1-6) have been producing daily solutions. Highlighted here are stations LRA 1-3 located on the same landslide at LBNL. While historical ground surface displacement related to this landslide has yet to be characterized and quantified, it is well defined as shown in the 1935 air photo in Figure 2.9 and has been the object of extensive subsurface investigations. Already, a clear signal at each of these 3 stations is apparent, showing down-slope displacements of up to 2cm and directly related to local precipitation. Time histories of daily solutions at stations LRA 1-3, from mid January through mid May 2012 are illustrated in Figure 2.10 and plotted against cumulative rainfall (solid line). Here, the daily solutions for each station’s North and East baselines (circles and triangles respectively) are taken with respect to a fixed station (P224) several kilometers to the South and are shown to be moving down-slope to the west and southwest, accelerating during rainfall events.

### 5.6 Acknowledgements

We gratefully acknowledge our financial support from the Lawrence Berkeley National Laboratory, Earth Science Division Director’s Fund.

### 5.7 References

Alan Kropp and Associates, Blakemont Area Geologic Study, Geologic Hazard Abatement District study, El Cerrito and Kensington CA., 2002.  
 Hilley, G.E., R. Bürgmann, A. Ferretti, F. Novali, and F. Rocca, Dynamics of Slow Moving Landslides From Permanent Scatterer Analysis, *Science*, 304, 1952-1955, 2004.  
 Quigley, K. C., R. Bürgmann, C. Giannico, and F. Novali, Seasonal Acceleration and Structure of Slow Moving Landslides in the Berkeley Hills, *Calif. Geol. Surv. Spec. Report 219, Proceedings of the Third Conference on Earthquake Hazards in the Eastern San Francisco Bay Area*; edited by Keith Knudsen, 169-178, 2010.

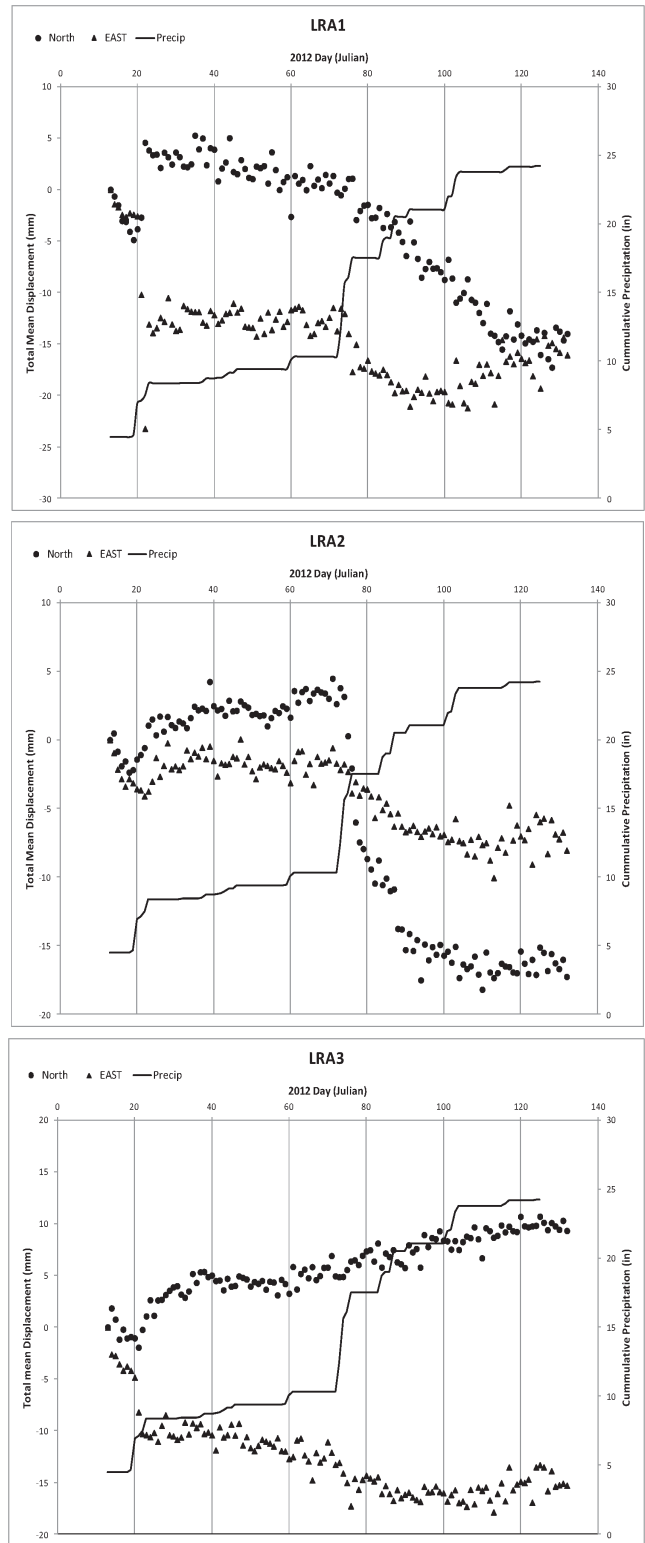


Figure 2.10: Displacement time histories of stations LRA 1-3 with respect to a reference GPS station (P224) to the south. Deviation from the North (circles) and East (triangles) baselines indicates down slope movement to the west and south-west, accelerating during periods of significant precipitation (line).

## 6 Investigating Fault Slip and Rheology Along the San Andreas Fault in the San Juan Bautista Region

Taka'aki Taira, Roland Bürgmann, Robert M. Nadeau, Douglas D. Dreger

### 6.1 Introduction

An improved understanding of the connection between seismic behavior and fault-zone rheology at depth is an essential step toward understanding the underlying mechanics of the faulting process. Spatially and temporally varying aftershock activities following large earthquakes are expected to be sensitive to stress-change magnitudes from the mainshock and spatial variations in rheological properties where aftershocks occur. A detailed analysis of aftershock sequences with the estimation of stress transfer from a mainshock therefore has the potential to illuminate the spatial variation in fault-zone rheology at seismogenic depth. We investigate the seismicity along the northernmost creeping section of the San Andreas fault near San Juan Bautista, California where an abundance of historical seismic and geodetic data is available.

### 6.2 Fault-Zone Rheology Inferred from Temporal Behavior of Aftershock Activity

We systematically examine spatiotemporal behaviors of the aftershock sequences following the 12 August 1998  $M_w$  5.1 San Juan Bautista (SJB) earthquake utilizing continuous seismic data. With the availability of over 20 years of historical seismic data (1984-2011), we make use of waveform data from about 13,000 SJB local earthquakes occurring within a 15 km radius of the epicenter of the 1998 SJB mainshock as template events to identify previously undetected aftershocks. This analysis resolves details of the aftershock activity in a zone at a depth of 9 km about 7 km northwest of the 1998 SJB mainshock (the blue rectangle shown in Figure 2.11). This aftershock zone is marked by one of the highest changes in seismicity rate. The aftershock zone experienced a cluster of earthquakes in the first month of the postseismic period. Except for this postseismic period, the background seismicity rate in this zone has been stable at low level (0.015/day). We infer that the aftershock activity revealed from our analysis was induced by the coseismic stress change from the 1998 SJB mainshock.

Our analysis indicates that the aftershock activity in this zone exhibits a delayed peak ( $\sim 20$  hours after the 1998 SJB mainshock) in the rate of aftershocks, preceded by a period of a very low rate of aftershocks just after the mainshock (Figure 2.12). Subsequently, the rate of aftershocks shows power-law decay with time for about one month, and then there was no clear aftershock activity in this zone. There is no larger aftershock that

could have initiated this sequence around the onset time of the observed delayed peak. This temporal behavior of aftershock activity is different from the predicted aftershock decay based on the model of *Dieterich* (1994). Instead, our observation is more consistent with the decay rate of aftershocks occurring in the transition zone between locked and stable slip, as simulated numerically by *Kaneko and Lapusta* (2008).

We find that the aftershock zone is located near the base of the seismogenic depth (9.2 km) inferred from the depth above which 95 percent of background seismicity occurs. We infer that the San Andreas fault at the SJB region below the seismogenic depth is loaded by deep-seated slip with a long-term slip rate of 2.3 cm/year. Thus, we expect a depth variation in frictional properties near the base of the seismogenic depth or the aftershock zone due to the transition zone from fault locking to fault creep, which would also support the idea that the spatial variation in frictional properties leads to the observed delayed peak and subsequent quiescence in the rate of aftershocks.

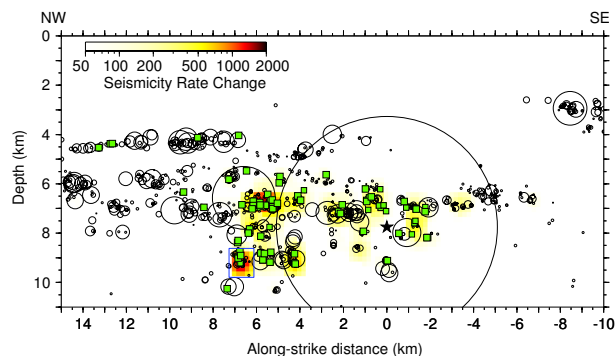


Figure 2.11: Cross-section view of seismicity rate change derived from the numbers of earthquakes occurring before (200 days) and after (30 days) the 1998 SJB mainshock. Black circles are microearthquakes occurring in the first 1000 days of the postseismic period of the 1998 SJB mainshock. Green squares are the identified short-lived ( $\sim 1$  month) repeating earthquake sequences or multiplets. Circle sizes are proportional to earthquake rupture sizes. The blue rectangle indicates the aftershock zone exhibiting a delayed peak in the rate of aftershocks (Figure 2.12). Also shown is the hypocenter of the 1998  $M_w$  5.1 SJB earthquake (star).

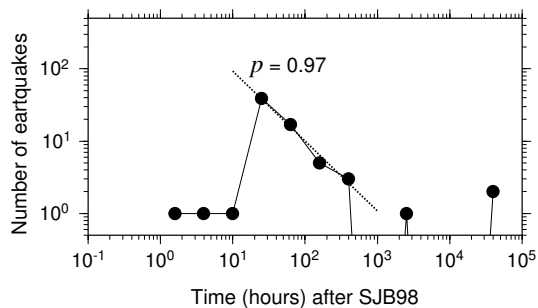


Figure 2.12: Number of earthquakes in the aftershock zone (the location is shown as the blue rectangle in Figure 2.11) following the 1998 SJB mainshock (SJB98). The peak in the rate of aftershocks is observed at about 20 hours after the mainshock. Subsequently, the rate of aftershocks decayed with the slope of  $\sim 1.0/\text{time}$  in a 1-month period, followed by seismic quiescence.

### 6.3 Spatiotemporal Pattern of Characteristically Repeating Earthquakes

Our analysis with continuous seismic data identifies the number of characteristically repeating microearthquake sequences associated with the 1998 SJB mainshock (Figure 2.11). The majority of these sequences have earthquakes occurring within the first 1 month of the post-seismic period. In other words, they reflect short-lived, accelerated repeater recurrences activated by the 1998 SJB mainshock. This temporal pattern could indicate that these sequences are located at rheological boundaries between stable and unstable sliding in which the coseismic stresses were accumulated, rather than that they represent small asperities surrounded by creeping areas. The sequences are localized in the northwest of the 1998 SJB hypocenter. Our kinematic slip inversion of the 1998 SJB mainshock suggests northwest directivity of the rupture propagation (see below and Figure 2.13). We expect larger stress concentrations from the 1998 SJB mainshock in the region northwest of the hypocenter, compared with those in southeast region. Thus, the spatiotemporal pattern of short-lived repeating earthquake sequences will delineate the spatially- and temporally-varying stress transfer induced by the 1998 SJB mainshock.

### 6.4 Rupture Process of the 1998 $M_w$ 5.1 San Juan Bautista Earthquake

Kaneko and Lapusta (2008) showed that a nonuniform coseismic stress change from a mainshock can play an important role in triggering aftershock activity following Omori's law for a certain period of time and then disappearing. A model of the stress transfer from the 1998 SJB mainshock is therefore essential. We estimate the slip distribution of the 1998  $M_w$  5.1 SJB earthquake using

a kinematic source inversion with an empirical Green's function (eGf) approach (Dreger, 1994). We use a  $M$  3.1 foreshock occurring 8 minutes before the mainshock to extract the moment rate function (MRF) of the mainshock through the deconvolution process. The MRFs obtained from distributed broadband stations indicate northward directivity (Figure 2.13a). Our preliminary result shows the 1998 SJB mainshock has a concentrated slip patch with a radius on the order of 50-100 m, with peak slip of about 40 cm (Figure 2.13b). Our next step is to evaluate the spatial variation in Coulomb stress change based on our fault slip model and to explore the variability of fault frictional properties along the San Andreas fault in the SJB region.

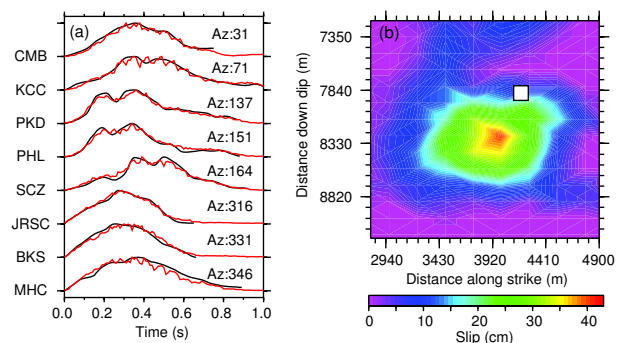


Figure 2.13: (a) Moment rate functions (MRFs) obtained by empirical Greens function deconvolution (black lines). The MRFs show that the pulse width narrows at stations JRSC and BKS (northwest from the 1998 SJB mainshock), indicating rupture directivity to the northwest. Also shown is the synthetic data (red lines) from the slip model shown in Figure 2.13b. (b) Slip distribution obtained for the 1998  $M_w$  5.1 SJB earthquake from the inversion of the eight MRFs shown in Figure 2.13a. The hypocenter is plotted as the white square.

### 6.5 Acknowledgements

We thank R. Turner, P. Audet, and I. Johanson for discussion, and the Northern California Earthquake Data Center (NCEDC) for data collection and distribution. This work is supported by the National Science Foundation EAR-0951430.

### 6.6 References

- Dieterich, J. H., A constitutive law for rate of earthquake production and its application to earthquake clustering, *J. Geophys. Res.*, *99*, 2601-2618, 1994.
- Dreger, D. S., Empirical Green's function study of the January 17, 1994 Northridge, California earthquake, *Geophys. Res. Lett.*, *21*, 2633-2636, doi:10.1029/94GL02661, 1994.
- Kaneko, Y., and N. Lapusta, Variability of earthquake nucleation in continuum models of rate-and-state faults and implications for aftershock rates, *J. Geophys. Res.*, *113*, B12312, doi:10.1029/2007JB005154, 2008.

# 7 Aseismic Slip and Fault Interaction from Repeating Earthquakes in the Loma Prieta Aftershock Zone

Ryan C. Turner, Robert M. Nadeau, and Roland Bürgmann

## 7.1 Introduction

Along creeping sections of the San Andreas and other faults, small asperities in the fault zone load and fail in characteristic repeating earthquake sequences. By calculating their slip based on moment magnitude, they can be used as sub-surface creepmeters. Here, we use these virtual creepmeters to examine and compare slip rates on both the northwestern end of the creeping section of the San Andreas fault (SAF) near San Juan Bautista and the creeping section of the nearby Sargent Fault (SF). While creep on the SAF increases dramatically in response to the 1989 Loma Prieta earthquake (LP), the SF shows very little response, consistent with static stress change models that put this section of the fault in a stress shadow. After about ten years, the SAF creep rate falls back closer to plate rates and begins creeping coherently in time with the SF, indicating a mutual driving force in the system.

## 7.2 Activities

The main study area was comprised of two rectangular swatches aligned along the strike of the SAF (Figure 2.14). The study areas overlap with and extend to the northwest the existing catalog of repeating earthquake sequences and, for the sake of capturing the local extent of the repeaters, extend beyond the creeping section of the central SAF. The areas were chosen to include neighboring sub-parallel faults in the search for repeating earthquake activity, particularly the Sargent Fault (SF) which is known to have documented aseismic dextral creep (Prescott and Burford, 1976). Repeating earthquake sequences were identified by the method of Nadeau and McEvilly (2004). The repeater catalog was also extended to the southeast and now includes the entire central creeping region of the SAF.

## 7.3 Findings

Before the LP earthquake, the slip rates on the SAF and SF do not appear to have had much correlation (Figure 2.15c). After October 1989, the LP rupture clearly has a large influence on the SAF slip rate southeast of about 160 km in our strike-parallel coordinate system, inducing strong rate increases of both pre-existing repeaters and non-repeating aftershocks. The SAF slip rate peaked at 20 cm/year before gradually falling back closer to the interseismic rate of 1cm/yr (Figure 2.15). Meanwhile, the SF creep rate inferred from the repeaters does

not experience any such excursion but does begin gradually increasing, a trend it follows for the next nine years. About 10 years after LP, the SAF and SF begin slipping in a correlated manner, their slip rates rising and falling with similar timing and amplitude.

On the SF, LP aftershocks occur almost exclusively to the northwest of the repeaters, consistent with the creeping-to-locked transition zone being at the edge of a LP stress shadow at about 156 km in our strike-parallel coordinate system. This is contrasted with the aftershock activity on the SAF, which overlaps with the northwestern SAF repeaters. So, while there was an increase in seismicity on the northwestern SF as reported by Reasenberg and Simpson (1997), that increase did not extend into the creeping section of the SF as it did on the SAF.

The static stress changes associated with LP dramatically accelerated slip on the SAF, consistent with measurements of increased surface creep (Behr et al., 1997). That we do not see a dramatic increase in slip rate on the SF seems to agree with the static stress changes on the SF associated with LP (Simpson and Reasenberg, 1994).

## 7.4 Acknowledgements

Background seismicity data taken from Felix Waldhauser's Double-difference Earthquake Catalog for Northern California (1984-2009) - (NCAeqDD.v200912.1). This work is supported through National Science Foundation grant EAR-0951430. Data provided by the Northern California Earthquake Data Center (NCEDC).

## 7.5 References

- Behr, J., R. Bilham, P. Bodin, K. Breckenridge, and A. G. Sylvester, Increased Surface Creep Rates in the San Andreas fault Southeast of the Loma Prieta Mainshock. *U.S.G.S. Professional Paper 1550-D*, pages D179-D192, 1997.
- Nadeau, R. M. and T. V. McEvilly, Periodic Pulsing of Characteristic Microearthquakes on the San Andreas fault, *Science*, 303, 220-222, 2004.
- Prescott, W.H. and R. O. Burford, Slip on the Sargent Fault, *BSSA*, 66(3): pages 1013-1016, June 1976
- Reasenberg, P. A. and R. W. Simpson, Response of Regional Seismicity to the Static Stress Change Produced by the Loma Prieta Earthquake, *U.S.G.S. Professional Paper 1550-D*, pages D49-D71, 1997.
- Simpson R. W. and P. A. Reasenberg. Earthquake Induced Static Stress Changes on Central California Faults, *U.S.G.S. Professional Paper 1550-F*, pages F55-F89, 1994.

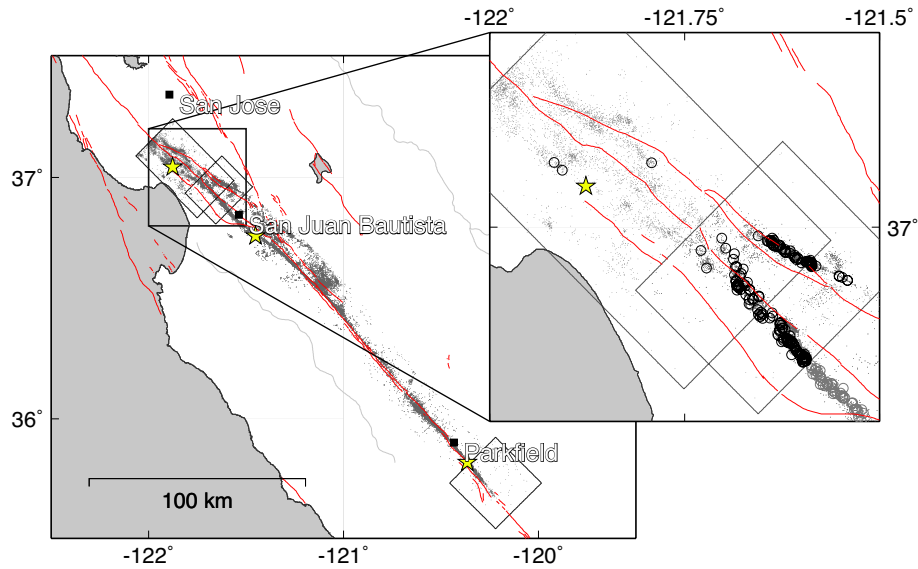


Figure 2.14: Background seismicity in gray points, newly discovered repeaters in black circles (inset). Boxes show extensions of existing catalog. Stars show epicenters of LP EQ and 2004 Parkfield event.

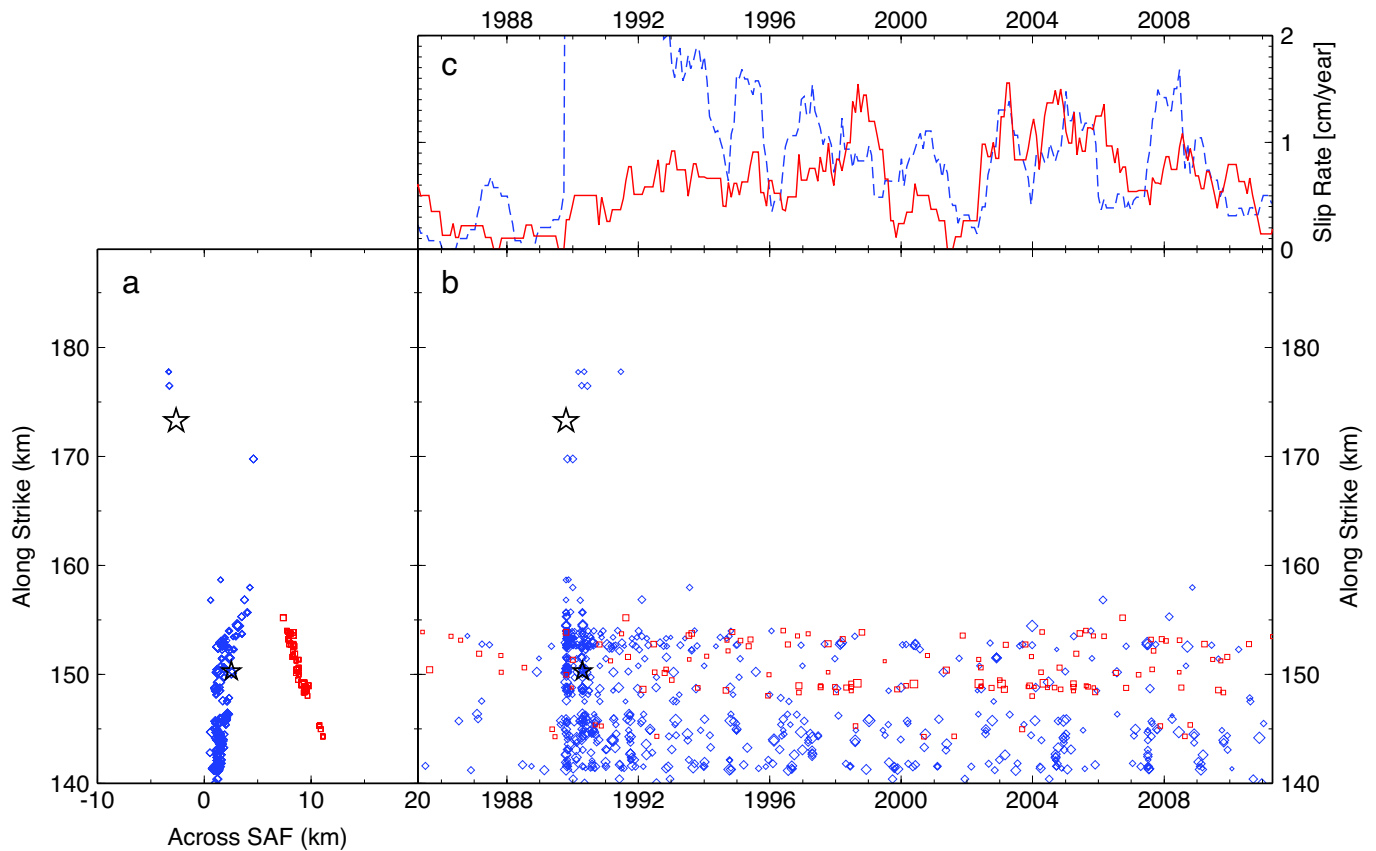


Figure 2.15: a) Repeaters in map view where the y-axis is the distance along strike from Parkfield and the x-axis is the distance from the general strike of the SAF. b) Repeaters in time, along strike. c) Slip rates in cm/yr, calculated from repeating earthquake sequences. Slip rates on the SAF immediately after LP are well off this scale, maxing out at  $\sim 20$  cm/yr. Blue/diamond/dashed events are on the SAF, red/square/solid on the SF.

# 8 Surface Slip during Large Owens Valley Earthquakes from EarthScope Lidar

Elizabeth Haddon (SFSU), Colin Amos, Roland Bürgmann

## 8.1 Introduction

The moment magnitude ( $M_w$ ) 7.4-7.9 Owens Valley earthquake of 1872 is one of the three largest historic earthquakes to impact the state of California. Despite a rupture length of less than 120 km (Amos *et al.*, 2012), ground motions associated with this event were similar or stronger at regional distances compared to large San Andreas earthquakes (Hough and Hutton, 2008). Recent availability of high-resolution lidar topography spanning the surface rupture enables reevaluation of the amount and extent of surface slip during the 1872 and earlier events. These refined paleoseismic parameters allow better characterization of the estimated moment release associated with Owens Valley surface ruptures.

## 8.2 Methods

We capitalize on the 2007 EarthScope lidar topographic dataset to locate, assess and measure laterally displaced geomorphic features using high-resolution (50 cm) bare-earth topography and analysis tools recently developed and described in Zielke *et al.* (2012). We compile over fifty new measurements of lateral offset, and, where possible, test the precision of lidar-based methods by comparing our results to the published measurements of surface slip during the 1872 event (Figure 2.16). Assuming that channel incision generally occurs on shorter timescales than earthquake events, the smallest offsets correspond to the 1872 event. Similarly, progressively larger-offset groups are attributed to earlier surface ruptures.

## 8.3 Findings

Our preliminary findings shed light on the history and size of paleoearthquakes on the Owens Valley fault. The cumulative density of lateral offset measurements is distinctly peaked at values corresponding to the most recent event and earlier surface ruptures. Our results suggest that the horizontal displacement for the 1872 Owens Valley earthquake averaged  $4.9 \pm 1.1$  m (Figure 2.16). This value is similar to, albeit smaller than, previous estimates based on field measurements ( $6 \pm 2$  m; Beanland and Clark, 1994). A subsidiary peak at  $\sim 8$  m may reflect slip variability during the 1872 rupture, or a smaller event with a poorly understood spatial extent. A more prominent peak occurs at  $12.5 \pm 1.2$  m, possibly corresponding to the penultimate earthquake (PE), which occurred at ca. 10 ka (Bacon and Pezzopane, 2007). If so, the total slip distribution implies a similar rupture length for

1872 and the PE (Figure 2.17). A less-distinct peak of cumulative offsets that cluster at  $17.7 \pm 1.8$  m may represent the antepenultimate event (APE, Figure 2.16). This event implies a similar magnitude of surface slip (ca. 5 m) to the 1872 surface rupture. Taken together, our results imply some variability in the amount of surface slip during Owens Valley surface ruptures, although it appears that large earthquakes repeatedly rupture the same fault extent.

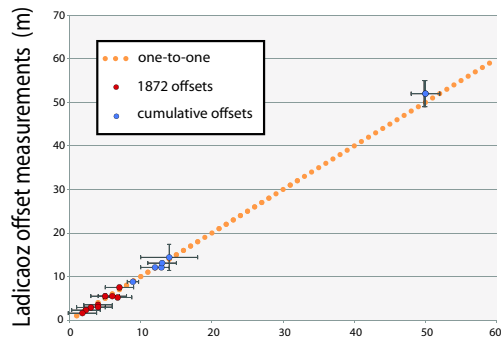
The revised average value of lateral offset of  $4.9 \pm 1.1$  m favors an estimated  $M_w$  7.6 for the 1872 Owens Valley using the scaling relationships of Wells and Coppersmith (1994) and a fault width of  $\sim 20$  km (Hough and Hutton, 2008). As such, anomalously high ground motions observed at regional distances may result from attenuation differences (Bakun, 2006; Hough and Hutton, 2008) or differences in the energetics of Owens Valley surface ruptures in comparison with San Andreas events.

## 8.4 Acknowledgements

This research is supported by Southern California Earthquake Center Award 12140.

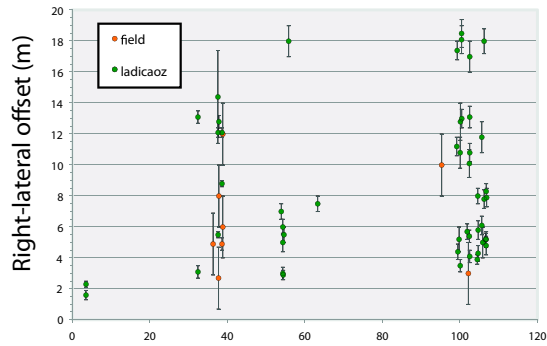
## 8.5 References

- Amos, C. B., Lutz, A., Unruh, J. R., Jayko, A. S., and Mahan, S. A., 2012, Refining the southern extent of the 1872 Owens Valley earthquake rupture - Paleoseismic investigations at Sage Flat and Haiwee Meadows, California, Final Technical Report to the U.S. Geological Survey National Earthquake Hazards Reduction Program, Award Number G09AP00133.
- Beanland, S., and Clark, M.M., 1994, The Owens Valley fault zone, eastern California, and surface faulting associated with the 1872 earthquake: *U.S. Geological Survey Bulletin* 1982, 29 p.
- Bacon, S. N., and Pezzopane, S. K., 2007, A 25,000-year record of earthquakes on the Owens Valley fault near Lone Pine, California: Implications for recurrence intervals, slip rates, and segmentation models: *Geological Society of America Bulletin*, v. 119, no. 7-8, p. 823-847.
- Bakun, W. H., 2006, MMI attenuation and historical earthquakes in the Basin and Range province of western North America: *Bull. Seismol. Soc. Am.* 96, 2206-2220.
- Hough, S. E., and Hutton, K., 2008, Revisiting the 1872 Owens Valley, California, earthquake: *Bulletin of the Seismological Society of America*, v. 98, no. 2, p. 931-949.
- Wells, D., and K. Coppersmith, 1994, New empirical relationships among magnitude, rupture length, rupture width, rupture area, and surface displacement: *Bull. Seismol. Soc. Am.* 84, 974-1002.
- Zielke, O., Arrowsmith, J. R., 2012, LaDiCaoz and LiDARimager - MATLAB GUIs for LiDAR data handling



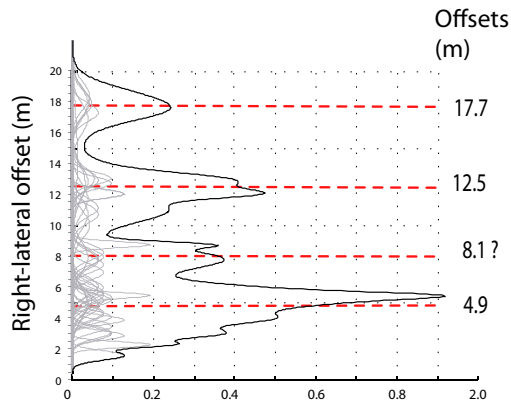
**A**

Field offset measurements (m)



**B**

Distance from southern rupture boundary (km)



**C**

Cumulative kernel offset density

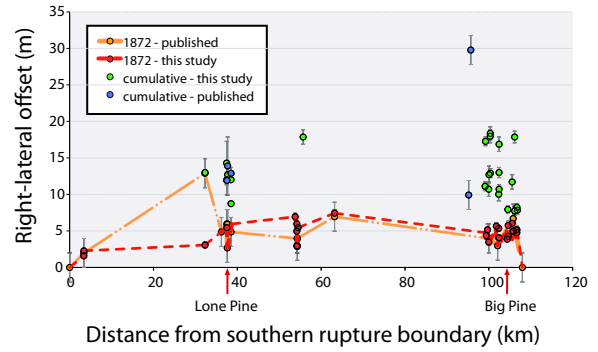


Figure 2.17: Surface slip distribution associated with the 1872 event (red line). Our measurements suggest average dextral slip of  $4.9 \pm 1.1$  m in 1872. The orange line represents the slip distribution as determined by previous field investigations.

and lateral displacement measurement: *Geosphere*, February 2012; v. 8; no. 1; p. 206-221.

Figure 2.16: (A) Plot of lidar field-derived lateral offset measurements. Lidar measurements were made using the LaDi-CaOZ MATLAB graphical user interface. (B) Compiled lateral offset measurements spanning the length of the OVF. (C) The cumulative density of offset measurements is distinctly peaked at  $4.9 \pm 1.1$  m, corresponding to surface slip during the 1872 event. Other peaks may correspond to cumulative offset from earlier events.

## 9 Testing the Temporal Persistence of Slip Rate Along the Little Lake Fault, Eastern California Shear Zone

Colin Amos, Sarah Brownlee (Wayne State), Dylan Rood (LLNL), Roland Bürgmann, G. Burch Fisher (UCSB), Paul Renne (BGC), Angela Jayko (USGS)

### 9.1 Introduction

In the eastern California shear zone (ECSZ), short-term interseismic strain rates measured from geodesy outpace longer-term geologic measurements of fault slip-rate by a factor of about two. This discrepancy characterizes slip rates both summed across the zone as a whole (Oskin *et al.*, 2008) and along individual structures. An early InSAR study in the northern Mojave Desert (Peltzer *et al.*, 2001) exemplifies the latter through demonstration of rapid interseismic deformation focused on the Little Lake and Blackwater faults (Figure 2.18). The magnitude of this strain suggests up to 7 mm/yr of dextral strike slip, despite modest Quaternary slip-rates of 0.5 mm/yr for the Blackwater fault (Oskin and Iriondo, 2004). Conversely, the sinistral Garlock fault, a cross-cutting conjugate to the Little Lake - Blackwater faults displays the opposite sense of rate discrepancy. There, geodetic data indicates that interseismic strain accumulates at a slower average rate than suggested by older, offset geologic markers (Figure 2.19). A potential explanation for this mismatch is that the Garlock and Little Lake-Blackwater faults undergo alternating periods of relatively slow and fast fault slip, corresponding with earthquake clusters along each zone (Dolan *et al.*, 2007). As such, understanding the nature of short and long-term variations in fault slip-rate in the ECSZ has clear implications for seismic hazards in southern California, as well as for interactions and interconnectivity among fault networks within zones of distributed shear.

### 9.2 Methods

Here, we test the persistence of rapid, decadal strain accumulation along the Little Lake fault (Figure 2.18) through combination of new geologic fault slip-rates and InSAR measurements. Geologic constraints exploit a series of fluvial landforms spanning the Little Lake fault, emplaced during intermittent outflows of the Pleistocene Owens River. New geologic mapping and ground-based lidar surveying of these features provide fault-slip measurements for landforms of varying age. Geochronologic control on these features relies on new  $^{40}\text{Ar}/^{39}\text{Ar}$  dating of Quaternary basalts and  $^{10}\text{Be}$  exposure dating of outwash boulders on Late-Pleistocene terrace surfaces. New measurements of interseismic strain spanning the Little Lake - Blackwater and Garlock faults utilize an updated catalog of ERS and Envisat data spanning the last decade and a half.

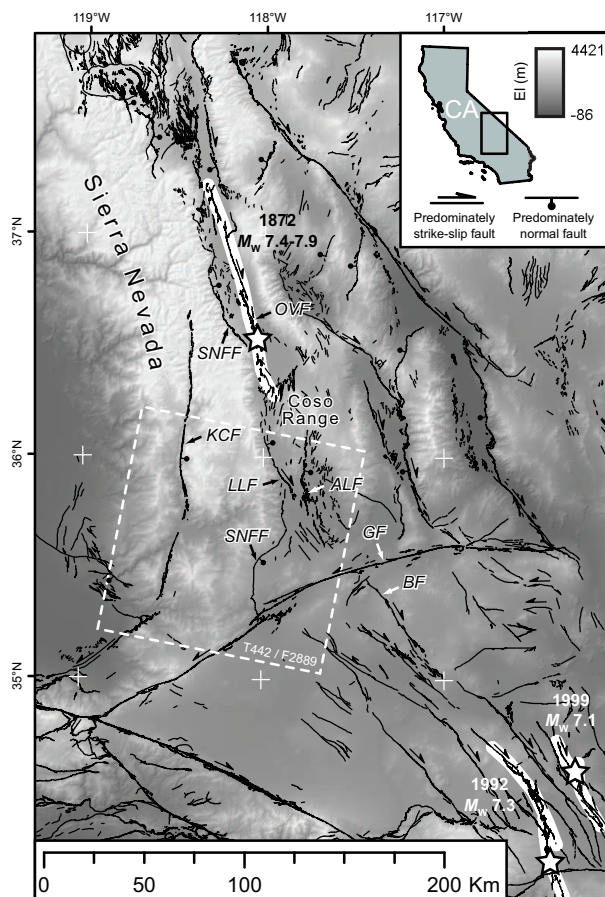


Figure 2.18: Overview of active faults and regional topography of the eastern California shear zone (ECSZ) and southern Walker Lane belt (WLB). Labeled faults are abbreviated as follows: ALF-Airport Lake fault, BF-Blackwater fault, GF-Garlock fault, KCF-Kern Canyon fault, LLF-Little Lake fault, OVF-Owens Valley fault, SNFF-Sierra Nevada frontal fault. Major historical earthquake surface ruptures in the ECSZ and WLB are outlined in white, with stars denoting epicentral locations. Radar scene T442/F2889 is outlined by the dashed white box.

### 9.3 Findings

Geologic slip rates measured from displaced landforms along the Little Lake fault suggest modest, sustained dextral slip averaging ca. 0.7 mm/yr over the past ca. 65 to 200 ky (Figure 2.19). This rate agrees well with Qua-

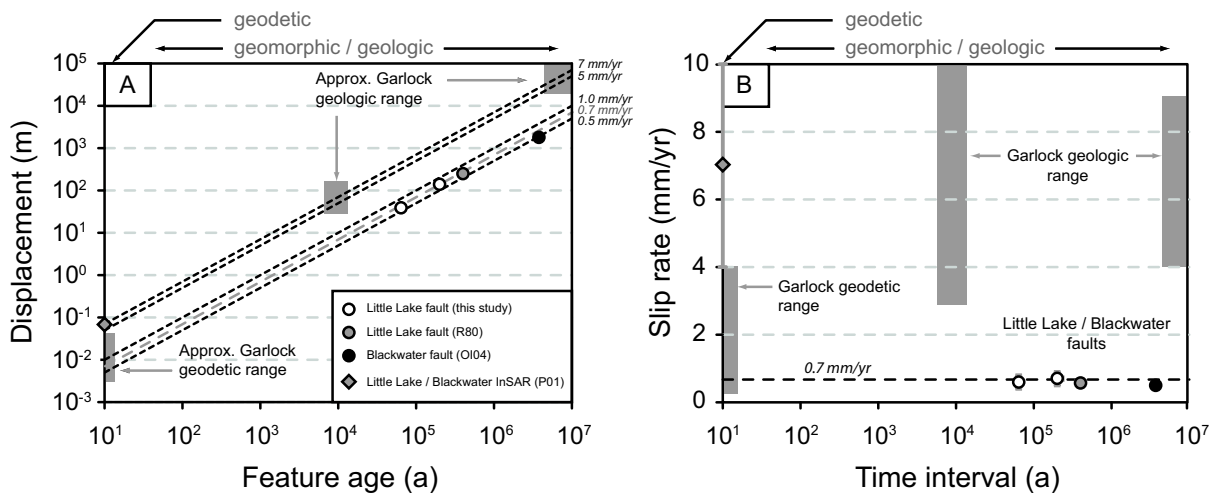


Figure 2.19: Compiled dextral displacements (A) and corresponding fault slip rates (B) as a function of age for the Little Lake, Blackwater, and Garlock faults. Linear regressions in (A) indicate constant slip rates through time. Geodetic measurements represent interseismic deformation measured from InSAR and GPS. See *Ganev et al. (2012)* for a summary of Garlock fault measurements. References in legend: OI04 - *Oskin and Iriondo (2004)*; P01 - *Peltzer et al. (2001)*; R80 - *Roquemore (1980)*.

ternary averaged slip rates along the Blackwater fault, and is substantially slower than geologic slip rates for the Garlock structure. As such, our data suggests that temporal variations in slip, if they occur, happen at shorter time scales than  $10^4$ - $10^5$  years. Although feasible at the time scale of individual earthquakes or earthquake clusters ( $10^3$  yr), our preliminary InSAR results demonstrate similar, modest rates of interseismic strain accumulation along the Little Lake fault. Taken together, our work suggests that relatively rapid strain measured in earlier InSAR studies is transient over decadal periods and does not reflect long-term oscillations between the Little Lake-Blackwater and Garlock faults. Future work will better constrain recent rates of interseismic strain accumulation in this area using InSAR and will investigate the possibility that short-term interseismic strain transients reflect fault interaction and acceleration following nearby earthquakes in the ECSZ (Figure 2.18).

## 9.4 Acknowledgements

This research was supported by NSF Postdoctoral Fellowship Award EAR0847990 to Amos.

## 9.5 References

- Dolan, J. F., Bowman, D. D., and Sammis, C. G., 2007, Long-range and long-term fault interactions in Southern California: *Geology*, v. 35, no. 9, p. 855-858.
- Ganev, P. N., Dolan, J. F., McGill, S. F., and Frankel, K. L., 2012, Constancy of geologic slip rate along the central Garlock fault: implications for strain accumulation and release in southern California: *Geophysical Journal International*, in press.

Oskin, M., and Iriondo, A., 2004, Large-magnitude transient strain accumulation on the Blackwater fault, Eastern California shear zone: *Geology*, v. 32, no. 4, p. 313-316.

Oskin, M., Perg, L., Shelef, E., Strane, M., Gurney, E., Singer, B., and Zhang, X., 2008, Elevated shear zone loading rate during an earthquake cluster in eastern California: *Geology*, v. 36, no. 6, p. 507-510.

Peltzer, G., Crampe, F., Hensley, S., and Rosen, P., 2001, Transient strain accumulation and fault interaction in the Eastern California shear zone: *Geology*, v. 29, no. 11, p. 975-978.

Roquemore, G., 1980, Structure, tectonics, and stress-field of the Coso-Range, Inyo-County, California: *Journal of Geophysical Research*, v. 85, no. NB5, p. 2434-2440.

# 10 Examining the Mechanical Behavior and Evolution of the Southern San Andreas Fault System through Determination of Late Quaternary Slip Rates and Distinct Element Simulations

Kimberly Blisniuk, Roland Bürgmann, Juli Morgan (Rice University), Tom Fournier (Rice University), Warren Sharp (Berkeley Geochronology Center)

## 10.1 Introduction

To better understand the processes driving the kinematic and mechanical evolution of the southern San Andreas Fault System (SAFS) we combine (1) geologic field mapping of offset landforms, (2) Quaternary geochronology to obtain precise estimates of fault slip rates, and (3) distinct element models (DEM) to simulate the behavior and interactions of faults within the system. The southern San Andreas fault zone of the SAFS is an ideal structure to investigate and model processes of crustal deformation because a high rate of strain is localized on a relatively simple set of faults, the Mission Creek and Banning faults. Furthermore, it is the most poorly understood section of the southern SAFS with respect to slip rate and timing of past large-magnitude earthquakes; therefore, its seismic hazard is difficult to quantify. Nonetheless, the seismic hazard that it presents is likely to be high since this section of the fault system is the only major section that has not ruptured in historic time. The last earthquake to rupture occurred over 300 years ago c. 1690. Accordingly, the long lapse time since the last surface rupture implies that this section of the SAFS is in the late phase of its earthquake cycle, and that strain accumulated over the past 300 years is likely to be relieved in a large-magnitude earthquake.

## 10.2 Preliminary Field Observations and Sample Collection

Four study sites located on the southern San Andreas fault zone have been identified to constrain geologic slip rates. At these sites, we have conducted detailed geomorphic mapping and initial sample collection from: (1) 2 of 3 channels completely beheaded from Pushawalla Canyon offset by the Mission Creek fault (Figure 2.20); (2) offset late Pleistocene and Holocene alluvial fan deposits (assessed based on surface and soil characteristics) on the Mission Creek fault at Dell Wash, just south of Pushawalla Canyon (Figure 2.20); (3) a late Pleistocene fan deposit offset by the Banning fault located between Thousand Palms Canyon and Pushawalla Canyon (Figure 2.20); and (4) an offset Holocene alluvial fan deposit (assessed based on surface and soil characteristics) offset along 2 strands of the Mission Creek fault at Thermal Wash (not shown).

## 10.3 Geochronology

Multiple Quaternary dating techniques, namely, surface exposure using cosmogenic  $^{10}\text{Be}$  isotopes and U-

series of pedogenic carbonate clast-coatings, will be applied to reliably constrain fault slip rates. The combination of these methods can significantly improve the reliability of landform dating because exposure ages from cosmogenic isotopes can be biased by post-depositional surface processes and inherited nuclides, while U-series dating of pedogenic carbonate provides minimum ages for alluvium because carbonate accumulation ensues after deposition of the host material. However, the factors controlling precision and accuracy of the two techniques are relatively independent. Thus, combining them can significantly improve the reliability of landform dating and ultimately yield more accurate slip rates.

## 10.4 Distinct Element Models

To illustrate the potential of DEMs, scaled 2-D simulations of a fault zone comprising two fault strands (1 km long, spaced 0.6 km across) are shown in Figure 2.21. In the model,  $\sim 15,000$  particles with radii of 3 to 4 m are confined between two horizontal walls, and interparticle bonds with an interparticle friction of 0.3 are applied at the contacts, except along two prescribed fault surfaces (F1 and F2 in Figure 2.21) within the domain. Moving the top and bottom walls in opposite directions, under constant confining pressure, imposes right-lateral shear strain on the zone. As expected, shear deformation is localized onto the prescribed fault surfaces. The two fault strands exhibit rapid temporally variable activity as slip transfers between them; slip along the fault surfaces also varies spatially, as a function of fault locking and release, which is directly correlated with increasing and decreasing differential stress. In this scaled system, individual fault strand inactivity can persist for as long as 30 increments (i.e.,  $\sim 13.5$  m of relative wall displacement). In a general sense, the duration of fault inactivity is proportional to the applied normal stress, reflecting its influence on fault locking. This shows that 2-D DEMs may be a useful tool to evaluate the observed patterns of fault system behavior, as they permit the tracking of fault evolution and associated local stress field changes, which can highlight specific mechanical processes governing deformation across the SAFS.

## 10.5 Acknowledgements

This project is funded by NSF's Earth Science Postdoctoral Fellowship program awarded to Kimberly Blis-

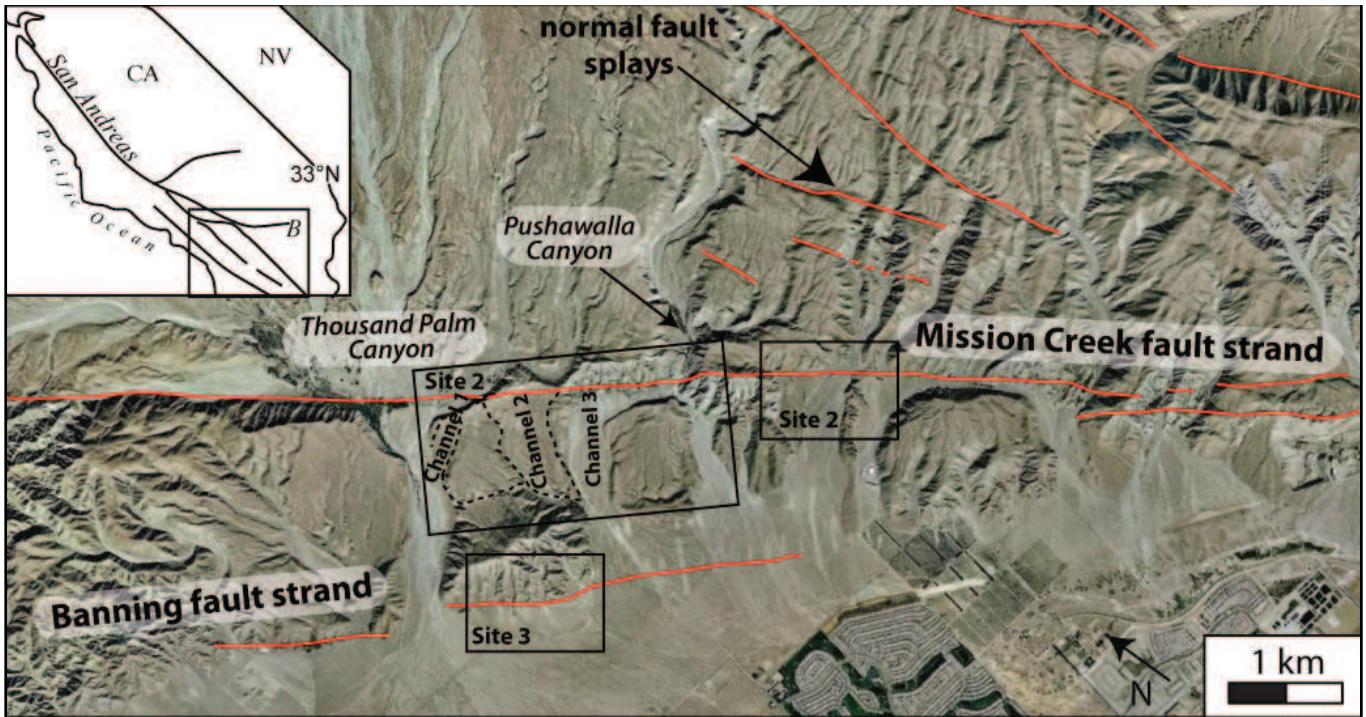


Figure 2.20: Preliminary interpretation of a GoogleEarth image of sites 1 through 3 (Indio Hills/Thousand Palms Oasis) showing the location of dextrally offset channels and alluvial fans along the Mission Creek and Banning faults of the southern San Andreas fault zone.

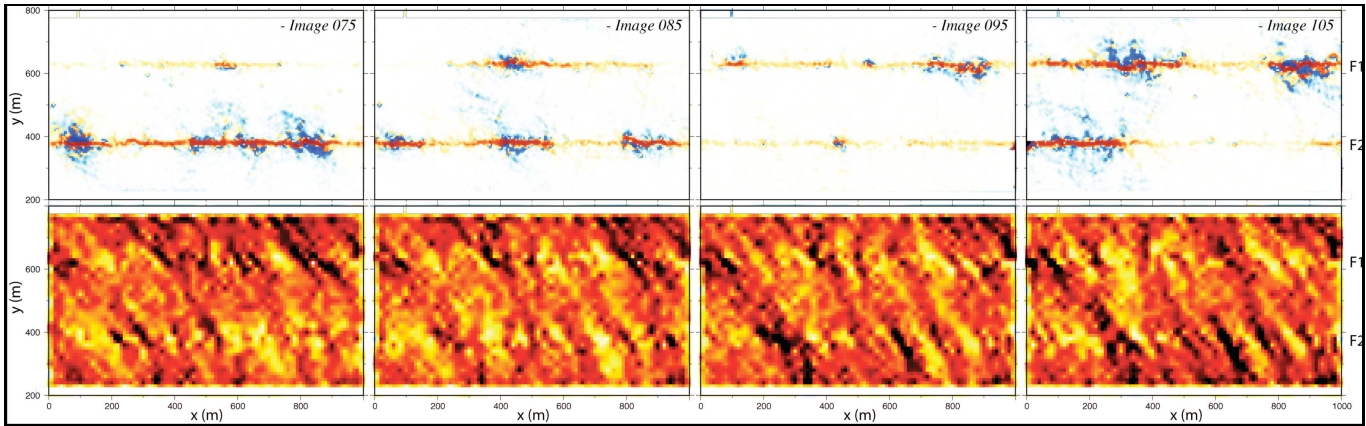


Figure 2.21: Sequence of incremental strain (top panels) and differential stress (bottom panels) distributions in a simulated two fault system, undergoing right lateral shear at a constant far-field strain rate, under a confining pressure of 30 MPa. Images record incremental slip over 0.45 m of relative wall displacement (0.075 % shear strain), but are plotted at intervals of 4.5 m displacement. Red and blue colors denote right- and left-lateral shear strain, respectively, with color intensity scaled with slip magnitude. Right-lateral slip is localized onto the fault surfaces, but shows significant variations over time, and transfer of slip between fault strands. Blue "bursts" adjacent to the fault surfaces indicate earthquake-like slip events on the fault strand as locked zones are released, causing rebound of the adjacent wall rocks. Inclined zones of high differential stress (hotter colors) support compressive stresses within the domain, and correlate with locked zones along the faults. Stress releases correspond with fault rupture events (Images courtesy of J. Morgan and T. Fournier).

niuk under grant number NSF EAR-0757608

# 11 Investigating Fault Slip Budget in the Mendocino Triple Junction

Taka'aki Taira

## 11.1 Introduction

High-quality seismic and geodetic data from dense networks have revealed that the Mendocino Triple Junction (MTJ) Zone, California experiences a wide variety of transient fault slip, including earthquakes, slow slip events, and tectonic tremors (Figure 2.22a). Detecting these transient deformation fields with estimations in the locations of responsible deformation areas is a fundamental first step in addressing the slip budget in the MTJ zone. Additionally, an analysis of historical seismic data continuously recorded by broadband seismic stations identifies characteristically repeating earthquake sequences along the Mendocino Fracture Zone. Spatiotemporal properties in these sequences would allow us to infer aseismic fault slip surrounding the sequences.

## 11.2 Transient Deformation in 2008

Geodetic measurements of the MTJ zone with GPS arrays detected an aseismic slip episode with the west component of displacement up to 8 mm (Figure 2.22b). GPS time series have suggested that this aseismic slip episode may have nucleated near Weaverville, CA in March 2008 and propagated to the northwest over a 2-month period. At the same time, broadband seismic records have revealed that an area of northernmost California (e.g., Yreka) experienced an episode of tectonic tremors. Tectonic tremor observed consists of intermittent weak seismic signals at relatively low frequency (1-5 Hz). An array of broadband stations ( $\sim 30$  stations) was temporally deployed at the Cape Mendocino area in 2007-2009 through the Flexible Array Mendocino Experiment (e.g., *Porritt et al.*, 2011). These Mendocino broadband data significantly improve detectability of tectonic tremor signals and enhance the spatial resolution in the locations of tectonic tremors. We systematically analyzed high-quality broadband data to identify and locate tectonic tremors. Following *Ide* (2012), we used a waveform-envelope correlation method to detect tectonic tremors. Our analysis showed that a slow migration occurs parallel to the strike of the subducting slab at an average velocity of about 3-4 km/day (Figure 2.23). The observed temporal correlation between the aseismic slip transient and the tectonic tremor activity may suggest that a single mechanism is mainly responsible for nucleating these transient deformations. We also note that toward the end of the transient deformations (e.g., aseismic slip and tremor) in the end of April 2008, a normal-faulting event with  $M_w=5.3$  occurred around the aseismic deformation area. Although we do not yet estimate the spatial extent of

the aseismic slip transient and its temporal behavior, the stress from the aseismic slip transient may have triggered this extensional earthquake. Similar stress interactions between aseismic slip transients and extensional earthquake activity are observed in other subduction zones. *Liu et al.* (2007) have observed a cluster of extensional earthquakes in Guerrero, Mexico during 2006 that is temporally correlated with a large aseismic deformation transient. The Guerrero observation in *Liu et al.* (2007) showed that the extensional earthquakes corresponded to the initiation of the aseismic deformation transient, indicating that the aseismic deformation transient seems to be initiated by extensional earthquakes. Thus, the underlying mechanisms of the sequential transient deformations observed in the MTJ zone and in the Guerrero region would be different. Nevertheless, we speculate that similar stress transfer processes are involved in these two sequential deformations.

## 11.3 Characteristically Repeating Microearthquakes

By utilizing waveforms from  $\sim 5,000$  MTJ local earthquakes ( $M > 2.5$  in 1992-2011), we have been identifying repeating microearthquakes in the MTJ zone (Figure 2.24), detecting numerous and distributed sites of repeating microearthquake activity along the Mendocino Fracture Zone (red circles shown in Figure 2.22a). Their recurrence intervals are about 2-3 years, which may be the result of aseismic fault slip surrounding the sequences.

## 11.4 Acknowledgements

This work is supported by the U.S. Geological Survey NEHRP program under grant number G11AP20168.

## 11.5 References

- Ide, S., Variety and spatial heterogeneity of tectonic tremor worldwide, *J. Geophys. Res.*, *117*, B03302, doi:10.1029/2011JB008840, 2012.
- Liu, Y., J.R. Rice, K.M. Larson, Seismicity variations associated with aseismic transients in Guerrero, Mexico, 1995-2006, *Earth and Planetary Science Letters*, *462*, 493-504, 2007.
- McCrory, P.A., J.L. Blair, D.H. Oppenheimer, S. R. Walter, Depth to the Juan de Fuca slab beneath the Cascadia subduction margin: A 3-D model for sorting earthquakes, U. S. Geol. Surv. Data Series, DS-91, 2004.
- Porritt, R.W., R.M. Allen, D.C. Boyarko, M.R. Brudzinski, Investigation of Cascadia segmentation with ambient noise tomography, *Earth Planet. Sci. Lett.*, *185*, 67-76, doi:10.1016/j.epsl.2011.06.026, 2011.

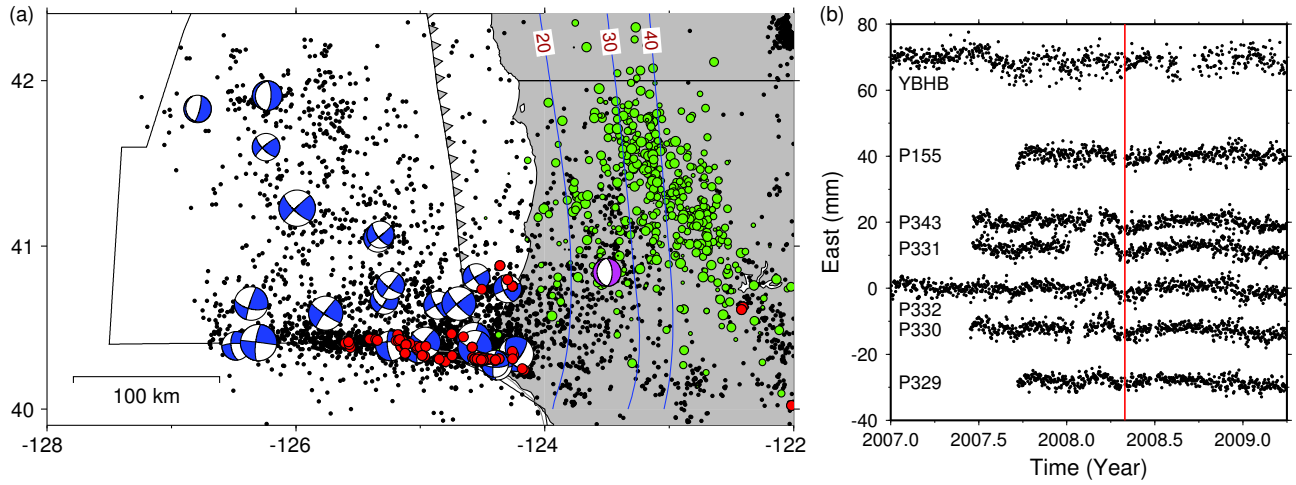


Figure 2.22: (a) Location of the MTJ earthquakes (black circles) between 1984 and present from the Northern California Earthquake Data Center (NCEDC) catalog. Green circles are identified tectonic tremors in 2008, identified from our analysis. Red circles are characteristically repeating earthquake sequences. Also shown are focal mechanisms for  $M > 5$  earthquakes determined from the NCEDC moment tensor analysis. The purple one is the 2008  $M_w$  5.3 normal-faulting earthquake. Blue lines are the plate interface from *McCrory et al.* (2004). (b) GPS time series in the east-west component determined by the Pacific Northwest Geodetic Array (PANGA). Black positions are daily GPS station positions in mm. The red line is the occurrence of the 2008  $M_w$  5.3 normal-faulting earthquake.

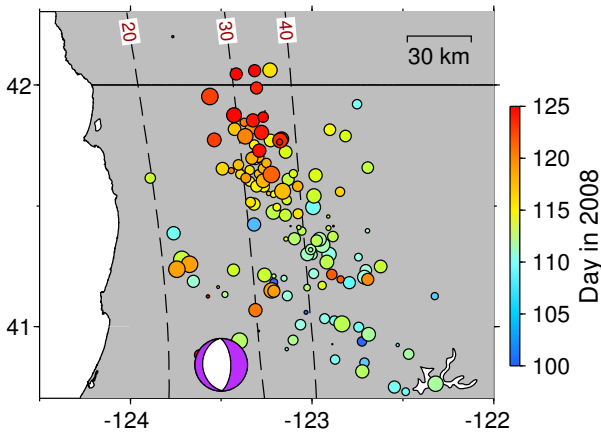


Figure 2.23: Tremor epicenters (circles color coded by time) during the transient deformation in 2008. About 150 tectonic tremors are identified. The circle sizes are inversely proportional to the uncertainty in the tremor locations. The focal mechanism shown in purple is the 2008  $M_w$  5.3 normal-faulting earthquake. Also shown is the plate interface geometry (contoured at 10-km intervals) from *McCrory et al.* (2004).

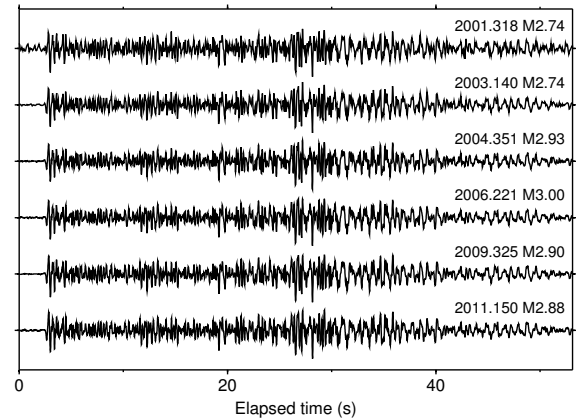


Figure 2.24: Repeating earthquake sequences identified in our analysis recorded at station WDC. The average event magnitude is around 2.8.

## 12 Incipient Faulting near Lake Pillsbury, CA

Amanda M. Thomas, Roland Bürgmann, Douglas S. Dreger

### 12.1 Anomalous Seismic Activity

In March of 2000, a swarm of earthquake activity lasting approximately six months and culminating in an  $M_w$  4.4 earthquake occurred along the eastern edge of the Middle Mountain block (Hayes *et al.*, 2006), between the Ma'acama and Bartlett Springs faults in Northern California. The swarm began with a month-long period of intense microseismicity that preceded the shallow  $M_w$  4.4 event which occurred on May 17, 2000. Over the course of the next three months, microseismicity at depths of 3 to 8 km propagated to the southeast and eventually a second large  $M_w$  4.0 earthquake occurred at the southeast end of the seismic lineament. The area sustained elevated earthquake activity for the next 6 years and between 2006 and 2007 another intense swarm culminated in a  $M_w$  4.8 earthquake. This event was similarly preceded by very energetic microseismicity.

Precise earthquake locations (Waldhauser *et al.*, 2008) from both swarms illuminate discontinuous, geometrically complex structures that roughly parallel the strike of faults within the San Andreas fault (SAF) system. In the south, a small fraction of the seismicity occurs shallowly around 2 km, however the majority of hypocenters are aftershocks of the  $M_w$  4.0 event and cluster between 5 and 8 km depth on a plane dipping 70°NE. Continuing northwest along strike, seismicity shallows and localizes onto a near vertical structure extending from 1 to 6 km depth, near the hypocenter of the  $M_w$  4.4. Further north, shallow, diffuse seismicity extends between the surface and 3 km depth and hypocenters are located as much as 3 km off fault. In this same area deeper events, which mostly consist of aftershocks from the  $M_w$  4.8 event, delineate a N-S striking plane dipping 70°NE.

To further constrain the geometry and structural maturity of the lineament we compute double-couple focal mechanisms for all events with 25 or more first motion observations and full-waveform moment tensors for the three largest events (Hardebeck and Shearer, 2002; Dreger *et al.*, 2000). First motion solutions generally have large uncertainties in strike, rake, and dip, which are primarily due to gaps in the takeoff angle particularly before the installation of the Transportable Array stations prior to the 2006-7 swarm. However, the similarity of nearby first motion solutions and agreement with the independent analyses of McLaren *et al.* (2007) and Hayes *et al.* (2006) suggests that solutions may be useful in constraining lineament geometry. Figure 1 compares the moment tensor solutions for the 2000  $M_w$  4.4, 2000  $M_w$  4.0, and 2007  $M_w$  4.8 earthquakes, populations of fault plane so-

lutions of nearby earthquakes, and the geometry defined by the earthquake hypocenters. In the southern swarm, focal mechanism and moment tensor solutions indicate that nearly all events are right-lateral strike-slip earthquakes that occur on structures striking parallel to the Ma'acama and Bartlett Springs faults. Some of these events, particularly those associated with the  $M_w$  4.4, occur on vertically dipping fault planes, however others, including the  $M_w$  4.0, slip on more shallowly dipping structures that are not optimally oriented. In the northern swarm, mechanisms are highly variable and consist of predominantly right-lateral strike-slip and normal faulting events. Both the first motions and hypocenter locations indicate faulting below 2 km depth occurs along a N10°W trending plane that dips 70°E. The moment tensor solution for the  $M_w$  4.8 has a similar strike but dips 79° which differs by 9° from the dip inferred from the hypocenters. The 90% confidence interval on the dip angle of  $M_w$  4.8 solution spans a dip range that includes 70°, however the 80% confidence intervals do not, suggesting this event may have slipped on a plane with a different orientation than that delineated by the hypocenters. While uncertainties in the best-fit geometries were not considered we note this discrepancy because it suggests that the  $M_w$  4.8 may have involved the fracture of intact rock.

### 12.2 Comparison to Incipient Faulting in the Field

Earthquake swarms are a relatively common occurrence and have been linked to aseismic slip, pore fluid migration, and volcanic activity (see Roland and McGuire, 2009 and references therein). The geometric complexity, earthquake hypocenters, and focal mechanisms of the seismic lineament suggest that it may be an incipient fault (Bawden *et al.*, 1999). Similar fault geometries have been documented extensively in field studies of the initial stages of shear zone development (Martel, 1988). Structural complexity arises for two reasons. First, faults take advantage of preexisting weaknesses, which may have developed in either an earlier tectonic event or in the same tectonic event (Crider and Peacock, 2004). These zones of weakness typically have poor connectivity and are generally neither coplanar nor optimally oriented. Second, to form a through-going fault while still exploiting these weaknesses, secondary fractures are generated in response to the stress fields surrounding en echelon cracks (Martel *et al.*, 1988; Martel, 1990; Crider and Peacock, 2004). Similarly, the seismic lineament is

structurally segmented with abrupt changes in geometry between the south and north and a general lack of any geometric definition in the shallow events in the north. The colocation of the lineament and the Bucknell Creek fault in the south and with relic dipping structures in the north suggests the lineament may be exploiting pre-existing structure as it propagates northward. Additionally, many of the normal events have strikes coincident with the  $\sim$ N-S direction of the maximum compressive stress suggesting that small-scale extensional faulting occurs between the two structures.

Focal mechanisms and deformation style also vary markedly along strike. In the south first motion mechanisms are mostly right-lateral strike-slip events that have strikes and dips consistent with the structure delineated by the seismicity. In the north, both the variety of mechanisms and the inconsistency between the geometry delineated by the seismicity and that of the moment tensor for the  $M_w$  4.8 event argue for immature faulting. In a survey of northern California focal mechanisms, *Castillo and Ellsworth* (1993) find that right-lateral transform motion between the North American and Pacific Plates often occurs on structures dipping between  $50^\circ$  and  $75^\circ$ . They suggest these structures may have formed as reverse faults in the forearc of the Cascadia subduction zone and furthermore, due to the way in which this deformation is accommodated, will eventually evolve to a more energetically favorable, vertical strike-slip geometry common to the majority of faults within the SAF system (*Castillo and Ellsworth*, 1993). If their interpretation is correct, then the  $M_w$  4.8 earthquake likely reflects the transition between these two styles of deformation because it occurred as a strike-slip event on a  $70^\circ$  dipping structure about 10 km north of the more mature southern section of the Bucknell Creek lineament. Focal mechanisms on the Bartlett Springs fault at roughly the same latitude exhibit a similar transition between deformation on dipping planes to near-vertical geometries (*Castillo and Ellsworth*, 1993). This suggests that preexisting zones of weakness localize deformation which concentrates stresses and facilitates the development of a new fault zone in a mechanically favorable orientation.

### 12.3 Acknowledgements

This work is funded by the Geological Society of America Student Research Grant and a National Science Foundation Graduate Research Fellowship.

### 12.4 References

Bawden, G. W., Michael, A. J., and Kellogg, L. H., 1999, Birth of a fault: Connecting the Kern County and Walker Pass, California, earthquakes. *Geology*, v. 27, p. 601-604.

Castillo, D. A., and Ellsworth, W. L., 1993, Seismotectonics of the San Andreas fault system between Point Arena and Cape Mendocino in northern California: Implication for the

development and evolution of a young transform. *Journal of Geophysical Research*, v. 98, p. 65436560.

Crider, J. G., and Peacock, D. C. P., 2004, Initiation of brittle faults in the upper crust: a review of field observations. *Journal of Structural Geology*, v. 26, p. 691-707, doi: 10.1016/j.jsg.2003.07.007.

Dreger, D. S., Tkali, H., and Johnston, M., 2000, Dilational Processes Accompanying Earthquakes in the Long Valley Caldera. *Science*, v. 288, p. 122-125.

Hardebeck, J.L., Shearer P.M., 2002, A New Method for Determining First-Motion Focal Mechanisms. *Bulletin of the Seismological Society of America*, v.92, p.2264-2276.

Hayes, G. P., Johnson C. B., and Furlong K. P., 2006, Evidence for melt injection in the crust of northern California?. *Earth and Planetary Science Letters*, v. 248, p. 638-649, doi: 10.1016/j.epsl.2006.05.008.

Huffman M. E., 1969, Engineering Geology of Garrett Tunnel and Potter Valley Conveyance System. *State of California Department of Water Resources*, Memorandum Report.

Kelsey, H. M., and Carver, G. A., 1988, Late Neogene and Quaternary tectonics associated with northward growth of the San Andreas transform fault, northern California. *Journal of Geophysical Research*, v. 93, p. 47974819.

Martel, S. J., Pollard, D. D., and Segall, P., 1988, Development of simple strike-slip-fault zones, Mount Abbot Quadrangle, Sierra-Nevada, California. *Geological Society of America Bulletin*, v. 100, p. 1451-1465.

Martel, S. J., 1990, Formation of compound strike-slip fault zones, Mount Abbot quadrangle, California. *Journal of Structural Geology*, v. 12, p. 869877, 879882.

McLaren, M. K., Wooddell, K. E., Page, W. D., van der Elst, N., Stanton, M. A., and Walter, S. R., 2007, The McCreary Glade Earthquake Sequence: Possible Reactivation of Ancient Structures Near Lake Pillsbury, Northern Coast Ranges, Mendocino County, California: *Eos Transactions, AGU*, v.88, no.52, Fall Meet. Suppl., Abstract S21A-0245.

Powell, R. E., and Weldon, R. J., 1992, Evolution of the San Andreas fault. *Annual Review of Earth and Planetary Sciences*, v. 20, p. 431-468, doi: 10.1146/annurev.earth.20.1.431.

Roland, E. and J. J. McGuire, 2009, Earthquake Swarms on Transform Faults, *Geophys. J. Int.* v. 178, p. 1677-1690, doi: 10.1111/j.1365-246X.2009.04214.x.

Waldhauser, F. and Schaff, D. P., 2008, Large-scale relocation of two decades of Northern California seismicity using cross-correlation and double-difference methods. *Journal of Geophysical Research*, v. 113, B08311, doi:10.1029/2007JB005479.

## 13 Measurements of PBO Borehole Seismometer Orientations

Taka'aki Taira, Kathleen M. Hodgkinson (UNAVCO), Otina Fox (UNAVCO), David Mencin (UNAVCO)

### 13.1 Introduction

Borehole observations from Plate Boundary Observatory (PBO) seismometers yield a substantially lower detection threshold for lower-amplitude earthquakes and non-volcanic tremors. The three components of PBO borehole data have the potential to improve the identification of seismic phases that will provide high-resolution spatio-temporal monitoring of these lower-amplitude tectonic events. However, the orientations of PBO borehole sensors are not yet well-documented because it is fundamentally difficult to install borehole sensors with a specified orientation, particularly in the horizontal component. A robust estimate of borehole sensor orientations is thus very important for fully utilizing borehole seismic data for investigations of earthquake source and Earth structure. We present a simple method for identifying borehole sensor orientations in the horizontal component based on a waveform cross-correlation analysis and show the result for the PBO stations deployed in Anza, California, in which a number of broadband stations are installed near the PBO borehole stations (Figure 2.25). The primary objective of this project is to provide the necessary information in the instrument responses for the PBO borehole seismic sensors, to allow a broad cross-section of the research community to make use of the PBO borehole seismic data.

### 13.2 PBO Borehole Data

PBO borehole data improve the detectability of lower-magnitude earthquakes (Figure 2.26). The magnitude sensitivity of the Southern California Seismic Network (SCSN) is geared toward providing completeness down to at least M 1.4 in the Anza region (Kane *et al.*, 2007). However, the low noise recordings from a dense array of PBO borehole stations in the Anza region indicate that these stations could be capable of recording events with good signal to noise down to magnitudes approaching 0 (Figure 2.26). These lower magnitude data can provide a significantly greater number of events for investigating the underlying mechanics of the faulting process.

### 13.3 Horizontal PBO Sensor Orientation

The cross-correlation method used is based on the principle that highly similar long-period waveforms ( $> 20$  s) will be observed at collocated borehole and reference broadband seismic sensors. The method involves performing a grid search over all possible values of sensor azimuths for borehole data, rotating borehole data with

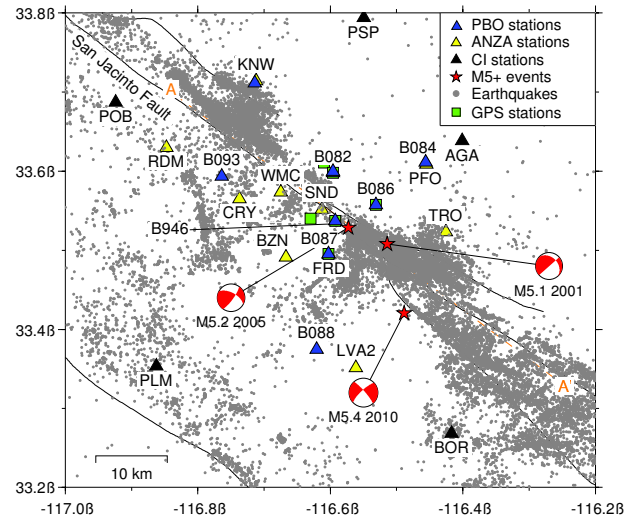


Figure 2.25: Location of the Anza earthquakes (gray circles) during 1984-2005 from *Lin et al.* (2007). Also shown are M  $> 5$  earthquakes (red stars) from the SCSN catalog since 1985. Triangles are seismic stations. Blue triangles are the PBO borehole stations. Black and yellow ones are the USGS seismic stations and the broadband stations of the Anza Broadband Seismic Network, respectively. Also shown are the five GPS stations (green squares).

the assigned sensor azimuth into the transverse and longitudinal directions, and computing the average cross-correlation coefficient between the rotated borehole and reference broadband data for a pair of transverse and longitudinal components. The best-fitting borehole sensor azimuth is identified, in which the average cross-correlation coefficient takes its maximum (dashed red line in Figure 2.27). The 95 percent confidence interval (dashed blue lines in Figure 2.27) is estimated with a Fisher transform (Baisch and Bokelmann, 2001).

### 13.4 References

- Baisch, S., G.H.R. Bokelmann, Seismic waveform attributes before and after the Loma Prieta earthquake: Scattering change near the earthquake and temporal recovery, *J. Geophys. Res.*, 106(B8), 16,323-16,337, doi:10.1029/2001JB000151, 2001.
- Kane, D.L., D. Kilb, A.S. Berg, V.G. Martynov, Quantifying the remote triggering capabilities of large earthquakes using data from The ANZA Seismic Network Catalog (Southern California), *J. Geophys. Res.*, 112, B11302, doi:10.1029/2006JB004714, 2007.

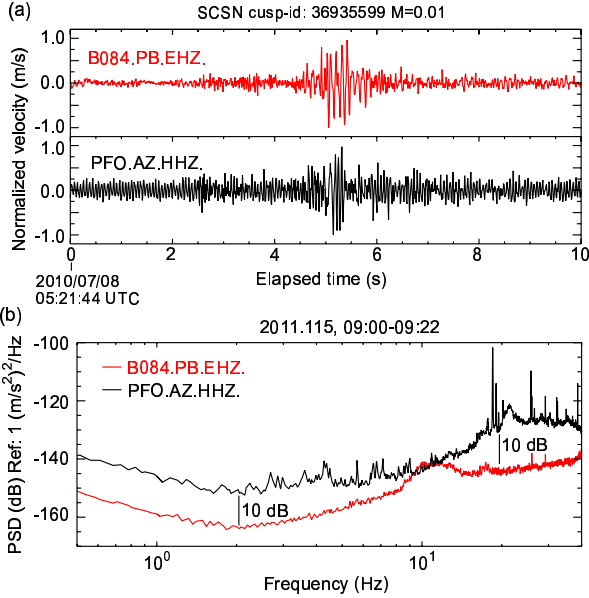


Figure 2.26: Comparison of seismic waveforms recorded at borehole and surface stations. (a) Observed seismograms recorded at the PBO borehole (red, B084) and the ANZA broadband station (black, PFO) for an M 0.01 Anza earthquake. This event is the smallest event in the 2010  $M_w$  5.4 Anza aftershock sequence listed in the SCSN catalog. A 1.0 Hz highpass filter was applied and the amplitudes of those two waveforms were normalized by their maximum amplitudes. Those two stations are collocated (see Figure 2.25 for the station locations). (b) Power spectral density (PSD) of background noise for the PBO borehole, B084.PB.EHZ (red) and the Anza surface, PFO.AZ.HHZ (black) stations. PSDs were calculated with a  $\sim 22$ -minute data window (131,072 data points), 2011.115, 09:00-09:22. This time period was chosen as one of the seismically quiet periods in March through May, 2011 from IRIS quality control measurement results (<http://www.iris.washington.edu/servlet/quackquery/>). This example demonstrates that the noise level of station B084 is  $\sim 10$  dB less than that of station PFO in the frequency range of 1-40 Hz (except for the 8-12 Hz band) and indicates that borehole records allow us to identify lower-magnitude earthquakes.

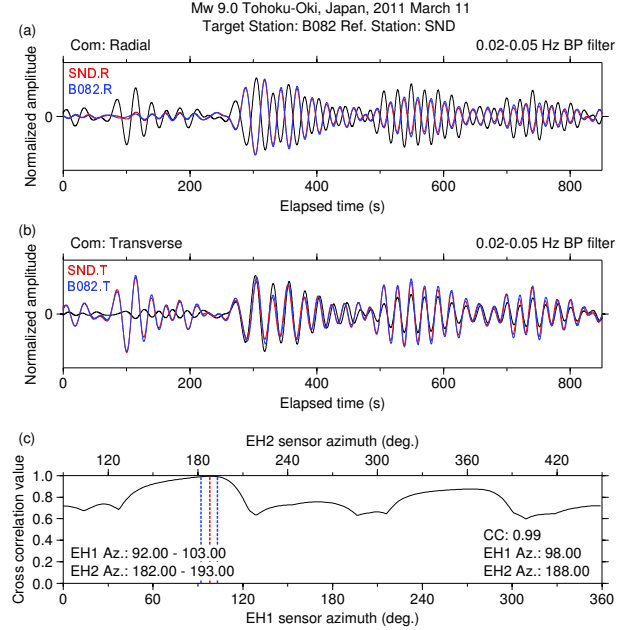


Figure 2.27: B082 sensor orientation estimate using the cross-correlation method. Observed waveforms (20-50 sec) in (a) the radial and (b) the transverse components from station SND (red) and B082 (blue) for the 2011  $M_w$  9.0 Tohoku-Oki Japan earthquake. Also shown are the rotated waveforms for station B082 (black) with assigned sensor azimuths EH1=0 degree and EH2=90 degrees. (c) Cross-correlation values between station SND and B082 as a function of sensor azimuth/orientation. The relative orientation of two horizontal components from station B082 is fixed to be constant (90 degrees or -90 degrees). We determine that the sensor orientations of station B082 EH1 and EH2 horizontal channels are 98 degrees and 188 degrees, respectively (dashed red line), with the cross-correlation value of 0.99. The high cross-correlation values obtained indicate that our measurement of the PBO sensor orientations is robust. The 95 percent confidence interval (dashed blue lines) for the sensor orientation estimate is 92-103 degrees for the EH1 channel (182-193 degrees for the EH2 channel).

# 14 Spatiotemporal Behaviors in Earthquake Multiplets at the Geysers Geothermal Field, CA

Taka'aki Taira

## 14.1 Introduction

The Geysers geothermal field is located in northern California and is characterized by a high rate of microseismicity. The Geysers seismicity is spatially and temporally correlated with geothermal production and injection well activity. The Geysers area is thought to be subject to a regional tectonic stress field associated with the strike-slip relative motion between the North American and Pacific plates (Oppenheimer, 1986). Many naturally occurring fractures may be stressed to near failure, and thus a small perturbation in the stress field could lead to failure (Majer and Peterson, 2007).

One of the important signatures of the Geysers microseismicity involves earthquake multiplets, or families of earthquakes with similar waveforms. Spatiotemporal variations in the state of stress or migration of geothermal fluids near the multiplet source area are reflected by changes in multiplet occurrence in time and space (Thelen et al., 2011). We identify Geysers multiplets and investigate their spatiotemporal behaviors.

## 14.2 Multiplet Catalog in the Geysers Geothermal Area

We construct a multiplet catalog using broadband seismic data recorded at station GDXB. This station is located near the center of the Geysers geothermal area (Figure 2.28) and has been operational since the middle of 2006. The background noise level above 1 Hz at station GDXB appears to be lowest, compared with those at other seismic stations in the Geysers area. We focus on the data from station GDXB and analyze over 65,000 Geysers local earthquakes (May 2006 through Dec. 2011) detected by the Northern California Seismic System earthquake catalog.

A 8-24 Hz bandpass filter and a 5.12-s time window from the direct P-wave are used to identify multiplets. This time window typically includes the direct S-wave arrivals. We measure cross-correlation values for 400 million seismogram pairs and use 0.95 for the waveform cross-correlation threshold for identifying multiplets (Figure 2.29). This threshold minimizes the possibility of falsely detecting two events as an earthquake multiplet. We find around 650 earthquake multiplets. The majority of them are earthquake doublets. We calculate the recurrence intervals and differences in seismic magnitudes for earthquake multiplets (Figure 2.30).

It appears the distribution of the recurrence intervals obtained has a peak at 30-50 days, although doublets

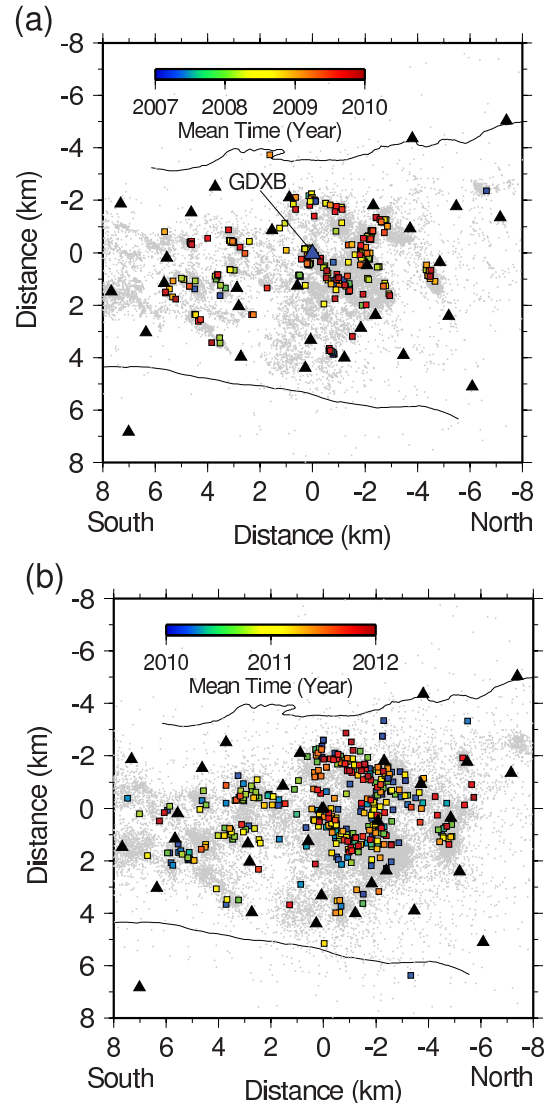


Figure 2.28: Geysers multiplets (squares) during (a) 2007-2009 and (b) 2010-2012, identified by our analysis. Triangles are seismic stations. Gray dots are the background seismicity determined by NCEDC.

or multiplets would be less likely to occur within a few minutes of each other than within a month of each other (Figure 2.30a). The magnitude difference is close to zero, indicating that the multiplet events have event sizes comparable to each other (Figure 2.30b). This result suggests that multiplets or doublets are not mainshock-aftershock sequences. The shorter recurrence interval with simi-

lar event size for Geysers multiplets is consistent with those for multiplets observed during eruptions at volcanoes (e.g., *Thelen et al.*, 2011) in which magma or geothermal fluid migration would lead to the occurrence of multiplets, rather than stress perturbations. We infer that the occurrence of Geysers multiplets is primarily governed by hydrothermal fluid migration. The catalog of Geysers multiplets appears to indicate increased multiplet activity after 2010 (Figure 2.28). In the future, we will examine spatial and temporal correlations between the multiplet seismicity and geothermal production and injection well activity.

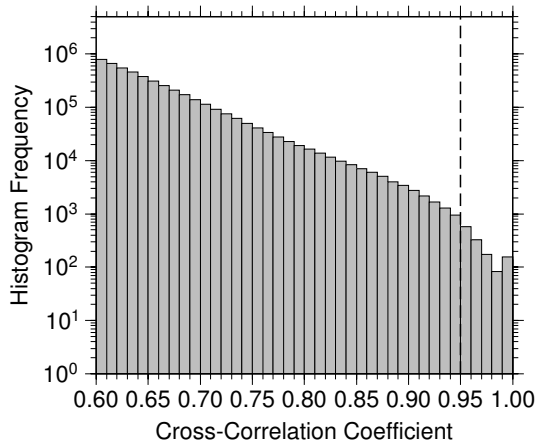


Figure 2.29: Histogram of cross-correlation values ( $> 0.6$ ) for the Geysers local earthquakes analyzed.

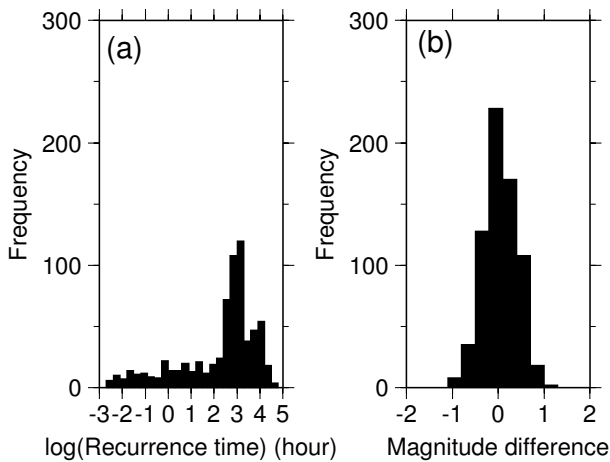


Figure 2.30: Distributions of (a) recurrence intervals and (b) magnitude differences for the Geysers multiplets

### 14.3 Acknowledgements

We thank F. Massin for discussion, NCEDC and LBNL for data collection and distribution. This work is supported by the National Science Foundation EAR-1053211.

### 14.4 References

Majer, E., J. E. Peterson, The impact of injection on seismicity at The Geysers California Geothermal Field, *International Journal of Rock Mechanics and Mining Sciences*, 44, 1079-1090, 2007.

Oppenheimer, D.H., Extensional tectonics at the Geysers geothermal area, California, *J. Geophys. Res.*, 91(B11), 11,463-11,476, doi:10.1029/JB091iB11p11463, 1986.

Thelen, W., S. Malone, M. West, Multiplets: Their behavior and utility at dacitic and andesitic volcanic centers, *J. Geophys. Res.*, 116, B08210, 16pp., DOI:10.1029/2010JB007924, 2011. .

# 15 A systematic analysis of seismic moment tensor for seismicity at The Geysers Geothermal Field, California

Sierra Boyd, Douglas Dreger, Peggy Hellweg, Taka'aki Taira, Jennifer Taggart, Tom Weldon, and Peter Lombard

## 15.1 Introduction

Forty  $M > 3$  earthquakes located at The Geysers Geothermal Field were selected from the UC Berkeley Moment Tensor Catalog for in depth analysis of seismic moment tensor solutions, uncertainties, and well resolved source-type. Deviatoric and full moment tensor solutions were computed, and statistical tests were employed to assess solution stability, resolution, and significance. The general moment tensor can be decomposed in a multitude of ways, and in this study we examine the pure isotropic (explosion/implosion ISO), double-couple (DC), volume Compensated Linear Vector Dipole (CLVD) sources, as well as compound sources such as DC+CLVD, DC+ISO, and tensile-crack+DC source models. The solutions are cataloged. A single event that occurred on October 12, 1996 at the southern edge of the field was found to have a statistically significant isotropic component.

## 15.2 Methodology

We invert three-component, complete waveform data for deviatoric and full, six-element moment tensors using the method outlined in *Minson and Dreger, 2008*. The broadband velocity data is instrument corrected with reported pole-zero response functions, integrated to displacement and bandpass filtered with an acausal, 4-pole, Butterworth bandpass filter with a 0.02 to 0.05 Hz or 0.02 to 0.10 Hz passband. In addition to finding best fitting solutions we apply the F-test to determine the significance of models with higher degrees of freedom, Jackknife tests to assess the stability of solutions due to station configuration, bootstrap residuals to characterize random, aleatoric uncertainties in the solutions, and utilize the Network Sensitivity Solution (NSS; *Ford et al., 2010*) to map the full moment tensor solution for the complete source-type solution space as proposed by *Hudson et al., 1989*. All of these tests require significant computational effort and therefore a staged approach is taken in which if a solution is largely double-couple no additional analysis is performed. If a solution has large deviatoric non-double-couple components (e.g. CLVD), or if a full moment tensor has large non-double-couple terms, an F-test is first performed to assess significance. If that test indicates that there is a large improvement in fit with the non-double-couple terms then the additional Jackknife, bootstrap and NSS analyses are performed.

We found that depth sensitivity using data filtered between 0.02 to 0.05 Hz is fairly limited, so we therefore

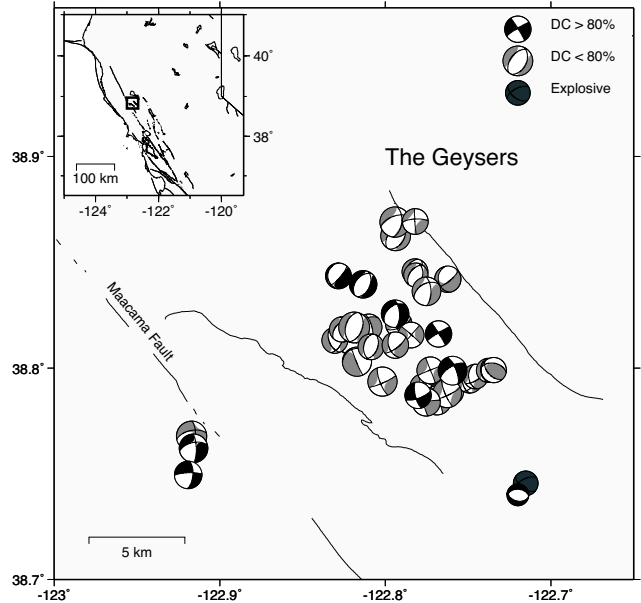


Figure 2.31: Map showing moment tensor solutions of the 40 studied events.

restrain our analysis to event depths determined from the NCSS and LBNL catalogs. In the future, with better-calibrated velocity models and/or using the local Calpine seismic data we may be able to improve on moment tensor based source depth determination. However, for now we assume that the depths reported in the catalog are well determined and focus on the recovery of the seismic moment tensor source parameters.

## 15.3 Results

In Figure 2.31 moment tensor solutions are shown for the studied events. The black solutions are for events that have solutions with DC components larger than 80% of the total seismic moment, whereas the gray solutions show the cases with large non-double-couple components (DC < 80%). On the whole the solutions show a trend in which the T-axis is oriented E-ESE; however, solutions vary from relatively rare strike-slip cases to more common normal faulting events, and CLVD solutions that accommodate both DC types. The CLVD solutions have a roughly horizontal, E-ESE trending major vector dipole in tension. There is one solution for an event on October 12, 1996 in the southern region of the field that has a large isotropic moment tensor solution. The DC event

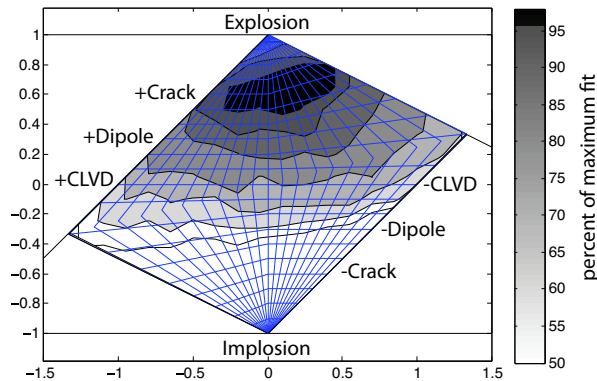


Figure 2.32: Network sensitivity solution for the October 12, 1996 event.

located nearby shows an unusual east-west striking normal solution. The deviatoric solution for the October 12, 1996 has the same orientation.

The F-test is used to compare the ratio of the goodness of fit of the full and deviatoric moment tensor solutions. Most events do not rise above a level of statistical significance of 50%; however, the October 12, 1996 event (large circle) does show a statistical significance of 99% for a solution using 10 three-component stations. The Jackknife test is performed by inverting all combinations of 9 and 8 stations from the full 10 station set. The results of the Jackknife test reveal a stable solution that is substantially non-double-couple with a large tensile isotropic component. These tests show that no single station, or particular azimuth is biasing results toward a non-double-couple solution.

The network sensitivity solution (NSS; Ford *et al.*, 2010) is a method to map maximum fit surface in a source-type representation. This method searches in a brute force manner an order of 10 million uniformly distributed moment tensor solutions. This technique was developed to examine the uniqueness and possible trade-offs in solutions due to sparse network configurations and to changes in available station coverage. Here it can be used in a comparative sense to illustrate differences and overlap of solutions using different data sets. For the October 12, 1996 event we show the maximum fit surface considering 20 million uniformly distributed moment tensors, shown in Figure 2.32. The darker gray fields are showing 90, 95, 98% of the best fit solution. The double-couples and deviatoric solutions fit at best only 80% of the best fit solution.

## 15.4 Conclusions

We investigate source models for stability and significance of forty events at The Geysers Geothermal Field. Of these events 9 are found to be dominantly double-

couple, 30 are found to deviate significantly from a double-couple solution, and 1 is found to have a statistically significant isotropic component. We use the NSS to determine confidence regions of possible source types of events at The Geysers Geothermal Field. The results of the NSS for the October 12, 1996 event shown in Figure 2 suggest a solution that is a combination of double-couple and volumetric expansion. Our previous results identified the full moment tensor solution as having a statistically significant volumetric component based on the F-test.

## 15.5 Acknowledgements

This work was supported by the Assistant Secretary for Energy Efficiency and Renewable Energy, Office of Geothermal Technologies, of the U. S. Department of Energy under Contract No. DE-EE0002756.

## 15.6 References

- Ford, S.R., W.R. Walter and D.S. Dreger, Event discrimination using regional moment tensors with teleseismic-P constraints, *Bull. Seism. Soc. Am.*, 108, 883-884, 2012.
- Ford, S.R., D.S. Dreger, and W.R. Walter, Network sensitivity solutions for regional moment tensor inversions, *Bull. Seism. Soc. Am.*, 100, 1962-1970, 2010.
- Hudson, J.A., R.G. Pearce, and R.M. Rogers, Source type plot for inversion of the moment tensor, *J. Geophys. Res.*, 9(B1), 765-774, 1989.
- Minson, S. and D. Dreger, Stable inversion for complete moment tensors, *Geophys. Journ. Int.*, 174, 585-592, 2008.

# 16 Joint Inversion of Seismic and Geodetic Data for the Source of the 4th March 2010 $M_w$ 6.3 Jia-Shian, SW Taiwan, Earthquake

Mong-Han Huang, Douglas Dreger, Roland Bürgmann, and Seung-Hoon Yoo

## 16.1 Introduction

The March 2010 Jia-Shian ( $M_w$  6.3) earthquake occurred in southwestern Taiwan and caused moderate damage (Figure 2.33a). No surface rupture was observed, reflecting a deep source that is relatively rare in west Taiwan. We develop finite-source models using a combination of seismic waveform data (strong motion and broadband stations), GPS, and InSAR to understand the rupture process and slip distribution of this event. The main shock is mainly a reverse event with a small left-lateral component. The rupture's centroid source depth is 19 km based on a series of moment tensor solution tests with improved 1D Greens functions. The primary slip asperity of the preferred model is about 20 km in diameter and ranges in depth from 22 to 13 km. The peak slip is 42.51 cm, and the total scalar seismic moment is  $3.25 \times 10^{18}$  N m. Both the main shock and aftershocks are located at the transition zone where the depth of the regional basal decollement deepens from central to south Taiwan. In addition, the P and T axes of this event are rotated about 40 degrees counterclockwise from the direction of the current plate collision. Hence, the deviation of the compressional stress exhibited by this event may be a regional perturbation of a pre-existing geologic structure.

## 16.2 Inversion and Result

We use a linear least squares inversion code based on *Kaverina et al.* (2002), in which the finite source is discretized with a finite distribution of point sources in both space and time. A damped, linear least squares inversion with a positivity constraint (allowing only for thrust dip-slip component) is used to determine the distribution of slip in space and time. A single time window is used with a fixed dislocation rise time (0.5 s) propagating away from the source with constant rupture velocity (4.2 km/s). Spatial smoothing with linear equations minimizing differences in slip between subfaults is applied to stabilize the seismic and geodetic inversion. Different weighting and smoothing parameters are applied to the simultaneous inversion using the method proposed by *Kaverina et al.* (2002). The Green's functions for southern Taiwan are taken from *Chi and Dreger* (2004). For the geodetic inversion, the geodetic Greens functions are computed by assuming the same layered elastic structure as for the seismic inversion. A  $50 \times 50$  km NW dipping fault geometry with 625 subfaults was considered for the inversions. The coseismic slip distribution is estimated

both from the inversion of each data set separately and jointly.

Seven strong motion and three broadband seismic stations are used for the seismic inversion, and 108 GPS stations and 3 ALOS PALSAR interferograms are used for the geodetic inversion. The joint inversion shows coseismic slip covering a  $15 \times 20$  km area northwest of the hypocenter (Figure 2.33c) with an average slip of 15 cm and a peak slip of 42.5 cm.

## 16.3 Discussion and Conclusion

The orientation of the P and T axes of the main shock and aftershocks is different from the direction of the current plate collision (Figure 2.33d,e). However, the crustal scale (0-30 km) strain rate based on the SW Taiwan regional seismicity and focal mechanism inversions (*Mouthereau et al.*, 2009) shows ENE-WSW compression near the Jia-Shian epicenter. This ENE-WSW compression has the same orientations as the P axes of the main shock and most of the aftershocks, which agree with the ambient strain distribution at the source depth. To conclude, the Jia-Shian event occurred along the boundary between the Western Foothills and the Central Range. The current surface strain rate is not consistent with the stress orientations in the upper crust of the Jia-Shian event. Combining all of the observations suggests that this event may be due to the reactivation of a pre-existing geological structure that is not necessarily participating in the current plate collision. Details of the kinematics or the geometry of the structure will be needed to confirm this.

## 16.4 Acknowledgements

We thank the Institute of Earth Science, Academia Sinica, Taiwan for providing seismic and geodetic data. We thank H.-H. Huang of National Taiwan University for providing the aftershock catalog.

## 16.5 References

- Kaverina, A., Dreger, D., and Price, E., The combined inversion of seismic and geodetic data for the source process of the 16 October 1999  $M_w$  7.1 Hector Mine, California earthquake, *Bull. Seismol. Soc. Am.*, 92, 1266-1280, 2002.
- Mouthereau, F., C., Fillon, and K.-F. Ma, Distribution of strain rates in the Taiwan orogenic wedge, *Earth Planet. Sci. Lett.*, 284, 361-385, 2009.
- Saikia, C. K., Modified frequency-wave-number algorithm for regional seismograms using Filons quadrature-modeling of L(g) waves in eastern North America, *Geophys. J. Int.*, 118, 142-158, 1994.

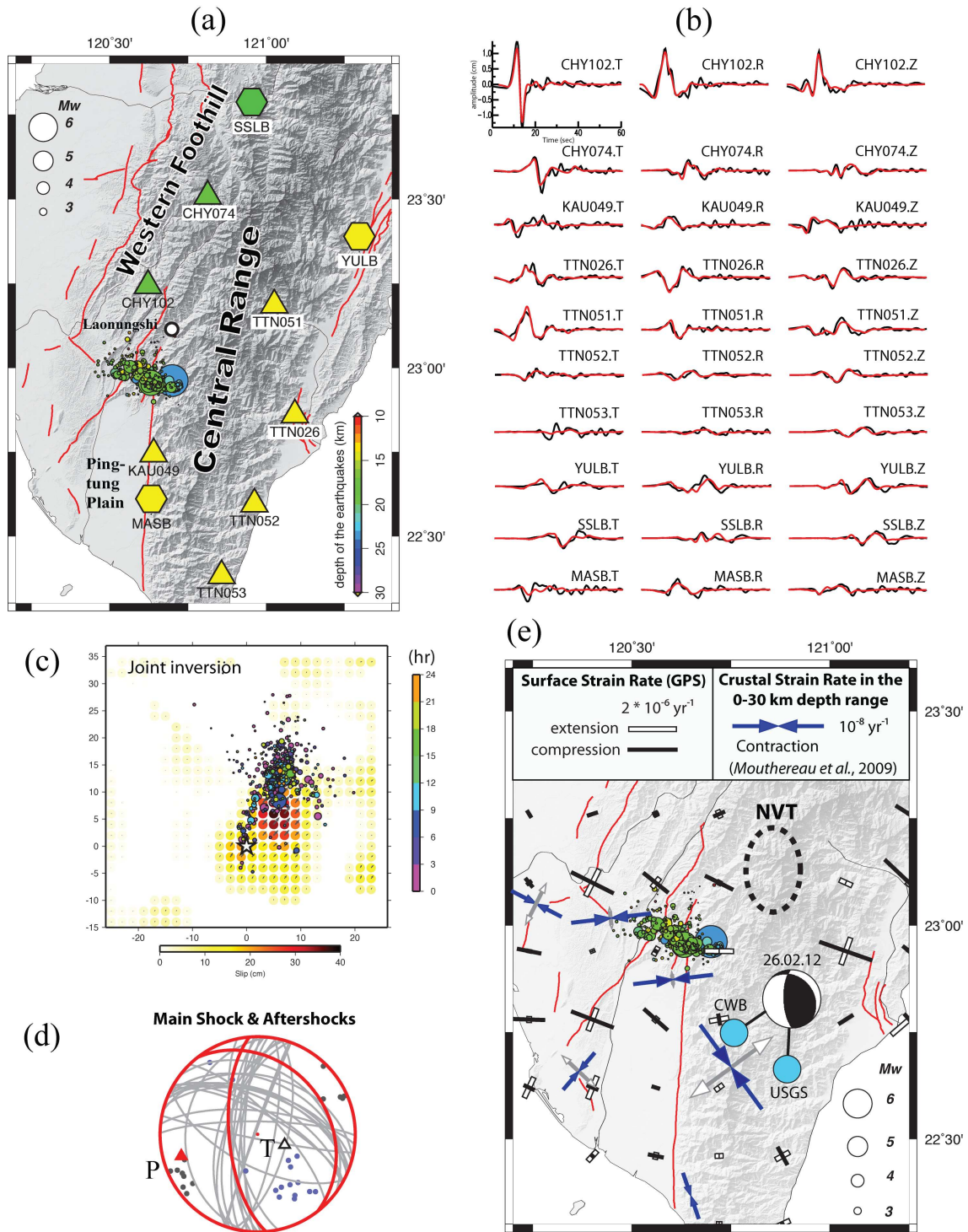


Figure 2.33: (a) Selected strong motion stations (triangles) and broadband stations (hexagons). The green and yellow stations belong to the west and east Taiwan velocity models, respectively. The Jia-Shian main shock and aftershocks are color coded by depth. (b) The comparison of synthetic (red) and seismic data (black) from the joint inversion. (c) Joint inversion result (variance reduction of seismic data: 74.8%; GPS: 64.9%; InSAR: 77.0%). Black arrows represent the slip direction and amplitude for each subfault. The colored circles are aftershocks since the main shock in hours. (d) P and T axes of the main shock (red and white triangles) and aftershocks (grey and dark blue circles). (e) The surface strain rate (black and white bars) and crustal scale (0-30 km) strain rate (dark blue arrows). The beach ball diagram shows the most recent earthquake in this region with a focal mechanism similar to the Jia-Shian event, which may imply an extension of this structure to the southeast. NVT indicates the region of triggered non-volcanic tremors in the Central Range.

# 17 Deciphering the Mystery of the Great Indian Ocean Earthquakes

Kelly Wiseman and Roland Bürgmann

## 17.1 Introduction

On April 11, 2012, there were two magnitude 8+ earthquakes off the west coast of northern Sumatra, Indonesia. The first was a magnitude 8.6 and the second was a magnitude 8.2, two hours later. Both of these earthquakes were a result of strike-slip faulting within the oceanic lithosphere of the broadly distributed India-Australia plate boundary zone. Unlike the nearby 2004 magnitude 9.2 Sumatra megathrust earthquake that produced a disastrous tsunami, these earthquakes involved mostly horizontal motion and initiated more than 380 km from the Sumatra mainland, thereby limiting the shaking and tsunami damage. Although these earthquakes quickly faded from the news once the tsunami warnings were canceled, the magnitude 8.6 mainshock is incredibly significant as it holds the distinction of being both the largest instrumentally recorded strike-slip earthquake and the largest earthquake within the interior of a tectonic plate. Early geophysical studies have revealed another noteworthy aspect of these events, that the mainshock involved sequential ruptures of multiple fault planes oriented nearly perpendicular to each other. Here we discuss the unusual geological conditions within the Indian Ocean basin that allow for such a large, complex intraplate earthquake and relate the timing of these events to the 2004 megathrust earthquake.

## 17.2 Relation to the 2004 Sumatra-Andaman earthquake

The 2004 Sumatra megathrust earthquake fundamentally changed the stress state in the surrounding lithosphere and seismicity rates have been enhanced throughout Southeast Asia in the years following the great earthquake. The yellow and blue beach balls in Figure 2.34b,c ([www.globalcmt.org](http://www.globalcmt.org)) depict the focal mechanisms for all of the strike-slip earthquakes in the incoming Indian and Australian plates, west of the Sunda trench, during the years between the 2004 and 2012 earthquakes. The mechanisms are very similar to the focal mechanisms for the two April, 2012 earthquakes (shown in red), and are consistent with either left-lateral strike-slip motion on the N-S oriented fractures, or right-lateral motion on E-W oriented planes.

The 2012 mainshock initiated at 20 km depth and the aftershock pattern (gray dots in Figure 2.34a, USGS NEIC catalog), along with preliminary back-projection rupture propagation models (Meng *et al.*, 2012), suggests complex rupture on multiple fault planes. It appears that the mainshock started with bilateral shear away from the

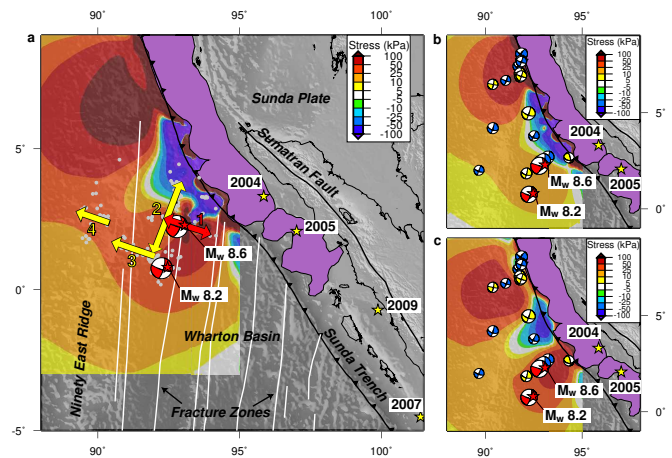


Figure 2.34: Recent stress changes in the Indian Ocean. (a) Total stresses induced by the 2004 and 2005 megathrust earthquakes (purple regions) plus the 2012 foreshock resolved at the hypocentral depth of the magnitude 8.6 earthquake into the orientation of the initial E-W fault plane. The red-and-white beach balls depict the focal mechanisms for the two 2012 magnitude 8+ earthquakes. The epicenters for the first 12 days of the 2012 aftershock sequence are marked with gray dots (USGS NEIC catalog). The fault planes are based on Meng *et al.* (2012) and the fracture zones are from Singh *et al.* (2011). (b) Coseismic stresses induced by the 2004 and 2005 earthquakes. The yellow focal mechanisms highlight the strike-slip earthquakes during the first two months following the 2004 earthquake and the blue focal mechanisms depict earthquakes after the first two months and before the 2012 mainshock. (c) Postseismic stresses induced by the 2004 and 2005 earthquakes.

hypocenter on an E-W oriented plane (red fault segment in Figure 2.34a) and then bilaterally ruptured a N-S oriented plane to the west of the hypocenter (yellow segment labeled 2). It ended with slip on two additional E-W oriented segments to the south, near the eventual magnitude 8.2 aftershock (yellow segments labeled 3 and 4) (Delescluse *et al.*, 2007). The 2012 mainshock was able to grow to such a large magnitude because it was able to continue rupturing beyond the initial E-W fault plane, on multiple nearby faults in the weak, heavily fractured northern Wharton Basin. This complex rupture scenario is similar to the second largest Wharton Basin earthquake, a magnitude 7.9 earthquake in June 2000, that started as left-lateral strike-slip motion on a

N-S plane and ended as oblique motion on an E-W plane (Abercrombie *et al.*, 2003). Half of the focal mechanisms for the 2012 aftershocks show oblique motion, indicating that the magnitude 8.6 earthquake may have included an oblique sub-event as well.

We have calculated the stresses induced by the 2004 (Chlieh *et al.*, 2007) and 2005 (Konca *et al.*, 2007) megathrust earthquakes at the hypocenter of the magnitude 8.6 earthquake in order to determine if the 2012 earthquakes were triggered events. We modeled the static, coseismic stress perturbations from the two nearby megathrust ruptures and the time-dependent perturbations resulting from postseismic relaxation of the upper mantle following the megathrust events. The 2004 earthquake contributed most of the stress changes at the 2012 hypocenter and further to the north spanning the zone of enhanced strike-slip activity. The rate of strike-slip activity in the northern Wharton Basin increased greatly in the initial months following the 2004 earthquake (yellow beach balls in Figure 2.34b,c), and continued at a lower level up until the 2012 earthquakes. The combined coseismic stress perturbation from the 2004 and 2005 earthquakes was  $\sim 18$  kPa at the hypocenter (Figure 2.34b), with similar values when resolving stress on either the E-W or N-S fault plane orientation. The additional stress perturbations from postseismic deformation can explain the continued strike-slip activity during the years following the 2004 earthquake (blue beach balls in Figure 2.34b,c). By April 2012, the postseismic stress perturbation from the megathrust earthquakes was  $\sim 4$  times larger than the induced coseismic stresses at the 2012 hypocenter, highlighting the importance of postseismic deformation for triggering earthquakes away from the coseismic rupture plane. (Figure 2.34c). A magnitude 7.2 foreshock,  $\sim 25$  km NE of the mainshock in January 2012, involved right-lateral slip on an E-W oriented fault and added a final push before the April events.

### 17.3 Discussion

The high strain-rates within the Wharton Basin enable strike-slip earthquakes over a wide portion of the plate interior, and the stresses imparted to the oceanic lithosphere by the 2004 earthquake induced a spike in these strike-slip earthquakes. This behavior is particular to the Equatorial region of the Indian Ocean basin, as we did not see triggered strike-slip earthquakes in the Pacific plate following the 2011 Tohoku earthquake. The 2012 magnitude 8+ events were the latest in this collection of post-2004 strike-slip earthquakes and the additional stress imparted to the lithosphere from the postseismic deformation can explain the time delay between the 2004 and 2012 earthquakes. The 2012 mainshock was so large because it was able to rupture multiple weak spots within the oceanic lithosphere, including four separate fault planes. The annual moment rate for

the entire Wharton Basin, that actively deforms down to  $20^\circ\text{S}$ , is  $\sim 3.5 \times 10^{19}$  Nm/yr (Delescluse and Chamot-Rooke, 2007), and these two magnitude 8+ strike-slip earthquakes released  $\sim 270$  years of accumulated seismic moment. The northern portion of Wharton Basin is the highest straining region in the diffuse India-Australia boundary zone, accommodating roughly 1 cm/yr of N-S left-lateral shear (Delescluse and Chamot-Rooke, 2007), so this region should have shorter earthquake repeat times, on the order of 500-1000 years, than the rest of the region. Over the past millennia, the megathrust earthquake periodicity for the southern end of the 2004 rupture has been roughly 400-600 years (Meltzner *et al.*, 2010), therefore these great oceanic strike-slip earthquakes may coincide with the great Sunda megathrust earthquakes every 1-2 cycles. Although these 2012 earthquakes did not cause much damage or casualties, they highlight the risk that very large earthquakes can occur within the interior of a plate, and that unexpected events can be triggered well after great megathrust earthquakes.

### 17.4 Acknowledgments

This work is supported by the National Science Foundation grant EAR 0738299.

### 17.5 References

- Abercrombie *et al.*, The June 2000  $M_w$  7.9 earthquakes south of Sumatra: Deformation in the India-Australia Plate, *J. Geophys. Res.*, 108, B1,2018, 2003.
- Chlieh *et al.*, Coseismic slip and afterslip of the great  $M_w$  9.15 Sumatra-Andaman earthquake of 2004, *Bull. Seismol. Soc. Am.*, 97, S152-S173, 2007.
- Delescluse and Chamot-Rooke, Instantaneous deformation and kinematics of the India-Australia Plate, *Geophys. J. Int.*, 168, 818-842, 2007.
- Konca *et al.*, Rupture kinematics of the 2005  $M_w$  8.6 Nias-Simeulue earthquake from the joint inversion of seismic and geodetic data, *Bull. Seismol. Soc. Am.*, 97, S307-S322, 2007.
- Meng *et al.*, Back-projection results 4/11/2012 ( $M_w$  8.6), offshore Sumatra, Indonesia, [http://tectonics.caltech.edu/slip-history/2012\\_Sumatra/back\\_projection](http://tectonics.caltech.edu/slip-history/2012_Sumatra/back_projection), 2012.
- Meltzner *et al.*, Coral evidence for earthquake recurrence and an A.D. 1390-1455 cluster at the south end of the 2004 Aceh-Andaman rupture, *J. Geophys. Res.*, 115, B10402, 2010.
- Singh *et al.*, Extremely thin crust in the Indian Ocean possibly resulting from Plume-Ridge Interaction, *Geophys. J. Int.*, 184, 29-42, 2011.

# 18 Source Spectral Variation and Yield Estimation Derived from High Frequency P and S Coda

Seung-Hoon Yoo, Kevin Mayeda, and Douglas Dreger

## 18.1 Introduction

Identifying Underground Nuclear Explosions (UNEs) and discriminating them from natural earthquakes is a critical issue for the verification of the Comprehensive nuclear-Test-Ban Treaty (CTBT). The earthquake source is described as a shear dislocation on a fault plane, which generates both P- and S-wave at the source. On the other hand, the nuclear explosion source is described as an isotropic volumetric expansion, which theoretically generates only P-waves without S-waves. However, significant S-wave generation is commonly observed from explosion sources and the mechanism remains controversial. A number of explanations (e.g., phase interaction and conversion at the free-surface or any other near source boundary, Rg generation by a compensated linear vector dipole source (CLVD), scattering due to topography, spallation, rock damage, etc) were proposed but a unifying model does not present. To enhance the identification and discrimination capability of explosions, a more comprehensive understanding of explosion sources including primary and secondary process are essential.

We analyze seismic coda waves from the near-source explosions to better understand the generation and properties of the scattered P and S wavefields. The well-instrumented experiments provide us with excellent data from which to document the characteristic spectral shape (e.g., tamped single-fired with variety explosives, ripple-fired), relative partitioning between P and S-waves.

## 18.2 Data and Method

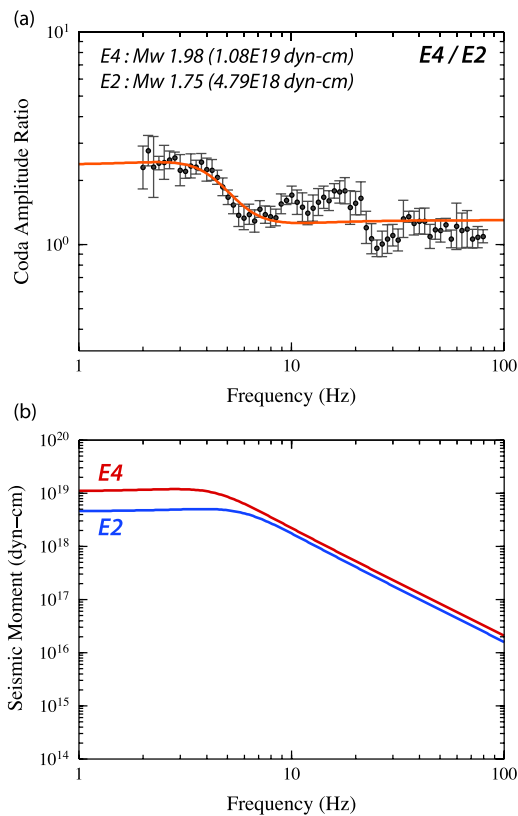
We report on two near-source explosion data sets. In the first case, we examine tamped single-fired explosions, which are conducted in Barre granite during the 2008 New England Damage Experiment (NEDE) (*Leidig et al.*, 2009). The experiment included the detonation of five small (135 to 270 lbs) chemical explosions in relatively unfractured, homogeneous Barre granite in Vermont. To examine a hypothesis that different damage would lead to possible variations in S-wave generation, the explosions (black powder, ANFO, Composition B) were designed with variable velocities of detonations (VOD) ranging from 0.5 to 8 km/sec. In the second case, we analyze five explosions (a delay-fired production blast and four single-fired shots) using ANFO explosive at a Massachusetts quarry. For the production shot, the total explosives used was 20,377 lbs with the typical delay between the holes in each row being 16 msec and the delays between rows being 106 msec. The four single-fired shots were detonated with different amount of explosive ranging from 132 to 788 lbs.

The five shots in each experiment are closely located within several tens of meters. We assume that all shots in each experiment share common path effects and apply the coda ratio method (*Mayeda et al.*, 2007). We measure coda amplitudes for 3-components and narrow frequency bands (1/2 octave bandwidth with 1/8 octave overlapping) with central frequencies ranging between 2 to 80 Hz (NEDE) and 42 Hz (a Massachusetts quarry experiment). We form the average spectral ratios ratio between the high and low yield explosions over stations and components. A total of 19 short-period stations (2.8-30 km) were averaged for NEDE and 7 broadband stations (1.3-4.5 km) and 10 short-period stations (0.5-5.3 km) were averaged for a Massachusetts quarry experiment (Figure 2.35A). Then, we perform a grid-search using the MM71 explosion source model (*Mueller and Murphy*, 1971) to get the theoretical source spectra. We also perform time-domain full moment tensor inversion for selected high yield explosions (Figure 2.35B). Independent seismic moment estimates are needed to convert the dimensionless coda amplitudes to an absolute physical unit. This is also very important to get a stable estimate of source spectrum by constraining the long period coda ratio in the source model search. Using the derived theoretical source spectra and independent seismic moment, we calibrate all measured coda amplitudes to source spectra for the other explosions (Figure 2.35C).

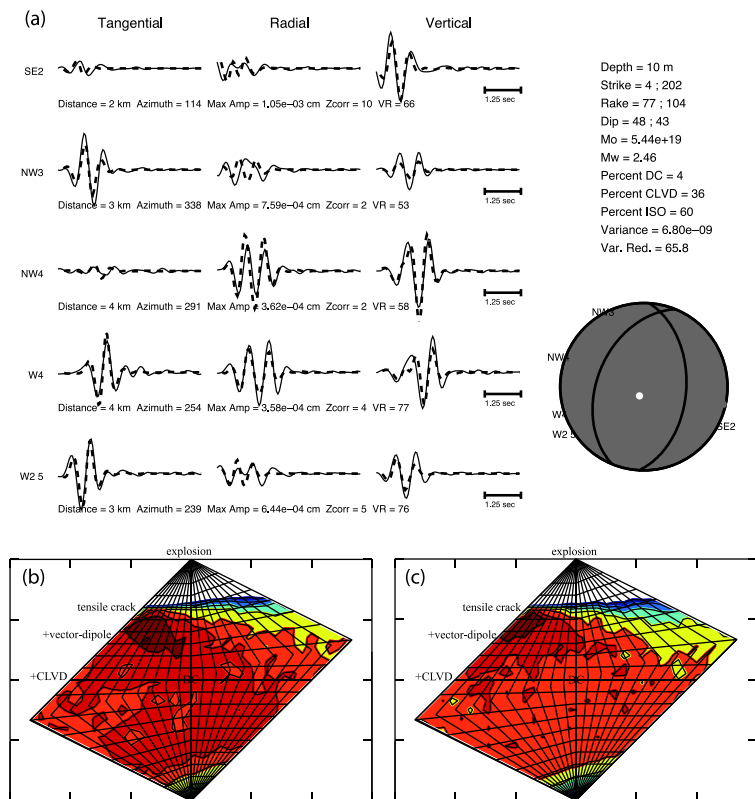
## 18.3 Preliminary Results

From NEDE source spectra, we found the source spectrum for the black powder shot (slow burning explosive) falls off rapidly at high frequency compared to the source spectra of ANFO and Composition B. However, the black powder shot produced spectral amplitudes comparable to that of the ANFO shot below 5 Hz. Composition B (fast burning explosive) explosions effectively radiate more high frequency energy, however it is deficient in low frequency S-wave energy. The Composition B shot produced significantly smaller spectral amplitudes than the black powder shot below 5 Hz. We also found that there is a factor of  $\sim 2$  difference in seismic moment for similar yield shots between the NEDE and a Massachusetts quarry data due to the venting effect. In the source spectrum of the ripple-fired shot, we clearly see the modulation peaks at theoretical modulation frequencies based on the delay times.

### A. Coda Spectral Ratio



### B. Full Moment Tensor Analysis



### C. Coda-derived Source Spectra

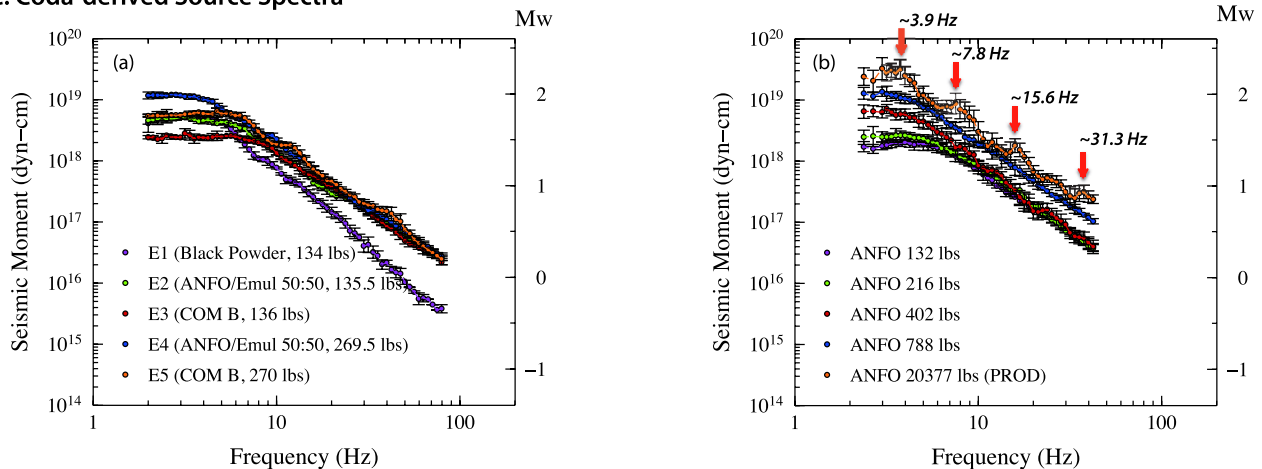


Figure 2.35: A: Averaged coda spectral ratio between the E4 and E2 shots in NEDE experiment (a) and the corresponding theoretical source spectra (b). B: Full moment tensor inversion result (a) and network sensitivity analysis using 3 stations (b) and 5 stations (c) for the production shot in a Massachusetts quarry experiment. C: Coda-derived source spectra for the NEDE shots (a) and a Massachusetts quarry shots (b).

## 18.4 Acknowledgements

This work was supported by Weston Geophysical Corp.

## 18.5 References

Leidig, M., R. Martin, P. Boyd, J. Bonner, and A. Stroujkova, Quantification of rock damage from small explosions and its effect on shear-wave generation: phase I homogenous crystalline rock, in *Proceedings of the 2009 Monitoring Research Review: Ground-Based Nuclear Explosion Monitoring Technologies*, 1, 492-501, 2009.

Mayeda, K., L. Malagnini, and W.R. Walter, A new spectral ratio method using narrow band coda envelopes: Evidence for non-self-similarity in the Hector Mine sequence, *Geophys. Res. Lett.*, 34, L11303, doi:10.1029/2007/GL030041, 2007.

Mueller, C.S., and J.R. Murphy, Seismic characteristics of underground nuclear detonations, Part I: seismic spectrum scaling, *Bull. Seism. Soc. Am.*, 61, 1675-1692, 1971.

# 19 Regional Moment Tensor Inversion for Shallow Sources: the Effects of Free-Surface Vanishing Traction

Andrea Chiang and Douglas S. Dreger

## 19.1 Introduction

For the nuclear explosion source-type identification problem the uncertainty in a solution is as important as the best fitting parameters (*Ford et al.*, 2009), and there are concerns about bias that can be introduced through velocity structure and corresponding Green’s functions, as well as due to the shallow depth of burial. A potential issue for shallow seismic sources that are effectively at the free-surface between the ground and air is that the vanishing traction at the free-surface can cause the associated vertical dip-slip (DS) Green’s functions to have vanishing amplitudes (*Julian et al.*, 1998), which in turn results in the indeterminacy of the  $M_{xz}$  and  $M_{yz}$  components of the moment tensor and bias in the moment tensor solution. The effects of the free-surface on the stability of the moment tensor method become important as we continue to investigate and improve the capabilities of regional full moment tensor inversion for source-type identification and discrimination. It is important to understand the effects for discriminating shallow explosive sources in nuclear monitoring, but free-surface effects could also be important in natural systems that have shallow seismicity such as volcanoes and geothermal systems.

## 19.2 Methods

In this study, we generated a suite of velocity models by introducing a shallow velocity gradient to the 1D reference model (*Song et al.*, 1996). This is accomplished by splitting the top 2.5-km thick layer in the reference model into two separate layers. We systematically adjusted the thickness and velocity of the two new layers (Figure 2.36a), but constrained the variations of the two parameters by maintaining the same vertical travel time as the reference model. The purpose of the study was to generate different but comparable velocity models.

For each 1D model, we generated Green’s functions at regional distances (100 to 400 km) with source depths ranging from 0.2 to 3.5 km. Using the same set of Green’s functions, we generated two types of synthetic data with different source mechanisms: a pure explosion case and a composite case (double-couple and explosion) with an F-factor of 1 (*Burger et al.*, 1986). Random Gaussian white noise of 20% was added to the synthetic data. Then we used a 10 to 50 seconds causal bandpass butterworth filter to filter the synthetic data and the Green’s functions. We implemented a semi-ideal four-station coverage for the inversion, consisting of source-to-receiver distances

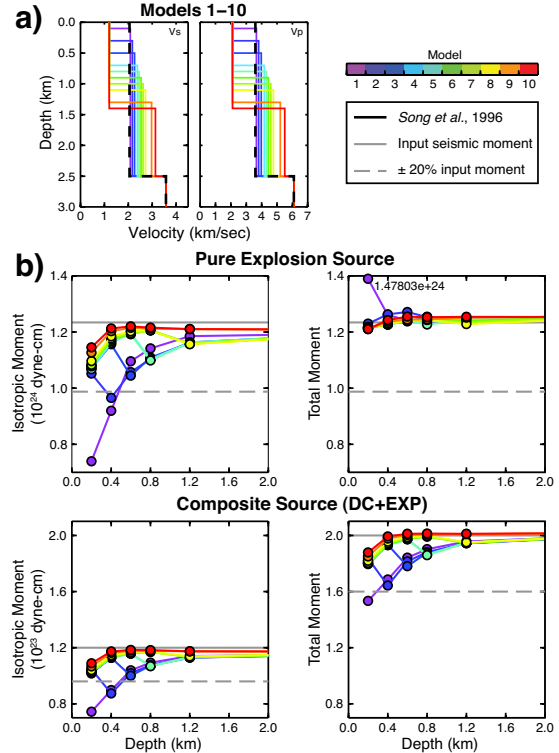


Figure 2.36: (a) Velocity models 1 to 10 of the 59 models tested. (b) Isotropic and total scalar seismic moments for pure explosion and composite source (double-couple and explosion) mechanisms. Results are based on Green’s functions computed using the velocity models in part (a).

distributed at increasing 100 km increments from 100 to 400 km, and in semi-regular azimuths. The linear inversion problem yields six independent components of  $M_{ij}$ .

## 19.3 Velocity Model Dependence

Of the 59 velocity models tested, those with a shallow velocity gradient in the upper 1.5 km have little to no bias in their isotropic and total moment estimates, and all estimates fall within the 20% noise level for both the explosion source and the composite source. Similarly, moment estimates from models with a shallow velocity gradient in the upper 1.5 to 2.0 km are within 20% of the input values at depths greater than 0.4 km. Although the total moment estimates for the composite case exhibit greater deviations from the true input value at source

depths shallower than 0.4 km, the bias in the isotropic moment is less significant (Figure 2.36b).

In most cases the full moment tensor inversion successfully recovers the correct mechanism for both the pure explosion case and the composite case over the targeted depth range ( $< 1$  km) for nuclear explosions (Figure 2.37). Free-surface vanishing traction has little effect on recovering the correct mechanism for models with a shallow velocity gradient. The inversion can still recover the correct mechanism for models without a strong shallow velocity gradient at depths greater than 0.5 km; the bias in source mechanism is significant only at depths shallower than 0.4 km.

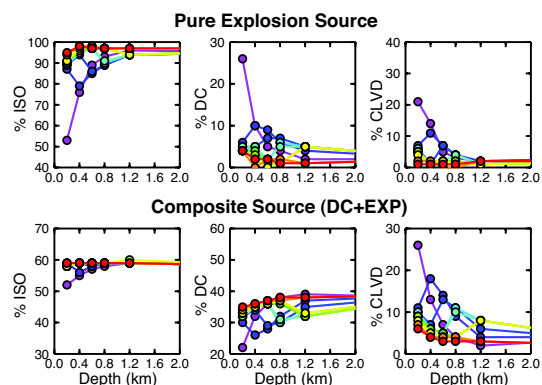


Figure 2.37: Full moment tensor solutions including shear (DC), compensated linear vector dipole (CLVD), and net volume change (ISO), for the different models tested in Figure 2.36a.

## 19.4 Frequency Dependence

The Littleton quarry blast is an excellent dataset in terms of understanding the effects of free-surface vanishing traction with real data. These chemical explosions are approximately 10 m in depth and are recorded at up to several km distances. Therefore the data represents a rather severe source-station geometry in terms of vanishing traction issues. It is possible to obtain a robust full moment tensor solution that is composed dominantly of an isotropic or explosive component; however the data provide the opportunity to evaluate capabilities of moment tensor inversion as a function of frequency.

Using five broadband stations at distances between 1.3 and 4.4 km from the production shot, we inverted for the best-fit moment tensor solutions and computed the Network Sensitivity Solutions (NSS) for different passbands. Indeed as we move towards longer periods, the moment tensor solution degrades and we obtain the incorrect source mechanism. Although the effects of free-surface vanishing traction may contribute to the degradation of the moment tensor solution as we go towards

longer periods, our preliminary analysis suggests noise in the data and possibly station geometry have a more significant effect on the method’s capabilities in seismic source analysis. A more thorough analysis is needed to assess the different factors that contribute to the errors in the inversion.

## 19.5 Discussions

Synthetic testing indicates that the DS Green’s functions associated with the  $M_{xz}$  and  $M_{yz}$  components are affected by the vanishing traction at the free-surface in the period range we are interested, between 10 and 50 seconds period. The amplitudes of the Green’s functions decrease systematically, but the waveforms look similar over the targeted depth range for nuclear explosions with little phase distortion. Our preliminary results show the degree in which free-surface vanishing traction affects the moment tensor solution depends strongly on the velocity model. Velocity models with a shallow velocity gradient show little to no bias in the isotropic and total scalar seismic moment, for both pure explosion source and composite source mechanisms. Similarly, we can retrieve the correct mechanism for these models using the full moment tensor inversion. One possible explanation is that models with a shallow velocity gradient have more complicated waveforms, and thus provide more constraint on the moment tensor inversion. Theoretically, as we go towards longer periods, the effects of vanishing traction would be more severe as the wavelength increases. Initial analysis of the Littleton dataset suggests errors due to noise may be more significant than the effects of vanishing traction. Further analysis is needed to separate out the different sources of error.

## 19.6 Acknowledgements

We acknowledge funding from the Air Force Research Laboratory, contract FA9453-10-C-0263 that is supporting this research.

## 19.7 References

- Burger, R.W., T. Lay, T.C. Wallace, and L.J. Burdick, Evidence of tectonic release in long-period S waves from underground nuclear explosions at the Novaya Zemlya test sites, *Bull. Seismol. Soc. Amer.*, *76*, 733-755, 1986.
- Ford, S.R., D.S. Dreger, and W.R. Walter, Identifying isotropic events using a regional moment tensor inversion, *J. Geophys. Res.*, *14*, B01306, 2009. doi:10.1029/2008jb005743.
- Ford, S.R., D.S. Dreger, and W.R. Walter, Network Sensitivity Solutions for Regional Moment-Tensor Inversions, *Bull. Seismol. Soc. Amer.*, *100*, 1962-1970, 2010.
- Julian, B.R., A.D. Miller, and G.R. Foulger, Non-double-couple earthquakes 1. Theory, *Rev. Geophys.*, *36*, 525-549, 1998. doi:10.1029/98rg00716.
- Song, X.J., D.V. Helmberger, and L. Zhao, Broad-Band Modelling of Regional Seismograms: the Basin and Range Crustal Structure, *Geophys. J. Int.*, *125*, 15-29, 1996. doi:10.1111/j.1365-246X.1996.tb06531.

## 20 ShakeAlert: A Unified EEW System for California

Margaret Hellweg, Richard Allen, Maren Böse (Caltech), Holly Brown, Georgia Cua (ETH), Egill Hauksson (Caltech), Thomas Heaton (Caltech), Margaret Hellweg, Ivan Henson, Serdar Kuyuk, Doug Neuhauser

### 20.1 Introduction

Earthquake Early Warning (EEW) is a method of rapidly identifying an earthquake in progress and transmitting alerts to nearby population centers before damaging ground shaking arrives. The first few seconds of the initial P-wave arrivals at one or more stations are used to detect the event, and predict magnitude and peak shaking. Detections from several stations are combined to locate the event. A warning of imminent shaking can be used to activate automatic safety measures, such as slowing trains, isolating sensitive equipment, or opening elevator doors. Warnings can also be sent directly to the public via cell phone, computer, television, or radio.

With support from the United States Geological Survey (USGS), the California Integrated Seismic Network (CISN) hosted a three-year proof of concept project for EEW algorithms in 2006-2009. Following that successful project, the Berkeley Seismological Laboratory (BSL) together with its CISN EEW partners, the California Institute of Technology (Caltech), and the Swiss Institute of Technology Zürich (ETH), is collaborating on an integrated, end-to-end demonstration system for real-time EEW in California. The new system, called CISN ShakeAlert, is capable of continuous long-term operation and rapidly provides alerts to test users in the state.

### 20.2 Project Status

The ShakeAlert system combines the best aspects of the three methods from the proof-of-concept project. Caltech's OnSite algorithm uses P-wave data from the single station nearest the epicenter to provide extremely rapid estimates of likely ground shaking. The BSL's ElarmS algorithm and ETH's Virtual Seismologist algorithm use data from several stations around an event epicenter to produce a slightly slower but more reliable estimate of magnitude and location. Combining these methods produces an algorithm which has the speed of a single-station method but is then promptly confirmed and adjusted by additional station data to form a more accurate description of the event. When an identified event exceeds a defined combination of magnitude, ground shaking intensity and statistical likelihood, information is broadcast to system users. Currently, during the development phase, only project participants receive event information. In January 2012, test users outside the seismological community began to receive alert information. The recipients include the state's emergency operations center at the California Emergency Management

Agency (CalEMA). A schematic diagram of the end-to-end system is shown in Figure 2.38.

### 20.3 ElarmS Developments

During the past year, we have worked extensively to improve UC Berkeley's contribution to the system, ElarmS and the Decision Module (see Section 21). We implemented updated and streamlined waveform processing software. As a result, data are now available several seconds earlier than before, especially data from Q330 data loggers. This new waveform processing system is now on our operational computers, improving robustness and reliability. In addition, we have released and are operating a revised version of the ElarmS code, ElarmS-2. During the proof of concept phase, the code detecting earthquakes and preparing alerts was simply the original research software. During the current project, we have rewritten and modernized the ElarmS software. The new version has been the operational version since March 2012, and is producing and publishing alerts for the entire state. Elarms-1 only published alerts for the greater San Francisco Bay Area. Results from Elarms-2 are shown in the map of Figure 2.39. We have also been working hard to exclude false alerts from distant earthquakes.

### 20.4 Perspectives

July 2012 marks the end of the current USGS-funded project. We look forward to continuing to maintain, operate and improve the demonstration EEW system with continued support from the USGS, with particular emphasis on the interaction with EEW users. During the past year, we received support from the Moore Foundation, together with Caltech and the University of Washington, to begin development of a West Coast Earthquake Early Warning system. Important tasks for this project include the development of tools to quickly evaluate large and great earthquakes using GPS measurements and finite fault analysis. We envision including these new tools in our current operational system.

### 20.5 Acknowledgements

This project is supported at UC Berkeley by USGS Cooperative Agreement G09AC00259, at Caltech by Agreement G09AC00258, at USC/CEC by Agreement G09AC00255 and at ETH Zürich by Agreement G09AC00256. Funding from the Moore Foundation is under project number GALA 3024.

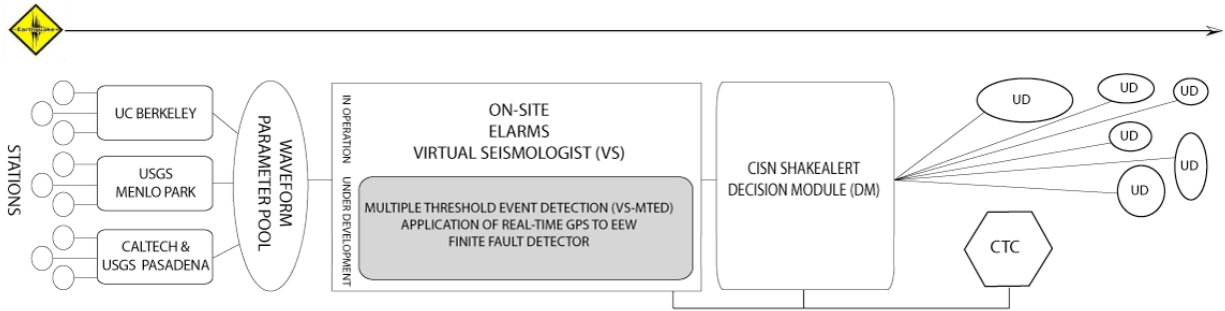


Figure 2.38: Components of the ShakeAlert EEW System. From left to right, the elements of the system are waveform processing, event detection, decision module (DM), CISN ShakeAlert user displays (UD), and the CISN testing center (CTC) software. *Waveform Processing:* Each data center processes telemetered digital waveform data collected from seismic stations throughout California. Critical waveform parameters are calculated from this data, then dumped into a statewide parameter pool. *Event Detection:* From the parameters, CISN’s EEW algorithms rapidly detect and characterize an event within seconds of its initiation. Several EEW detection algorithms run in parallel to provide the Decision Module with the best available source parameters. *Decision Module:* The DM combines earthquake information from each algorithm and delivers a “ShakeAlert” xml message about an earthquake in progress to subscribed users. *CISN ShakeAlert User Displays:* The ShakeAlert UD receives xml messages from the DM and displays their content in a simple and easily understandable way. *CISN Testing Center Software:* The CTC Software provides automated and interactive performance evaluations of ShakeAlert forecasts.

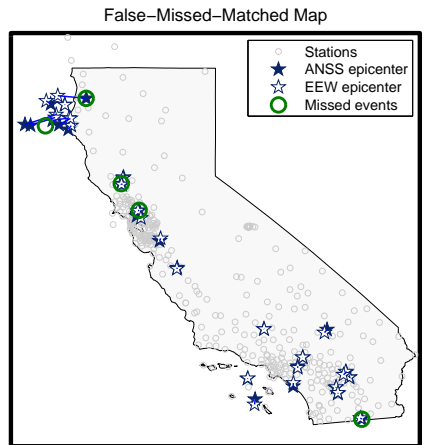


Figure 2.39: Map of California showing earthquakes from 6 Dec 2011 - 11 Jun 2012 with  $M > 3.4$  for which ElarmS-2 produced alerts. Solid stars - ANSS epicenter; hollow stars - ElarmS-2 epicenter; circles - missed events. There were no false events (ElarmS-2 alerts when no earthquake was reported by CISN network operators) during this interval. At the edges of the network where station coverage is poor, like Cape Mendocino in Northern California, ElarmS-2 may mislocate events, but in most cases it still detects and reports them.

## 21 ElarmS Earthquake Early Warning

H. Serdar Kuyuk, Holly Brown, Richard Allen, Douglas Neuhauser, Ivan Henson and Margaret Hellweg

### 21.1 Introduction

ElarmS is a network-based earthquake early warning (EEW) algorithm developed at UC Berkeley for rapid earthquake detection, location and hazard assessment. ElarmS operates as part of the greater ShakeAlert EEW system, an ongoing project by the California Integrated Seismic Network (CISN). ShakeAlert combines three different EEW algorithms, one of which is ElarmS, into a unified system for providing warnings for events throughout the state. Output from the three algorithms is integrated by the ShakeAlert DecisionModule into a single alert messaging system. In this past year, the alert messages generated are being sent to external test users from several public and private, industry and governmental groups.

ElarmS consists of two primary modules: (1) a waveform processing algorithm, which runs in parallel at UC Berkeley, Caltech, and USGS Menlo Park to continuously filter real time seismic data, and (2) a single state-wide event detection algorithm which operates at UC Berkeley. The event detection module analyzes the incoming data from the three waveform processing streams and identifies earthquakes in progress.

### 21.2 Current Progress

From March 2011 to April 2012 ElarmS was sending event messages to ShakeAlert DecisionModule for events in the San Francisco Bay Area and Central Coast. In 2010 and 2011, we developed second generation ElarmS waveform processing and event detection algorithms, based in C++ for speed and adaptability. New more flexible communication software connects the remote waveform processing modules to the event detector. The new event detection module (E2) utilizes the established location and magnitude relations, but has an updated method of associating triggers together to form events. With the new updates E2 has been processing statewide real-time data since April 2012. Its new capabilities include: a) a split event check to prevent dual event alerts for a single event; b) linear teleseismic filtering to reduce teleseismic phase triggers; c) use of 1-second data package from BK network to increase speed; d) replay capability for past earthquake events; e) improved magnitude determination for southern California; f) improved location estimation; g) specific algorithms for offshore events; h) dynamic integration of station data from throughout California.

We are continuously inspecting and assessing system performance on a weekly basis. The assessment software

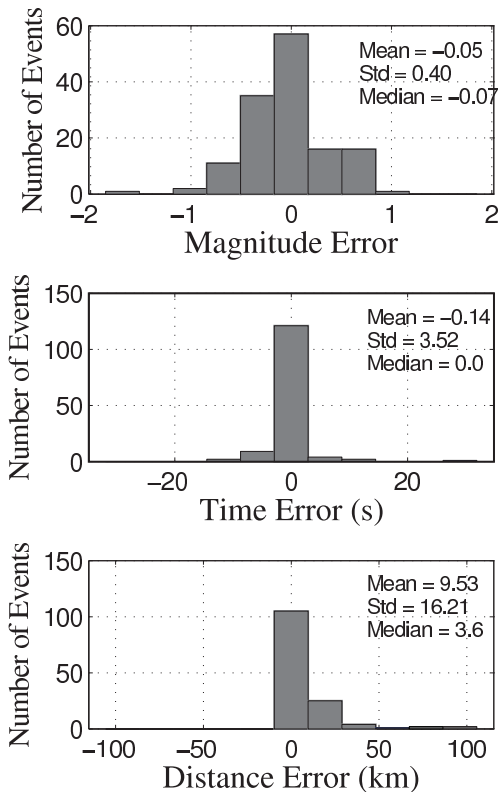


Figure 2.40: Performance of E2 for events  $M > 2.5$  for about 4 months. Standard deviation of the magnitude, and origin time error are 0.4, 3.52 respectively. The median epicenter location error is 3.6 km.

automatically evaluates station latencies, promptness of alerts, accuracy of magnitude, location, and ground-shaking estimates, and number of successful event detections, false alarms, and missed events. This information is evaluated and E2 is being optimized based on performance.

In offline tests of performance using the latest version (Ev2.2) applied to the data from a period of  $\sim 4$  months (December 6, 2011 to April 20, 2012) we find that E2 detected 164 events of magnitude 2.5 or greater in California and sent 4 false alerts, of which 3 are due to a single teleseismic event. In this period 22 events are declared with magnitude greater than 3.5 with 2 false and only one missed earthquake. For the greater Bay Area, 11 events were detected with magnitude greater than 3.5 with no false and no missed events. Figure 2.40 shows the performance of E2 for events  $M > 2.5$  for the same period.

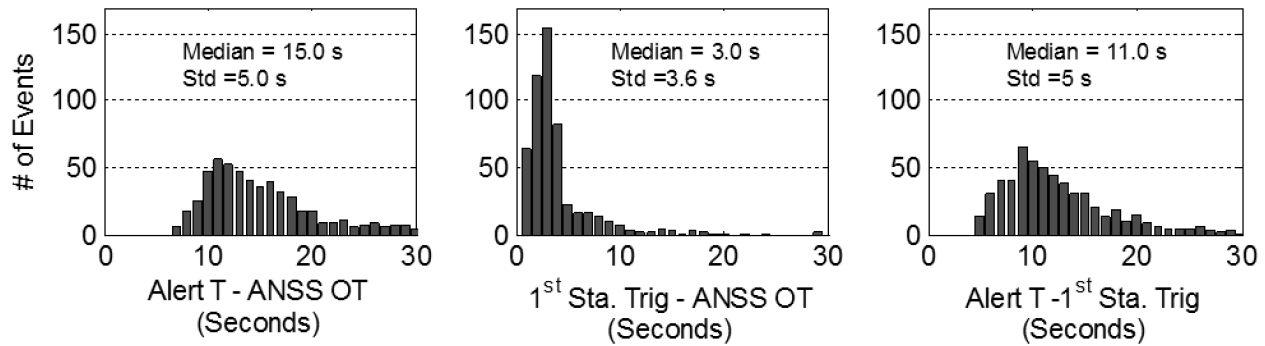


Figure 2.41: On average E2 declares events 15 seconds after origin time with a 5 second standard deviation. The initial P-waves take an average of 3 seconds to reach the first station, and the communications, processing and algorithms require an average of 11 seconds to declare an earthquake.

On average, E2 declared events 15 seconds after the origin time with a 5 second standard deviation. Initial P-waves take an average of 3 seconds to reach the first station, meaning that the communications, processing and algorithms require an average of 11 seconds to declare an earthquake (Figure 2.41).

### 21.3 Future Perspective

a) Investigation of GPS: in 2011 we also began investigating the use of GPS for earthquake early warning, focusing on the  $M_w$  7.2 El Mayor-Cucapah earthquake, which had both real-time GPS and seismic data available. We developed a simple algorithm to extract the permanent displacement at GPS sites starting one oscillation after triggering on the dynamic long period signal. The estimate is continually improved with time. These permanent displacements can then be inverted for source characteristics given an approximate estimate of the fault plane. Initial results suggest that GPS would provide a valuable contribution to EEW. The new approach provides an independent estimate of magnitude, which is particularly important for the largest events. This approach is now being improved upon and applied to the  $M_w$  9.0 2011 Tohoku-oki earthquake (see 22 in this volume).

b) Artificial Neural Network based pattern recognition of false events: in 2012 we began testing an Artificial Neural Network (ANN) filter at the end of ElarmS offline processing stream as a final "quakefilter" to catch false alerts before they are released to users. The ANN reads input data (an earthquake alert message) and the desired output (true or false) for a large dataset of sample events, and optimizes a mapping function between inputs and outputs. That function can then be utilized on future events to filter out alerts with a high probability of being false.

When ElarmS requires four stations to confirm an event -which is the case for the current online system-

the ANN could not improve on the current ElarmS results which has a 4% false alert rate. When ElarmS is reconfigured (offline) to send alert messages with only two or three stations the number of false alerts increases significantly. However, application of the ANN halves the false alert rate, from 15% to 8%.

One possible approach is therefore to allow ElarmS to detect events with just 2 or 3 triggers, apply the ANN filter to reduce false alerts, and then release the event alerts indicating the higher probability of a false alert. Once an event has four stations reporting, ElarmS would bypass the ANN completely and revert to the current standard alert criteria, thus avoiding any risk of the ANN mistakenly filtering out a real earthquake unlike the events it has seen to date, e.g. a very large earthquake. However, the ANN presents the option of sending faster, lower-certainty alerts, which would then be confirmed or improved seconds later when four stations have triggered. As always, users could choose whether to receive the earlier, lower certainty alerts or not.

### 21.4 Acknowledgements

This project is funded by USGS/NEHRP award G09AC00259 and by the Gordon and Betty Moore Foundation.

### 21.5 References

- Brown, H., R.M. Allen, M. Hellweg, O. Khainovski, D. Neuhauser, and A. Souf, Development of the ElarmS methodology for earthquake early warning: Realtime application in California and offline testing in Japan, *Soil Dynamics and Earthquake Engineering.*, 31, 188-200, 2011.
- Allen, R.M., Seconds before the big one, *Scientific American*, 2011.
- Allen, R.M. and A. Ziv. Application of real-time GPS to earthquake early warning, *Geophys. Res. Lett.*, 38, 2011.

## 22 Earthquake Early Warning with GPS Data

Simona Colombelli (University of Naples) and Richard Allen

### 22.1 Introduction

The combined use of seismic and geodetic observations is now a common practice for finite-fault modeling and seismic source parametrization. With the advent of high-rate 1Hz GPS stations the seismological community has recently begun looking at GPS data as a valid complement to the seismic-based methodologies for Earthquake Early Warning (EEW).

In the standard approaches to early warning, the initial portion of the P-wave signal is used to rapidly characterize the earthquake magnitude and to predict the expected ground shaking at a target site, before the arrival of the most damaging waves. Whether the final magnitude of an earthquake can be predicted while the rupture process is underway, still represents a controversial issue; the point is that the limitations of the standard approaches when applied to giant earthquakes have become evident after the experience of the  $M_w$  9.0, 2011 Tohoku-Oki earthquake.

Here we explore the application of GPS data to EEW and investigate whether they can be used to provide reliable and independent magnitude estimations. The large size and the complex rupture process, together with the huge number of high-quality GPS records available, make the 2011 Tohoku-Oki earthquake a unique and ideal case-study for our purposes.

### 22.2 Seismic vs. GPS data

Because EEW systems are essentially applied to moderate-to-strong earthquakes, large, dynamic, accelerometric sensors are generally used for real-time seismic applications. These instruments are able to record unsaturated signals without risk of clipping at the arrival of the strongest shaking. Accelerometer waveforms are usually integrated twice to obtain displacement time-series and a high-pass causal Butterworth filter is finally applied to remove the artificial effects and long-period drifts introduced by the double integration operation (Boore, 2002). The application of the high-pass filter, while removing the artificial distortions, reduces the low-frequency content of the recorded waveforms, resulting in the complete loss of the low-frequency energy radiated by the source and of the static displacement component. The effect of such a filtering is even more relevant for very large earthquakes, whose corner frequency is expected to be lower or comparable with the cut-off filtering frequency (typically 0.075 Hz). Since GPS stations are able to register directly the ground displacement without any risk of saturating and any need of compli-

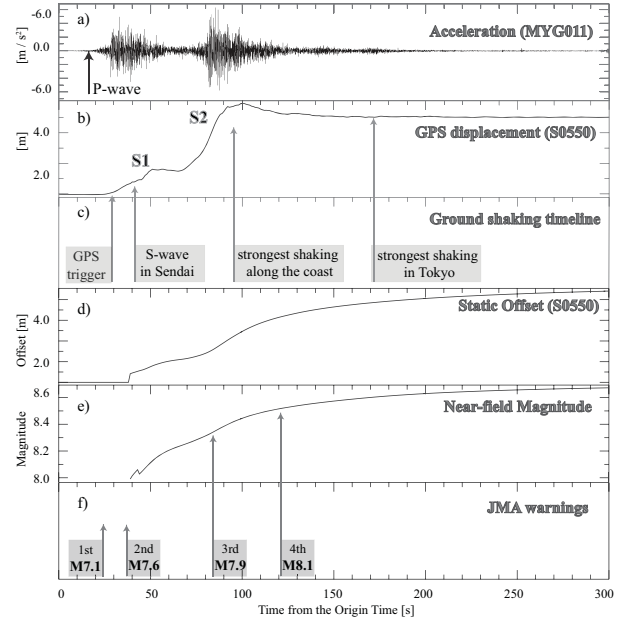


Figure 2.42: a) acceleration waveform at the closest seismic station (MYG011); b) displacement waveform at the closest GPS station (S0550), co-located with MYG011 station; c) timeline showing when the GPS information is available with respect to the time at which the strongest shaking occurs in the Sendai and Tokyo regions; d) output of the algorithm for the static offset extraction at the S0550 station; e) magnitude estimation from the closest GPS station with the point source and the near-field condition approximations; f) timeline of the JMA warnings and magnitude updates.

ated artificial corrections, geodetic displacement time-series represent the complementary contribution to the high-frequency information provided by seismic data.

Figure 2.42 shows a comparison between the acceleration (a) and the GPS displacement (b) waveforms of the Tohoku-Oki earthquake, recorded at two co-located stations (MYG011 from the K-Net network and S0550 from the GEONET network, respectively). Both records show evidence of two main phases (denoted as S1 and S2 in the figure) that correspond to two distinctive, time delayed episodes of slip release during the rupture process (Lee *et al.*, 2011). The GPS displacement starts to be evident later than the P-wave arrival on the seismic record and approximately at the same time of the S-wave arrival and the period of strong shaking. As it can be inferred from the timeline of Figure 2.42c, the P-wave onset at the

closest seismic station (MYG011) occurs approximately 15 seconds after the Origin Time (O.T.), while the first GPS information is available around 40 seconds after the O.T. The maximum amplitude on the GPS record for both phases is almost coherent in time with the arrival of the strongest shaking (on the acceleration waveform) at the same place. However, this does not prevent the use of these data and the issuance of a warning with the expected ground shaking at more distant sites. For example, in the Tokyo region the maximum shaking occurs about 170 seconds after the O.T., well after the GPS displacement has reached its maximum value at the closest station.

### 22.3 Real-Time offset extraction

We analyzed the co-seismic ground deformations produced by the 2011 Tohoku-Oki earthquake collected by the Japanese GPS Earth Observation Network (GEONET) (*Sagiya*, 2004). In order to extract the permanent displacement, we used the algorithm developed by *Allen and Ziv* (2011). The algorithm looks for a trigger along the records and declares the first-arrival onset when a pre-determined condition on the short-term vs. long-term average is satisfied (*Allen*, 1978). Starting from the trigger time, a running average is then computed along the waveforms and is delivered as a real-time estimation of the static offset. As an example, Figure 2.42d shows the permanent displacement extracted from the S0550 station.

The running average computation is expected to remove the dynamic component of the signal, which would affect the estimation of the static offset. However, to prevent the possible inclusion of a dynamic oscillation, the algorithm starts to deliver the running average after two trigger-amplitude crossings or 10 seconds after the trigger time, whichever comes first.

### 22.4 Rapid magnitude estimation

The static displacement resulting from the algorithm is then used to obtain a fast estimation of the earthquake magnitude. A quick and preliminary estimation of the earthquake size can be obtained by adopting the theoretical scaling relationship between the earthquake magnitude and the near-field static offset. In case of a very small fault (i.e., a point source) and at short distances from the source (i.e., in the near-field condition), the primary component of the static displacement  $u$  can be written as:

$$u \propto \frac{1}{4\pi\mu R^2} M_0(t)$$

where  $\mu$  is the rigidity modulus of the medium,  $R$  the hypocentral distance and  $M_0(t)$  the seismic moment. We applied the previous formula to the static offset of the closest station. The result is plotted in Figure 2.42e and

shows that the magnitude is fairly well reproduced, despite the approximations and the limited conditions of the formula. This is especially true when our result is compared with the output of the JMA warning system (Figure 2.42f), whose magnitude estimations were largely underestimated for the entire duration of the event. However, a weak systematic underestimation of the final magnitude value (with respect to the official value,  $M_w = 9.0$ ) is evident from the plot. We infer that this underestimation is essentially due to the point source approximation, whose effect may become significant whereas the extended dimension of the fault cannot be neglected.

An approach that may be more robust is inversion for the static slip on the fault plane, which allows consideration of the contributions from the entire fault plane and may provide a better estimation of the earthquake magnitude. We are currently working on the implementation of a real-time static slip inversion scheme using a constant-slip, rectangular source embedded in a homogeneous half-space (*Okada*, 1985). Our goal is to develop an efficient methodology for both the rapid determination of the event size and for the near real-time estimation of the rupture area. This would allow for a correct evaluation of the expected ground shaking at the target sites, that represents, without doubt, the most important aspect of the practical implementation of an early warning system and the most relevant information to be provided to the non-expert, end-user audience.

### 22.5 Acknowledgements

This work was supported by the University of Naples Federico II and a grant from the Moore Foundation.

### 22.6 References

- Allen, R.V. Automatic earthquake recognition and timing from single traces, *Bull. Seism. Soc. Am.*, 68, 5, 1521-1532, 1978.
- Allen, R.M. and A. Ziv. Application of real-time GPS to earthquake early warning, *Geophys. Res. Lett.*, 38, 2011.
- Boore, D.M. Comments on Baseline Correction of Digital Strong-Motion Data: Examples from the 1999 Hector Mine, California, Earthquake, *Bull. Seism. Soc. Am.*, 92, 4, 1543-1560, 2002.
- Lee, S.-J., B.-S. Huang, M. Ando, H.-C. Chiu, and J.-H. Wang. Evidence of large scale repeating slip during the 2011 Tohoku-Oki earthquake, *Geophys. Res. Lett.*, 38, 2011.
- Okada, Y. Surface deformation due to shear and tensile faults in a half-space, *Bull. Seism. Soc. Am.*, 75, 4, 1135-1154, 1985.
- Sagiya, T. A decade of GEONET: 19942003 The continuous GPS observation in Japan and its impact on earthquake studies, *Earth Planets Space*, 56, xxixxi, 2004.

## 23 GPS Rapid Response to Moderate Earthquakes: A Case Study of the Alum Rock Earthquake

Ingrid A. Johanson

### 23.1 Introduction

The 2007 M5.5 Alum Rock earthquake is used to investigate the possible performance of real-time GPS stations in the San Francisco Bay Area. The Alum Rock earthquake was a moderate earthquake on the Calaveras fault, near several GPS stations with 1 sample per second (sps) data available. Murray-Moraleda and Simpson (2009) found nearby stations to have several mm of coseismic displacement from daily processed results, and found some to have measurable postseismic displacements (see first figure at right). The Alum Rock earthquake is used in these tests because it is the largest earthquake in the SF Bay Area since 1 Hz GPS data has been widely collected. However, it represents the smaller end of earthquakes that are likely to have detectable offsets using epoch-by-epoch processing. These tests therefore show the capabilities of high-rate GPS for a challengingly small event.

### 23.2 Real-time vs. Rapid Post-processing

While real-time processing of GPS data is capable of providing measurements of displacement within seconds of its occurrence, post-processing provides results with lower noise levels, leading to better precision. The differences will be especially important for a moderate earthquake with offsets of less than  $\sim 1$ cm. GPS may not be critical in earthquake early warning for a moderate event, but it can still provide information that will be useful for rapid response. In frames A1, B1, and C1 of Figure 2.43, 1 sps GPS observations were processed with TrackRT in rewind mode (developed by Tom Herring at MIT) and with IGS Ultra-rapid orbit files. In general the processing provided clean results with a high percentage of resolved integer ambiguities and over a six-hour period the 4 stations had a RMS of 000.

These can be compared with frames A2, B2, and C2, which show post-processing using Track and Ultra-Rapid orbits with data from 2 hours before the event origin time and up to just 1 minute after. These results have considerably less long period noise and in the cases of A2 and B2 clearly show an offset that was not visually apparent in the real-time results. Processing of data up to 10 minutes after the earthquake origin is shown in frames A3, B3, and C3, and does not show major differences with processing up to just a minute after. Nor does processing of the entire day of data (not shown). This indicates that rapid post-processing can produce time series

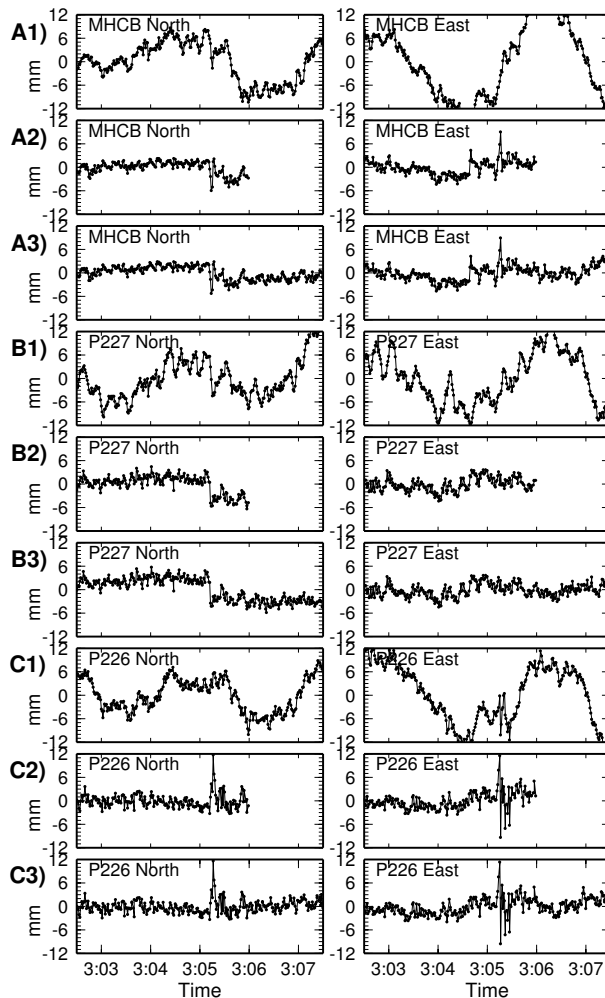


Figure 2.43: Time series of East and North motions for A) MHC B, B) P227 and C) P226. Frames numbered with 1) are from TrackRT rewind, 2) are post-processed with Track with up to 1 minute of post-earthquake data, 3) have 10 minutes of post-earthquake data. Note that the plots are in GPS time, such that the earthquake origin time would plot as 3:05:09.

that are just as precise as those covering a longer time span and considerably less noisy than real-time. With post-processing after only one minute, results could be available within 2-3 minutes for use in fault plane determination and finite fault models and could easily be repeated at various intervals for earthquakes with longer shaking.

### 23.3 Offset determination

The second comparison is between two methods to measure the size of an offset at the time of the earthquake. In this section, only post-processed results were used. The time of the offset was treated as a known and evaluation windows of 10, 30 and 45 seconds were tested. In all cases the before-event timespan was equal to the after-event timespan.

The median method defines the pre- and post-earthquake positions as the median positions during the evaluation windows. It has the advantage of being relatively insensitive to the large excursions in position that can happen during shaking. However, it has the disadvantage that it will continue to evolve with time. That is, it will include the effects of long wavelength noise or rapid postseismic motions. This method performed best with the smallest evaluation window tested (10s) and produced offsets that matched the size of the offsets from daily observations to a reasonable degree (Figure 2.44B).

The line-fitting method fits lines to the displacements before and after the offset time, within the evaluation windows. Unlike in the median method, the pre- and post- positions are extrapolated to the offset time and it is determined from their difference. This mitigates the effect of long-wavelength drift, but leads to large fluctuations in calculated offset in the first 10-15 seconds. This method tends to overestimate the offsets when the 10s window is used and even with the 30s window (shown in Figure 2.44A), the sizes of the offsets are as much as twice that of the results from daily solutions. However this method provided good azimuth estimates and a very good fit to station MHCB.

### 23.4 Conclusions

For rapid response applications during a moderate earthquake, there is still useful information to be gained by using rapid post-processing. The post-processed results will provide less noisy displacements and more accurate offset estimates. Post-processing can occur 1 minute after an event (or even sooner) and provide results in 2-3 minutes. To determine the offsets, either the median or the line-fitting methods will provide reasonable results. The line fitting method provides better azimuths in this case study, which would be important for fault plane determination. However the overshoot in size could lead to overestimates of the amount of slip in an inversion.

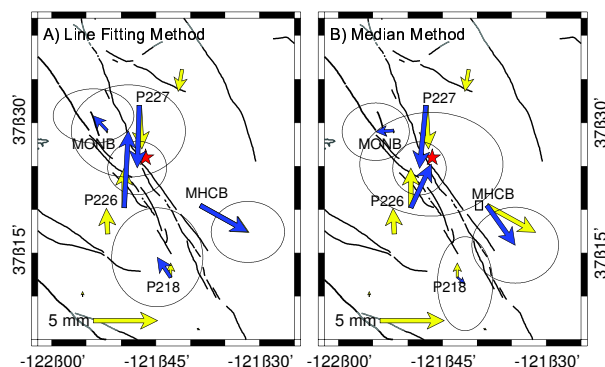


Figure 2.44: Velocity fields showing offsets determined from A) the line-fitting method and B) the median method (blue vectors). In both cases, these are from post-processing using up to 1 minute of post-earthquake data. The rapid results are compared to coseismic offsets determined by Murray-Moraleda and Simpson (2009) from post-processed daily GPS solutions (yellow vectors). The Alum Rock epicenter is shown by the red star.

### 23.5 References

Murray-Moraleda, J. R., and R. W. Simpson, Geodetically Inferred Coseismic and Postseismic Slip due to the M 5.4 31 October 2007 Alum Rock Earthquake. *Bull. Seismol. Soc. Am.*, 99(5), 2784-2800, 2009.

## 24 Using Smartphones to Detect Earthquakes

Qingkai Kong, Richard Allen, Stephen Thompson, Jonathan D. Bray, Ana Luz Acevedo-Cabrera

### 24.1 Introduction

We are exploring the use of accelerometers in smartphones to record earthquakes. We have developed an application for Android phones based on previous work with iPhones to record the acceleration in real time. These records can be saved on the local phone or transmitted back to a server in real time. A series of shake table tests were conducted (and more tests will be conducted soon) to evaluate the performance of the accelerometers in these smartphones by comparing them with high quality accelerometers. We also recorded different human activities using these smartphones. Different features were extracted from the recordings and were used to distinguish earthquakes from daily activities. We implemented a classifier algorithm based on an artificial neural network, which shows a 99.7% successful rate for distinguishing earthquakes from certain typical human activities

### 24.2 Data Sources

Two kinds of smartphones have been used in this research: iPhone and Android phones. The applications on these phones are iShake and droidShake. Data was collected mainly in three ways: (1) Continuous recording of different human activities, e.g. walking, running, sitting, taking the bus, etc. (2) Trigger-based data from various users sent to a server. This method requires that the phone stay steady for certain amount of time. Then, if the acceleration exceeds the pre-determined threshold, it triggers the algorithm to send data before and after the trigger to the server. (3) Data recorded during the shake table tests with earthquake input signals. These three types of data were used to distinguish earthquake signals from non-earthquake signals.

### 24.3 Detection Method and Classifier

A high pass filter was first applied to the data in real time to eliminate the baseline offset. Then the filtered data was divided into segments using a series of sliding windows. From each of the sliding windows, three parameters were extracted to characterize different types of signals, including maximum number of zero crossings from the three components, peak acceleration, and the ratio of peak velocity over peak acceleration from the vector sum of the three components. These three parameters were then used as input to train the neural network to distinguish earthquakes from non-earthquake signals.

A 10-fold cross validation method was used to determine the optimal size of the time window and the num-

Table 2.1: Confusion Matrix

		Target Class		%
		Non-EQ	EQ	
Predict Class	Non-EQ	584	3	99.5%
	EQ	1	582	99.8%
%		99.8%	99.5%	99.7%

ber of neurons in the neural network. Based on the cross validation results, a 150 sample length of time window was found to be optimum, and one hidden layer with 19 neurons was used to configure the neural network.

### 24.4 Results

The output of the neural network is “earthquake” or “non-earthquake.” The results are shown in the confusion matrix in Table 2.1. The overall success rate is 99.7%. Figure 2.45 shows the peak acceleration and maximum number of zero crossings for different activities and earthquake signals. It is obvious that these two parameters alone could distinguish most of the earthquakes from other human activities. The test of the neural network is shown in Figure 2.46

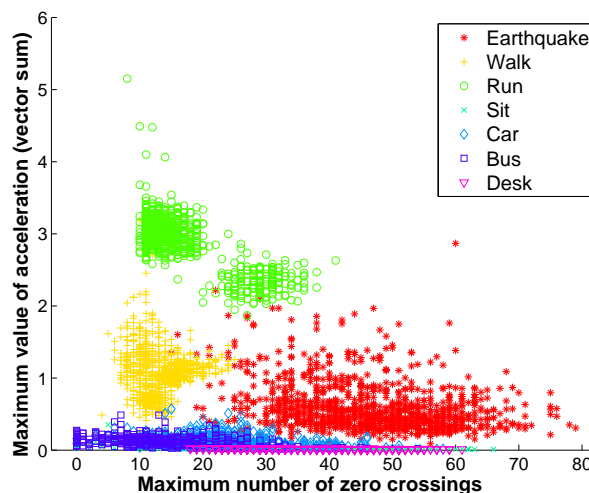


Figure 2.45: Maximum value of acceleration vs maximum number of zero crossings

### 24.5 Conclusion and Future Work

This initial study shows the potential of using smartphones to detect earthquakes. By using multiple phones in the future, we can achieve higher accuracy. A network

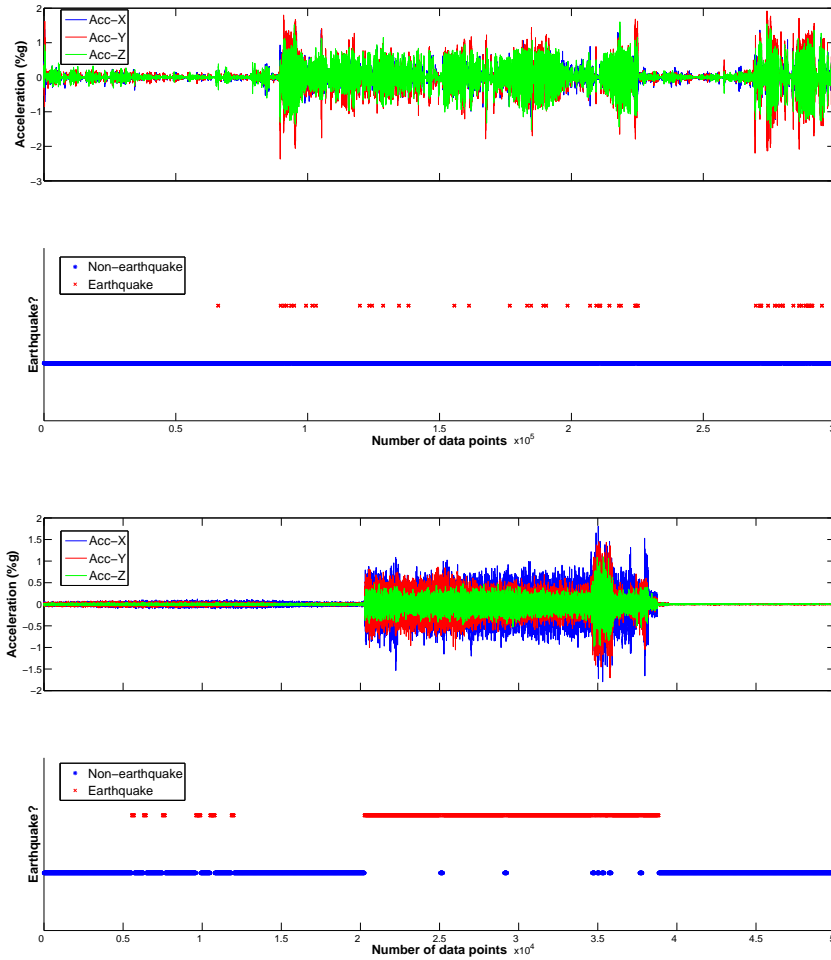


Figure 2.46: Algorithm Test: Figures show the detection of non-earthquakes and earthquakes using the artificial neural network model developed. The upper two panels show the waveform and the detector output for an accelerogram recorded for different random activities. This random record consisted of various activities within about two hours, including walking, running, jumping, riding in a vehicle, and so on. In 97% of cases, the windows were classified correctly as non-earthquake signals. The lower two panels show the detection using data recorded by the phone when it was placed on a shake table. Once the shake table starts to move, the algorithm correctly classifies most of the movement as an earthquake.

consisting of these smartphones may work as a supplemental network to the current traditional network for scientific research and real-time applications.

## 24.6 Acknowledgements

The shake table tests for the iPhones were arranged and conducted by Jonathan Bray, Alex Bayen, Shideh Dashti, and Jack Reilly. This project is funded by Deutsche Telekom and CITRIS. Markus Neubrand, Angela Nicoara, Louis Schreier and Arno Puder from Deutsche Telekom provided the Android phones and the droidShake application.

## 24.7 References

- Bao, L. and Intille, S. S., Activity recognition from user-annotated acceleration data, In *Proc. of the 2nd Int. Conf. on Pervasive Computing*, 1-17, 2004.
- Dashti, S., Reilly, J., Bray, J.D., Bayen, A., Glaser, S. and Mari, E., iShake: Using Personal Devices to Deliver Rapid Semi-Qualitative Earthquake Shaking Information, *GeoEngineering Report, Depart. of Civil and Environ. Engineering, Univ. of California, Berkeley*, 2011.
- M. Fahriddin, M. G. Song, J. Y. Kim, and S. Y. Na, Human Activity Recognition Using New Multi-Sensor Module in Mobile Environment, 2011.

# 25 Probing the Deep Rheology of Tibet: Constraints from 2008 $M_w$ 7.9 Wenchuan, China Earthquake

Mong-Han Huang and Roland Bürgmann

## 25.1 Introduction

The time-dependent surface deformation after a large earthquake reflects the response to the redistribution of stresses induced by the earthquake and can be used to probe the viscous strength of the lithosphere. However, processes such as aseismic afterslip and aftershock-related deformation can also contribute to the postseismic deformation. The 2008  $M_w$  7.9 Wenchuan earthquake occurred on the eastern flank of the Tibetan Plateau and its postseismic deformation gives us an opportunity to examine the long lasting question of whether the growth of the Tibetan Plateau is by brittle crustal thickening or by lower crustal flow. We use finite element modeling of viscoelastic relaxation with lateral heterogeneity applied for the calculation of the 1.5 year postseismic displacement. A layered dislocation model is also tested for contributions of afterslip on the down-dip extension of the rupture or a shallow detachment. In the SW Longmenshan, the lower crustal flow model can explain the near- to far-field deformation in space and time. In the NE Longmenshan, the lower crustal flow alone cannot produce the localized deformation observed there. As a result, the postseismic displacement of the Wenchuan earthquake is dominated by the relaxation from the lower crust, but locally contributed to by the afterslip on the shallow part.

## 25.2 Method and Data

We use both an analytical solution (Pollitz, 1992) and finite element modeling software *ABAQUS<sup>TM</sup>* to calculate the postseismic deformation due to viscoelastic relaxation. The Wenchuan earthquake fault geometry is based on Shen *et al.*, 2009, based on geodetic inversion of coseismic deformation. Our simplified fault geometry is composed of five segments with different slip rates, extends to a depth of 20 km, and runs along the 285 km Longmenshan fault zone (Figure 2.47c). Thirty-six cGPS stations are deployed on both sides of the Longmenshan fault zone and obtain about 1.5 years of postseismic displacement observations (Figure 2.47c,d). Twenty two ENVISAT interferograms are generated using the software ROI PAC 3.0, and the 90 m SRTM DEM is used to correct the phase due to the topography. The InSAR time series obtained from the 22 interferograms reveals the postseismic displacement from June 2008 to December 2009.

## 25.3 Results

The InSAR time series shows 7-9 cm postseismic displacement in line of sight in the near-field 1.5 years after the Wenchuan main shock, and drops to 3-6 cm in the region 50 km away from the surface rupture (Figure 2.47b). In addition, surface creep is observed in the NE Longmenshan, which implies that shallow afterslips occurred in the NE region. All cGPS time series data show transient displacements in the horizontal and vertical components. The 1.5 year observations show southeastward displacement in the SW and northeastward displacement in the NE Longmenshan. Significant postseismic uplift in the SW Longmenshan is observed from the GPS measurements (Figure 2.47c) as well as the InSAR time series (Figure 2.47b).

The results of the numerical modeling show that an inferred 35 km thick lower crustal flow with viscosity of  $2 \times 10^{18}$  Ps s under eastern Tibet can explain both spatial and temporal patterns of the postseismic displacement. On the other hand, the best fitting afterslip model requires more than 50 cm of slip below 40 km depth, which might be below the brittle-ductile transition zone and is unlikely to produce such a high dislocation in a short time scale. Besides, there is no significant correlation between the repeating microearthquakes (data by Li *et al.*, 2011) after the main shock and the afterslip model. Consequently, in the SW Longmenshan, the lower crustal flow model can explain the near- to far-field postdeformation in space and time. However, the afterslip on the shallow part of the fault plane appears to contribute to the deformation along this strike-slip dominated portion of the rupture.

## 25.4 Acknowledgements

We thank Prof. Z.-K. Shen of Beijing for providing the GPS time series. M.-H. Huang thanks Prof. Andy Freed for instruction on *ABAQUS<sup>TM</sup>*. This work is supported by NSF grant (EAR 0738298).

## 25.5 References

- Li, L., Q. Chen, F. Niu, and J. Su, Deep slip rates along the Longmen Shan fault zone estimated from repeating microearthquakes. *J. Geophys. Res.*, 116, B09310, doi:10.1029/2011JB008406, 2011.
- Pollitz, F., Postseismic relaxation theory on a spherical earth. *Bull. Seism. Soc. Am.*, 82, 1, 422-453, 1992.
- Shen, Z.K., J. Sun, P. Zhang, Y. Wan, M. Wang, R. Bürgmann, Y. Zeng, W. Gan, H. Hiao, and Q. Wang, Slip maxima at fault junctions and rupturing of barriers during the 2008 Wenchuan earthquake, *Nat. Geosci.*, 2, 718-724, doi:10.1038/NCEO636, 2009.

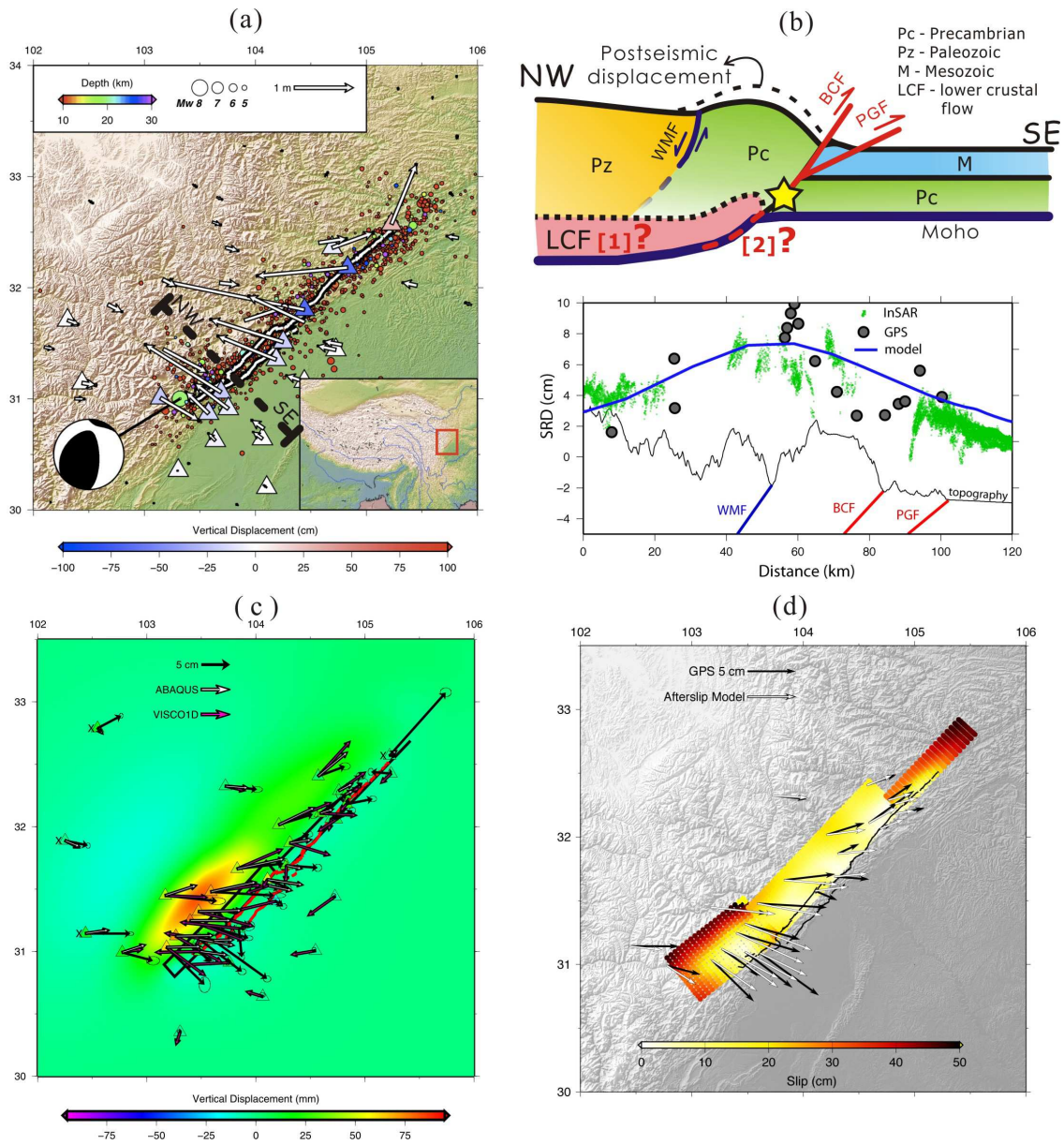


Figure 2.47: (a) The Wenchuan coseismic displacement. The white arrows are the GPS recorded coseismic displacement, and the colors in the triangles are the vertical displacement. The beach ball diagram shows the focal mechanism of the main shock, and the circles are the aftershocks color coded with depth. The white lines outline the coseismic surface rupture. The inset indicates the study area location at the edge of the Tibet Plateau. (b) Possible mechanism of Wenchuan postseismic deformation: [1] Relaxation of the lower viscous crust (pink region). [2] Afterslip in the down-dip extension of the earthquake fault. Lower figure shows the NW-SE profile of south Longmenshan (Figure 2.47a) with 1.5 years postseismic displacement observed by InSAR (green) and GPS (grey). The dark blue line is the forward model assuming viscoelastic relaxation from the lower crustal flow. (c) The predicted 1.5 years postseismic displacement. The black arrows are the GPS horizontal measurements, and the white and purple arrows are the *ABAQUS*<sup>TM</sup> and *VISCO1D* models, respectively. The background color is the *ABAQUS*<sup>TM</sup> predicted vertical displacement. (d) The afterslip model. The yellow to red circles are the fault geometry with down-dip extension to 60 km, color coded by afterslip. Note much larger slip located below 40 km that is probably below the brittle-ductile transition zone.

# 26 Global Waveform Tomography with the Spectral Element Method: A Second-Generation Upper-Mantle Model

Scott French, Vedran Lekic, and Barbara Romanowicz

## 26.1 Introduction

The SEMum model of Lekic and Romanowicz (2011) (SEMum v.1) was the first global  $V_S$  model obtained using spectral-element forward modeling (SEM: *Komatitsch and Vilotte, 1998*), and exhibits impressive amplitudes of heterogeneity in the upper 200km of the mantle compared to previous global models. Among other measures to make SEM-based modeling tractable, SEMum v.1 was developed using an homogenized crustal model of uniform 60km thickness (*Capdeville and Marigo, 2007*). While this choice is justifiable in the continents, it can potentially frustrate interpretation of shallow upper-mantle structure in the oceans. Here, we present an update to SEMum (SEMum v.2: *French et al., 2011*), which was obtained using an homogenized crust with more realistic laterally-varying thickness.

## 26.2 Methodology

Our approach to data processing and inversion largely mirrors that of Lekic and Romanowicz (2011). We employ a dataset identical to that of SEMum v.1, consisting of long-period ( $60 \leq T \leq 400$ s) three-component waveforms of 203 well-distributed global earthquakes ( $6.0 \leq M_w \leq 6.9$ ), as well as global group-velocity dispersion maps at  $25 \leq T \leq 150$ s (*Ritzwoller, pers. comm.*). Dispersion at  $T \leq 60$ s constrains our crustal model (Section 26.2), while, for consistency, the full period range is included in our mantle inversion.

Waveform inversion follows a hybrid approach, in which we forward model the global wavefield “exactly” using the SEM, while sensitivity kernels are calculated approximately using non-linear asymptotic coupling theory (NACT: *Li and Romanowicz, 1995*). The hybrid scheme represents a  $\geq 3$ x reduction in computation relative to a fully-numerical approach (*Tarantola, 1984*), and, together with the homogenized crustal model and mode-coupled SEM implementation (cSEM: *Capdeville et al., 2003*), renders SEM-based inversion tractable.

### Crustal structure

Since cSEM uses modes to model wave propagation in the core, SEM time stability is instead dictated by crustal structure. This condition may be relaxed by *homogenizing* the crust (*Capdeville and Marigo, 2007*), wherein thin discontinuous layers are replaced with a single, smooth anisotropic layer valid at long periods (*Backus, 1964*). Unlike SEMum v.1, we now adopt a *variable* homoge-

nized crustal-thickness: similar to Crust2.0 Moho depth (*Bassin et al., 2000*), but spatially filtered and limited to the interval between 30 and 60km. Given this prescribed geometry, we seek radially-anisotropic structure that fits the group-velocity dispersion data ( $T \leq 60$ s). Despite a 30km minimum thickness, the homogenized crust allows for  $\sim 4$ x SEM time-step prolongation relative to Crust2.0.

In NACT, we adopt a crustal-correction scheme similar the modified linear corrections (MLCs) of Lekic *et al.* (2010), with the exception that we do not limit ourselves to a small set of “regionalized” crustal models: we obtain continuously-parameterized corrections, that directly reflect lateral variation in the crustal layer. Further, we developed an efficient scheme for calculation of NACT sensitivity kernels that honor lateral variation in Moho topography, thereby simplifying the parameterization of, and inversion for, mantle structure. A detailed discussion of these approaches appears in French *et al.* (in prep).

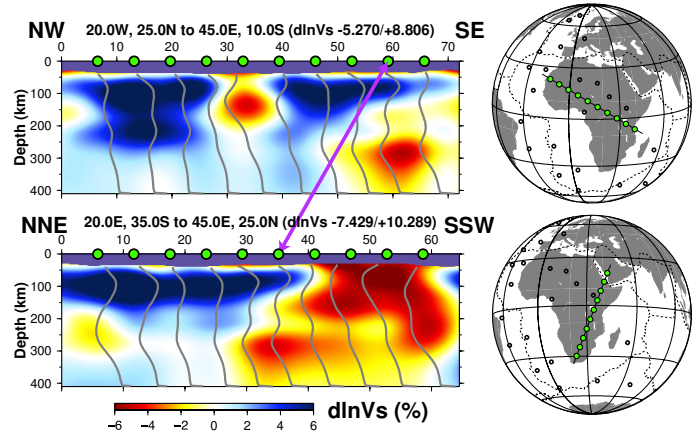


Figure 2.48: SEMum v.2  $V_S$  structure beneath Africa; gray profiles sample 1D  $V_S$ , paths cross where indicated.

## 26.3 Results and Future Work

SEMum v.2 results from two iterative updates to v.1, wherein waveform fits (Table 2.2) consistently improve. Like v.1, v.2 exhibits strong heterogeneity:  $>15\%$  peak-to-peak in close juxtaposition. For example, Figure 2.48 (lower panel) highlights the fast Kalahari and Tanzanian cratons, as well as very strong, bifurcated slow anomalies underlying the East African Rift through Afar, consistent with melt source-signature variation along the EAR (*Rogers et al., 2000*). Further, v.2 shows impressive low-velocity anomalies beneath numerous hotspots. Figure

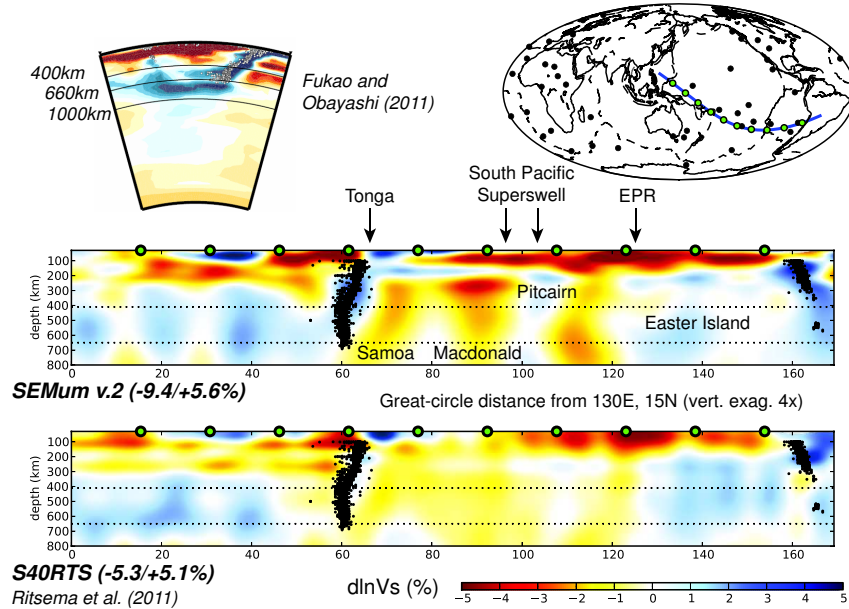


Figure 2.49: SEMum v.2 and S40RTS  $V_S$  structure beneath the South Pacific; deep seismicity highlights subducted slabs.

2.49 compares v.2 structure through the South Pacific with that of S40RTS (Ritsema *et al.*, 2011), highlighting strong columnar slow features beneath the Pacific superswell. Compare the prominent fast signatures of subducted slabs (South America, Tonga), and the similar pattern of slab stagnation west of Tonga, to that seen in the body-wave study of Fukao and Obayashi (2011, *pers. comm.*).

We are now preparing a manuscript for publication discussing SEMum v.2 methods and model structure, while also planning the next phase of our inversion: global adjoint tomography with SEMum v.2 as a starting model.

	<b>L</b>	<b>T</b>	<b>Z</b>
<b>fundamental</b>	66.0 [62.1]	75.4 [59.1]	67.6 [63.7]
<b>overtone</b>	80.2 [67.2]	70.9 [62.9]	78.1 [69.7]
<b>mixed</b>	73.3 [67.2]	81.6 [68.3]	75.7 [70.1]

Table 2.2: Waveform variance reduction (%) for SEMum v.2 and [v.1], by component and data type.

## 26.4 Acknowledgements

This work was supported by the NSF (NSF-EAR 0738284). SWF acknowledges support from the NSF Graduate Research Fellowship program. SEM calculations were performed on DOE NERSC resources.

## 26.5 References

Backus, G., Long-wave elastic anisotropy produced by horizontal layering, *J. Geophys. Res.*, 67, 4427-4440, 1962.

Bassin, C.G.L. & G. Masters, The current limits of resolution for surface wave tomography in North America, *EOS, Trans. Am. Geophys. Un.*, 81, 2000.

Capdeville, Y. & Marigo, J., Second order homogenization of the elastic wave equation for non-periodic layered media, *Geophys. J. Int.*, 170(2), 823-838, 2007.

Capdeville, Y., E. Chaljub, J.P. Vilotte, & J.P. Montagner, Coupling the spectral element method with a modal solution for elastic wave propagation in global earth models, *Geophys. J. Int.*, 152, 34-67, 2003.

French, S.W., V. Lekic, & B. Romanowicz, Toward global waveform tomography with the SEM: Improving upper-mantle images, Abstract S13C-02 presented at 2011 Fall Meeting, AGU, San Francisco, Calif., 5-9 Dec., 2011.

Komatitsch, D. and J.P. Vilotte, The spectral element method: an efficient tool to simulate the seismic response of 2D and 3D geological structures, *Bull. Seism. Soc. Am.*, 88(2), 368-392, 1998.

Lekic, V. & B. Romanowicz, Inferring upper-mantle structure by full waveform tomography with the spectral element method, *Geophys. J. Int.*, 185(2), 799-831, 2011.

Lekic, V., M. Panning, & B. Romanowicz, A simple method for improving crustal corrections in waveform tomography, *Geophys. J. Int.*, 182(1), 265-278, 2010.

Li, X.D. & B. Romanowicz, Comparison of global waveform inversions with and without considering cross-branch modal coupling, *Geophys. J. Int.*, 121, 695-709, 1995.

Tarantola, A., Inversion of seismic reflection data in the acoustic approximation, *Geophysics*, 49(8), 1259-1266, 1984.

Ritsema, J., A. Deuss, H.J. van Heijst, & J.H. Woodhouse, S40RTS, *Geophys. J. Int.*, 184, 1223-1236, 2011.

Rogers, N., R. Macdonald, J.G. Fitton, R. George, M. Smith, & B. Barreiro, Two mantle plumes beneath the East African rift system, *Earth Planet. Sci. Lett.*, 176, 387-400, 2000.

## 27 The DNA12 Seismic Velocity Model

Robert Porritt, Richard Allen, and Fred Pollitz

### 27.1 Introduction

The DNA velocity models have been following the rolling USArray from west to east. The initial model, DNA07 (Xue and Allen, 2010), used data from the earliest USArray deployment, the BDSN, and other regional networks. Obrebski *et. al.*, (2010) continue further east for DNA09, in which the interaction of the Yellowstone Plume and Juan de Fuca plate has a prominent role in the model. DNA10 updates the body wave dataset and develops the use of a joint inversion technique which uses Rayleigh wave phase velocities to constrain the upper lithosphere where teleseismic body waves rapidly lose resolving power (Obrebski *et al.*, 2011). In this research update we discuss the most recent generation of the DNA models, DNA12, in which we extend the dataset further east and include ambient seismic noise to resolve structure within the crust.

### 27.2 Method

The inclusion of surface wave data in the inversion provides constraints on the lithosphere allowing interpretation of structure from the surface through the mantle transition zone. However, the S-wave body-wave data is typically measured on the tangential component as it is a cleaner signal than the radial component. Nonetheless, in the presence of large anisotropic signals, there is a chance of mixing vertical and horizontal polarizations. To overcome this problem, we implement a rotation into the P-SV-SH coordinate frame with the predicted incidence angle (Bostock *et. al.*, 2001) and measure the arrival times on the three independent components.

The SV body wave delay times are jointly inverted with Rayleigh wave phase velocities. The phase velocities are generated by two independent methods. Teleseismic phase velocities are computed by Fred Pollitz using a non-plane wave method (Pollitz and Snoke, 2010). The phase velocities are updated from the dataset used in Obrebski *et. al.*, (2011) by using new USArray stations. Additionally, we employ ambient seismic noise to recover relatively short period phase velocities (Benson, *et. al.*, 2007). In this case, we update the dataset used in Porritt *et. al.*, (2011) to cover the continuous United States. The two surface wave models are joined by averaging with a period specific weighting parameter. This parameter allows for more weight to be given to the ambient noise at shorter periods where the ocean microseism produces strong ambient noise signal and more weight is given to the teleseismic phase velocities at longer periods where the signal is generally stable, but ambient noise has only

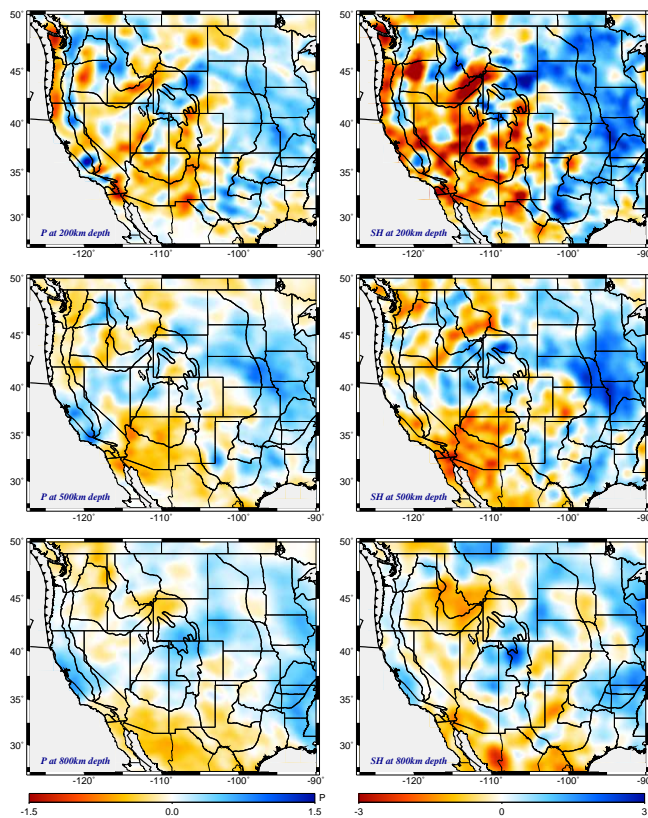


Figure 2.50: (left) Views of DNA12-P at various depths. (right) Corresponding views of DNA12-SH.

a weak signal.

### 27.3 Results

We focus this discussion on the Ancestral Rocky Mountains (ARM) region where there has been little resolution in previous versions of the DNA models. The ARM is a NW-SE trending series of uplifts and basins which formed in the mid-continent around 300Ma. Soreghan *et al.*, (2012) use potential field and active source seismic data to discuss the uplift and subsidence during the Mississippian through the Permian. They model the observed uplift as a NW-SE trending Cambrian rift system (the Southern Oklahoma Alucogen - SOA) being inverted due to crustal heterogeneity and a far-field horizontal stress field causing non-linear buckling. This horizontal stress field is attributed to the Ouachita-Marathon front which runs through southern Texas and was created by the collision of Africa with North America in the formation of Pangea (Kluth, 1986). Other authors (Algeo, 1992) have

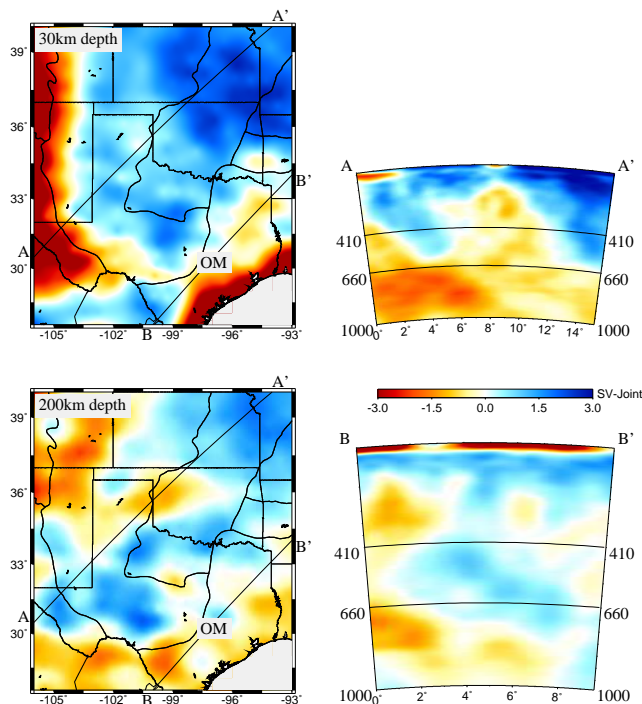


Figure 2.51: Views of the DNA12 model focused on the ARM. Maps at 30km and 200km depth are shown on the left with cross-section locations, physiographic boundaries, and state lines overlain. The Marathon-Ouachita Front (OM) is in southeast Texas near section B-B'.

suggested southward dipping subduction or wrenching of the Laurentia craton as the source of horizontal stress.

In Figure 2.51 we illustrate the velocity structure in the ARM region. The first feature we notice is the Ouachita-Marathon front in the 30km depth slice. The front is seen as a region of velocity contrasts where the generally high velocity cratonic lithosphere to the NW meets the area where the Pangean breakup occurred. In the asthenosphere, a high velocity body is imaged SW of the main uplifts dipping roughly to the NE and striking NW-SE. This high velocity body is distinct from the North American craton and the deeper Farallon slab system. One possible explanation is an independent subduction system which collided from the SW. Dating of igneous rocks in the ARM shows primarily Cambrian ages (Hogan and Gilbert, 1997) meaning any subduction in the region must have occurred 200 million years before the ARM uplift. Therefore we cannot conclude that subduction was the main force of ARM uplift, but a relic slab in the lithosphere could provide a buttress during the Pangean-forming orogeny, further forcing the stress into the SOA and resulting in the observed buckling.

## 27.4 Acknowledgements

We first thank UCB undergraduate Jenny Taing for picking a large portion of the teleseismic body wave data. Next, we thank Fred Pollitz for use of his surface wave phase velocities. Further, we wish to acknowledge the IRIS DMC webservices team who developed the Fetch-BulkData script we used for the data collection and the new collaborative earth model view. Additionally, we thank Earthscope and the Array Network Facility for the high quality data available through USArray. Finally, we thank NSF-EAR for funding this research as well as a UC Berkeley lab grant.

## 27.5 References

- Algeo, T.J., Continental-scale wrenching of south-western Laurussia during the Ouachita-Marathon orogeny and tectonic escape of the Llano block, *West Texas Geological Society Guidebook*, v. 9292, p. 115131, 1992.
- Bensen, G.D., M.H. Ritzwoller, M.P. Barmin, A.L. Levshin, F. Lin, M.P. Moschetti, N.M. Shapiro, and Y. Yang, Processing seismic ambient noise data to obtain reliable broadband surface wave dispersion measurements, *Geophys. J. Int.*, 169, 1239-1260, doi: 10.1111/j.1365-246X.2007.03374.x, 2007.
- Bostock, M. G., Rondenay, S., Schragge, D.S., Multiparameter two-dimensional version of scattered teleseismic body waves, 1. Theory for oblique incidence: *J. Geophys. Res.*, 106, 30,771-30,782, 2001.
- Hogan, J.P., and Gilbert, M.C., Intrusive style of A-type sheet granites in a rift environment: The Southern Oklahoma aulacogen, in Ojakangas, R.W., et al., eds., Middle Proterozoic to Cambrian rifting, central North America, *Geological Society of America Special Paper 312*, p. 299311, doi: 10.1130/0-8137-2312-4.299, 1997.
- Kluth, C.F., Plate tectonics of the Ancestral Rocky Mountains, in Peterson, J.A., ed., Paleotectonics and sedimentation in the Rocky Mountain region, United States, *American Association of Petroleum Geologists Memoir 41*, p. 353369, 1986.
- Obrebski, M., Allen, R.M., Xue, M., Hung S.H., Slab-plume interaction beneath the Pacific Northwest, *Geophys. Res. Lett.* 37, L14305, doi:10.1029/2010GL043489, 2010.
- Obrebski, M., Allen, R.M., Pollitz, F.F., Hung, S.H., Lithosphere-asthenosphere interaction beneath the western United States from the joint inversion of body-wave traveltimes and surface-wave phase velocities, *Geophys. J. Int.* 185, 1003-1021, doi:10.1111/j.1365-246X.2011.04990.x, 2011.
- Pollitz, F.F. and Snoke, J.A., Rayleigh-wave phase-velocity maps and three-dimensional shear-velocity structure of the western US from local non-plane surface-wave tomography, *Geophys. J. Int.*, 180, 1153-1169, 2010.
- Porritt, R.W., Allen, R.M., Boyarko, D.C., Brudzinski, M.R., Investigation of Cascadia Segmentation with Ambient Noise Tomography, *Earth Planet. Sci. Lett.* 185, 67-76, doi:10.1016/j.epsl.2011.06.026, 2011
- Soreghan, G.S., Keller, G.R., Gilbert, M.C., Chase, C.G., Sweet, D.E., Load-induced subsidence of the Ancestral Rocky Mountains recorded by preservation of Permian landscapes, *Geosphere*, 10.1130/GES00681.1, 2012
- Xue, M. and R.M. Allen, Mantle Structure Beneath the Western US and its Implications for Convection Processes, *J. Geophys. Res.*, 115, B07303, doi:10.1029/2008JB006079, 2010

## 28 Trust but Verify: a spot check for the new stratified model of upper mantle anisotropy beneath North America

Huaiyu Yuan and Vadim Levin (Rutgers University)

### 28.1 Research Summary

A newly developed 3D model of radially and azimuthally isotropic shear wave velocity beneath the North American continent (Yuan *et al.*, 2011; referred to as YR11 hereafter) resolves a long-standing argument regarding the provenance of seismic anisotropy (e.g. Silver, 1996; Vinnik *et al.*, 1984) with directional dependency of wave speed placed into both the lithosphere and the asthenosphere. As YR11 shows, the anisotropy domain of the North American continent is strongly stratified; large amplitude anisotropy domains are observed in both lithosphere and asthenosphere, suggesting that contributions to the core-refracted shear wave SKS splitting come from both lithosphere and asthenosphere.

Due to the continent-wide coverage, the new model has lateral resolution on the scale of 500 km and is expected to average, and thus possibly misrepresent, the structure in regions with abrupt lateral changes in properties. One such region is the New England Appalachians, where rifting and paleo-ocean closure have significantly reworked the passive continent margin (e.g., Thomas, 2006). The local tomography studies suggest a thin lithosphere ( $\sim 100$ km) in the region (e.g., Li *et al.*, 2003). This view is also supported by the P and S receiver function (RF) studies (e.g., Abt *et al.*, 2010).

On the other hand, azimuthal anisotropy in this region in YR11 shows in general a two-layered upper mantle (Fig. 2.52): a thick upper layer ( $>150$  km; with peak around 80 km) with the anisotropy direction at high angle to the plate motion (APM; Gripp and Gordon, 2002); and a deeper layer ( $>200$ km) whose anisotropy direction appears APM parallel (Fig. 1). This two-layered fast axis direction pattern is consistent with one of the earliest cases for stratified anisotropy built on data from this part of North America (Levin *et al.*, 1999), however the lithosphere thickness inferred from the abrupt depth dependent anisotropy is thicker than other studies.

We conduct two-layer single station shear wave splitting modeling at station HRV, and anisotropy P-receiver function analysis at the stations. Compared to the long period surface waveform modeling, these techniques have complementary sensitivity to the upper mantle anisotropy structure, therefore can provide high-quality constraints on the vertical and lateral variation in attributes of anisotropy. We compare (and contrast) these constraints with structure predicted for this location by the YR11 model. Our goals are both to test the new model in one place, and to develop a strategy for such testing.

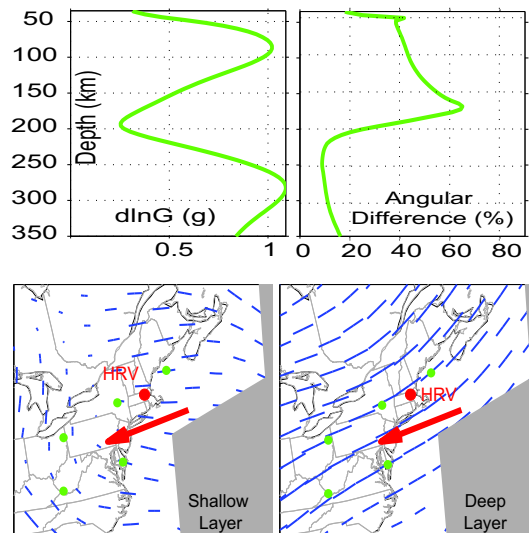


Figure 2.52: 1D azimuthal anisotropy strength (top left) and anisotropy angular difference with respect to the APM, averaged from model nodes (green dots) in the maps below, which shows the two-layer equivalent apparent fast axis directions (blue sticks) predicted from YR11 model: lithosphere, lower left; and asthenosphere, lower right. Red arrow shows the APM.

### 28.2 Results and Conclusions

We find ample evidence for sharp gradients in anisotropy within the upper mantle beneath northeastern North America. The depths where these gradients occur are consistent with the region of abrupt vertical change in anisotropic parameters of the new 3D model. Orientations of the symmetry axes suggested by polarity changes in receiver functions (Fig. 2.53) also agree with the model. Individual measurements of splitting in SKS phase from HRV vary with backazimuth, forming a characteristic  $\pi/2$  pattern (Fig. 2.54) that is well represented by two layers of anisotropy. This result confirms Levin *et al.* (1999) results with vastly larger amount of data. We find it very gratifying that parameters of anisotropy within the layers generally agree with both the new model and the old study. Orientations of fast anisotropic axis at  $\sim 100$  km depth suggested by the two methods are in good agreement as well: 100SE from SKS (Fig. 2.55) and 110-130 from RFs (Fig. 2.53).

We can thus infer that the fabric below  $\sim 100$  km is indeed aligned with plate motion, and that the transition from this fabric to another is abrupt. This transition may indicate a shallow LAB in the region, as evidenced by the negative velocity gradient following the orogenic trends

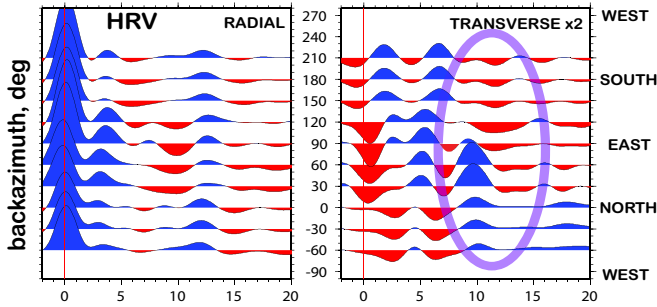


Figure 2.53: Receiver function azimuthal stacks at station HRV. Left radial component; right transverse component. Note change of polarity occurs around 10 sec (circled).

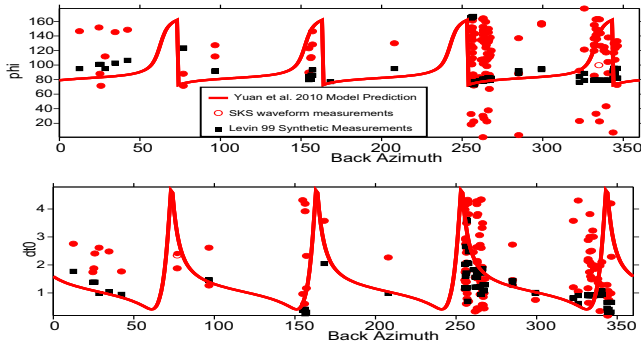


Figure 2.54: Model prediction (red curves, YR11) and data measurements for individual events, plotted against event back-azimuth. Measurements from *Levin et al.* (1999) model synthetic waveforms are plotted for comparison.

and the hotspot track shown in the updated shear-wave model of YR11 (Fig. 2.56).

### 28.3 Acknowledgements

We thank the IRIS DMC for providing the waveforms.

### 28.4 References

Abt, D., Fischer, K., French, S., Ford, H., Yuan, H. & Romanowicz, B. North American lithospheric discontinuity structure imaged by Ps and Sp receiver functions, *J. Geophys. Res.*, 115, B09301, 2010.

Gripp, A. & Gordon, R. Young tracks of hotspots and current plate velocities, *Geophys. J. Int.*, 150, 321-361, 2002.

Levin, V., Henza, A., Park, J. & Rodgers, A. Texture of mantle lithosphere along the Dead Sea Rift: recently imposed or inherited?, *Phys. Earth Planet. Int.*, 247, 157-170, 2006.

Li, A., Forsyth, D. & Fischer, K. Shear velocity structure and azimuthal anisotropy beneath eastern North America from Rayleigh wave inversion, *J. Geophys. Res.*, 108, 24 PP, 2003.

Silver, P. Seismic anisotropy beneath the continents; probing the depths of geology, *Annu. Rev. Earth Planet. Sci.*, 24, 385-432, 1996.

Thomas, W. Tectonic inheritance at a continental margin, *GSA Today*, 16, doi: 10.1130/1052-5173, 2006.

Vinnik, L., Kosarev, G. & Makeyeva, L. Anisotropy of the lithosphere according to the observations of SKS and SKKS waves, *Dokl. Akad. Nauk SSSR*, 278, 1335, 1984.

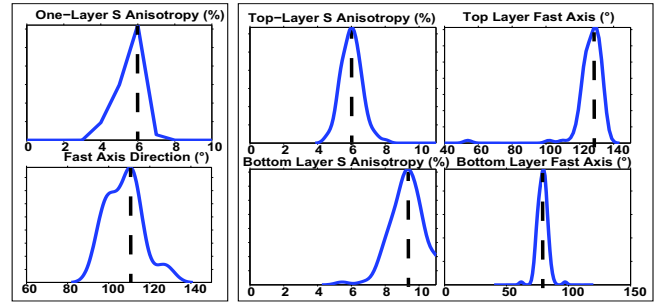


Figure 2.55: SKS 1-layer (left) and two-layer (right) modeling results. Plotted are probability density function of apparent fast axis (top) and slitting time (bottom) for each layer.

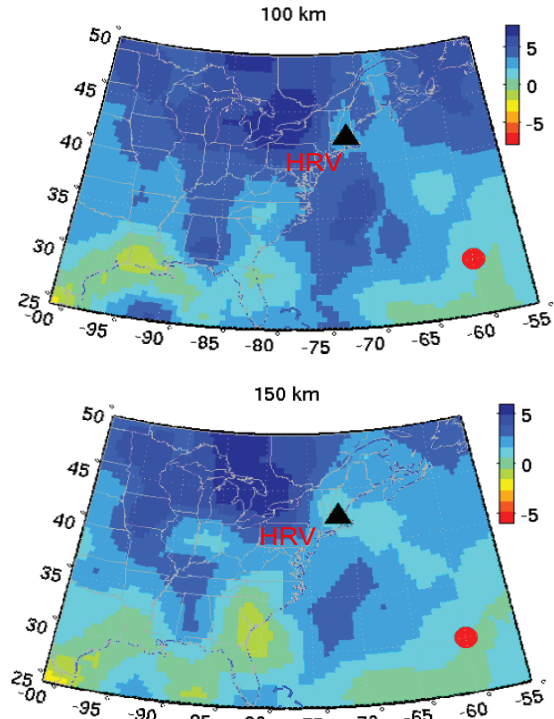


Figure 2.56: Model update of YR11, using ~200 local events and TA stations up to Oct. 2011. Note thinning of the lithosphere occurs near HRV. Red dot is Bermuda hotspot location.

Yuan, H., Romanowicz, B., Fischer, K. & Abt, D. 3-D shear wave radially and azimuthally anisotropic velocity model of the North American upper mantle, *Geophys. J. Int.*, 184, 1237-1260, 2011.

Yuan, H., Dueker, K. & Schutt, D. Testing five of the simplest upper mantle anisotropic velocity parameterizations using teleseismic S and SKS data from the Billings, Montana PASSCAL array., *J. Geophys. Res.*, 113, B03304, 03320 PP., 2008.

## 29 3-D Seismic Velocity Structure of the Hawaii Hotspot from Joint Inversion of Body Wave and Surface Wave Data

Cheng Cheng, Richard M Allen, Rob W Porritt

### 29.1 Introduction:

The Hawaii hotspot and the associated chain of islands have been long regarded as the case example of a deep-rooted mantle plume. However the efforts to detect a thermal plume seismically have been inconclusive. While the tomography model of *Wolfe et al.* (2009, 2011) suggests a lower mantle plume southeast of Hawaii, *Cao et al.* (2011) use scattering off the underside of the 660 km discontinuity to argue that the source of the hotspot is a broad region to the southwest. They image a broad down-warping of the 660 discontinuity that they interpret as being due to a hot region of the uppermost lower-mantle approximately 2000km wide. They suggest that the Hawaii volcanism is fed by small-scale convection in the upper mantle around the periphery of this broad lower-mantle feature.

Previous body wave tomography models may not be able to resolve between a continuous plume-like structure and separate anomalies at different depths resulting from small-scale mantle convection. In this study we combine the complementary sensitivities of body and surface-waves in order to improve resolution of mantle structure beneath Hawaii. The main limitation of body-wave tomography alone is the lack of resolution at shallow lithospheric depth where ray paths do not cross each other. By adding surface-wave constraints to the inversion as well, the resolution of the crustal and upper mantle structure is improved.

### 29.2 Data Processing:

We used data from the deployment of temporary broadband ocean-bottom seismometers (OBSs) of the Hawaiian Plume-Lithosphere Undersea Melt Experiment (PLUME), which was designed to determine mantle seismic velocity structure beneath the Hawaiian hotspot.

In a first step we oriented the PLUME OBS horizontal components using teleseismic P-wave particle motions. Generally we obtained stable and reliable orientations over a range of earthquake back-azimuths. Due to the high noise of the OBS data in some frequency bands we began by filtering in the period band of 0.04-1Hz. We measured  $\sim 1100$  P-wave relative arrival times on the vertical component and  $\sim 750$  S-wave relative arrival times (include direct S and SKS phases) on the SV component using multi-channel cross correlation. We use a total of  $\sim 70$  events which are distributed in as wide a range of back azimuth directions as possible. We also use surface wave constraints and apply the two-plane wave tomog-

raphy method to invert for the phase velocity structure. This tomography method, which also considers the finite frequency effects, inverts the phase data and amplitude information simultaneously for the phase velocity at each point across the region in addition to incoming wavefield parameters. We use surface waves from 71 events with magnitude greater than 5.8 to generate phase velocity maps from 25 sec to 100 sec. These maps clearly show the low velocities beneath the islands surrounded by relatively high phase velocity.

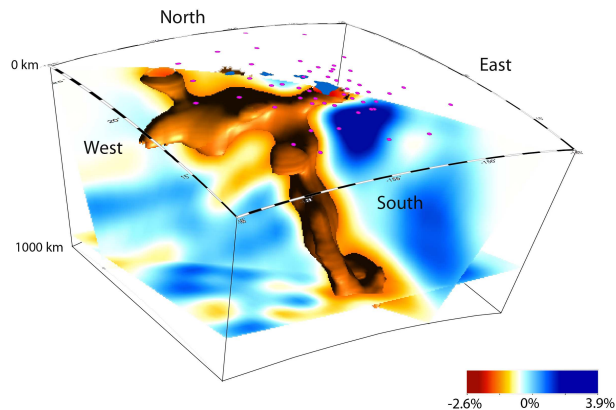


Figure 2.57: 3D view of our preliminary S-velocity model for the mantle beneath Hawaii. The location of the islands (blue) and the PLUME array (pink) are shown on the surface of the model volume.

### 29.3 Preliminary Results and Implications:

Figure 2.57 shows the S-velocity model derived from the body wave data. This shows the 3-D structure beneath the PLUME array to a depth of 1000km and reveals a several-hundred-kilometer-wide region of low velocities beneath Hawaii that dips to the southeast. The low velocities continue downward through the mantle transition zone and extend into the uppermost lower-mantle (although the resolution of lower mantle structure from this data set is limited). The independent P-wave images are generally consistent with S-wave structure. These images are consistent with the interpretation that the Hawaiian hotspot is the result of an upwelling high-temperature plume from the lower mantle. The broader upper-mantle low-velocity region immediately beneath the Hawaiian Is-

lands likely reflects the horizontal spreading of the plume material beneath the lithosphere.

We also obtain a preliminary result from the joint body-wave and surface-wave inversion (Figure 2.58). The same shallow low velocity zone is imaged along the island chain and the deeper part is identical to the body-wave inversion image. The low velocity to the southwest of the island is also clear to a depth of 600km as mentioned above. If the observation here is true, it will provide a hot environment for the 660km discontinuity to the west of the Hawaii and may give a new perspective to the plume origin debate.

## 29.4 References

Cao, Q. et al., Seismic Imaging of Transition Zone Discontinuities Suggests Hot Mantle West of Hawaii, *Science*, 332, 1068, 2011.

Obrebski, M., Allen, R. M., Xue, M., Hung, S-H., Slab-plume interaction beneath the Pacific Northwest, *Geophys. Res. Letters*, 37, 114305, 2010.

L. Cserepes, D. A. Yuen, On the possibility of a second kind of mantle plume. *Earth Planet. Sci. Lett.* 183, 61, 2000.

C. J. Wolfe et al., Mantle shear-wave velocity structure beneath the Hawaiian hot spot. *Science* 326, 1388, 2009.

C. J. Wolfe et al., Mantle P-wave velocity structure beneath the Hawaiian hotspot. *Earth Planet. Sci. Lett.* 303, 267, 2011.

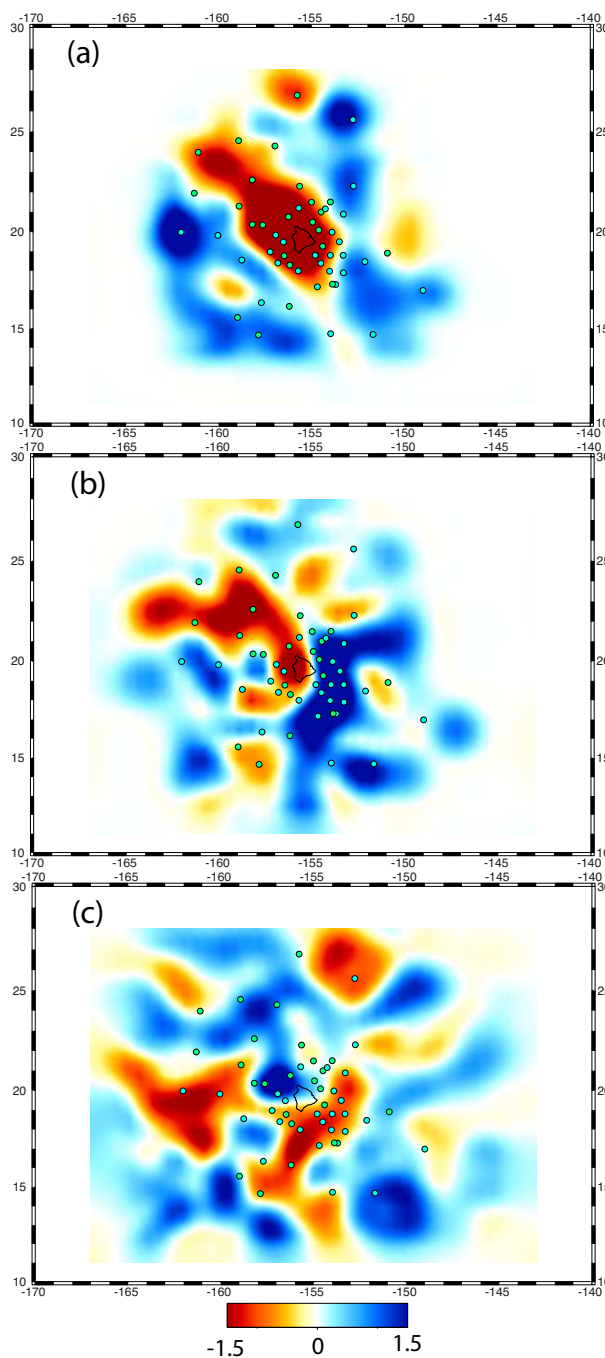


Figure 2.58: SV-velocity perturbation map around Hawaii at different depths using joint body- and surface-wave tomography. (a) 100 km (b) 300 km (c) 600 km depth

## 30 Azimuthal anisotropy in the Pacific upper mantle

Huaiyu Yuan and Barbara Romanowicz

### 30.1 Anisotropic Layering in North America

We recently developed a new three dimensional radially and azimuthally anisotropic model of the upper mantle in north America, using a combination of long-period 3-component surface and overtone waveforms, and SKS splitting measurements (*Yuan and Romanowicz, 2010*). We showed that: 1. azimuthal anisotropy is a powerful tool to detect layering in the upper mantle, revealing two domains in the cratonic lithosphere, separated by a sharp laterally varying boundary in the depth range 100-150 km, which seems to coincide with the mid-lithospheric boundary (MLD) found in receiver function studies; 2. contrary to receiver functions, azimuthal anisotropy also detects the lithosphere-asthenosphere boundary (LAB) as manifested by a change in the fast axis direction, which becomes quasi-parallel to the absolute plate motion below  $\sim 250$  km depth; and 3. a zone of stronger azimuthal anisotropy is found below the LAB both in the western US (peaking at depths of 100-150km) and in the craton (peaking at a depth of about 300 km).

### 30.2 Going to the global inversion

Here we show preliminary attempts at expanding our approach to the global scale with the goal, in particular, of determining whether our results can be generalized to other continents and oceans. We started with our most recent global upper mantle radially anisotropic shear velocity model, determined using the Spectral Element Method (*French et al.*, in prep) and augmenting the corresponding global dataset of initially 200 events and 10,000 long period waveforms, in order to ensure optimal azimuthal coverage of the globe. Depth parameterization is chosen so as to resolve the kind of layering seen in north America. Our preliminary results, which do not yet incorporate SKS splitting measurements (see discussion below), look promising as they confirm the layering found in North America, using a different, global dataset and starting model (Fig. 2.59).

### 30.3 Robust SKS measurements

In *Romanowicz and Yuan (2012)*, we show that back-azimuthally averaged splitting does not depend on the order of layers in the model and is correctly predicted by the formalism of *Montagner et al. (2000)*, which forms the basis of our joint inversion of surface waveforms and SKS splitting data. Robust station average measurements is contingent upon a wide back-azimuthal coverage of the

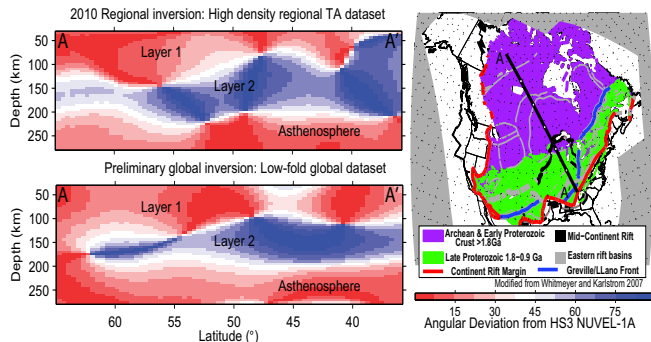


Figure 2.59: Two layered lithosphere in the North American craton shown by both the regional (top) and global (bottom) inversions. Color coded are anisotropy direction differences with respect to the HS3 NUVEL-1A absolute plate motion (APM; *Gripp and Gordon, 2002*). A promising three-layer anisotropy domain is observed, confirming the layering found in North America.

SKS events. A systematic evaluation of the global SKS datasets to obtain robust station averaged measurements is currently being performed, which is essential in recovering the deep azimuthal anisotropy at deep depth (*Yuan and Romanowicz, 2010*).

We therefore focus only the upper most mantle ( $< 250$  km) of the Pacific region, where earthquakes from the Pacific ring of fire have given the region an optimal azimuthal coverage. The available SKS measurements are sparse in the region (e.g., *Becker et al., 2012*), which as we showed in our previous study in North America are needed in continents where the lithosphere is thick ( $\sim 200$ - $250$  km). For the Pacific region, however, the oceanic lithosphere is relatively thin (e.g., *Rychert and Shearer, 2011; Schmerr, 2012*), thus the natural depth resolution of the surface waveforms allows us to look into both the lithosphere and asthenosphere and their interactions.

### 30.4 Pacific Layering

Anisotropy stratification of the Pacific upper mantle was reported in early azimuthal anisotropy studies (e.g., *Montagner, 2002; Smith et al., 2004; Maggi et al., 2006*). Our initial results (Fig. 2.60) show at shallow depths (70-100km) a domain of anisotropy with a general northward fast axis direction beneath the old (e.g. west of Hawaii  $> 80$ Ma, *Muller et al. 2008*) portion of the plate. The direction is consistent with the paleo-pacific plate motion (e.g., *Muller et al., 2008*). Within this shallow domain an east-west direction, which seems to follow the fracture zones (e.g., *Smith et al., 2004*), is observed where the

plate is young.

Below 150 km depth, there is a deeper anisotropy domain whose fast axis direction is in good agreement with the current Pacific plate motion direction (HS3-NUVEL 1A; *Gripp and Gordon, 2002*). This deep anisotropy domain seems stronger in amplitude, and spatially correlates with the low velocity channel in the asthenosphere (e.g. *Montagner 2002*). Perturbations to the anisotropy domain are observed near the Hawaii hotspot and the Pacific/Eurasia subduction region.

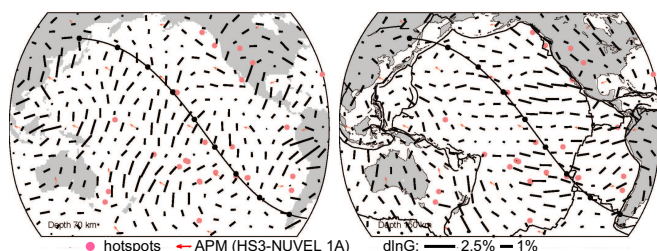


Figure 2.60: Two anisotropic domains in the Pacific Ocean. Azimuthal anisotropy direction and strength (shown as the black sticks) at 70- (left) and 150-km (right), respectively. The APM in HS3-NUVEL 1A model is illustrated in small red arrows. Ridges and hotspots are indicated.

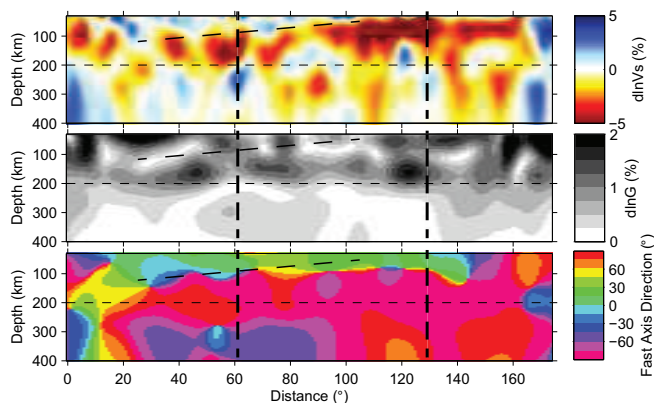


Figure 2.61: Depth cross-sections of isotropic Vs (top), azimuthal anisotropy strength G (middle) and fast axis directions (bottom). The location of the cross-section is shown in (Fig. 2.60). Black broken line indicates the bottom of the oceanic lithosphere inferred from Vs and G. Vertical dashed lines show the location of the Hawaii hotspot and the East Pacific Rise. The APM directions are in general NWW (light purple) in the Pacific.

The Vs depth cross-section from our group’s most recent global model (~300-km horizontal resolution; *French et al. in prep.*) shows age-progressive thickening of the high velocities away from the ridge (Fig. 2.61). Remarkably the boundary of the two anisotropy domains, corresponding to those discussed in (Fig. 2.60), also follows the age progressive pattern at similar depths. Clearly the paleo- or current APM parallel direction is

associated with each domain, respectively, a strong indication that the past and present time plate motions have been preserved in the upper mantle.

### 30.5 Summary

We expand our regional azimuthal anisotropy inversion to the global scale. With the current low data-fold waveforms, we are able to re-produce the layered lithospheric anisotropy pattern found in our previous studies. While robust SKS data are yet to be incorporated to address deep anisotropy in the cratonic upper mantle worldwide, promising results indicate that that the Pacific ocean upper mantle is also anisotropically layered, with depth dependent domains that record past and current plate motions.

### 30.6 Acknowledgements

This work was supported by NSF/EarthScope program grants EAR-0643060 and EAR-0738284.

### 30.7 References

Becker, T.W., Lebedev, S. and Long, M.D., 2012. On the relationship between azimuthal anisotropy from shear wave splitting and surface wave tomography, *J. Geophys. Res.*, 117, B01306.

Gripp, A.E. and Gordon, R.G., 2002. Young tracks of hotspots and current plate velocities, *Geophys. J. Int.*, 150, 321-361.

Lekic, V. and Romanowicz, B., 2011. Inferring upper-mantle structure by full waveform tomography with the spectral element method, *Geophys. J. Int.*, 185, 799-831.

Maggi, A., Debayle, E., Priestley, K. and Barruol, G., 2006. Azimuthal anisotropy of the Pacific region, *Earth Planet. Sci. Lett.*, 250, 53-71.

Montagner, J.-P., Griot-Pommeroy, D.-A. and Lave, J., 2000. How to relate body wave and surface wave anisotropy?, *J. Geophys. Res.*, 105, 19,015-019,027.

Montagner, J.P., 2002. Upper mantle low anisotropy channels below the Pacific Plate, *Earth Planet. Sci. Lett.*, 202, 263-274.

Muller, R.D., Sdrolias, M., Gaina, C. and Roest, W.R., 2008. Age, spreading rates, and spreading asymmetry of the world’s ocean crust, *Geochem. Geophys. Geosyst.*, 9, Q04006.

Romanowicz, B. and Yuan, H., 2012. On the interpretation of SKS splitting measurements in the presence of several layers of anisotropy, *Geophys. J. Int.*, 188, 1129-1140.

Rychert, C.A. and Shearer, P.M., 2011. Imaging the lithosphere-asthenosphere boundary beneath the Pacific using SS waveform modeling, *J. Geophys. Res.*, 116, B07307.

Schmerr, N., 2012. The Gutenberg Discontinuity: Melt at the Lithosphere-Asthenosphere Boundary, *Science*, 335, 1480-1483.

Smith, D.B., Ritzwoller, M.H. and Shapiro, N.M., 2004. Stratification of anisotropy in the Pacific upper mantle, *J. Geophys. Res.*, 109, B11309.

Yuan, H. and Romanowicz, B., 2010. Lithospheric layering in the North American craton, *Nature*, 466, 1063-1068.

# 31 Anisotropic Upper Mantle Shear-wave Structure of East Asia from Waveform Inversion

Jiajun Chong, Huaiyu Yuan, Scott French, Barbara Romanowicz, and Sidao Ni (KLDG)

## 31.1 Introduction

East Asia is a region that is seismically active and is surrounded by active tectonic belts, such as the Himalaya collision zone, western Pacific subduction zones and the Tianshan-Baikal tectonic belt. Seismic anisotropic tomography can shed light on the complex crust and upper mantle dynamics of this region, which is the subject of much debate. In this study, we applied time domain full waveform tomography to image the 3D isotropic and anisotropic upper mantle shear velocity structure of East Asia. We present preliminary modeling results of the first iteration and discuss their tectonic implications.

## 31.2 Data and Inversion

Three component waveforms of teleseismic and far regional events ( $15^\circ \leq \Delta \leq 165^\circ$ ) with magnitude ranges from  $M_w$  6.0 to  $M_w$  7.0 and source duration time less than 10 sec are collected from 133 permanent and 563 temporary broadband seismic stations in East Asia. Wave-packets of both fundamental and overtone modes, filtered between 60 and 400 sec, are picked automatically according to the similarity between data and synthetic waveforms, and later checked manually to get high quality data. Wavepackets corresponding to event-station paths that sample the region considered are weighted according to path redundancy and signal to noise ratio. These waveforms (1467 events) together with the dataset used for the global tomography (*Lekic and Romanowicz, 2011*) provide us with good density and azimuthal coverage in the target region.

The model is laterally parameterized with spherical splines and vertically in terms of cubic splines. We correct waveforms for the effects of 3D structure outside of the region with a starting global anisotropic upper mantle shear velocity model based on waveform inversion using the Spectral Element Method (*Lekic and Romanowicz, 2011*), updated for more realistic crustal thickness (*French et al., 2011*). We also invert for the 3D structure of the target region using normal mode non-linear asymptotic coupling theory (*NACT, Li and Romanowicz, 1995*).

## 31.3 Preliminary Result

After one iteration, the isotropic ( $V_s$ ) and radial anisotropic ( $\xi = (V_{sh}/V_{sv})^2$ ) model in the target region is updated to a spherical spline level of 6 and 5, equivalent to a spherical harmonic of about degree 92 and 46 for  $V_s$  and  $\xi$ , respectively. The following 2D maps

show the perturbations of  $V_s$  (Figure 2.62) with respect to the new 1D average model of the target region and the radial anisotropic structure (Figure 2.63) at a depth of 150 km. The map view of  $V_s$  perturbation with respect to the 1D regional mean velocity model shows dominant fast (west) and slow (east) velocity domains separated by Altai-Qilian orogenic belts. The anisotropic structure generally agrees well with the tectonics in target region.

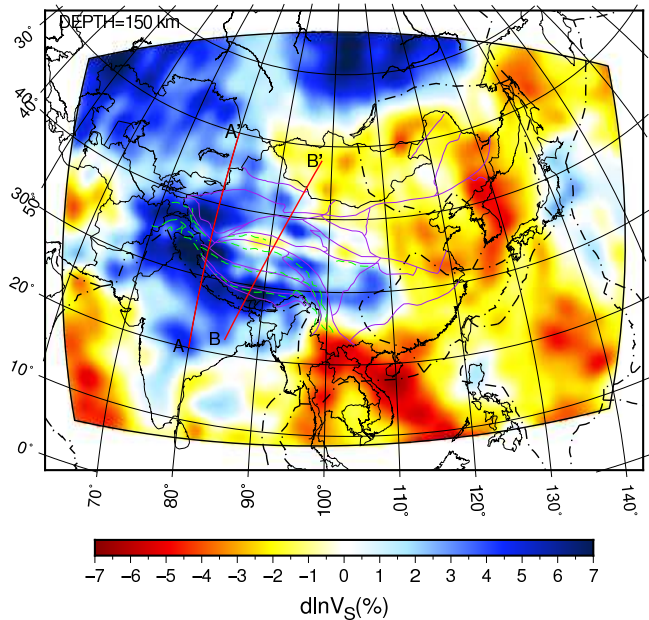


Figure 2.62: Map view of  $V_s$  perturbation at a depth of 150 km. It shows dominant fast (west) and slow (east) velocity domains separated by Altai/Qilian orogenic belts. Red lines are the location of depth cross-sections in Figure 2.64 and Figure 2.65. Purple lines are the boundaries of major tectonic blocks, and black dashed lines mark the plate boundaries.

Depth cross-sections in the Tibet region, as shown in Figure 2.64 and Figure 2.65, indicate that the Indian plate may have subducted northward beneath Tibet with different dipping angles and north reach in the western (Figure 2.64) and eastern part (Figure 2.65) of Tibet. A high velocity anomaly has been found beneath east Tibet which may be the subducted Asian lithosphere. We also found that strong low velocity structure extends down to 100+ km in the central and north regions of Tibet, which also has been found in early studies (*Brandon and Romanowicz, 1986, Bourjot and Romanowicz, 1992*).

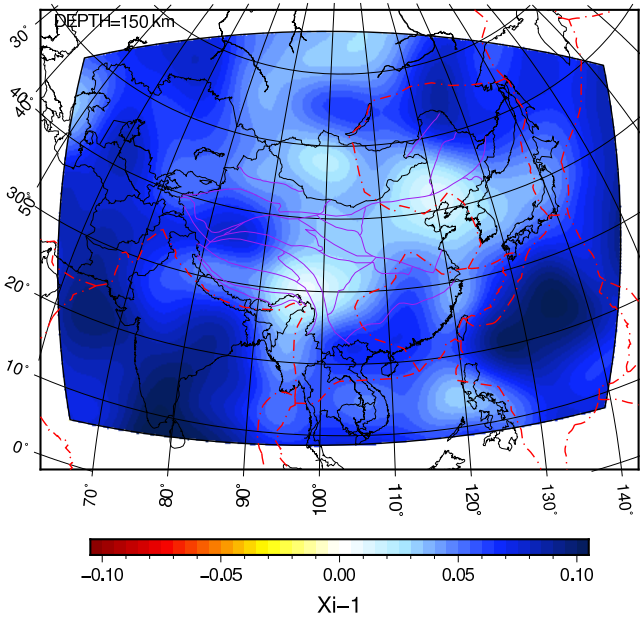


Figure 2.63: Map view of anisotropic structure ( $\xi - 1$ ) at a depth of 150 km.

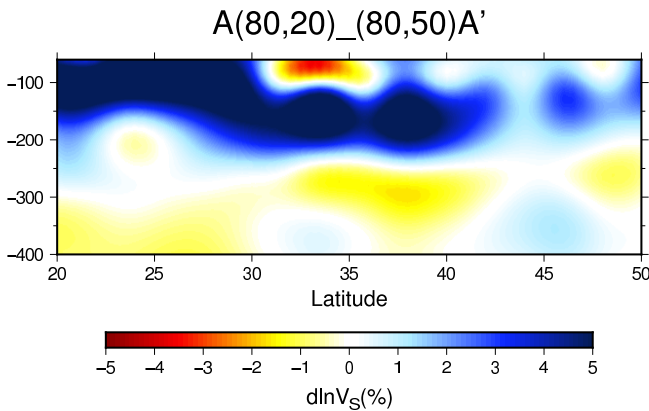


Figure 2.64: Depth cross-section along AA' in Figure 2.62, shows that the Indian plate has reached the south boundary of the Tarim Block around 35° north with a relatively large dipping angle.

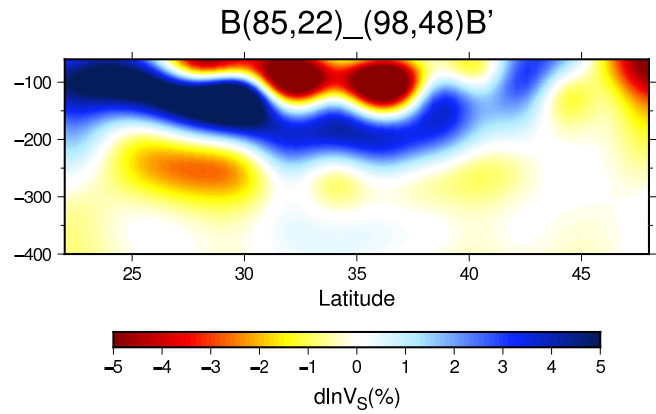


Figure 2.65: Depth cross-section along BB' in Figure 2.62, shows that the Indian plate may have reached the Bangong-Nujiang suture around 32° north. The Asian lithosphere may also have subducted southward beneath Tibet.

### 31.4 Conclusions

We present a preliminary anisotropic upper mantle model of East Asia based on time domain waveform inversion. Our model shows some features that agree well with tectonics in the target region and some structures that haven't been imaged before. We plan to do more iterations to improve the waveform fit and resolution. We will also combine waveform inversion with SKS splitting data to invert for azimuthal anisotropy, as in *Yuan and Romanowicz, (2010)* for North America.

### 31.5 Acknowledgements

This work was supported by NSF grant EAR 0738284.

### 31.6 References

V. Lekic, and B. Romanowicz, Inferring upper mantle structure by full waveform tomography with the Spectral Element Method, *Geophys. J. Int.*, 2011.  
 X.D. Li, and B. Romanowicz, Comparison of global waveform inversions with and without considering cross-branch modal coupling, *Geophys. J. Int.*, 1995.  
 Brandon and Romanowicz, A "NO-LID" zone in the central Chang-Tang platform of Tibet: evidence from pure path phase velocity measurements of long period Rayleigh waves, *JGR.*, 1986  
 Bourjot and Romanowicz, Crust and upper mantle tomography in Tibet using surface waves, *GRL.*, 1992  
 H. Yuan and B. Romanowicz, Lithospheric layering in the North American craton, *Nature*, 2010

## 32 An Exceptionally Large ULVZ at the Base of the Mantle near Hawaii

Sanne Cottaar and Barbara Romanowicz

### 32.1 Introduction

The lowermost lower mantle, also called the D", is a thermo-chemical boundary layer, presenting many intriguing observations. Global shear velocity tomography of shear velocities show strong degrees 2 and 3, dominated by two large low shear velocity provinces (LLSVP); one under Africa and one under the Pacific. Local studies on smaller scales show the occurrence of thin (tens of kilometers), intermittent ultra-low velocity zones (ULVZ). In this study we forward model the location, geometry and velocity reduction of one such ULVZ beneath the central Pacific on the basis of striking waveform complexities in shear (diffracted) phases.

### 32.2 Data and observations

The striking complexities appear in North American seismic data from events in the New Ireland Region, Papua-New Guinea. In particular, we model a 2010 event that has significant energy towards North America and good coverage thanks to the USArray Transportable Array. A nearby event in 2003 has less dense coverage (*To et al.*, 2011), but offers extended coverage from the Nars-Baja array to the south. The main observation is the occurrence of a postcursor in the period band 10-30 seconds. The postcursor is delayed by more than 30 seconds compared to the main phase with a move-out as a function of azimuth up to 50 seconds. Beamforming analysis on these delayed phases shows they are originating in a localized area in the lowermost lower mantle.

Additional azimuthal coverage comes from S/ScS phases from Fiji events to stations in Alaska. The observed delayed ScS phases (~15 seconds) help further constrain the uncertainty in location.

### 32.3 Forward modeling results

Synthetic data are forward modeled using a sandwiched version of CSEM (Coupled Spectral Element Method, *Capdeville et al.*, 2003). This method is computationally effective by only solving for the full 3D model, in the lowermost part of the mantle and coupling to a normal mode solution for a 1D model in the rest of the Earth.

Based on the beamforming and ray-theoretical analysis of the travel time results, we consider a simplified cylindrical shape for the ULVZ (see Figure 2.66). Our final model has a width of ~900 km and a height of ~20 km, thus having a large width:height aspect ratio. The velocity reduction is ~20% and the cylinder is centered

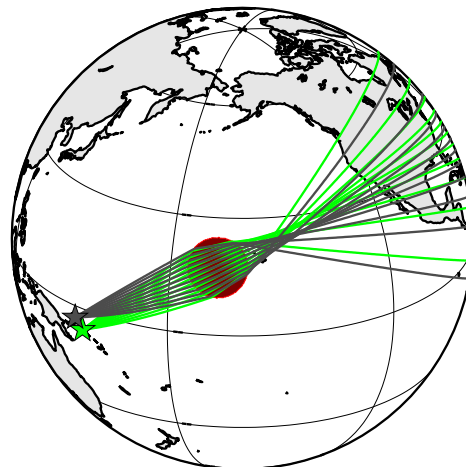


Figure 2.66: Ray-theoretical interpretation of the lens-like behavior of the ULVZ creating the postcursors. The 2010 event is shown in dark gray and the 2003 event in light gray. The dark circle indicates the location of the base of the final model.

roughly 11 degrees to the southwest of Hawaii. Figure 2.67 shows synthetic traces with and without a ULVZ alongside observations of the 2010 event. The different parameters have different uncertainties and trade-offs.

*Height:* The height of the ULVZ is fairly well constrained by the frequency dependence of the observations. Only periods below 30 seconds appear sensitive to this structure, while no postcursors are seen at longer periods. Similar frequency dependence can be seen in synthetics for models with heights between 15 and 25 km.

*Width and velocity reduction:* Clearly there is a trade-off in the size and the strength of the velocity reduction. However, when the ULVZ is too localized, the postcursors become smaller in amplitude. At the other end, when the ULVZ is large and weak, the move-out of the postcursor changes. Taking into account these constraints, error margins still remain on the order of 100 km in width and several percent in velocity reduction.

*Location:* Core-diffracted phases have a path-integrated sensitivity similar to that of surface waves. This creates an anisotropic uncertainty in location when modeling one event. Orthogonal to the direction of propagation, the location is well-constrained (as the postcursor move-out with azimuths would shift when shifting

the model). Along path the uncertainty in location is large. Combining the events for the New Ireland Region with the complexities seen in traces from a Fiji event towards Alaska further constrained the location to be SW of Hawaii. Uncertainties in latitude and longitude are on the order of several degrees.

### 32.4 Discussion

This data set has allowed us to map the full, though simplified, geometry of a ULVZ. The modeled ULVZ is much wider than ULVZs previously were thought to be (on the order of  $> 100$  km). The location of this ULVZ is close to the northern boundary of the Pacific LLSVP. ULVZs have been modeled as chemically-distinct ridge-like features that are swept up at the LLSVP boundaries (McNamara *et al.*, 2010). In our modeling, our best model is cylindrical, but uncertainty on the precise shape remains. Furthermore, it is tempting to speculate on the relationship of the unusually large ULVZ and the close vertical proximity with the hotspot with the largest plume flux (Jellinek and Manga, 2004). Possibly the ULVZ could lie at the base of a whole mantle plume, and entrainment off the ULVZ could be the source of the dichotomy in geochemical isotope measurements in lavas on Hawaii (Weis *et al.*, 2011). The exact relationships between ULVZs, LLSVPs and hotspots remain elusive, but this new class of structures needs to be accounted for in geodynamical and mineral physical studies of the deep mantle.

### 32.5 Acknowledgements

We thank Akiko To for helpful discussions. This work is supported by NSF/CSEDI grant 067513.

### 32.6 References

Capdeville, Y., B. Romanowicz, and A. To, Coupling spectral elements and modes in a spherical earth: an extension to the sandwich case, *Geophys. J. Int.*, 154, 44-57, 2003

Jellinek, M. and M. Manga, Links between long-lived hot spots, mantle plumes, D" and plate tectonics. *Rev. of Geophys.*, 42, RG3002, 2004

Mégnin, C. and B. Romanowicz, The three-dimensional shear velocity structure of the mantle from the inversion of body, surface and higher-mode waveforms, *Geophys. J. Int.*, 143, 709-728, 2000

McNamara, A., E. Garnero and S. Rost, Tracking deep mantle reservoirs with ultra-low velocity zones. *Earth Plan. Sci. Lett.*, 299, 1-9, 2010

To, A., Fukao, Y., Tsuboi, SI, Evidence for a thick and localized ultra low shear velocity zone at the base of the mantle beneath the central Pacific, *Earth Plan. Sci. Lett.*, 184, 119-133, 2011

Weis, D., M. Garcia, J. Rhodes, M. Jellinek and J. Scoates, Role of the deep mantle in generating the compositional asymmetry of the Hawaiian mantle plume. *Nature*, 4, 831-833, 2011

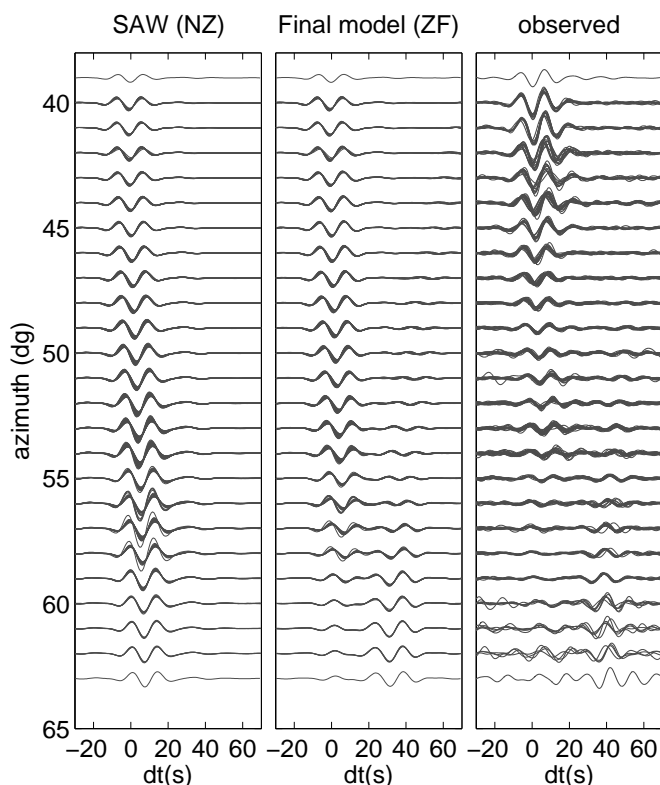


Figure 2.67: *Panel one:* 3D synthetics for shear diffracted phases of the 2010 event. Background model is SAW24B16 (Mégnin and Romanowicz, 2000). Panel shows 316 traces in one-degree azimuth bins. Traces are filtered between 10 and 20s. *Panel 2:* Same data set, but with the preferred cylindrical ULVZ included in the model. *Panel 3:* Observed data, filtered by the same frequency band.

## 33 Do "double SS precursors" mean double discontinuities?

Zhao Zheng and Barbara Romanowicz

### 33.1 Introduction

SS precursors are the underside reflections from the upper mantle discontinuities such as those at 410 and 660 km. They are important tools for studying the existence and characteristics of mantle discontinuities both on the global and regional scales (see *Deuss, 2009* for a review). Due to their sensitivity at the midpoint between source and receiver, coverage for oceanic regions is achieved where other methods such as receiver functions and triplications are not feasible. Their amplitudes are generally small (5-10% of the main phase), at or below noise level. Stacking is therefore necessary. Midpoint stacking over geographical bins with radius of  $10^\circ$  has been common. Recently, the deployment of the US Transportable Array (TA) allows unprecedented density of ray coverage and brings new opportunities to try and resolve finer scale discontinuity characteristics for much broader regions.

### 33.2 Double SS precursors

Here we present observations of SS precursors from an  $m_b$  6.7, depth 38 km earthquake in 2010 recorded at TA (Fig. 2.68). The magnitude is optimal in that the precursor signals are strong, while the source time function is simple. A shallow depth prevents precursor interference. The epicentral distances fall in the range  $120$ - $150^\circ$ , which is very suitable for an SS precursor study. We look at the transverse component displacement seismograms filtered in 20-100 seconds. In this particular case, the S660S precursors are strong enough to be identified on individual seismograms across the array without any stacking (Fig. 2.69a). Two signals around the theoretical S660S arrival time can be tracked coherently across the profile. In conventional interpretation, this would imply two discontinuity reflectors in the bounce point region. Vespagram analysis confirms that both signals have a slowness close to the theoretical value for S660S.

We attempt to fit the observations with 1D and 3D modeling. The 1D model is PREM (Dziewonski and An-

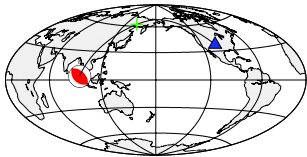


Figure 2.68: SS ray path from the event to TA (triangle). The cross denotes bounce point.

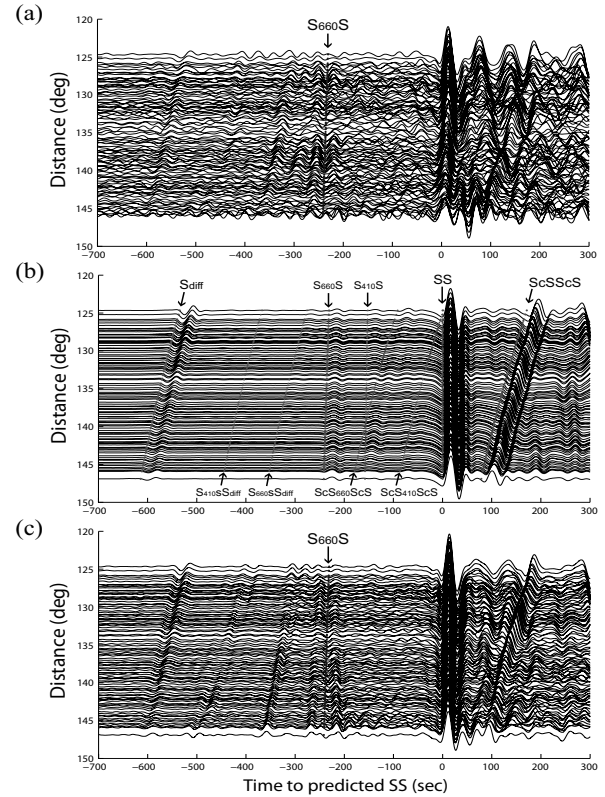


Figure 2.69: Transverse component record sections of (a) observed waveforms, (b) 1D synthetics and (c) 3D synthetics for stations in the azimuth range of  $20$ - $23^\circ$ , aligned on the theoretical arrivals of the main phase SS. Major seismic phases and their associated precursors are marked by dotted lines on the 1D synthetics, for reference.

derson, 1981). For the 3D, a global tomographic shear velocity model S362ANI (*Kustowski et al., 2008*) is used with CRUST2.0 (*Bassin et al., 2000*); the Spectral Element Method (*Komatitsch and Tromp, 2002a,b*) is employed for simulation. As Fig. 2.69 shows, while only one S660S is present on the 1D synthetics as expected, "double precursors" are seen on 3D synthetics with correct slownesses, although only one 660-discontinuity is present in the model, which is intriguing.

### 33.3 The result of double discontinuities?

Next we try to pinpoint the structure that is responsible for the "double precursors" seen on the 3D synthetics. We first consider a modified 3D model in which only the

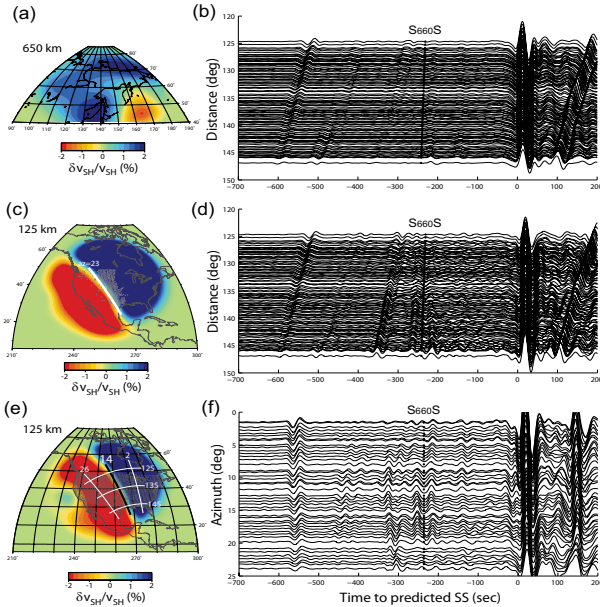


Figure 2.70: 3D models (left panels) and corresponding synthetics (right panels). Top: A model with bounce point 3D structure only. Middle: A model with receiver-side structure only. Dots denote TA stations. Bottom: A modified receiver-side model, in which the velocity boundary is shifted eastward. An expanded set of virtual receivers (dots) is used. The lines indicate equi-azimuth and equi-distance curves. (For color figure, see [http://earthquakes.berkeley.edu/annual\\_report/](http://earthquakes.berkeley.edu/annual_report/))

heterogeneities in the bounce point region are preserved (Fig. 2.70a). To our surprise, the "double precursor" phenomenon disappears (Fig. 2.70b). We then try a model with receiver side 3D structure only (Fig. 2.70c). The corresponding synthetics (Fig. 2.70d) turns out to be capable of reproducing the "double precursors". In this velocity model, a sharp contrast between the fast craton east of the Rocky Mountain Front and the slower western US is present in the North American upper mantle, a prominent feature also seen in numerous continental scale tomography studies (e.g. *van der Lee and Frederiksen, 2005; Marone et al., 2007; Nettles and Dziewonski, 2008; Yuan et al., 2011*). This boundary is sub-parallel to the great circle paths for the event studied here, leading to a conjecture that the apparent "double precursors" are in fact artifacts due to scattering at the boundary.

In order to test this conjecture, we construct another model (Fig. 2.70e) in which the boundary is significantly shifted eastwards while its orientation still tracks the great circle ray path direction. We also expand the array of virtual receivers to the entire US in order to cover a broad range of azimuths across the boundary. The corresponding synthetics (Fig. 2.70f) are arranged by increasing azimuth (from east to west roughly). It is seen that for receivers far away from the boundary there is only one precursor (the later one); whereas the other wiggle (the

earlier one) picks up as receivers approach the boundary (azimuth  $\sim 14^\circ$ ), thus confirming the conjecture. Further analysis of particle motions and comparison of transverse and radial component waveforms reveal the "precursors" are radial energy leaking to transverse component due to scattering (*Zheng and Romanowicz, 2012*).

### 33.4 Conclusions

We find that apparent SS precursors may not necessarily reflect the characteristics of mantle discontinuities in the bounce point region, as often assumed by conventional precursor travel time studies. Heterogeneities away from the bounce point region are able to generate artificial "precursors" in a coherent and therefore misleading way. This raises a caution for identifying and interpreting SS (and PP) precursors. As much as the USArray provides hope for improving resolution of precursor studies, care must be taken.

### 33.5 Acknowledgements

This work was supported by NSF EAR grant #0738284. We thank Scott French for help to compute SEM synthetics.

### 33.6 References

- Bassin, C., G. Laske and G. Masters, The current limits of resolution for surface wave tomography in North America, *EOS, Trans. Am. Geophys. Un.*, **F897**, 81, 2000.
- Deuss, A., Global observations of mantle discontinuities using SS and PP precursors, *Surv. Geophys.*, **30**, 301-326, 2005.
- Dziewonski, A. and D. Anderson, Preliminary reference Earth model, *Phys. Earth Planet. Inter.*, **25**, 297-356, 1981.
- Kustowski, B., G. Ekstrom and A. Dziewonski, Anisotropic shear-wave velocity structure of the Earth's mantle: a global model, *J. Geophys. Res.*, **113**, 2008.
- Komatitsch, D. and Tromp, J., Spectral-element simulations of global seismic wave propagation-I. Validation, *Geophys. J. Int.*, **149**, 390-412, 2002a.
- Komatitsch, D. and Tromp, J., Spectral-element simulations of global seismic wave propagation-II. Three-dimensional models, oceans, rotation and self-gravitation, *Geophys. J. Int.*, **150**, 303-318, 2002b.
- Marone, F., Gung, Y. and Romanowicz, B., Three-dimensional radial anisotropic structure of the North American upper mantle from inversion of surface waveform data, *Geophys. J. Int.*, **171**, 206-222, 2007.
- Nettles, M., and Dziewonski, A.M., Radially anisotropic shear velocity structure of the upper mantle globally and beneath North America, *J. Geophys. Res.*, **113**, B02303, 2008.
- Van der Lee, S. and Frederiksen, A., SurfaceWave Tomography applied to the North American Upper Mantle, in *Seismic Earth: Array Analysis of Broadband Seismograms*, eds Nolet, G. and Levander, A., pp. 67-80, Geophysical Monograph Series 157, American Geophysical Union, 2005.
- Yuan, H., Romanowicz, B., Fischer, K. M. and Abt, D., 3-D shear wave radially and azimuthally anisotropic velocity model of the North American upper mantle, *Geophys. J. Int.*, **184**, 1237-1260, 2011.
- Zheng, Z. and Romanowicz, B., Do "double SS precursors" mean double discontinuities?, *Geophys. J. Int.* (submitted), 2012.

## 34 Inversion of Receiver Functions without Deconvolution

Thomas Bodin, Huaiyu Yuan, Barbara Romanowicz

### 34.1 Introduction

The coda of teleseismic P-waves contains a large number of phases generated at interfaces beneath the receiver that contain a significant amount of information on seismic structure. However, these phases are buried in microseismic noise, and convolved with the source time function (Figure 2.71). Hence, the vertical  $\mathbf{V}(t)$  and horizontal (radial)  $\mathbf{H}(t)$  components of a seismogram for a P plane wave can be written as:

$$\mathbf{V}(t) = \mathbf{s}(t) * \mathbf{v}(t) * \mathbf{I}(t) \quad (2.3)$$

$$\mathbf{H}(t) = \mathbf{s}(t) * \mathbf{h}(t) * \mathbf{I}(t) \quad (2.4)$$

Where  $s(t)$  is the source time function,  $\mathbf{v}(t)$  and  $\mathbf{h}(t)$  are the vertical and radial impulse response function of the near receiver structure, and  $\mathbf{I}(t)$  is the instrument response.

The problem of isolating the structure effect is overcome by a method developed in the 1970's now widely used in seismology. The idea is to deconvolve the vertical component from the horizontal components to produce a time series called a 'receiver function' (RF) (Vinnik, 1977):

$$\mathbf{R}_{obs}(t) = \frac{\mathbf{H}(t)}{\mathbf{V}(t)} * \mathbf{G}(t) = \frac{\mathbf{h}(t)}{\mathbf{v}(t)} * \mathbf{G}(t) \quad (2.5)$$

where the fraction refers to a deconvolution (or spectral division). Note that the Receiver function is smoothed with a Gaussian filter  $\mathbf{G}(t)$  in order to eliminate high frequency errors introduced during the deconvolution (see Figure 2.72). The smoothed receiver function waveform can be directly interpreted by visual inspection, or inverted in the time domain for a S-wave velocity model of the crust and uppermost mantle beneath the receiver.

Although inversion of RFs has been extensively used for the last 30 years, there are two well known drawbacks: 1) The deconvolution is an unstable numerical procedure that needs to be damped. This results in a loss of resolution and introduces errors in the receiver function, with a trade-off between the two effects as shown in Figure 2.71. 2) It is difficult to estimate the nature and level of uncertainties in the observed receiver function. That is, there is no clear way to theoretically propagate the noise present in different components of the seismogram into errors in the deconvolved waveform (Di Bona et al, 1998). Following ideas of Menke and Levin (2003), here we present a novel approach that avoids deconvolution, and hence directly overcomes these two problems.

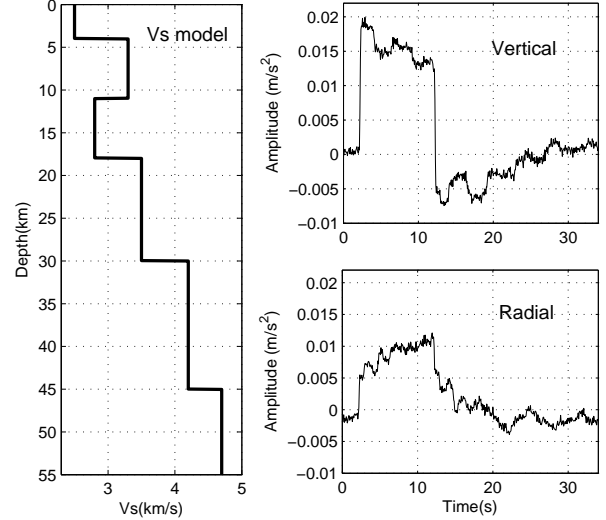


Figure 2.71: Synthetic seismograms computed for an incident plane P-wave traversing layered Earth model. The source time function is a box car function and some white Gaussian noise has been added with standard deviation of 2% the maximum amplitude.

### 34.2 A Cross-convolution Misfit Function

We use the cross-convolution misfit function that was proposed by Menke and Levin (2003) for inversion of SKS splitting measurements. If  $\mathbf{v}_p(t, \mathbf{m})$ , and  $\mathbf{h}_p(t, \mathbf{m})$  are predicted structure response functions for a given model  $\mathbf{m}$ , we can convolve equation (1) by  $\mathbf{h}_p(t, \mathbf{m})$ , and (2) by  $\mathbf{v}_p(t, \mathbf{m})$ :

$$\mathbf{h}_p(t, \mathbf{m}) * \mathbf{V}(t) = \mathbf{s}(t) * \mathbf{v}(t) * \mathbf{I}(t) * \mathbf{h}_p(t, \mathbf{m}) \quad (2.6)$$

$$\mathbf{v}_p(t, \mathbf{m}) * \mathbf{H}(t) = \mathbf{s}(t) * \mathbf{h}(t) * \mathbf{I}(t) * \mathbf{v}_p(t, \mathbf{m}) \quad (2.7)$$

The misfit function is then defined as the difference between the left sides of (2.6) and (2.7).

$$\Phi(\mathbf{m}) = \|\mathbf{v}_p(t, \mathbf{m}) * \mathbf{H}(t) - \mathbf{h}_p(t, \mathbf{m}) * \mathbf{V}(t)\|^2 \quad (2.8)$$

which minimizes when  $\mathbf{v}_p(t, \mathbf{m}) = \mathbf{v}(t)$  and  $\mathbf{h}_p(t, \mathbf{m}) = \mathbf{h}(t)$ .

This misfit function is equivalent to the distance between the observed and predicted receiver functions. However, 1) it does not require any deconvolution procedure, no damping parameter needs to be chosen, and hence no processing errors are introduced; 2) The chi-squared  $\chi^2$  (or log-likelihood) probability density function can be easily derived from errors statistics in seismograms  $\mathbf{V}(t)$ , and  $\mathbf{H}(t)$ .

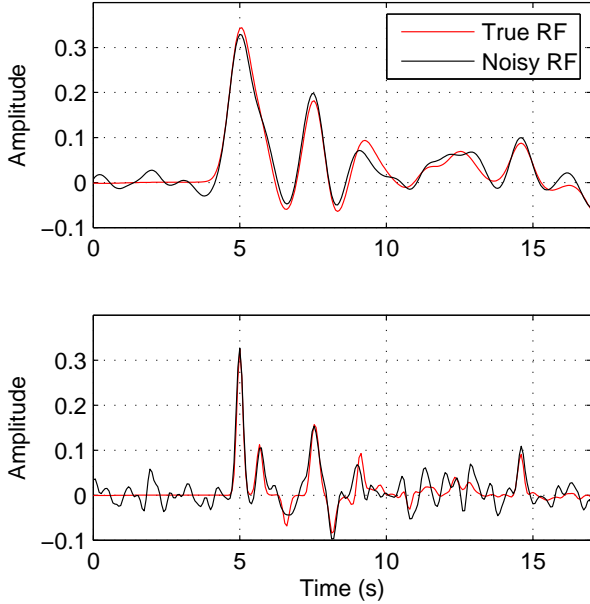


Figure 2.72: Receiver functions computed from seismograms in Figure 2.71 for two Gaussian filters compared with "true" receiver functions. This illustrates the trade-off between resolution and variance. Smoothing the waveform stabilizes the deconvolution at the cost of losing resolution. There is no mathematical model for the noise introduced by deconvolution.

Since discrete convolution in time is a simple summation, and since seismograms can be seen as corrupted by random errors, each sample of the signal obtained after discrete convolution is then a sum of random variables, whose statistics are straightforward to calculate with algebra of random variables. This is not the case with deconvolution schemes.

For example, let us assume as shown in Figure 2.71 a simple case where  $\mathbf{V}(t)$ , and  $\mathbf{H}(t)$  contain independent, and normally distributed random errors (i.e. Gaussian white noise) with standard deviation  $\sigma$ . It can be easily shown that the chi-squared statistic for the misfit function  $\Phi$  is:

$$\chi^2 = \frac{\Phi}{\sigma^2 (\sum_{i=1}^n (\mathbf{h}_p^i)^2 + \sum_{i=1}^n (\mathbf{v}_p^i)^2)} \quad (2.9)$$

where  $n$  is the number of samples in the signal.

### 34.3 Bayesian Inversion

A correct mathematical form for the chi squared distribution allows us to write the likelihood function which measures the probability that the predicted and observed data are consistent given a mathematical model for the random noise distribution. While error statistics in the data and in the misfit function are not indispensable in

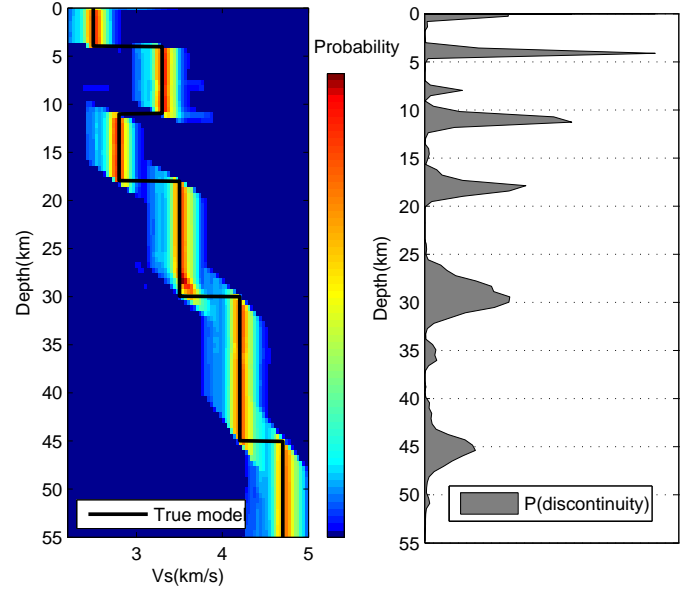


Figure 2.73: Seismograms in Figure 2.71 are inverted for a layered Vs model with an expanded Bayesian Inversion using cross-convolution. The solution is a large ensemble of 1D profiles representing the probability of the model given the data. Left: Probability for Vs at each depth. Right: probability of having a discontinuity at each depth. (For color figure, see [http://earthquakes.berkeley.edu/annual\\_report/](http://earthquakes.berkeley.edu/annual_report/))

optimization based inversion, i.e. where one only seeks the maximum likelihood model, they become crucial in a Bayesian sampling framework. This is because uncertainty estimates do not affect the best fitting solution, or peak of the likelihood function, but strongly determine the shape (and width) of the likelihood function in model space. In this way, the cross-convolution misfit function enables us to carry out a proper Bayesian inversion which correctly propagates errors in the data toward model uncertainties (Figure 2.73). Data are taken as they are, with no need of arbitrarily defined stabilization parameters (i.e. water level, or width of Gaussian filters), which may bias the solution in a statistical sense.

### 34.4 References

- Di Bona, M. and others, Variance estimate in frequency-domain deconvolution for teleseismic receiver function computation, *GJI.*, 134, 2, 634-646, 1998
- Menke, W. and Levin, V., The cross-convolution method for interpreting SKS splitting observations, with application to one and two-layer anisotropic earth models, *GJI*, 154, 2, 379-392, 2003
- Vinnik, L.P., Detection of waves converted from P to SV in the mantle, *Phys. Earth and Plan. Int.*, 95 39-45, 15, 1977.

## 35 Surface-Wave Methods for Monitoring Subsurface Properties in Permafrost Soils

Shan Dou, Jonathan Ajo-Franklin (LBNL), and Douglas Dreger

### 35.1 Introduction

Permafrost (frozen ground that remains at or below 0°C for at least two consecutive years) covers 24% of northern circumpolar continents (Zhang *et al.* 1999). Thawing permafrost in a warming climate can cause hazards of serious concern: (1) Significant amounts of greenhouse gases can be released into the atmosphere due to large-scale microbial decomposition of organic matter that are previously preserved in frozen soils; (2) Thermokarst subsidence in ice-rich permafrost can further intensify the thaw of frozen ground as well as cause severe damage to infrastructure and transportation networks. Both incremental processes (e.g. active layer thickening and talik formation) and transient phenomena (e.g. thaw-induced ground surface settlement and slope instability) affect the rate of permafrost degradation and the detrimental impacts on climate change. Substantial amounts of supercooled water (liquid water that stays unfrozen below 0°C) exist in permafrost soils. Such unfrozen water not only enables carbon-related microbial activities even in subzero temperatures but also makes the subsurface water/ice content not directly predictable using only temperature information. All these aforementioned issues point to the necessity of permafrost monitoring in various spatial and temporal scales. Thermal monitoring in deep boreholes, despite being one of the most common monitoring approaches, only provides one-dimensional plot-scale measurements that do not directly indicate ground ice content. In addition, deep boreholes in permafrost are generally scarce because of the high cost and logistical difficulties, especially in remote Arctic and Subarctic regions. In contrast, geophysical monitoring methods can provide information on subsurface properties over field-scale areas (e.g. hundreds of meters laterally and vertically) at a comparatively low cost and with minimal disturbance to the natural environment. Geophysical monitoring approaches also have the potential for automated acquisition using permanent or semi-permanent sensor networks, a distinct advantage in regions that are difficult to access and in inhospitable environments.

Permafrost characterization and monitoring with geophysical methods relies on properties that differ between frozen and unfrozen materials. The most frequently used geophysical properties for studies of periglacial environments include *electrical resistivity*, *dielectric permittivity* and *seismic velocity*. Among other properties of frozen soils, *ground ice content* is a key factor when estimat-

ing risk level of environmental hazard in the context of global warming. Though electrical methods usually require less effort in data acquisition and processing, they often result in difficulties in differentiating between ice and air and are often limited to shallower targets. Seismic methods, on the other hand, do not suffer from such problems and thus are particularly suitable for assessing ground ice content, both as an independent method and a complementary approach to be combined with other geophysical monitoring techniques.

### 35.2 Methodologies

[1] **Permafrost Analysis Based on Surface Wave Methods (SWMs):** Seismic sources at a free-surface impart approximately 2/3 of the radiated energy to surface waves (Woods, 1968). Rich information is carried by the surface wave train owing to its geometric dispersion properties: Surface waves of different frequencies penetrate into different subsurface depth ranges and thus travel with different apparent velocities. Standard seismic equipment for reflection/refraction acquisitions can be directly used for gathering high quality surface wave data. The propagation of surface waves is primarily controlled by the soil shear velocity, thus potentially providing information on soil frame properties, including ice content as well as shear strength. For subsurface soil profiles that contain pronounced low velocity layers, both near-surface reflection and refraction approaches have limited application. Assuming a reasonable survey geometry, surface wave methods provide an attractive approach for characterizing low velocity layers, a category of structures which includes deep partially thawed regions of interest in permafrost environments.

[2] **Continuous Active Source Seismic Monitoring (CASSM):** Semi-permanently deployed seismic systems with fixed sources and receivers have recently been used in monitoring subsurface processes, including near-surface stress changes (Silver *et al.* 2007), subsurface movement of supercritical CO<sub>2</sub> (Daley *et al.* , 2007, 2011), hydrofracture initiation and propagation (Ajo-Franklin, *et al.*, 2011), and seismic velocity changes in fault zones prior to seismic activity (Niu *et al.* , 2008). This strategy, referred to as continuous active source seismic monitoring (CASSM), allows both high precision in detecting subtle changes and excellent temporal sampling on the order of minutes. CASSM systems, for the purpose of time-lapse seismic measurements, could help us gain an in-depth understanding of subsurface processes

in frozen soils that are both continuous and threshold-driven. Combining CASSM with Multichannel Analysis of Surface Waves (MASW) (e.g. *Park et al.*, 1999) could be a compelling direction for the development of permafrost monitoring systems.

### 35.3 Preliminary Results

[1] **Development of a Physics-based Four-phase Rock Physics Model:** Rock physics models, which link geophysical observables to microstructure and phase composition, are not only important for interpreting geophysical results but also provide a priori information (e.g. constraints) that is critical for the inverse problem itself. Frozen soils have four constituents: soil particles, ice, liquid water, and air. It is therefore most reasonable to include these four phases into the permafrost model. We selected contact cement theory (CCT) (*Dvorkin et al.*, 1994; *Dvorkin and Nur*, 1996; *Jacoby et al.*, 1996; *Dvorkin et al.*, 1999) to model characteristics of the grain-ice solid skeleton. and White’s patchy saturation model (*White*, 1975; *Dutta and Odé*, 1979a,b; *Dutta and Seriff*, 1979) to account for the effects of water and air. Figure 2.74 shows seismic velocities (predicted based on our rock physics model) as a function of time for Barrow, Alaska. The velocity variations correlate well with the soil temperature changes, and the effect of residual unfrozen water content is clearly visible at the freeze-thaw transition due to unfrozen waters held by fine-grained silty soils below 20 cm from the ground surface.

[2] **May 2012 Seismic Survey at Barrow, Alaska:** An active-source (sledge-hammer) seismic survey was conducted in early May of 2012 at Barrow, Alaska. The survey used 48 vertical 10 Hz geophones with 1.1 m spacing. Preliminary frequency-phase velocity (f-v) domain analyses along the seismic lines have shown strong presence of overtone energy, which could be indicative of the existence of low shear-velocity layers whose effects are dominant within the survey’s sensitivity range. However, the difficulties in identifying and separating the overtones have required adaptations in the inversion method used for analyzing the field data. The approach we are developing, a modeless MASW waveform inversion scheme, will hopefully provide a robust inversion approach for scenarios where the presence of overtones obscures picking for the fundamental Rayleigh mode.

[3] **Development of an MASW CASSM System:** Longer term deployments in the arctic, particularly those monitoring subtle diurnal or seasonal property variations, will require semi-permanent active source surface wave monitoring systems. We have initiated development of such a system based on a combination of a commodity electromechanical transducer and the CASSM acquisition infrastructure developed for borehole measurements (e.g. *Daley et al.*, 2007, *Ajo-Franklin et al.*, 2011). The system is currently being bench tested; we anticipate lo-

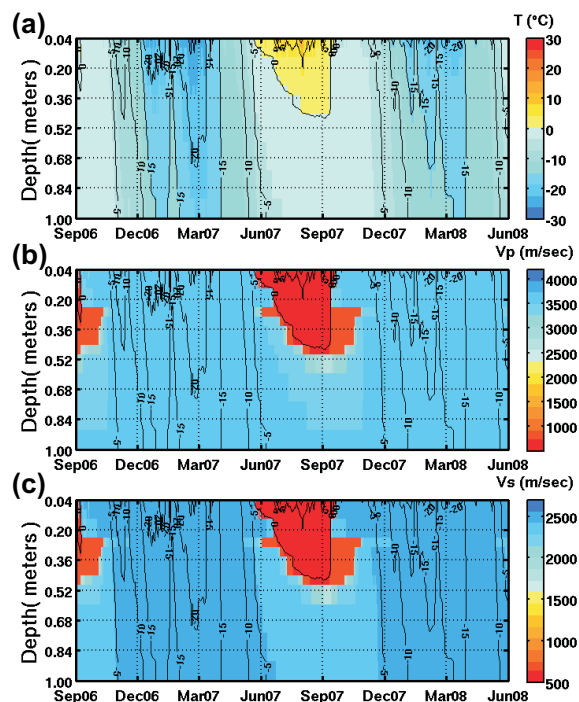


Figure 2.74: (a) Daily soil temperatures at Barrow for the period 09/01/2006 to 06/01/2008; (b) Predicted time-lapse variations of compressional wave velocities for the same time period; (c) Predicted time-lapse variations of shear wave velocities were calculated for the same time period.

cal field deployments in the next quarter followed by tests in the arctic in CY 2013.

### 35.4 Acknowledgements

This study is sponsored by the Office of Biological and Environmental Research within the U.S. Department of Energy’s Office of Science as part of the Next Generation Ecosystem Experiment (NGEE-Arctic).

### 35.5 References

Dvorkin, J., J. Berryman, and A. Nur, Elastic moduli of cemented sphere packs, *Mechanics of Materials*, 31, 461-469, 1999.

Ajo-Franklin, J., T. Daley, B. Butler-Veytia, J. Peterson, Y. Wu, B. Kelly, and S.S. Hubbard, Multi-level continuous active source seismic monitoring (ML-CASSM): Mapping shallow hydrofracture evolution at a TCE contaminated site, *SEG Expanded Abstract*, 30, 2011.

Daley, T. M., R.D. Solbau, J.B. Ajo-Franklin, and S.M. Benson, Continuous active-source seismic monitoring of CO2 injection in a brine aquifer, *Geophysics*, 72(5), A57-A61, 2007.

Park, C. B., R. D. Miller, and J. Xia, Multichannel analysis of surface waves, *Geophysics*, 64, 800-808, 1999.

# Chapter 3

## BSL Operations

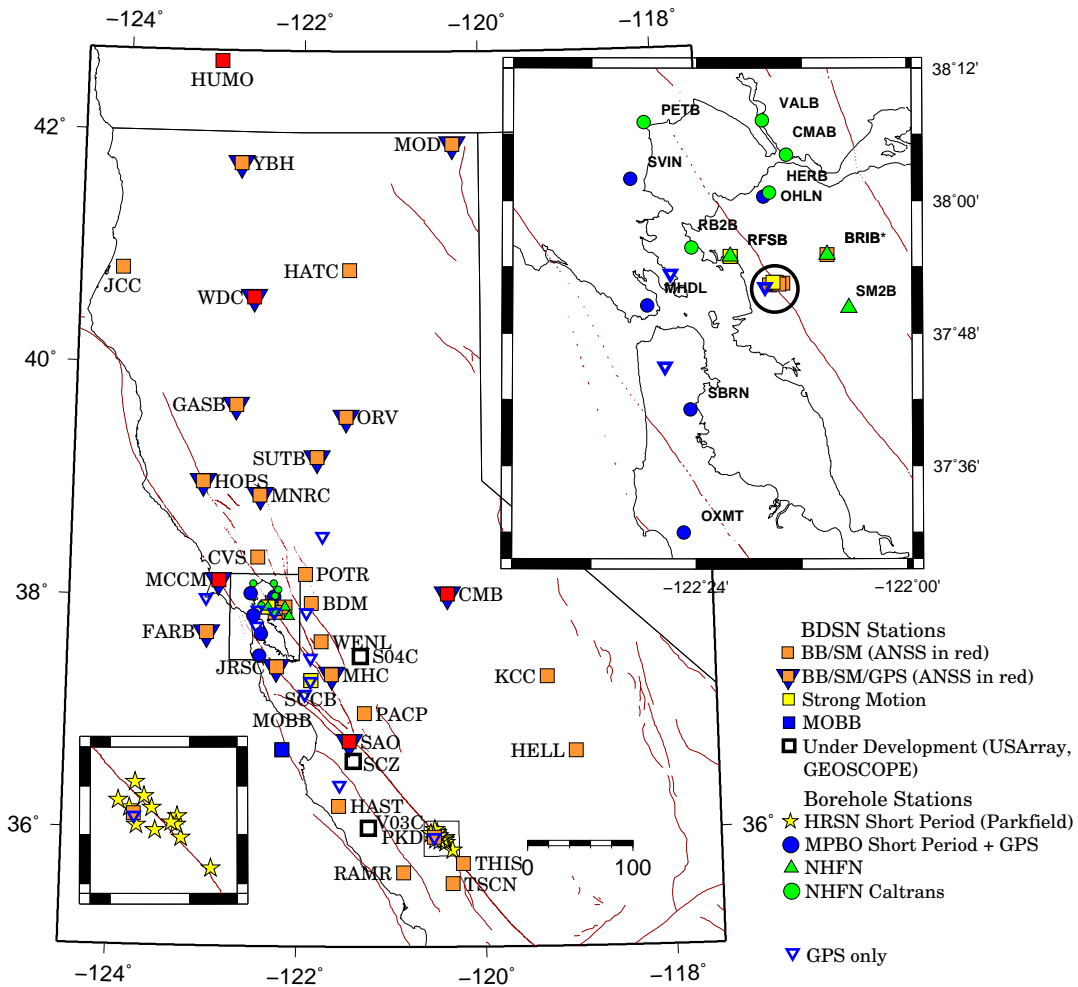


Figure 3.1: Map illustrating the distribution of BSL networks in Northern and Central California. USGS and CalEMA contribute to operating these stations. ANSS backbone stations are shown in red. In the upper right inset map, the shown stations in the circle include BRK, BKS, and CMSB on the Berkeley campus and VAK, BL88, and BL67 on the campus of the Lawrence Berkeley Lab. \* Station BRIB is also a GPS and mPBO site. Boundaries for the lower left inset map are 120.65°- 120.2°West, 35.78°- 36.08°North. Abbreviations: BB/SM - Broadband/Strong Motion; BB/SM/GPS - Broadband/Strong Motion/GPS

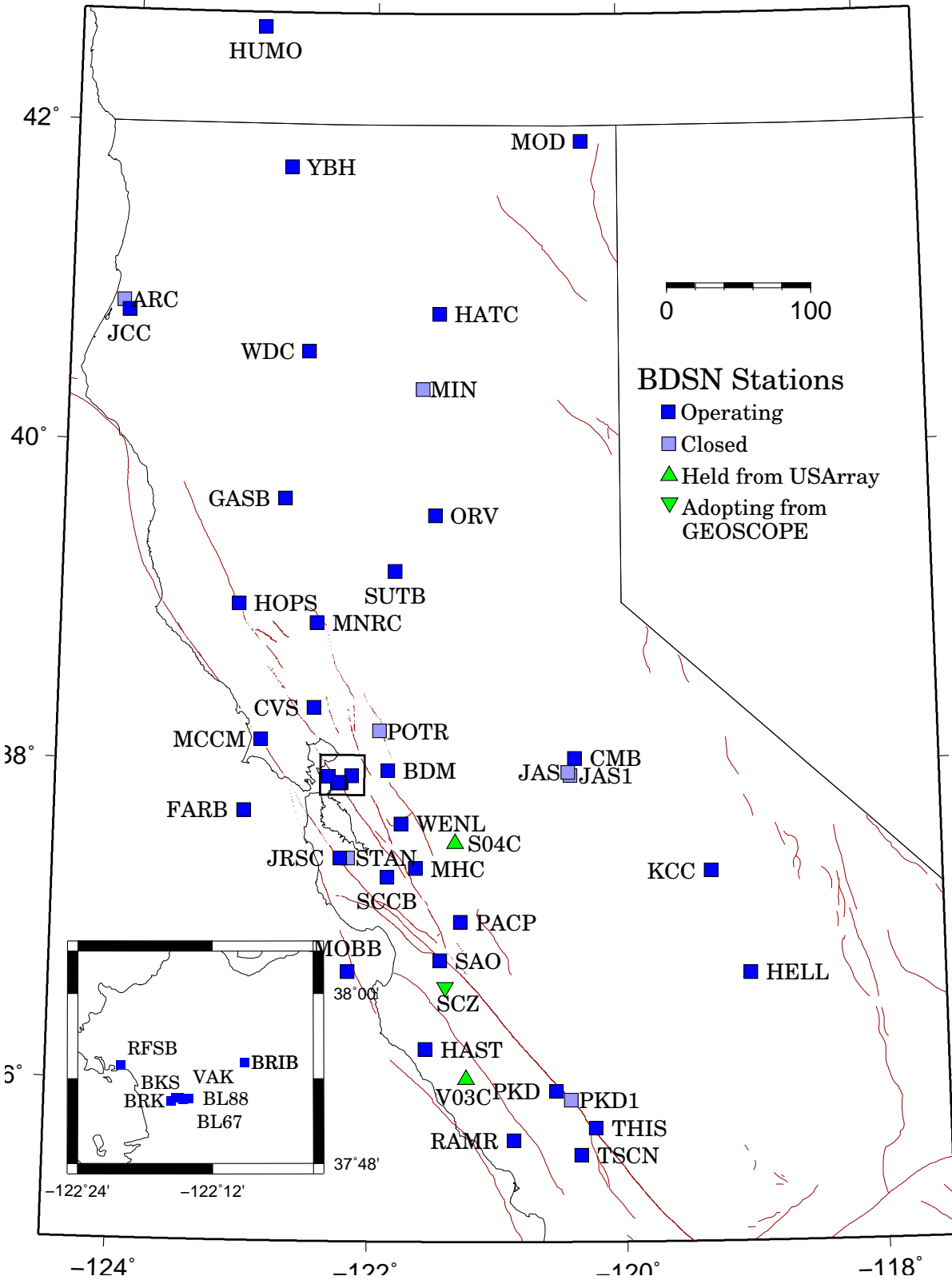


Figure 3.2: Map illustrating the distribution of BDSN stations in Northern and Central California. In the inset map, the order of the stations from left to right is: RFSB, BRK, BL88, VAK, BL67, BKS, BRIB.

# 1 Berkeley Digital Seismic Network

## 1.1 Introduction

The Berkeley Digital Seismic Network (BDSN) is a regional network of very broadband and strong motion seismic stations spanning Northern California and linked to UC Berkeley through continuous telemetry (Figure 3.2 and Table 3.1). The network is designed to monitor regional seismic activity as well as to provide high quality data for research in regional and global broadband seismology.

Since 1991, the BDSN has grown from the original three broadband stations installed in 1986-87 (BKS, SAO, MHC) to 37 stations, including an ocean-bottom seismometer in Monterey Bay (MOBB). We take particular pride in high quality installations, which often involve lengthy searches for appropriate sites away from sources of low-frequency noise as well as continuous improvements in installation procedures and careful monitoring of noise conditions and problems. This year, field and operation efforts have been directed toward the completion of station upgrades, funded by the American Recovery and Reinvestment Act (ARRA), and the installation of stations for the TremorScope project (see Research Section 3). Engineering and research efforts were also devoted to several projects to develop and test new instrumentation (see Operational Section 7). We have been testing the Quanterra environmental add-on, the QEP. In addition, the BSL is part of a team that is developing and testing a newly designed very broadband (VBB) sensor to replace the STS-1 seismometer.

The expansion of our network to increase the density of state-of-the-art strong motion/broadband seismic stations and improve the joint earthquake notification system in this seismically hazardous region, one of BSL's long term goals, is coordinated with other institutions and is contingent on the availability of funding. In the past (2010-2011), in cooperation with and with support from the Lawrence Berkeley National Laboratory (LBNL), we installed and are collecting data from three sites on the LBNL Campus (VAK, BL88 and BL67). We have been working to develop a site for LBNL equipment in the Lawson Adit on the UCB campus, very close to the fault. This effort is close to bearing fruit. We also received funds from the Gordon and Betty Moore Foundation for TremorScope (see Section 3). As part of this exciting project for monitoring non-volcanic tremor sources along the San Andreas Fault south of Parkfield, the BDSN will be augmented by a network of four high-quality borehole stations and four surface stations. The first two surface stations were installed in the Spring and are collecting data.

Data quality and the integrity of the established net-

work are just as important as network growth, so existing network stations must be preserved. The first generation of broadband seismometers installed by the BSL has been operating for almost 25 years. With funding and equipment from the ARRA, we were able to replace old data loggers at 25 stations. The upgrade of the last remaining BDSN station to have an old Quanterra data logger was completed in June 2011. We continue to exercise vigilance and to commit time and resources to repairs and upgrades as necessary.

## 1.2 BDSN Overview

Thirty three of the BDSN sites are equipped with three-component broadband seismometers and strong-motion accelerometers, and with 24- or 26-bit digital data acquisition systems or data loggers. Three additional sites (BL88, RFSB and SCCB) consist of a strong-motion accelerometer and a 24-bit digital data logger. The ocean-bottom station MOBB is equipped with a three component broadband seismometer with integrated digitizer and a differential pressure gauge (DPG). Data from all BDSN stations are transmitted to UC Berkeley using continuous telemetry. Continuous telemetry from MOBB was implemented early in 2009. Unfortunately, the underwater cable was trawled and damaged several times, until it failed in late February 2010. The cable was finally replaced in June 2011. In order to avoid data loss during utility disruptions, each site has batteries to supply power for three days; many are accessible via a dialup phone line. The combination of high-dynamic range sensors and digital data loggers ensures that the BDSN has the capability to record the full range of earthquake motion required for source and structure studies. Table 3.2 lists the instrumentation at each site.

Most BDSN stations have Streckeisen STS-1 or STS-2 three-component broadband sensors (*Wielandt and Streckeisen, 1982; Wielandt and Steim, 1986*). A Guralp CMG-3T broadband sensor contributed by LLNL is deployed in a post-hole installation at BRIB. The new TremorScope sites also have Guralp CMT-3T broadband seismometers. A Guralp CMG-1T is deployed at MOBB. All stations, except the TremorScope sites, have either Kinematics FBA-ES-T or Metrozet TSA-1 accelerometers with  $\pm 2$  g dynamic range. At TremorScope accelerometers are Guralp CMG-5T units, also with  $\pm 2$  g dynamic range. Since the end of June 2011, there are no longer any Q680, Q730, or Q4120 Quanterra data loggers in the BDSN. The sites with Quanterras all have Q330, Q330HR or Q330S data loggers. The Quanterra data loggers employ FIR filters to extract data streams at a variety of sampling rates. The same is true for the

Code	Net	Latitude	Longitude	Elev (m)	Over (m)	Date	Location
BDM	BK	37.9540	-121.8655	219.8	34.7	1998/11 -	Black Diamond Mines, Antioch
BKS	BK	37.8762	-122.2356	243.9	25.6	1988/01 -	Byerly Vault, Berkeley
BL67	BK	37.8749	-122.2543	736.18	0	2011/04 -	LBNL Building 67, Berkeley
BL88	BK	37.8772	-122.2543	602.21	0	2011/01 -	LBNL Building 88, Berkeley
BRIB	BK	37.9189	-122.1518	219.7	2.5	1995/06 -	Briones Reservation, Orinda
BRK	BK	37.8735	-122.2610	49.4	2.7	1994/03 -	Haviland Hall, Berkeley
CMB	BK	38.0346	-120.3865	697.0	2	1986/10 -	Columbia College, Columbia
CVS	BK	38.3453	-122.4584	295.1	23.2	1997/10 -	Carmenet Vineyard, Sonoma
FARB	BK	37.6978	-123.0011	-18.5	0	1997/03 -	Farallon Island
GASB	BK	39.6547	-122.716	1354.8	2	2005/09 -	Alder Springs
HAST	BK	36.3887	-121.5514	542.0	3	2006/02 -	Carmel Valley
HATC	BK	40.8161	-121.4612	1009.3	3	2005/05 -	Hat Creek
HELL	BK	36.6801	-119.0228	1140.0	3	2005/04 -	Miramonte
HOPS	BK	38.9935	-123.0723	299.1	3	1994/10 -	Hopland Field Stat., Hopland
HUMO	BK	42.6071	-122.9567	554.9	50	2002/06 -	Hull Mountain, Oregon
JCC	BK	40.8175	-124.0296	27.2	0	2001/04 -	Jacoby Creek
JRSC	BK	37.4037	-122.2387	70.5	0	1994/07 -	Jasper Ridge, Stanford
KCC	BK	37.3236	-119.3187	888.1	87.3	1995/11 -	Kaiser Creek
MCCM	BK	38.1448	-122.8802	-7.7	2	2006/02 -	Marconi Conference Center, Marshall
MHC	BK	37.3416	-121.6426	1250.4	0	1987/10 -	Lick Obs., Mt. Hamilton
MNRC	BK	38.8787	-122.4428	704.8	3	2003/06 -	McLaughlin Mine, Lower Lake
MOBB	BK	36.6907	-122.1660	-1036.5	1	2002/04 -	Monterey Bay
MOD	BK	41.9025	-120.3029	1554.5	5	1999/10 -	Modoc Plateau
ORV	BK	39.5545	-121.5004	334.7	0	1992/07 -	Oroville
PACP	BK	37.0080	-121.2870	844	0	2003/06 -	Pacheco Peak
PKD	BK	35.9452	-120.5416	583.0	3	1996/08 -	Bear Valley Ranch, Parkfield
RAMR	BK	37.9161	-122.3361	416.8	3	2004/11 -	Ramage Ranch
RFSB	BK	37.9161	-122.3361	-26.7	0	2001/02 -	RFS, Richmond
SAO	BK	36.7640	-121.4472	317.2	3	1988/01 -	San Andreas Obs., Hollister
SCCB	BK	37.2874	-121.8642	98	0	2000/04 -	SCC Comm., Santa Clara
SUTB	BK	39.2291	-121.7861	252.0	3	2005/10 -	Sutter Buttes
THIS	BK	35.7140	-120.2370	623.0	0	2012/05 -	South End of Cholame Valley, Shandon
TSCN	BK	35.5440	-121.3481	476.47	0	2012/03 -	Shell Creek North, Shandon
VAK	BK	37.8775	-122.2489	266.0	10	2010/08 -	LBNL Building 46, Berkeley
WDC	BK	40.5799	-122.5411	268.3	75	1992/07 -	Whiskeytown
WENL	BK	37.6221	-121.7570	138.9	30.3	1997/06 -	Wente Vineyards, Livermore
YBH	BK	41.7320	-122.7104	1059.7	60.4	1993/07 -	Yreka Blue Horn Mine, Yreka

Table 3.1: Stations of the Berkeley Digital Seismic Network currently in operation. Each BDSN station is listed with its station code, network id, location, operational dates, and site description. The latitude and longitude (in degrees) are given in the WGS84 reference frame, and the elevation (in meters) is relative to the WGS84 reference ellipsoid. The elevation is either the elevation of the pier (for stations sited on the surface or in mining drifts) or the elevation of the well head (for stations sited in boreholes). The overburden is given in meters. The date indicates either the upgrade or installation time.

Code	Broadband	Strong-motion	Data logger	GPS	Other	Telemetry	Dial-up
BDM	STS-2	FBA-ES-T	Q330HR			FR	
BKS	STS-1	FBA-ES-T	Q330HR		E300, Baseplates	FR	X
BL67	CMG-3T	FBA-ES-T	Q330S			LAN	
BL88		FBA-ES-T	Q330S			R	
BRIB	CMG-3T	FBA-ES-T	Q330HR	X	Strainmeter, EM	FR	X
BRK	STS-2	FBA-ES-T	Q330HR			LAN	
CMB	STS-1	FBA-ES-T	Q330HR	X	E300, Baseplates	FR	X
CVS	STS-2	FBA-ES-T	Q330HR			FR	
FARB	STS-2	FBA-ES-T	Q330HR	X		R-FR/R	
GASB	STS-2	FBA-ES-T	Q330HR	X		R-FR	
HAST	STS-2	FBA-ES-T	Q330HR			R-Sat	
HATC	STS-2	FBA-ES-T	Q330HR			T1	
HELL	STS-2	FBA-ES-T	Q330			R-Sat	
HOPS	STS-1	FBA-ES-T	Q330HR	X	E300, Baseplates	FR	X
HUMO	STS-2	FBA-ES-T	Q330HR			VSAT	X
JCC	STS-2	FBA-ES-T	Q330HR			FR	X
JRSC	STS-2	TSA-100S	Q330HR			Mi-LAN	X
KCC	STS-1	FBA-ES-T	Q330HR		E300, Baseplates	R-Mi-FR	X
MCCM	STS-2	FBA-ES-T	Q330HR			VSAT	
MHC	STS-1	FBA-ES-T	Q330HR	X		FR	X
MNRC	STS-2	FBA-ES-T	Q330HR	X		Sat	X
MOBB	CMG-1T		DM24		OCM, DPG	LAN	
MOD	STS-1*	FBA-ES-T	Q330HR	X	Baseplates	VSAT	X
ORV	STS-1	FBA-ES-T	Q330HR	X	Baseplates	FR	X
PACP	STS-2	FBA-ES-T	Q330HR			Mi/FR	
PKD	STS-2	FBA-ES-T	Q330HR	X	EM	R-Mi-T1	X
RAMR	STS-2	FBA-ES-T	Q330			R-FR	X
RFSB		FBA-ES-T	Q330HR			FR	
SAO	STS-1	FBA-ES-T	Q330HR	X	Baseplates, EM	FR	X
SCCB		TSA-100S	Q330HR	X		FR	
SUTB	STS-2	FBA-ES-T	Q330HR	X		R-FR	
THIS	CMG-3T	CMG-5TC	DM24	X		R-Mi	
TSCN	CMG-3T	CMG-5TC	DM24	X		R-Mi	
VAK	CMG-3T	FBA-ES-T	Q330S			R	
WDC	STS-2	FBA-ES-T	Q330HR	X		FR	X
WENL	STS-2	FBA-ES-T	Q330HR			FR	
YBH	STS-1,STS-2	FBA-ES-T	Q330HR, Q330**	X	E300, Baseplates	FR	X

Table 3.2: Instrumentation of the BDSN as of 06/30/2012. Except for BL88, RFSB, SCCB, and MOBB, each BDSN station consists of collocated broadband and strong-motion sensors, with a 24-bit or 26-bit data logger and GPS timing. The stations BL88, RFSB, and SCCB are strong-motion only, while MOBB has only a broadband sensor. Additional columns indicate collocated GPS receivers as part of the BARD network (GPS) and additional equipment (Other), such as warplless baseplates, new STS-1 electronics (E300) or electromagnetic sensors (EM). The OBS station MOBB also has a ocean current meter (OCM) and differential pressure gauge (DPG). The main and alternate telemetry paths are summarized for each station. FR - frame relay circuit, LAN - ethernet, Mi - microwave, R - radio, Sat - Commercial Satellite, T1 - T1 line, VSAT - USGS ANSS satellite link. An entry like R-Mi-FR indicates telemetry over several links, in this case, radio to microwave to frame relay. (\*) During 2011-2012, the STS-1 at this station was replaced by an STS-2. (\*\*) YBH is CTBT auxiliary seismic station AS-109. It has a high-gain STS-2.

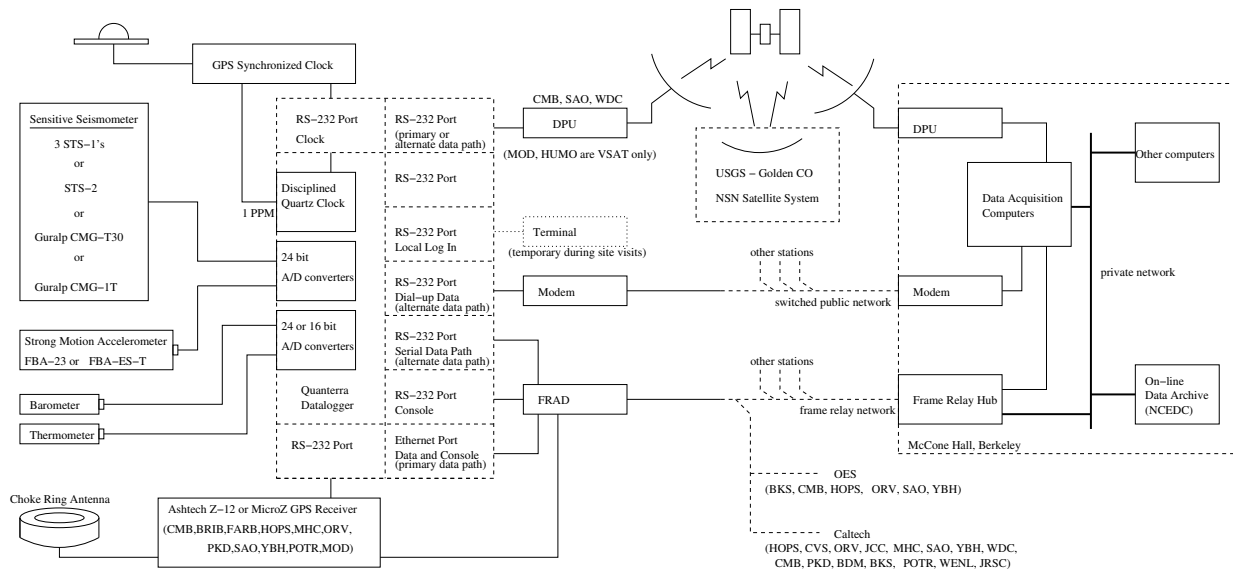


Figure 3.3: Schematic diagram showing the flow of data from the sensors through the data loggers to the central acquisition facilities of the BSL.

Guralp DM24 digitizers at the TremorScope sites and at MOBB. With the ARRA data logger upgrade, several conventions changed: All sites received SEED location codes, with the data logger for the broadband and strong motion sensors having the location code “00,” and accelerometer channels are now designated with “HN?” rather than “HL?”. In addition, the BDSN stations now record continuous data at 0.1, 1.0, 40, and 100 samples per second (Table 3.3). In the past, other sample rates may have been available (see past annual reports).

When the broadband network was upgraded during the 1990s, a grant from the CalREN Foundation (California Research and Education Network) in 1994 enabled the BSL to convert data telemetry from analog leased lines to digital frame relay. The frame-relay network uses digital phone circuits which support 56 Kbit/s to 1.5 Mbit/s throughput. Today, 22 of the BDSN sites use frame-relay telemetry for all or part of their communications system. Other stations send their data to the data center via satellite, Internet, microwave, and/or radio (see Table 3.2).

As described in Operational Section 7, data from the BDSN are acquired centrally at the BSL. These data are used for rapid earthquake reporting as well as for routine earthquake analysis (Operational Sections 2 and 8). As part of routine quality control (Operational Section 7), power spectral density (PSD) analyses are performed continuously and are available on the Internet (<http://www.ncedc.org/ncedc/PDF/>). The occurrence of a significant teleseism also provides the opportunity to review station health and calibration. Figure 3.4 displays BDSN waveforms for the  $M_w$  8.6 earthquake that

occurred West of Sumatra on April 11, 2012.

BDSN data are archived and available at the Northern California Earthquake Data Center. This is described in detail in Operational Section 6.

Sensor	Channel	Rate (sps)	Mode	FIR
BB	VH?	0.1	C	Ac
BB	LH?	1	C	Ac
BB	BH?	40	C	Ac
BB	HH?	80/100	C	Ca
SM	LN?	1	C	Ac
SM	BN?	20/40	C	Ac
SM	HN?	80/100	C	Ca&Ac

Table 3.3: Typical data streams currently acquired at BDSN stations, with channel name, sampling rate, sampling mode, and the FIR filter type. BB indicates broadband; SM indicates strong-motion; C continuous; Ac acausal; Ca causal. The LN and BN strong-motion channels are not transmitted over the continuous telemetry but are available on the Quanterra disk system if needed. The HH and HN channels are now all recorded and telemetered continuously at 100 sps and most have causal filtering. In the past, SM channels have been named HL? (BL?, LL?). For past sampling rates, see earlier annual reports.

### Electromagnetic Observatories

In 1995, in collaboration with Dr. Frank Morrison, the BSL installed two well-characterized electric and mag-

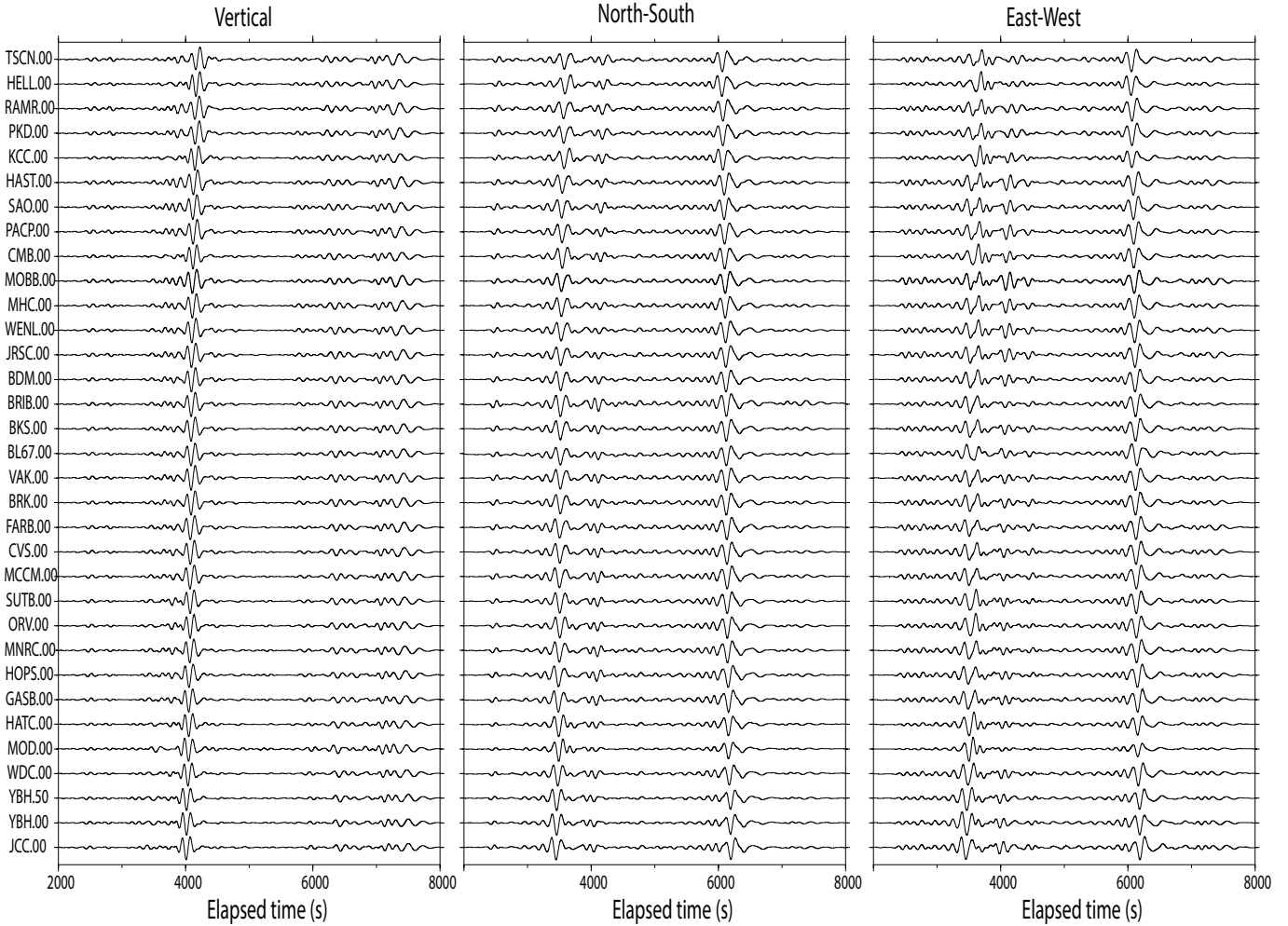


Figure 3.4: Long period (100-333 s period) waveforms recorded across BDSN from the  $M_w$  8.6 teleseism which occurred on April 11, 2012, off the west coast of northern Sumatra at 2.311 N, 93.063 E. The traces are deconvolved to ground velocity, scaled by their maximum values, and ordered from bottom to top by distance from the epicenter. The highly similar waveforms recorded across the BDSN provide evidence that the broadband sensors are operating within their nominal specifications.

netic field measuring systems at two sites along the San Andreas Fault which are part of the Berkeley Digital Seismic Network. Since then, magnetotelluric (MT) data have been continuously recorded at 40 Hz and 1 Hz and archived at the NCEDC (Table 3.4). At least one set of orthogonal electric dipoles measures the vector horizontal electric field,  $E$ , and three orthogonal magnetic sensors measure the vector magnetic field,  $B$ . These reference sites, now referred to as electromagnetic (EM) observatories, are collocated with seismometer sites so that the field data share the same time base, data acquisition, telemetry, and archiving system as the seismometer outputs.

The MT observatories are located at Parkfield (PKD1, PKD), 300 km south of the San Francisco Bay Area,

Sensor	Channel	Rate (sps)	Mode	FIR
Magnetic	VT?	0.1	C	Ac
Magnetic	LT?	1	C	Ac
Magnetic	BT?	40	C	Ac
Electric	VQ?	0.1	C	Ac
Electric	LQ?	1	C	Ac
Electric	BQ?	40	C	Ac

Table 3.4: Typical MT data streams acquired at SAO, PKD, BRIB, and JRSC with channel name, sampling rate, sampling mode, and FIR filter type. C indicates continuous; Ac acausal. Data loggers for these systems have not been upgraded/replaced.

and Hollister (SAO), halfway between San Francisco and Parkfield (Figure 3.2). In 1995, initial sites were established at PKD1 and SAO, separated by a distance of 150 km, and equipped with three induction coils and two 100 m electric dipoles. PKD1 was established as a temporary seismic site, and when a permanent site (PKD) was found, a third MT observatory was installed in 1999 with three induction coils, two 100 m electric dipoles, and two 200 m electric dipoles. PKD and PKD1 ran in parallel for one month in 1999, and then the MT observatory at PKD1 was closed. Starting in 2004, new electromagnetic instrumentation was installed at various Bay Area sites in cooperation with Simon Klemperer at Stanford University. Sensors are installed at JRSC (2004), MHDL (2006) and BRIB (2006/2007).

Data at the MT sites are fed to Quanterra data loggers, shared with the collocated BDSN stations, synchronized in time by GPS, and sent to the BSL via dedicated communication links.

In October 2009, the EM coils at SAO were found to be not working. They were removed and returned to the manufacturer (EMI Schlumberger). They have not yet been reinstalled at SAO. EM/MT equipment at PKD was evaluated in August of 2008. There, the data logger was removed from the PKD EM/MT system and has not yet been returned.

Since it began in 1995, the EM/MT effort has suffered from minimal funding.

### 1.3 2011-2012 Activities

#### Station Upgrades, Maintenance, and Repairs

Given the remoteness of the off-campus stations, BDSN data acquisition equipment and systems are designed, configured, and installed so that they are both cost effective and reliable. As a result, there is little need for regular station visits. Nonetheless, many of the broadband seismometers installed by BSL are from the first generation and are about 25 years old.

In the summer of 2009, the USGS received ARRA funds, among other things, to upgrade and improve seismic stations operated as part of the Advanced National Seismic System (ANSS). The BSL benefitted from those funds. We received the new model of Quanterra data logger, the Q330HR, as government-furnished equipment (GFE). Over the course of the next two years, we installed the Q330HR, replacing the old Quanterras at 25 BDSN seismic stations. In addition, under the ARRA all remaining Kinometrics FBA-23 accelerometers have been replaced with Kinometrics' newer, lower noise model, the FBA-ES-T.

In addition to the equipment upgrades, we used support from the ARRA project to implement alternative, and less expensive, telemetry options at two stations, at JRSC, on Stanford University's Jasper Ridge Biological

Preserve, and at MNRC, on UC Davis's McLaughlin Reserve.

Finally, some ARRA money was used to purchase Quanterra Environmental Packages (QEP) and SETRA pressure sensors for our quietest sites. Over the years the environmental sensors (pressure, temperature, humidity) installed at many of the sites had died. In addition, the Q330 has only 6 input channels, which we use for the seismometer and accelerometer components. The QEP offer additional digitizing capacity as well as rudimentary environmental sensors (pressure, temperature, humidity). To ensure high quality pressure measurements for reducing long period noise in the very broadband recordings, we purchased and will also install the SETRA pressure sensors. During the Spring 2012, we installed all QEP packages and SETRA pressure sensors in a huddle test on the roof of McCone Hall. We have been analyzing the data from that test to corroborate calibration information and evaluate their performance.

In addition, over the past two years, we have been able to purchase and install new electronics, the E300 from Metrozet, for five of our STS-1 sites, KCC, HOPS, BKS, CMB and YBH. Funds for this equipment have come from our IRIS/GSN grant and from our funding from the California Emergency Management Agency (CalEMA).

As always, some of the BSL's technical efforts were directed toward maintaining and repairing existing instrumentation, stations, and infrastructure. While expanding the network continues to be a long term goal of BSL, it is equally important to assure the integrity of the established network and preserve data quality.

#### New Stations

Two new stations were installed as part of the TremorScope project in the past year, TSCN and THIS. These two stations are surface stations, installed vaults made from plastic septic tanks. To provide thermal mass and reduce noise, the tanks are surrounded by several cubic yards of concrete. Data flow from the stations by radio to USGS microwave hubs at Black Mt. and Hog Canyon. We have been evaluating data from each of these sites, to assess station design and develop improvements for the remaining two surface stations to be installed. We have permitted three of the four borehole locations and have begun to develop plans for the boreholes.

#### The Monterey Bay Ocean Bottom Seismic Observatory (MOBB)

The Monterey Ocean Bottom Broadband observatory (MOBB) is a collaborative project between the Monterey Bay Aquarium Research Institute (MBARI) and the BSL. Supported by funds from the Packard Foundation to MBARI, from NSF/OCE, and from UC Berkeley to the BSL, its goal has been to install and operate a long-term seafloor broadband station as a first step

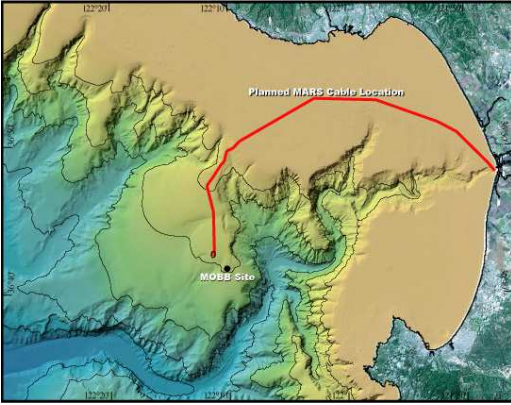


Figure 3.5: Location of the MOBB station in Monterey Bay, California, against seafloor and land topography. The path of the MARS cable is indicated by the solid line.

toward extending the onshore broadband seismic network in Northern California to the seaward side of the North-America/Pacific plate boundary, providing better azimuthal coverage for regional earthquake and structure studies. It also serves the important goal of evaluating background noise in near-shore buried ocean floor seismic systems, such as may be installed as part of temporary deployments of “leap-frogging” arrays (e.g. Ocean Mantle Dynamics Workshop, September 2002). The project has been described in detail in BSL annual reports since 2002 and in several publications (e.g. *Romanowicz et al.*, 2003, 2006).

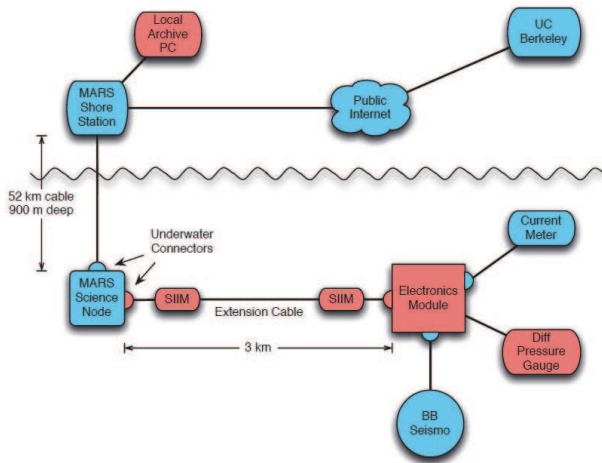


Figure 3.6: Components of the cabled observatory: the MOBB system integrated into the MARS network. MARS-provided components are shown in blue, and components installed or modified by the MOBB team are shown in pink.

The MARS (Monterey Accelerated Research System) observatory (Figure 3.5, <http://www.mbari.org/mars/>) comprises a 52 km electro-optical cable that extends from a shore facility in Moss Landing out to a seafloor node in Monterey Bay (Figure 3.5). The cable was deployed in the spring of 2007, and node installation was completed in November 2008. It now can provide power and data to as many as eight science experiments through underwater electrical connectors. MOBB, located ~3 km from the node, is one of the first instruments to be connected to the cable. The connection was established on February 28, 2009, through an extension cable installed by the ROV *Ventana*, with the help of a cable-laying toolsled. The data interface at the MARS node is 10/100 Mbit/s Ethernet, which can directly support cables of no more than 100 m in length. To send data over the required 3 km distance, the signals pass through a Science Instrument Interface Module (SIIM) at each end of the extension cable (Figure 3.6). The SIIMs convert the MARS Ethernet signals to Digital Subscriber Line (DSL) signals, which are converted back to Ethernet signals close to the MOBB system. Power from the MARS node is sent over the extension cable at 375 VDC, and then converted to 28 VDC in the distal SIIM for use by the MOBB system. The connection to the MARS node eliminates the need for periodic exchange of the battery and data package using ROV and ship. At the same time, it allows us to acquire seismic data from the seafloor in real time (*Romanowicz et al.*, 2009).

The electronics module in the MOBB system was refurbished to support the connection to the MARS observatory. The low-power autonomous data logger was replaced with a PC/104 computer stack running embedded Linux. This new computer runs an Object Ring Buffer (ORB), whose function is to collect data from the various MOBB sensors and forward it to another ORB running on a computer at the MARS shore station. There, the data are archived and then forwarded to a third ORB running at the UC Berkeley Seismological Laboratory. The Linux system acquires data from the various systems on the sea floor: from the Guralp digitizer included in the seismometer package (via RS232) and from a Q330 Quanterra 24 bit A/D converter which digitizes data from the DPG (via Ethernet). It also polls and receives data (via RS232) from the current meter. The data are available through the NCEDC. MOBB data are currently not included in routine earthquake processing as the sampling rate, 20 sps, is relatively low for picking. During the past year, we have implemented a procedure to include “cleaned” MOBB data into the moment tensor analysis program as a first step to using it in earthquake monitoring (see below).

After one year of continuous operation, the MOBB real-time telemetry ceased abruptly as a result of repeated trawling of the extension cable, which was not

buried, even though the observatory is located in a protected zone. We obtained funds from NSF/OCE to replace the 3.2 km cable in late 2010, and decided to “go the extra mile” to bury the cable to protect it better from such future occurrences. The MBARI team built a custom-made basket for the ROV Ventana to carry and bury the cable out, while laying it out. The cable was laid out on June 22, 2012 from the Western Flyer and plugged into the MARS system. The next day, the team dropped and installed the datalogger package and the MOBB data came back on-line.

### Developing a Noise Removal Procedure for MOBB Seismic Data

On seismograms recorded at ocean bottom seismic (OBS) stations, infragravity-induced noise is generally more dominant on the vertical component than on horizontal components (e.g. *Webb*, 1998). In the absence of other noise and signal sources, the vertical displacement and the pressure are nearly perfectly coherent in the period range 20-200 sec as the seafloor deforms under pressure loading. Because the infragravity noise is continually present in a passband critical for the detection and analysis of seismic surface waves, it is important to suppress the infragravity noise in OBS data. The method we use combines the pressure observations with measurements of the transfer function between vertical seismic and pressure recordings to predict the vertical component deformation signal induced by infragravity waves. The predicted noise signal is then removed from the vertical seismic data in either the frequency or the time domain (*Dolenc et al.*, 2007). In the past year, BSL implemented the noise removal procedure developed by *Dolenc et al.* (2007) into the Moment Tensor Review Interface. This allows the suppression of infragravity-induced noise in MOBB OBS seismic data, improving their suitability for determining moment tensors of moderate earthquakes. The transfer function between the vertical seismic and differential pressure gauge (DPG) signals was first calculated from one year of data taken from March 2009 to March 2010. In the data preprocessing for the moment tensor analysis, the transfer function is combined with pressure measurements for a 3-hour period to predict the vertical component deformation signal induced by infragravity waves. The predicted deformation signal is then removed from the recorded vertical component data in the frequency domain. As a result, most of the infragravity-induced noise is removed. An example of the improvement in signal quality is given in Figure 3.7. Here, we used the transfer function to remove infragravity-induced noise on the vertical component for the 2009 Mw 4.3 Morgan Hill earthquake, and confirmed that the method successfully recovered seismic phases that were previously hidden in the infragravity-induced noise. The data was then used for moment tensor

analysis in the 10-100 sec period range.

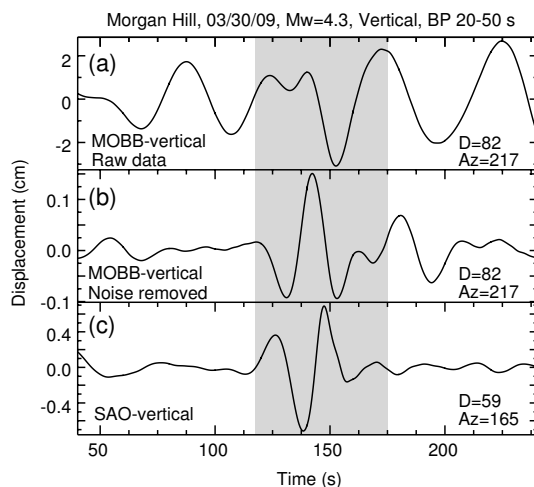


Figure 3.7: Example of the infragravity-induced noise removal procedure for the 2009 Mw 4.3 Morgan Hill earthquake. (a) Original MOBB vertical seismogram and (b) MOBB vertical data after removal of the coherent DPG record by using the transfer function. (c) Station SAO vertical record. A 20-50 sec bandpass filter was applied to all seismic records. Note that the noise-corrected record in (b) shows the earthquake signal (gray area). Also shown are distance (D) in km between earthquake and station and azimuths (Az) in degree from north.

### Very Long Period Stations of the BDSN

Great earthquakes excite normal modes in frequency bands around 1 mHz, well below those of smaller earthquakes. The April 11, 2012, M8.6 earthquake which occurred off the west coast of northern Sumatra provided an opportunity to look at the noise levels in these bands at the very broadband BDSN stations, those equipped with STS1s and the very broadband CMG-1T. Figure 3.8 shows spectra in the band from 0.2 mHz to 2 mHz, with clear normal mode peaks for stations YBH, ORV, BKS, CMB and MOBB. SCZ, is a Geoscope station with STS1s in the Central California Coast Ranges. The BSL has been invited to adopt and upgrade this station, which is hosted by UC Santa Cruz. MOBB, the ocean bottom station off of Monterey Bay is just as quiet in this band as other stations such as BKS and CMB. Spectra are not shown for HOPS, KCC, MHC and SAO which are noisy or have glitches. KCC is often noisy because of flowing water. We will review the other stations and resolve the problems causing the noise.

### 1.4 Acknowledgements

Under Barbara Romanowicz’s general supervision, Peggy Hellweg and Doug Neuhauser oversee the BDSN

data acquisition operations, and Bill Karavas heads the engineering team. Aaron Enright, John Friday, Joshua Miller, Taka'aki Taira, and Bob Uhrhammer contribute to the operation of the BDSN. The network upgrades and improvements were funded through the ARRA (American Recovery and Reinvestment Act), under USGS award number G09AC00487. The new STS-1 electronics, E300s, installed at five of our stations, were purchased with funds from an IRIS/GSN grant and from CalEMA.

MOBB is a collaboration between the BSL and MBARI, involving Barbara Romanowicz, Taka'aki Taira, and Doug Neuhauser from the BSL, and Paul McGill from MBARI. The MBARI team also has included Steve Etchemendy (Director of Marine Operations), Jon Erickson, John Ferreira, Tony Ramirez, and Craig Dawe. The MOBB effort at the BSL is supported by UC Berkeley funds. MBARI supports the dives and data recovery. The MOBB seismometer package was funded by NSF/OCE grant #9911392. The development of the interface for connection to the MARS cable is funded by NSF/OCE grant #0648302.

Taka'aki Taira, and Peggy Hellweg contributed to the preparation of this section.

## 1.5 References

Cox, C., T. Deaton and S. Webb, A deep-sea differential pressure gauge, *J. Atm. Ocean. Tech.*, 1, 237-245, 1984.

Crawford W. C., and S. C. Webb, Identifying and removing tilt noise from low-frequency (<0.1 Hz) seafloor vertical seismic data, *Bull. Seis. Soc. Am.*, 90, 952-963, 2000.

Dolenc, D., B. Romanowicz, R. Uhrhammer, P. McGill, D. Neuhauser, and D. Stakes, Identifying and removing noise from the Monterey ocean bottom broadband seismic station (MOBB) data, *Geochem. Geophys. Geosyst.*, 8, Q02005, doi:10.1029/2006GC001403 (2007).

Murdock, J., and C. Hutt, A new event detector designed for the Seismic Research Observatories, *USGS Open-File Report 83-0785*, 39 pp., 1983.

Romanowicz, B., D. Stakes, R. Uhrhammer, P. McGill, D. Neuhauser, T. Ramirez, and D. Dolenc, The MOBB experiment: a prototype permanent off-shore ocean bottom broadband station, *EOS Trans. AGU*, Aug 28 issue, 2003.

Romanowicz, B., D. Stakes, D. Dolenc, D. Neuhauser, P. McGill, R. Uhrhammer, and T. Ramirez, The Monterey Bay Broadband Ocean bottom seismic observatory, *Ann. Geophys.*, 49, 607-623, 2006.

Romanowicz, B., P. McGill, D. Neuhauser and D. Dolenc, Acquiring real time data from the broadband ocean bottom seismic observatory at Monterey Bay (MOBB), *Seismol. Res. Lett.*, 80, 197-202, 2009.

Webb, S. C., Broad seismology and noise under the ocean, *Rev. Geophys* 36, 105-142, 1998.

Wielandt, E., and J. Steim, A digital very broadband seismograph, *Ann. Geophys.*, 4, 227-232, 1986.

Wielandt, E., and G. Streckeisen, The leaf spring seismometer: design and performance, *Bull. Seis. Soc. Am.*, 72, 2349-2367, 1982.

Zürn, W., and R. Widmer, On noise reduction in vertical seismic records below 2 mHz using local barometric pressure, *Geophys. Res. Lett.*, 22, 3537-3540, 1995.

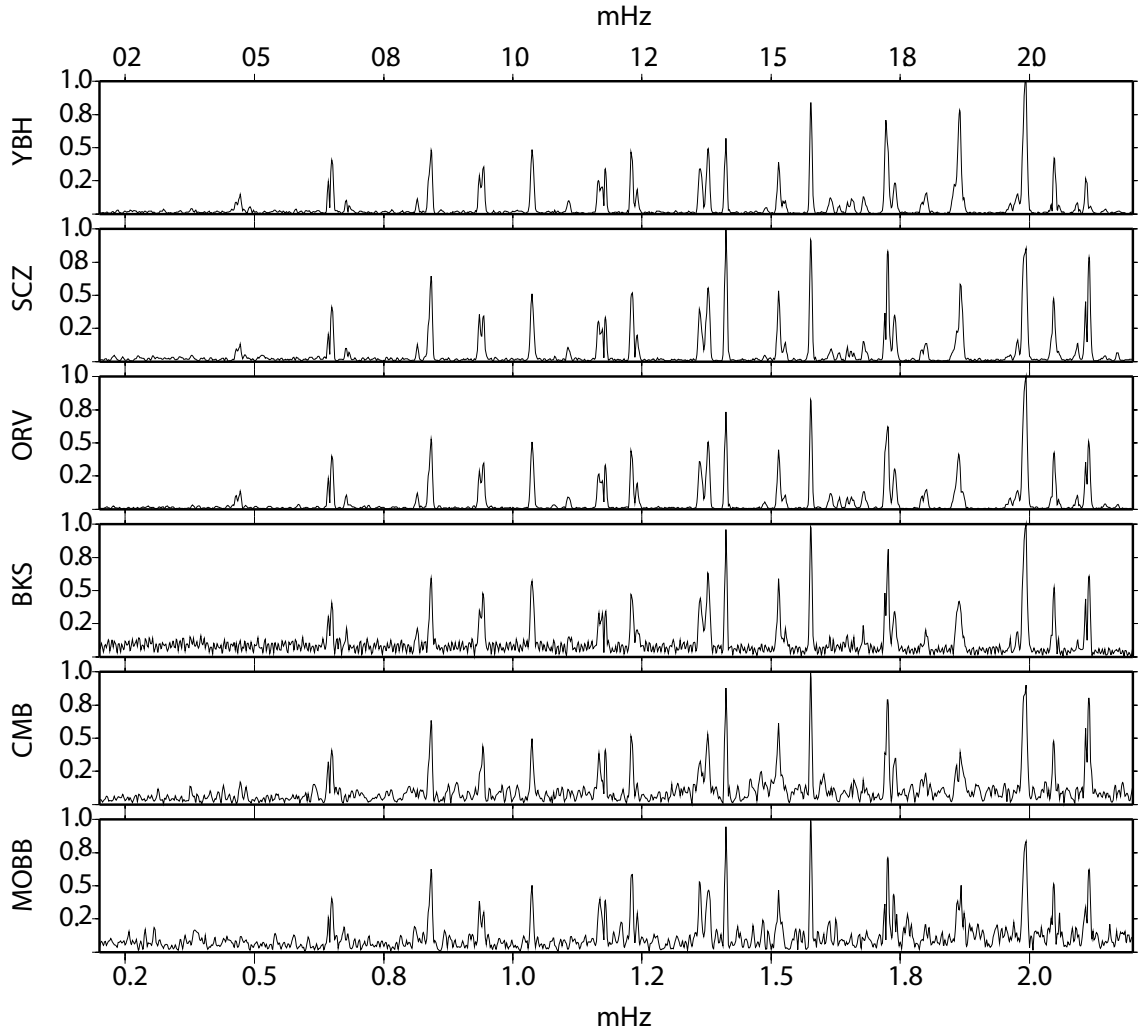


Figure 3.8: Normal mode spectra for the April 11, 2012, M8.6 earthquake which occurred off the west coast of northern Sumatra for the BDSN STS1 stations, MOBB (CMG-1T) and SCZ, a Geoscope station in Central California. Data are converted to acceleration and taken from a 120 hour window starting 0.05 hours after the origin time. A Hann taper has been applied prior to the Fourier transform. The spectra are normalized. Spectra from HOPS, KCC, MHC and SAO are not shown due to noise in their traces. Clearly YBH and ORV have the lowest noise, but the noise in this band at MOBB is similar to other stations such as BKS and CMB.

## 2 California Integrated Seismic Network

### 2.1 Introduction

Advances in technology have made it possible to integrate separate earthquake monitoring networks into a single seismic system as well as to unify earthquake monitoring instrumentation. In California, this effort began in the south with the TriNet Project. There, Caltech, the California Geological Survey (CGS), and the USGS created a unified seismic system for Southern California. With major funding provided by the Federal Emergency Management Agency (FEMA), the California Governor's Emergency Management Agency (CalEMA), and the USGS, monitoring infrastructure was upgraded and expanded, combining resources in a federal, state and university partnership. In 2000, the integration effort expanded to the entire state with the formation of the California Integrated Seismic Network (CISN, see 2000-2001 Annual Report). To this end, UC Berkeley and the USGS Menlo Park and Pasadena offices joined forces with Caltech and the CGS. The CISN is now in the twelfth year of collaboration and its eleventh year of funding from CalEMA.

### 2.2 CISN Background

#### Organization

The organizational goals, products, management, and responsibilities of the CISN member organizations are described in the founding memorandum of understanding and in the strategic and implementation plans. To facilitate activities among institutions, the CISN has three management centers:

- Southern California Earthquake Management Center: Caltech/USGS Pasadena
- Northern California Earthquake Management Center: UC Berkeley/USGS Menlo Park
- Engineering Strong Motion Data Center: California Geological Survey/USGS National Strong Motion Program

The Northern and Southern California Earthquake Management Centers operate as twin statewide earthquake processing centers, serving information on current earthquake activities, while the Engineering Strong Motion Data Center is responsible for producing engineering data products and distributing them to the engineering community.

The Steering Committee, made up of two representatives from each core institution and a representative from CalEMA, oversees CISN projects. The position of

chair rotates among the institutions; Ken Hudnut from the USGS Pasadena took over as chair of the Steering Committee in December 2010 from Barbara Romanowicz. Rob Graves will complete the USGS Pasadena term as Steering Committee chair.

An external Advisory Committee represents the interests of structural engineers, seismologists, emergency managers, industry, government, and utilities, and provides review and oversight. The Advisory Committee is chaired by Loren Turner of Caltrans. It last met in December 2011. Agendas from the meetings and the resulting reports may be accessed through the CISN website (<http://www.cisn.org/advisory>).

The Steering Committee has commissioned other committees, including a Program Management Group to address planning and coordination and a Standards Committee to resolve technical design and implementation issues.

In addition to the core members, other organizations contribute data that enhance the capabilities of the CISN. Contributing members include: University of California, Santa Barbara; University of California, San Diego; University of Nevada, Reno; University of Washington; California Department of Water Resources; Lawrence Livermore National Lab; and Pacific Gas and Electric Company.

#### CISN and ANSS

The USGS Advanced National Seismic System (ANSS) has developed along a regionalized model. Eight regions have been organized, with the CISN representing California. David Oppenheimer of the USGS represents the CISN on the ANSS National Implementation Committee (NIC).

The CISN has recently benefited from the American Recovery and Reinvestment Act (ARRA). The ANSS received funds from the ARRA to improve seismic monitoring throughout the nation and the world. In California, these funds were directed toward replacing old data loggers in both Northern and Southern California, as well as improving installations at individual stations and adding strong motion sites in the form of NetQuakes sensors. The BSL's ARRA-funded activities were mostly completed in previous years, and are described in the corresponding annual reports. The most recently completed ARRA-funded, and other, upgrades are described in are described in Operational Sections 1, 4 and 3.

As the ANSS moves forward, committees and working groups are established to address issues of interest. BSL faculty and staff have been involved in several working groups of the Technical Integration Committee, includ-

ing Doug Dreger, Peggy Hellweg, Pete Lombard, Doug Neuhauser, Bob Uhrhammer, and Stephane Zuzlewski.

### CISN and CalEMA

CalEMA has long had an interest in coordinated earthquake monitoring. The historical separation between Northern and Southern California and between strong-motion and weak-motion networks resulted in a complicated situation for earthquake response. Thus, CalEMA has been an advocate of increased coordination and collaboration in California earthquake monitoring and encouraged the development of the CISN. In FY 01-02, Governor Gray Davis requested support for the CISN, to be administered through CalEMA. Funding for the California Geological Survey, Caltech and UC Berkeley was made available in spring 2002, officially launching the statewide coordination efforts. Following the first year of funding, CalEMA support led to the establishment of 3-year contracts to UC Berkeley, Caltech, and the California Geological Survey for CISN activities. We have just completed the first year of the fourth three-year contract (2011-2014). Unfortunately, state funding to the CISN has been decreasing as the state’s budget problems have increased, putting pressure on our earthquake monitoring and reporting activities.

Past CISN-related activities are described in previous annual reports.

### 2.3 2011-2012 Activities

We have just completed the third full year of operation in the NCEMC (Northern California Earthquake Management Center) with the new suite of earthquake monitoring software. In the past, we have called this system the CISN software. In 2008, it was adopted by the ANSS as the system to be used by US regional networks for their operations and earthquake reporting, and it is now called the ANSS Quake Monitoring System, or AQMS. As AQMS is being implemented by other regional networks, BSL staff members are providing information and software support to the operators of those networks. The NCEMC made the switch to the AQMS software package in June 2009, and the software is now operating at the BSL and in Menlo Park. CISN funding from CalEMA contributed to this transition, and has supported a number of other activities at the BSL during the past year as well.

#### Northern California Earthquake Management Center

As part of their effort within the CISN, the BSL and the USGS Menlo Park are operating the AQMS software as the Northern California joint earthquake information system. Operational Section 8 describes the operation of

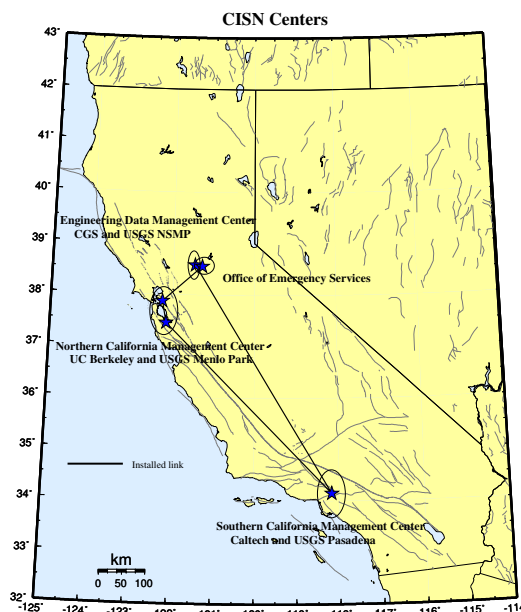


Figure 3.9: Map showing the geographical distribution of the CISN partners and centers. The communications “ring” is shown schematically with installed links (solid lines). It was initially a ring of dedicated T1 connections between the partners. The connections are now less robust, as reduced funding has required that the dedicated service was discontinued. Connections are now available as Internet tunnels.

this system and reports on progress in implementation and improvements.

For monitoring earthquakes in Northern California, the USGS Menlo Park and BSL have improved their communications infrastructure. The BSL and the USGS Menlo Park are currently connected by two dedicated T1 circuits. One circuit is supported by CalEMA funds, while the second circuit was installed in 2004-2005 (Figure 3.11) to support dedicated traffic between Berkeley and Menlo Park above and beyond that associated with the CISN.

Due to the decrease in funding, BSL has eliminated its second T1 for incoming data. BDSN data acquisition is now again limited to one frame-relay circuit, resulting in the reintroduction of a single point of failure.

In the long term, the BSL and USGS Menlo Park hope to be connected by high-bandwidth microwave or satellite service. Unfortunately, we have not yet been able to obtain funding for such an additional communication link, although we have recently explored prospects of a very high speed radio link between the two data centers.

### Statewide Integration

Despite the fact that AQMS software is now operating in both Northern and Southern California, efforts toward

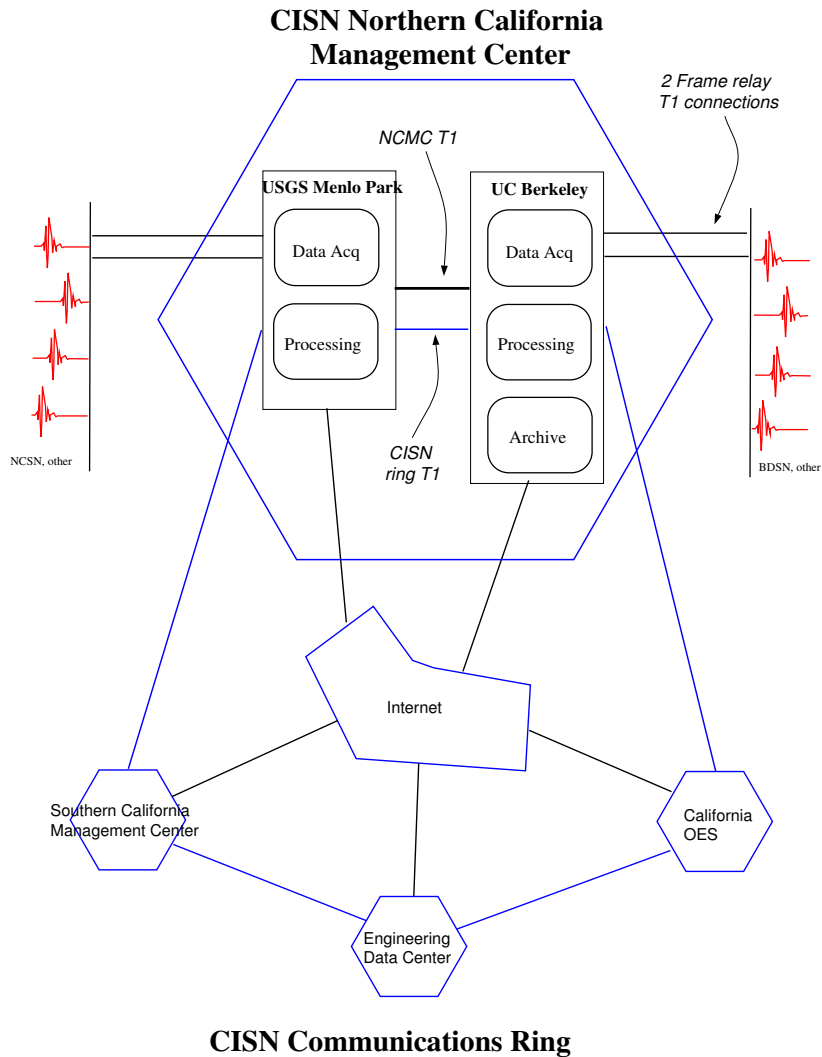


Figure 3.11: Schematic diagram illustrating the connectivity between the real-time processing systems at the USGS Menlo Park and UC Berkeley, forming the Northern California Management Center, and with other elements of the CISN.

statewide integration continue. BSL staff are involved in many elements of these efforts. The Standards Committee, chaired by Doug Neuhauser, continues to define and prioritize projects important to the ongoing development and operation of the statewide earthquake processing system and to establish working groups to address them (see minutes from meetings and conference calls at <http://www.cisn.org/standards/meetings.html>).

*Dual Station Feeds:* Early in the existence of CISN, “dual station feeds” were established for 30 stations (15 in Northern California and 15 in Southern California) (Figure 3.10). Because of decreases in funding and other issues, Northern California now sends data from 12 sta-

tions to Southern California in real time, and Southern California sends data from 10 to Northern California. The NCEMC uses data from the Southern California stations to estimate magnitudes on a routine basis. In addition, some of the stations are used in moment tensor inversions, a computation that is sensitive to the background noise level.

*Data Exchange:* Part of the AQMS software allows reduced amplitude timeseries to be produced and exchanged. Currently, these timeseries are being exchanged at the NCEMC, but not yet statewide. Using a common, and recently improved, format, the CISN partners continue to exchange observations of peak ground motion

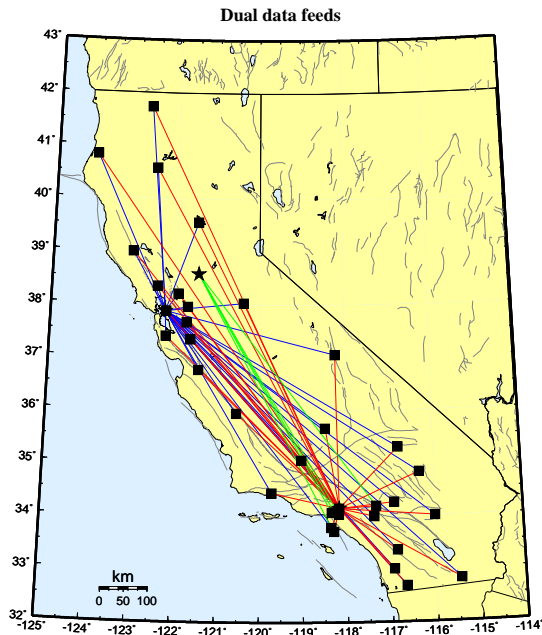


Figure 3.10: Map showing the original 30 stations selected to send data directly to the Northern and Southern California processing centers, and the 5 stations that send data directly to the Engineering Data Center and the Southern California processing center. Due to reductions in funding, now data from only 10 SC stations arrive directly at UCB and data from 12 UCB stations are sent to Caltech.

with one another following an event or a trigger. This step increases the robustness of generating products such as ShakeMap, since all CISM partners now exchange data directly with one another. This also improves the quality of ShakeMaps for events on the boundary between Northern and Southern California, such as the San Simeon earthquake, by allowing all data to be combined in a single map. Finally, this is a necessary step toward the goal of generating statewide ShakeMaps. In addition, datasets for events of interest to engineers are provided automatically to the Strong Motion and Engineering Data Center (SMEDC) in V0 format. We are now working to improve data exchange with the University of Nevada, Reno, for events occurring near the California/Nevada border.

*The Software Calibration & Standardization:* CISM partners have calibrated and standardized much of the software used for automatic earthquake processing and earthquake review, now the AQMS software. The AQMS software now serves as the real-time system operating in the NCEMC. The transition was made in June 2009.

*Local Magnitudes:* Since the transition to the AQMS software in Northern California in June 2009, local magnitudes are calculated throughout the state using the new  $\log A_o$  function and the associated station-specific corrections for broadband/strong motion stations, and also for strong-motion only stations. We are now focusing

magnitude development on adding vertical components, whether short period or broadband, and short period horizontal components to the new local magnitude system. A final component of the magnitude efforts is the determination of a magnitude reporting hierarchy. For the near future, each region will continue to use its own preferences for magnitude reporting.

*ShakeMap:* At present, ShakeMaps are generated on five systems within the CISM. Two systems in Pasadena generate “SoCal” Shakemaps; two systems in the Bay area generate “NoCal” Shakemaps; and one system in Sacramento generates ShakeMaps for all of California. The Sacramento system uses EIDS ( Earthquake Information Distribution System) to collect the authoritative event information for Northern and Southern California. In the CISM, we evaluated the new release of the program, ShakeMap 3.5. In early June, 2011, we finally made the transition to using ShakeMap 3.5 in production. We are evaluating updates to the ShakeMap package before recalculating ShakeMaps for all scenario events, and for all events in the catalog.

A second goal is to improve the robustness of ShakeMap generation and delivery by taking advantage of the fact that ShakeMaps are generated in the Bay Area, Pasadena, and Sacramento.

*Moment Tensor Analysis:* We have implemented an upgraded version of the complete waveform moment tensor code. This version allows the calculation of full moment tensor solutions, including an isotropic element. In the real time system, only deviatoric solutions will be allowed, but a reviewer may “turn on” the capability to allow full solutions. Using this new package, we are recalculating moment tensors for earthquakes in the Geysers and Long Valley regions, which appeared anomalous using the deviatoric code (see Research Section 15). We have also added code which allows us to use pressure-corrected data from our ocean-bottom station, MOBB (see Operational Section 1). We are working to implement the capability of using data from strong motion sensors in the moment tensor interface. This is useful in large events such as the 2010 Cucupa-El Mayor earthquake in Baja California. All broadband stations out to about 600 km were clipped.

*Location Codes:* The CISM adopted a standard for the use of “location” codes (part of the Standard for the Exchange of Earthquake Data [SEED] nomenclature to describe a timeseries based on station-network-channel-location) in the late fall of 2003. USGS and UC Berkeley developers modified the Earthworm software to support their use. After the transition at USGS Menlo Park away from the CUSP analysis system to Jiggle in late November 2006, all networks in the CISM implemented location codes in their systems. Now almost all stations in the BK and BP networks operated by the BLS have non-blank location codes. The major effort in this transition was

made along with the ARRA-funded upgrades of the data loggers. Surface data loggers digitizing seismic equipment have location code “00.” Borehole seismic stations have the location code “40.”

*Metadata Exchange:* Correct metadata are vital to CISN activities, as they are necessary to ensure valid interpretation of data. CISN is working on issues related to their reliable and timely exchange. The CISN Metadata Working Group compiled a list of metadata necessary for data processing and developed a model for their exchange. In this model, each CISN member is responsible for the metadata for its stations and for other stations that enter into CISN processing through it. For example, Menlo Park is responsible for the NSMP, Tremor, and PG&E stations, while Caltech is responsible for the Anza data. At the present time, dataless SEED volumes are used to exchange metadata between the NCEMC and the SCEMC. The Metadata Working Group has made progress toward implementing Station XML format in this year. This is a format for metadata exchange. This vehicle is expandable, and will probably allow exchange of a more comprehensive set of metadata than dataless SEED volumes, some of which may be necessary for other systems, for example in V0 formatted data.

*Standardization:* The CISN’s focus on standardization of software continues. The complete system is now implemented and providing real-time earthquake information in the NCEMC (see Operational Section 8). The software is currently being implemented at other regional networks of the ANSS.

*Earthquake Early Warning:* Caltech, the BSL and the ETH Zurich have been using CISN data in real time to test earthquake early warning algorithms and to develop a prototype earthquake early warning system (see sections 21, 20, 22 and 24; see also <http://www.cisn.org/eeew>). In 2010-2011, we achieved end-to-end processing, with events being published to a user display. In the past year, we have demonstrated the system to CalEMA, and it is now running at the CalEMA Warning Center in Sacramento. We have also recruited other test users, including BART, Google and other companies and agencies throughout California.

## CISN Display

CISN Display is an integrated Web-enabled earthquake notification system designed to provide earthquake information for emergency response at 24/7 operations centers. First responders, organizations with critical lifelines and infrastructure, and emergency responders are invited to register for an account at <http://www.cisn.org/software/cisndisplay.htm>.

The application provides users with maps of real-time seismicity and automatically provides access to Web-related earthquake products such as ShakeMaps. CISN Display also offers an open source GIS mapping tool

that allows users to plot freely available layers of public highways, roads and bridges, as well as private layers of organizational-specific infrastructure and facilities information. The current version of CISN Display is 1.4. Its primary enhancement over the previous version is the development of a kiosk mode for public display purposes.

## Earthquake Information Distribution

The USGS hosted a workshop in October 2004 to develop plans for the installation and use of the EIDS software. Doug Neuhauser and Pete Lombard participated in this workshop, which resulted in a document outlining the steps necessary for the installation and migration of the earthquake notification system from the current Quake Data Distribution Services (QDDS) to EIDS. The NCEMC uses the EIDS system for publishing earthquake information. In the meantime, the USGS has developed a new tool, the Product Distribution Layer (PDL), initially used for transferring so-called add-on information, such as ShakeMaps. The BSL has been using a PDL system to publish ShakeMaps since June, 2011. We are currently working with USGS in Golden to test and implement PDL for delivery of all real-time products, such as complete event information which includes the picks and amplitudes used for determination of location and magnitude; and other products such as moment tensors and fault plane solutions. Pete Lombard is fundamental to our progress in this effort.

## Outreach

Since FY 05-06, the CISN website ([www.cisn.org](http://www.cisn.org)) has been supported by two servers located at Berkeley and Caltech. The Web servers were set up so that the load could be distributed between them, providing improved access during times of high demand. With these servers, the CISN provided access to certain earthquake products directly from [www.cisn.org](http://www.cisn.org). For example, ShakeMaps are now served directly from the CISN website, in addition to being available from several USGS Web servers and the CGS. The design and content of <http://www.cisn.org> continues to evolve. The website is an important tool for CISN outreach as well as for communication and documentation among the CISN partners. We are now developing an updated version of this website.

The CISN supports a dedicated website for emergency managers. This website provides personalized access to earthquake information. Known as “myCISN,” the website is available at [eoc.cisn.org](http://eoc.cisn.org). To provide highly reliable access, the website is limited to registered users.

As part of the CISN, the BSL contributes each year to efforts to raise awareness of earthquakes and earthquake preparedness. The BSL is a member of the Earthquake Country Alliance, a state-wide organization of people,

institutions and agencies associated with earthquake response and research. In the past year, we publicized the state-wide ShakeOut on October 20, 2011 and participated in it. Due in part to our efforts, the entire UC Berkeley campus participated. We are now working toward the statewide California ShakeOut on October 18, 2012 at 10:18 (see <http://www.shakeout.org> for more information and to sign up).

## 2.4 Acknowledgements

CISN activities at the BSL are supported by funding from the California Emergency Management Agency, CalEMA.

Richard Allen and Peggy Hellweg are members of the CISN Steering Committee. Peggy Hellweg and Doug Neuhauser are members of the CISN Program Management Group, and Peggy leads the CISN project at the BSL with support from Doug Neuhauser. Doug Neuhauser is chair of the CISN Standards Committee, which includes Peggy Hellweg, Pete Lombard, Taka'aki Taira, and Stephane Zuzulewski as members.

Because of the breadth of the CISN project, many BSL staff members have been involved, including: Aaron Enright, John Friday, Peggy Hellweg, Ivan Henson, Ingrid Johanson, Bill Karavas, Pete Lombard, Joshua Miller, Doug Neuhauser, Charley Paffenbarger, Taka'aki Taira, Stephen Thompson, Bob Uhrhammer, and Stephane Zuzulewski. Peggy Hellweg contributed to this section. Additional information about the CISN is available through reports from the Program Management Group.

## 3 Northern Hayward Fault Network

### 3.1 Introduction

Complementary to the regional surface broadband and short-period networks, the Hayward Fault Network (HFN) (Figure 3.12 and Table 3.5) is a deployment of borehole-installed, wide-dynamic range seismographic stations along the Hayward Fault and throughout the San Francisco Bay toll bridges system. Development of the HFN initiated through a cooperative effort between the BSL (Berkeley Seismological Laboratory) and the USGS, with support from the USGS, Caltrans, EPRI, the University of California Campus/Laboratory Collaboration (CLC) program, LLNL (Lawrence Livermore National Laboratory), and LBNL (Lawrence Berkeley National Laboratory). The project's objectives included an initial characterization phase followed by a longer-term monitoring effort using a backbone of stations from among the initial characterization station set. Funding from Caltrans, has, in the past, allowed for some continued expansion of the backbone station set for additional coverage in critical locations.

The HFN consists of two components. The Northern Hayward Fault Network (NHFN), operated by the BSL, consists of 29 stations in various stages of development and operation. These include stations located on Bay Area bridges, at free-field locations, and now at sites of the Mini-PBO (mPBO) project (installed with support from NSF and the member institutions of the mPBO project). The NHFN is considered part of the Berkeley Digital Seismic Network (BDSN) and uses the network code BK. The Southern Hayward Fault Network (SHFN) is operated by the USGS and currently consists of five stations. This network is considered part of the Northern California Seismic Network (NCSN) and uses the network code NC. The purpose of the HFN is four-fold: 1) to contribute operational data to the Northern California Seismic System (NCSS) for real-time seismic monitoring, for response applications, and for the collection of basic data for long-term hazards mitigation; 2) to increase substantially the sensitivity of seismic data to low amplitude seismic signals; 3) to increase the recorded bandwidth for seismic events along the Hayward Fault; and 4) to obtain deep bedrock ground motion signals at the bridges from more frequent, small to moderate sized earthquakes.

In addition to the NHFN's contribution to real-time seismic monitoring in California, the mix of deep NHFN sites at near- and far- field sites and the high-sensitivity (high signal to noise), high-frequency broadband velocity and acceleration data recorded by the NHFN also contributes significantly to a variety of scientific objectives, including: a) investigating bridge responses to deep

strong ground motion signals from real earthquakes; b) obtaining a significantly lower detection threshold for microearthquakes and possible non-volcanic tremor signals in a noisy urban environment; c) increasing the resolution of the fault-zone seismic structure (e.g., in the vicinity of the Rodgers Creek/Hayward Fault step over); d) improving monitoring of spatial and temporal evolution of background and repeating seismicity (to magnitudes below  $M \sim 0.0$ ) to look for behavior indicating the nucleation of large, damaging earthquakes and to infer regions and rates of deep fault slip and slip deficit accumulation; e) investigating earthquake and fault scaling, mechanics, physics, and related fault processes; f) improving working models for the Hayward fault; and g) using these models to make source-specific response calculations for estimating strong ground shaking throughout the Bay Area.

Below, we focus primarily on activities associated with BSL operations of the NHFN component of the HFN.

### 3.2 NHFN Overview

The initial characterization period of HFN development ended in 1997. During that period, the NHFN sensors initially provided signals to on-site, stand-alone Quanterra Q730 and RefTek 72A-07 data loggers, and manual retrieval and download of data tapes was required. Also during the characterization period, the long-term monitoring phase of the project began, involving the gradual transition of backbone monitoring sites to 24-bit data acquisition and communication platforms with data telemetry to the BSL.

Over the years, Caltrans has provided additional support for the upgrade of some non-backbone sites to backbone operational status and for the addition of several entirely new sites into the monitoring backbone. Efforts at continued expansion are ongoing. In February of 2007, the stations of the mPBO project were also folded into the NHFN monitoring scheme, increasing the NHFN by five sites.

Of the 29 stations considered part of the NHFN history, nine (E17B, E07B, YBAB, W05B, SAFB, SM1B, DB1B, DB2B, DB3B) are non-backbone stations and were not originally envisioned as long-term monitoring stations. Because the borehole sensor packages at these sites could not be retrieved (having been grouted in downhole), the sites were mothballed for possible future reactivation. Support for reactivation of two of these mothballed sites (W05B and E07B) was eventually forthcoming and their reactivation is currently in progress, pending completion of the Bay Bridge retrofit. Efforts at acquiring funds for reactivation/upgrade of additional mothballed sites are ongoing.

Fifteen of the remaining 20 stations are currently op-

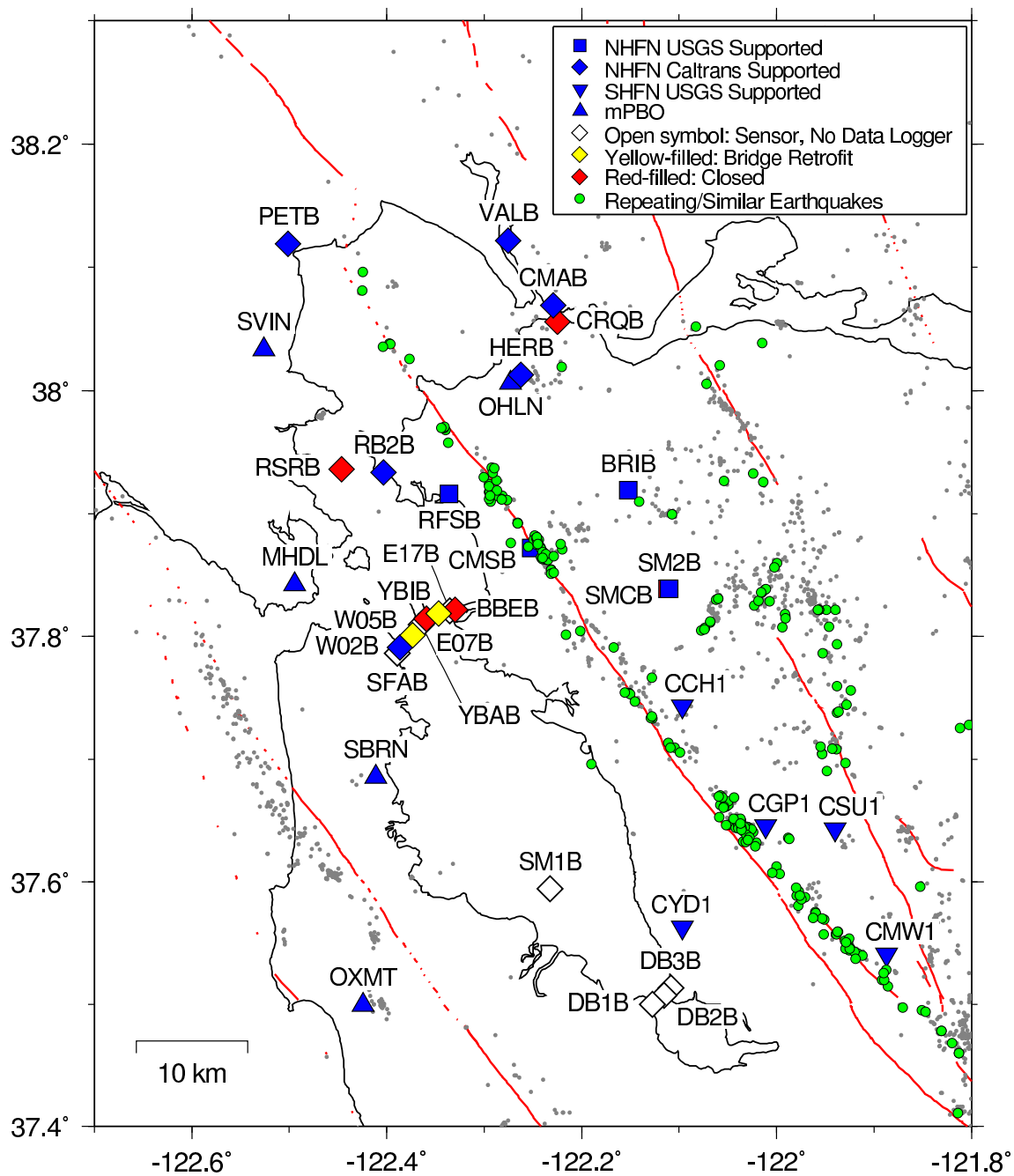


Figure 3.12: Map of HFN and mini-PBO stations. Diamonds are NHFN stations operated by the UC Berkeley Seismological Laboratory (BSL) with previous funding from Caltrans. Squares are BSL NHFN operated sites currently funded by the USGS. Inverted triangles are USGS SHFN sites. Triangles are former mini-PBO stations now part of the NHFN, operated by the BSL and funded by the USGS. Blue (black) are currently operational stations. Red (dark gray) are stations that recorded data in the past but are now closed, either due to replacement by higher quality installations (CRQB, SMCB) or due to complications and/or damage from earthquake retrofit activity on Bay Area bridges (RSRB, BBEB, YBIB). The color yellow represents sites whose installation is suspended pending completion of the Bay Bridge retrofit (W05B, E07B). Currently, station BBEB operates only as a telemetry repeater site due to damage from retrofit work. Other sites having downhole sensors but that are currently non-operational are represented as open symbols. These could potentially be brought on-line with funding support. Since 2007, the NHFN has been contributing arrival time picks to the Northern California Seismic System (NCSS) for location of Bay Area earthquakes. The small gray dots are double-difference relocations (*Waldhauser and Schaff, 2008*) that have made use of the NHFN picks. Green circles are locations of similar/repeating events occurring in the area (*Taka'aki Taira, personal communication*). Data for current and previously active NHFN and SHFN monitoring sites are all available through the NCEDC Web portal.

Sensor	Channel	Rate (sps)	Mode	FIR
Accelerometer	CL?	500.0	T	Ca
Accelerometer	CN?	500.0	T	Ca
Accelerometer	HL?	200.0	C	Ca
Accelerometer	HL?	100.0	C	Ca
Accelerometer	HN?	200.0	C	Ca
Accelerometer	BL?	20.0	C	Ac
Accelerometer	BN?	20.0	C	Ac
Accelerometer	LL?	1.0	C	Ac
Accelerometer	LN?	1.0	C	Ac
Geophone	DP?	500.0	T,C	Ca
Geophone	EP?	200.0	C	Ca
Geophone	EP?	100.0	C	Ca
Geophone	BP?	20.0	C	Ac
Geophone	SP?	20.0	C	Ac
Geophone	LP?	1.0	C	Ac

Table 3.7: Typical data streams acquired at NHFN sites, with channel name, sampling rate, sampling mode, and FIR filter type. C indicates continuous, T triggered, Ca causal, and Ac acausal. Typically, the DP1 continuous channel is archived and the remaining high sample rate data (i.e., CL?, CN?, DP2 and DP3 channels) are archived as triggered snippets. As telemetry options improve, progress is being made towards archiving higher sample rate and continuous data on more channels. Prior to September 2004, only triggered data was archived for all high sample rate channels. Of the stations that are currently operational, CMAB, HERB, BRIB, RFSB, CMSB, SM2B, W02B, and RB2B record at maximum sample rates of 500 Hz; VALB and PETB at maximum 200 Hz; and mPBO sites (SVIN, OHLN, MHDL, SBRN, OXMT) at maximum 100 Hz.

erational (VALB, PETB, CMAB, HERB, BRIB, RFSB, CMSB, SM2B, W02B, RB2B, SVIN, OHLN, MHDL, SBRN, OXMT), though operation of one of the sites (CMSB) has been temporarily suspended pending completion of construction at U.C. Berkeley’s Cal Memorial Stadium, and landowner construction at the OHLN site has temporarily disrupted operation at that site. These 15 sites include the five stations folded in from the mPBO project. They telemeter seismic data streams continuously into the BSL’s BDSN processing stream with subsequent archival in the Northern California Earthquake Data Center (NCEDC).

The five remaining stations have been decommissioned for various reasons ranging from the sites’ replacement with nearby higher quality installations (SMCB, CRQB) to irreparable site damage by outside influences such as bridge retrofit activity and construction (BBEB, YBIB, RSRB). Station BBEB, however, continues to operate as a telemetry relay site.

*Installation/Instrumentation:* The NHFN Sensor

packages are generally installed at depths ranging between 100 and 200 m, the non-backbone, non-operational Dumbarton Bridge sites being exceptions with sensors at multiple depths (Table 3.5).

The five former mPBO sites that are now part of the NHFN have 3-component borehole geophone packages. Velocity measurements for the mPBO sites are provided by Mark Products L-22 2 Hz geophones (Table 3.6). All the remaining backbone and non-backbone NHFN sites have six-component borehole sensor packages. The six-component packages were designed and fabricated at LBNL’s Geophysical Measurement Facility and have three channels of acceleration, provided by Wilcoxon 731A piezoelectric accelerometers, and three channels of velocity, provided by Oyo HS-1 4.5 Hz geophones.

The 0.1-400 Hz Wilcoxon accelerometers have lower self-noise than the geophones above about 25-30 Hz, and remain on scale and linear to 0.5 g. In tests performed in the Byerly vault at UC Berkeley, the Wilcoxon is considerably quieter than the FBA-23 at all periods, and is almost as quiet as the STS-2 between 1 and 50 Hz.

Currently six of the currently operational NHFN backbone sites have Quanterra data loggers, and nine of the operational sites have been upgraded with BASALT data loggers this year. All 15 of these sites telemeter continuously to the BSL, with the exception of CMSB which is temporarily off-line. Signals from these stations are digitized at a variety of data rates up to 500 Hz at 24-bit resolution (Table 3.7). The data loggers employ causal FIR filters at high data rates and acausal FIR filters at lower data rates (see: Table 3.5).

*Data Rates and Channels:* Because of limitations in telemetry bandwidth and local disk storage, 7 of the 10 (excluding CMAB, VALB and PETB) six-component NHFN stations transmit maximum 500 Hz data continuously on only 1 channel of geophone data (i.e., when operational, their vertical geophone channel). Triggered 500 Hz data for 3 additional channels with 180 second snippets are also transmitted. Station VALB also transmits data from only four channels; however, continuous data for all four channels are transmitted at a maximum of 200 Hz sampling. PETB transmits maximum 200 Hz data continuously on all six channels (three geophone, three accelerometer), and CMAB transmits maximum 500 Hz data continuously on all six channels. Continuous data for the channels of all 10 of these stations are also transmitted to the BSL at reduced sampling rates (20 and 1 sps). A Murdock, Hutt, and Halbert (MHH) event detection algorithm (Murdock and Hutt, 1983) is operated independently at each station on 500 sps data for trigger determinations. Because the accelerometer data is generally quieter, the

MHH detections are made locally using data from the Wilcoxon accelerometers when possible. However, there is a tendency for these powered sensors to fail, and, in such cases, geophone channels are substituted for the failed accelerometers. The five mPBO-originated sites all transmit their three-component continuous geophone data streams to the BSL at 100, 20, and 1 sps.

*Integration with the NCSS, SeisNetWatch, and SeismicQuery:* The NHFN is primarily a research network that complements regional surface networks by providing downhole recordings of very low amplitude seismic signals (e.g., from micro-earthquakes or non-volcanic tremor) at high gain, to high frequencies and with low noise. In addition, data streams from the NHFN are also integrated into the Northern California Seismic System (NCSS) real-time/automated processing stream for response applications and collection of basic data for long-term hazards mitigation. The NCSS is a joint USGS (Menlo Park) and Berkeley Seismological Laboratory (BSL) entity with earthquake reporting responsibility for Northern California, and data from networks operated by both institutions are processed jointly to fulfill this responsibility.

Through this integration, the NHFN picks, waveforms, and NCSS event locations and magnitudes are automatically entered into a database where they are immediately available to the public through the NCEDC and its DART (Data Available in Real Time) buffer. The capability for monitoring state of health information for all NHFN stations using SeisNetWatch also exists, and up-to-date dataless SEED formatted metadata is made available through the NCEDC with the SeismicQuery software tool.

### Station Maintenance

Identifying network maintenance issues involves, in part, automated and semi-automated tracking of power, telemetry and data gaps. In addition, regular inspection of the seismic waveforms and spectra are carried out on samples of background noise and of significant local, regional and teleseismic earthquakes. These efforts are carried out to identify problems that can result from a variety of operational issues including changes in background noise levels from anthropogenic sources; ground loops; failing, damaged or stolen instrumentation; and power and telemetry issues. Troubleshooting and remediation of such problems are carried out through a coordinated effort between data analysts and field engineers.

In addition to routine maintenance and trouble shooting efforts, performance enhancement measures are also carried out. For example, when a new station is added to the NHFN backbone, extensive testing and correction for sources of instrumental noise (e.g., grounding related issues) and telemetry through-put are carried out to op-

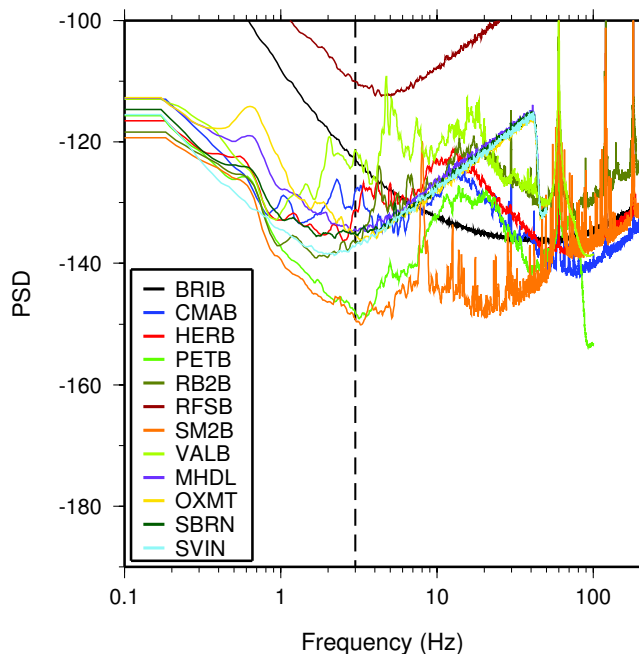


Figure 3.13: Plot showing typically observed background noise PSD for the vertical DP1/EP1 channels of the NHFN borehole stations as a function of frequency. The data are for a 1000 sec period on January 1, 2012 beginning at 01:00 (AM) local time. The PSD ranking (lowest to highest) of the non-mPBO stations (top panel) in operation at the time given at 3 Hz (near minimum PSD for most NHFN stations) is:

SM2B.BK.DP1 -149.943  
 PETB.BK.EP1 -148.286  
 RB2B.BK.DP1 -135.750  
 HERB.BK.DP1 -130.458  
 CMAB.BK.DP1 -127.173  
 BRIB.BK.DP1 -122.272  
 VALB.BK.EP1 -119.649  
 RFSB.BK.DP1 -108.857

PSD ranking (lowest to highest) for the EP1 channels of the 4 mPBO stations (lower panel) at the time given at 3 Hz) is:

SVIN.BK.EP1 -137.397  
 OXMT.BK.EP1 -135.051  
 SBRN.BK.EP1 -134.725  
 MHDL.BK.EP1 -133.816

Note that there is considerable variation in the general level and structure of the individual station background noise PSD estimates. For example the signals from many of the non-mPBO stations have 60 Hz noise (sometimes accompanied by 120 and 180 Hz harmonics), which is indicative of the presence of ground loops that need to be addressed. If noise spikes at the mPBO stations exist, they are not recorded due to the lower sampling rate of these data. Variations in PSD noise among the stations are also sometimes attributable to the stations' proximity to different cultural noise sources such as freeways or train-tracks, differences in depth of sensor installation, or to differences in local geologic conditions.

optimize the sensitivity of the station. Examples of maintenance and enhancement measures that are typically performed include: 1) testing of radio links to ascertain reasons for unusually large numbers of dropped packets; 2)

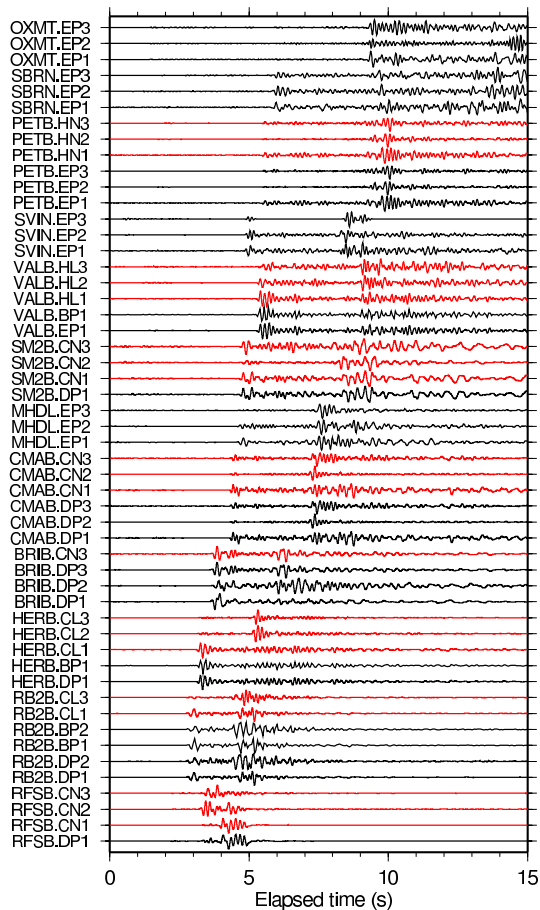


Figure 3.14: Plot of ground accelerations recorded on the geophones (black traces) and accelerometers (red/gray traces) of the 12 NHFN borehole stations in operation at the time of a recent Bay Area earthquake (5 March 2012,  $M_w$  4.0 near El Cerrito, CA). The traces are filtered with a 1-8 Hz bandpass filter, scaled by their maximum values, and ordered from bottom to top by distance from the epicenter.

troubleshooting sporadic problems with excessive telemetry dropouts; 3) manual power recycle and testing of hung data loggers; 4) replacing blown fuses or other problems relating to dead channels identified through remote monitoring at the BSL; 5) repairing telemetry and power supply problems when they arise; and 6) correcting problems that arise due to various causes, such as weather or cultural activity.

#### Quality Control

*Power Spectral Density Analyses:* One commonly used quality check on the performance of the borehole installed network includes assessment of the power spectral density (PSD) distributions of background noise. Figure 3.13 shows PSDs of background noise for vertical geophone components of the 12 NHFN stations operating at the time.

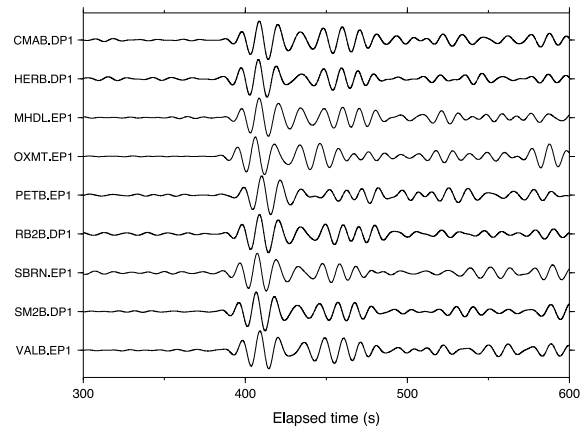


Figure 3.15: Plot of P-wave seismograms of the teleseismic  $M_w$  7.4 earthquake in Oaxaca, Mexico (Lat.: 16.662N; Lon.: 98.188W; depth 20 km) occurring on March 20, 2012 18:02:48 (UTC) recorded on the DP1/EP1 (vertical) channels of the 9 NHFN borehole stations. Data from BRIB, RFSB, and SVIN were not shown because of their lower signal-to-noise ratios. Here, vertical component geophone (velocity) data have been 0.07-0.12 Hz bandpass filtered and normalized by the maximum amplitude for each trace.

By periodically generating such plots, we can rapidly evaluate the network's recording of seismic signals across the wide high-frequency spectrum of the borehole NHFN sensors. Changes in the responses often indicate problems with the power, telemetry, or acquisition systems or with changing conditions in the vicinity of station installations that are adversely affecting the quality of the recorded seismograms. In general, background noise levels of the borehole NHFN stations are more variable and generally higher than those of the Parkfield HRSN borehole stations (see Parkfield Borehole Network section). This is due in large part to the significantly greater cultural noise in the Bay Area and the siting of several near-field NHFN sites in proximity to Bay Area bridges.

On average, the mPBO component of the NHFN sites (MHDLEP, OXMT, SBRN, SVIN in Figure 3.13) are more consistent with each other and throughout their spectral range. This is due in large part to the greater average depth of the mPBO sensors, the locations of mPBO stations in regions with generally less industrial and other cultural noise sources, and possibly to the absence of powered sensors (i.e. accelerometers) in their borehole sensor packages. The maximum sampling rate of 100 sps at these sites also limits their spectral range to a maximum of 40 Hz, below 60 Hz where power-line noise often becomes a problem.

One of the most pervasive problems at the other NHFN stations with higher sampling rates is power line noise (60 Hz and its harmonics at 120 and 180 Hz). See, for example the PSD spectrum of stations PETB, RB2B, and SM2B in Figure 3.13). This noise reduces the sensitivity of the MHH detectors and can corrupt research based on full waveform analyses. When NHFN stations are visited,

the engineer at the site and a seismologist at the BSL frequently work together to identify and correct ground-loop and inductive-coupling problems, which often at the root of this contamination.

*Real Event Displays:* Another method for rapid assessment of network performance is to generate and evaluate the seismograms from moderate local and large teleseismic earthquakes recorded by the NHFN stations. This is an essential component of NHFN operations because the seismic data from local, regional, and teleseismic events is telemetered directly to the BSL and made available to the Northern California Seismic System (NCSS) real-time/automated processing stream for seismic response applications within a few seconds of being recorded by the NHFN.

Shown in Figure 3.14 is an example display of NHFN geophone and accelerometer channels for a recent local Bay Area earthquake (5 March 2012,  $M_w$  4.0 near El Cerrito, CA). It is apparent from this simple display that in general both the velocity and accelerometer channels are operating correctly, though the EP3 channel from station SVIN shows a sensitivity issues that will need to be addresses. Not shown are station W02B recordings that showed no identifiable earthquake signal. The data logger at this station is known to be faulty, and the site is slated for a new BASALT data logger. Stations CMSB and OHLN were off-line at the time, due to landowner construction at those locations.

Figure 3.15 shows seismograms of the recent teleseismic  $M_w$  7.4 earthquake in Oaxaca, Mexico (Lat.: 16.662N; Lon.: 98.188W; depth 20 km) occurring on March 20, 2012 18:02:48 (UTC) On this date and for this frequency band (0.07-0.12 Hz), network performance appears good for the vertical (DP1 and EP1) channels for 9 of the stations in operation at the time.

Owing to their near similar source-receiver paths, signals from teleseismic events also serve as a good source for examining the relative polarities and responses of the BK borehole network station/components to seismic ground motion, after correction for differences in instrument response among the stations. By rapidly generating such plots (particularly with correction for instrument response) following large teleseismic events, quick assessment of the NHFN seismometer responses and polarities to real events is easily done and, if needed, corrective measures implemented with relatively little delay.

In Figure 3.15, data from BRIB, RFSB, and SVIN were not shown because of the low signal-to-noise ratios on their vertical components for this event. Stations CMSB, OHLN and W02B are also not shown because they did not record the event for reasons cited above. Both Figures 3.14 and 3.15 serve to illustrate the value of routine evaluation of both local (higher frequency) and teleseismic (lower frequency) events when monitoring the state of health of the NHFN.

### 3.3 2011-2012 Activities

As in every year, routine maintenance, operations, quality control, and data collection play an important part in our activities. In addition, last year, we received funds and government furnished equipment (GFE) data loggers from an American Recovery and Reinvestment Act award through the USGS to update equipment and improve station infrastructure. This year efforts at evaluating and optimizing station performance at the updated sites were carried out.

Other NHFN project activities have included: a) Specific station issues; b) efforts to obtain additional funds for future upgrade and expansion of the network; and c) leveraging NHFN activities through partnerships with various institutions outside of BSL

#### Specific Station issues

*BRIB.* This year borehole recordings from station BRIB have been showing significant degradation. As with most NHFN sites, the BRIB installation is a complex integration of telemetry, power, recording, and sensor instrumentation. The BRIB station is particularly complex in that it collects coincident multi-component surface, borehole, broadband, short-period velocity and accelerometer data. Hence, the problem at the root of the degradation was difficult to identify. After considerable collaborative efforts between analysts and field engineers it was determined that the problem related to the power system at the site. Which aspect of this system is responsible and corrective actions to be taken are still being worked out at this time.

*OHLN.* The dense Bay Area population requires that most NHFN stations be cited on developed land, and permission to use the sites is at the discretion of generous private or public landowners. Consequently, landowner development of their properties sometimes requires temporary cessation and modifications to our station installations to accommodate both the landowners and our needs. This has been the case for station OHLN this year, with OHLN being off-line for several months. Landowner construction at the site has now been completed and adaptive modifications of supply of power to OHLN are currently underway. We expect OHLN to be back on-line within a few weeks.

*W02B.* This site has experienced what appears to be a failure in the data acquisition system. The site is located on the western span of the Bay Bridge and access to the site is limited, requiring travel on Caltrans boats. Due to the absence of maintenance support for this previously Caltrans supported site, the station has also been neglected. We are now attempting to contact Caltrans to gain access, and plans are to carry out the long overdue general maintenance of the site and to install a new BASALT data logger there.

## Additional Funding

Operation of this Bay Area borehole network is funded by the Advanced National Seismic System (ANSS) and through a partnership with the California Department of Transportation (Caltrans). ANSS provides operations and maintenance (O&M) support for a fixed subset of nine operational stations that were initiated as part of previous projects in which the USGS was a participant. Caltrans has in the past provided support for development and O&M for the remaining stations that have been added to the network through Caltrans partnership grants. Caltrans has also provided additional support for upgrade and expansion when possible.

Due to the state budget crisis, Caltrans has been reviewing and modifying its financial commitments and its accounting practices relating to its funding of external projects, such as the NHFN project. Over the past two years, this has severely complicated efforts to receive previously approved NHFN funding from Caltrans, and has imposed many additional administrative road-blocks to acquiring additional Caltrans support. In June of 2010, our team held two meetings at Berkeley with our Caltrans contact and made a presentation at Caltrans in Sacramento to argue against O&M funding reductions and for further upgrade and expansion of the NHFN. These efforts resulted in a request by Caltrans for a proposal to install surface instruments at up to six of our borehole installations and to reactivate three currently mothballed NHFN sites. We submitted our proposal in September of 2010. Subsequently, a reduction in the Caltrans budget for external support resulted in a request from Caltrans for us to reduce the scope of the proposal we submitted. We promptly responded to this request and tentative approval was promised. Funding was held up for over a year however, by bureaucratic concerns and issues of proprietary rights. Haggling over these issues between the University of California (reaching as high as the UC Office of the President) and Caltrans over propriety rights has continued. At this time, these roadblocks have brought progress to a standstill, and, though we remain hopeful, formal approval for the proposed project is in doubt.

These delays have put on hold much of our work at maintaining, improving and expanding the Caltrans supported component of the NHFN, so that progress in this area this year has been limited. For the time being, we continue to maintain the previously Caltrans supported stations w/o external support, though at a greatly reduced effort. This is resulting in significantly longer down-time for failed stations and significantly degraded data from several of those stations in need of attention. Eventually, if future support is not forthcoming, these sites will need to be closed.

## Partnerships

The NHFN is heavily leveraged through partnerships with various institutions, and we have continued to nurture and expand these relationships. Over the past year, we have continued our collaborative partnerships with the USGS, St. Mary's College, and the Cal Maritime Academy, and we have continued to strive for ongoing collaboration with Caltrans. In addition, we and the BSL more generally have continued to coordinate with Lawrence Berkeley National Laboratory (LBNL) in their project to develop an LBNL array of borehole stations that provide complementary coverage to the NHFN.

## 3.4 Acknowledgments

Thomas V. McEvilly, who passed away in February 2002, was instrumental in developing the Hayward Fault Network, and, without his dedication and hard work, the creation and continued operation of the NHFN would not have been possible.

Under Robert Nadeau's and Doug Dreger's general supervision, Peggy Hellweg, Doug Neuhauser, Taka'aki Taira, and the engineering team (Bill Karavas, John Friday, Aaron Enright, and Joshua Miller) all contribute to the operation of the NHFN. Robert Nadeau and Taka'aki Taira prepared this NHFN operations section of the BSL Annual Report.

Support for the NHFN this year was provided by the USGS through the cooperative networks grant program (grant number G10AC00093). Over the years, Pat Hipley of Caltrans has been instrumental in the effort to continue to upgrade and expand the network. Larry Hutchings and William Foxall of LLNL have also been important collaborators on the project in past years.

## 3.5 References

- Rodgers, P.W., A.J. Martin, M.C. Robertson, M.M. Hsu, and D.B. Harris, Signal-Coil Calibration of Electromagnetic Seismometers, *Bull. Seism. Soc. Am.*, 85(3), 845-850, 1995.
- Murdock, J. and C. Hutt, A new event detector designed for the Seismic Research Observatories, *USGS Open-File-Report 83-0785*, 39 pages, 1983.
- Waldhauser, F. and D.P. Schaff, Large-scale relocation of two decades of Northern California seismicity using cross-correlation and double-difference methods, *J. Geophys. Res.*, 113, B08311, doi:10.1029/2007JB005479, 2008.

Code	Net	Latitude	Longitude	Elev (m)	Over (m)	Date	Location
VALB	BK	38.12150	-122.27530	-24.5	155.8	2005/11 - current	Napa River Bridge
PETB	BK	38.11890	-122.50110	-30.0	113.0	2010/09 - current	Petaluma River Bridge
CMAB	BK	38.06892	-122.22914	0.0	142.2	2009/12 - current	Cal Maritime Academy
CRQB	BK	38.05578	-122.22487	-25.0	38.4	1996/07 - 2010/05	CB
HERB	BK	38.01239	-122.26217	-18.0	217.0	2001/09 - current	Hercules
BRIB	BK	37.91886	-122.15179	222.2	108.8	1995/07 - current	BR, Orinda
RFSB	BK	37.91608	-122.33610	-27.3	91.4	1996/02 - current	RFS, Richmond
CMSB	BK	37.87195	-122.25168	94.7	167.6	1995/06 - current	CMS, Berkeley
SMCB	BK	37.83881	-122.11159	180.9	3.4	1998/02 - 2007/06	SMC, Moraga
SM2B	BK	37.83874	-122.11022	200.0	150.9	2007/06 - current	SMC, Moraga
SVIN	BK	38.03318	-122.52632	-27.5	152.4	2003/08 - current	mPBO, St. Vincent's school
OHLN	BK	38.00625	-122.27299	-0.5	196.7	2001/11 - current	mPBO, Ohlone Park
MHDL	BK	37.84232	-122.49431	94.5	151.9	2006/05 - current	mPBO, Marin Headlands
SBRN	BK	37.68561	-122.41127	4.0	161.5	2002/08 - current	mPBO, San Bruno Mtn.
OXMT	BK	37.49936	-122.42431	209.1	194.3	2003/12 - current	mPBO, Ox Mtn.
BBEB	BK	37.82160	-122.32975	-30.8	182.9	2002/09 - 2007/11	BB, Pier E23
E17B	BK	37.82086	-122.33534	TBD	160.0	1995/08 - unknown *	BB, Pier E17
E07B	BK	37.81847	-122.34688	TBD	134.0	1996/02 - unknown +	BB, Pier E7
YBIB	BK	37.81420	-122.35923	-27.0	61.0	1996/07 - 2000/08	BB, Pier E2
YBAB	BK	37.80940	-122.36450	TBD	3.0	1998/06 - unknown *	BB, YB Anchorage
W05B	BK	37.80100	-122.37370	TBD	36.3	1997/10 - unknown +	BB, Pier W5
W02B	BK	37.79112	-122.38632	-45.0	57.6	2003/06 - current	BB, Pier W2
SFAB	BK	37.78610	-122.38930	TBD	0.0	1998/06 - unknown *	BB, SF Anchorage
RSRB	BK	37.93575	-122.44648	-48.0	109.0	1997/06 - 2001/04	RSRB, Pier 34
RB2B	BK	37.93335	-122.40314	-18.0	133.5	2009/12 - current	RSRB, Pier 58
SM1B	BK	37.59403	-122.23242	TBD	298.0	not recorded *	SMB, Pier 343
DB3B	BK	37.51295	-122.10857	TBD	1.5	1994/09 - 1994/11 *	DB, Pier 44
					62.5	1994/09 - 1994/09 *	
					157.9	1994/07 - unknown *	
DB2B	BK	37.50687	-122.11566	TBD		1994/07 - unknown *	DB, Pier 27
					189.2	1992/07 - 1992/11 *	
DB1B	BK	37.49947	-122.12755	TBD	0.0	1994/07 - 1994/09 *	DB, Pier 1
					1.5	1994/09 - 1994/09 *	
					71.6	1994/09 - 1994/09 *	
					228.0	1993/08 - unknown *	
CCH1	NC	37.74332	-122.09657	345.0	119.0	1995/06 - current	Chabot
CGP1	NC	37.64545	-122.01128	461.0	121.0	1995/06 - current	Garin Park
CSU1	NC	37.64303	-121.94020	623.0	124.0	1995/11 - current	Sunol
CYD1	NC	37.56289	-122.09670	114.0	137.0	1996/11 - current	Coyote
CMW1	NC	37.54053	-121.88743	498.0	155.0	1995/06 - current	Mill Creek

Table 3.5: Stations of the Hayward Fault Network. Station code, network id, location, period of available data, and site description are included. For entries with “\*” and “+” in the date column, no monitoring data is available. For these sites, dates are periods when data was downloaded manually. These manually retrieved data are not available at the NCEDC, but may be available from Larry Hutchings (now at LBNL). Latitude and longitude (in degrees) are in WGS84 reference frame. Well head elevation (in meters) is relative to the WGS84 reference ellipsoid. Overburden (depth of sensor package below surface) is in meters. Abbreviations: TBD - to be determined; BB - Bay Bridge; BR - Briones Reserve; CMS - Cal Memorial Stadium; CB - Carquinez Bridge; DB - Dumbarton Bridge; mPBO - Mini-Plate Boundary Observatory; RFS - Richmond Field Station; RSRB - Richmond-San Rafael Bridge; SF - San Francisco; SMB - San Mateo Bridge; SMC - St. Mary's College; and YB - Yerba Buena. At the end of the initial characterization phase of the HFN project, the stations labeled with “\*” were mothballed with borehole sensors remaining cemented in place. Incorporation of the “+” stations into the monitoring backbone is work in progress. Proposal to Caltrans requesting support to bring more mothballed sites into the NHFN backbone is pending. Due to damage from Bay Bridge retrofit work, station BBEB no longer records seismic data but continues to operate as a telemetry relay station. Data collection at site CMSB has also been suspended temporarily to accommodate construction at Cal Memorial Stadium on the UC Berkeley campus. At OHLN, temporary suspension of data collection also occurred to accommodate landowner construction.

Site	Geophone	Accelerometer	Z	H1	H2	data logger	Notes	Telem.
VALB	Oyo HS-1	Wilcoxon 731A	-90	336	246	Q330		FR
PETB	Oyo HS-1	Wilcoxon 731A	-90	TBD	TBD	Q330		FR/Rad.
CMAB	Oyo HS-1	Wilcoxon 731A	-90	161	251	BASALT		Rad./VPN
CRQB	Oyo HS-1	Wilcoxon 731A	-90	68	338	None at Present		FR
HERB	Oyo HS-1	Wilcoxon 731A	-90	160	70	Q4120		FR
BRIB	Oyo HS-1	Wilcoxon 731A	-90	79	169	BASALT	Acc. failed, Dilat.	FR
RFSB	Oyo HS-1	Wilcoxon 731A	-90	346	256	BASALT		FR
CMSB	Oyo HS-1	Wilcoxon 731A	-90	19	109	Q4120		FR
SMCB	Oyo HS-1	Wilcoxon 731A	-90	76	166	None at present	Posthole	FR
SM2B	Oyo HS-1	Wilcoxon 731A	-90	TBD	TBD	BASALT		FR
SVIN	Mark L-22		-90	319	49	BASALT	Tensor.	FR/Rad.
OHLN	Mark L-22		-90	300	30	BASALT	Tensor.	FR
MHDL	Mark L-22		-90	64	154	BASALT	Tensor.	FR
SBRN	Mark L-22		-90	6	96	BASALT	Tensor.	FR
OXMT	Mark L-22		-90	120	210	BASALT	Tensor.	FR
BBEB	Oyo HS-1	Wilcoxon 731A	-90	19	109	None at present	Acc. failed	Radio
E17B	Oyo HS-1	Wilcoxon 731A	-90	TBD	TBD	None at present		
E07B	Oyo HS-1	Wilcoxon 731A	-90	TBD	TBD	None at present		
YBIB	Oyo HS-1	Wilcoxon 731A	-90	257	347	None at present	Z geop. failed	FR/Rad.
YBAB	Oyo HS-1	Wilcoxon 731A	-90	TBD	TBD	None at present		
W05B	Oyo HS-1	Wilcoxon 731A	-90	TBD	TBD	None at present		
W02B	Oyo HS-1	Wilcoxon 731A	-90	TBD	TBD	Q4120		Radio
SFAB	None	LLNL S-6000	TBD	TBD	TBD	None at present	Posthole	
RSRB	Oyo HS-1	Wilcoxon 731A	-90	50	140	None at present	2 acc. failed	FR
RB2B	Oyo HS-1	Wilcoxon 731A	-90	252	162	Q4120	1 acc. failed	FR
SM1B	Oyo HS-1	Wilcoxon 731A	-90	TBD	TBD	None at present		
DB3B	Oyo HS-1	Wilcoxon 731A	-90	TBD	TBD	None at present	Acc. failed	
DB2B	Oyo HS-1	Wilcoxon 731A	-90	TBD	TBD	None at present		
DB1B	Oyo HS-1	Wilcoxon 731A	-90	TBD	TBD	None at present	Acc. failed	
CCH1	Oyo HS-1	Wilcoxon 731A	-90	TBD	TBD	Nanometrics HRD24	Dilat.	Radio
CGP1	Oyo HS-1	Wilcoxon 731A	-90	TBD	TBD	Nanometrics HRD24	Dilat.	Radio
CSU1	Oyo HS-1	Wilcoxon 731A	-90	TBD	TBD	Nanometrics HRD24	Dilat.	Radio
CYD1	Oyo HS-1	Wilcoxon 731A	-90	TBD	TBD	Nanometrics HRD24	Dilat.	Radio
CMW1	Oyo HS-1	Wilcoxon 731A	-90	TBD	TBD	Nanometrics HRD24	Dilat.	Radio

Table 3.6: Instrumentation of the HFN as of 06/30/2011. Every HFN downhole package consists of collocated 3-component geophones and accelerometers, with the exception of mPBO sites which have only 3-component geophones and are also collecting tensor strainmeter data. Six HFN sites (five of the SHFN and one of the NHFN) also have dilatometers (Dilat.). The five SHFN sites have Nanometrics data loggers with radio telemetry to the USGS and eventually from there to the NCEDC for archiving. Currently, six NHFN sites have Quanterra data loggers, eight have been upgraded with ARRA funding and one (CMAB) with Caltrans funding to BASALT data loggers with local storage capacity. Of these 15 sites, 14 are currently telemetering continuous data to the BSL for archiving at the NCEDC, and 1 site (CMSB) is temporarily shutdown due to construction at the Cal Memorial stadium on the U.C. Berkeley Campus. Five additional backbone sites have been decommissioned for reasons ranging from the sites' replacement with nearby higher quality installations (SMCB, CRQB) to irreparable site damage by outside influences such as bridge retrofit activity and construction (BBEB, YBIB, RSRB). Station BBEB, however, continues to operate as a telemetry relay site. The component orientation of the sensors (vertical (Z): -90  $\Rightarrow$  positive counts up; horizontals (H1 and H2): azimuthal direction of positive counts in degrees clockwise from north) are given when known or labeled as TBD if they are yet to be determined. VPN is Virtual Private Network.

## 4 Parkfield Borehole Network (HRSN)

### 4.1 Introduction

The operation of the High Resolution Seismic Network (HRSN) at Parkfield, California began in 1987, as part of the United States Geological Survey (USGS) initiative known as the Parkfield Prediction Experiment (PPE) (*Bakun and Lindh, 1985*).

Figure 3.16 shows the location of the network, its relationship to the San Andreas fault, sites of significance from previous and ongoing experiments using the HRSN, clusters of repeating earthquakes being monitored by the network, nonvolcanic tremors recorded by the network and located using a joint station-pair double-difference tomography method (*Zhang et al., 2012*), and the epicenters of the 1966 and 2004 M6 earthquakes that motivated much of the research. The HRSN has recorded exceptionally high-quality data, owing to its 13 closely-spaced three-component borehole sensors (generally emplaced in the extremely low attenuation and background noise environment at 200 to 300 m depth [Table 3.8], its high-frequency, wide bandwidth recordings (0-100 Hz; 250 sps), and its sensitivity to very low amplitude seismic signals (e.g., recording signals from micro-earthquakes and non-volcanic tremors with equivalent magnitudes below 0.0  $M_L$ ).

Several aspects of the Parkfield region make it ideal for the study of small earthquakes and nonvolcanic tremors and their relationship to tectonic processes and large earthquakes. These include the fact that the network spans the SAFOD (San Andreas Fault Observatory at Depth) experimental zone, the nucleation region of earlier repeating magnitude 6 events and a significant portion of the transition from locked to creeping behavior on the San Andreas fault; the availability of three-dimensional P and S velocity models (*Michellini and McEvilly, 1991; Thurber et al., 2006*); a long-term HRSN seismicity catalog (complete to very low magnitudes and that includes over half of the M6 seismic cycle); a well-defined and relatively simple fault segment; the existence of deep nonvolcanic tremor (NVT) activity; and a relatively homogeneous mode of seismic energy release as indicated by the earthquake source mechanisms (over 90% right-lateral strike-slip).

In recent years, these features have also spurred additional investment in seismic instrumentation in the area that greatly enhances the HRSNs utility, including the ongoing installation of the TremorScope array (funded by the Moore foundation) and NFS's EarthScope SAFOD and PBO stations.

In a series of journal articles and Ph.D. theses, the cumulative, often unexpected, results of research by UC Berkeley and others using HRSN data trace the evolu-

tion of a new and exciting picture of the San Andreas fault zone, and they are forcing new thinking on the dynamic processes and conditions both within the seismogenic (upper  $\sim 15$  km) and sub-seismogenic depths ( $\sim 15$ -35 km), where recently discovered nonvolcanic tremors are occurring (*Nadeau and Dolenc, 2005*).

Parkfield has also become the focus of a major component of NSF's EarthScope (<http://www.earthscope.org>) project, known as the San Andreas Fault Observatory at Depth (SAFOD) (<http://www.earthscope.org/observatories/safod>). The SAFOD project is a comprehensive effort whose objectives include drilling into the hypocentral zone of repeating M  $\sim 2$  earthquakes on the San Andreas Fault at a depth of about 3 km and establishing a multi-stage geophysical observatory in the immediate proximity of these events. The purpose of such an observatory is to carry out a comprehensive suite of down-hole measurements in order to study the physical and chemical conditions under which earthquakes nucleate and rupture (*Hickman et al., 2004*). In these efforts, the HRSN plays a vital support role by recording seismic data used to directly constrain seismic signals recorded in the SAFOD main hole and by recording seismic events in the surrounding region to provide information on the larger scale fault zone processes that give rise to any changes observed in the main hole.

### 4.2 HRSN Overview

Installation of the HRSN deep (200-300 m) borehole sensors initiated in late 1986, and recording of triggered 500 sps earthquake data began in 1987. The HRSN sensors are 3-component geophones in a mutually orthogonal gimbaled package. This ensures that the sensor corresponding to channel DP1 is aligned vertically and that the others are aligned horizontally. The sensors are also cemented permanently in place, ensuring maximum repeatability of the sensors' responses to identical sources, and allowing for precise relative measurements with minimal need for corrections and assumptions associated with moving the sensors. Originally a 10 station network, fully operational by January 1988, the HRSN was expanded to 13 borehole stations in late July 2001, and the original recording systems (see previous Berkeley Seismological Laboratory [BSL] Annual Reports) were upgraded to 24 bit acquisition (Quanterra 730s) and 56K frame relay telemetry to UCB. As part of funding from the American Recovery and Reinvestment Act (ARRA), an additional replacement/upgrade of the Quanterra 730 acquisition systems to 24-bit BASALT acquisition systems is underway in 2010-2011 that is allowing for local site storage and later retrieval of data during periods of spo-

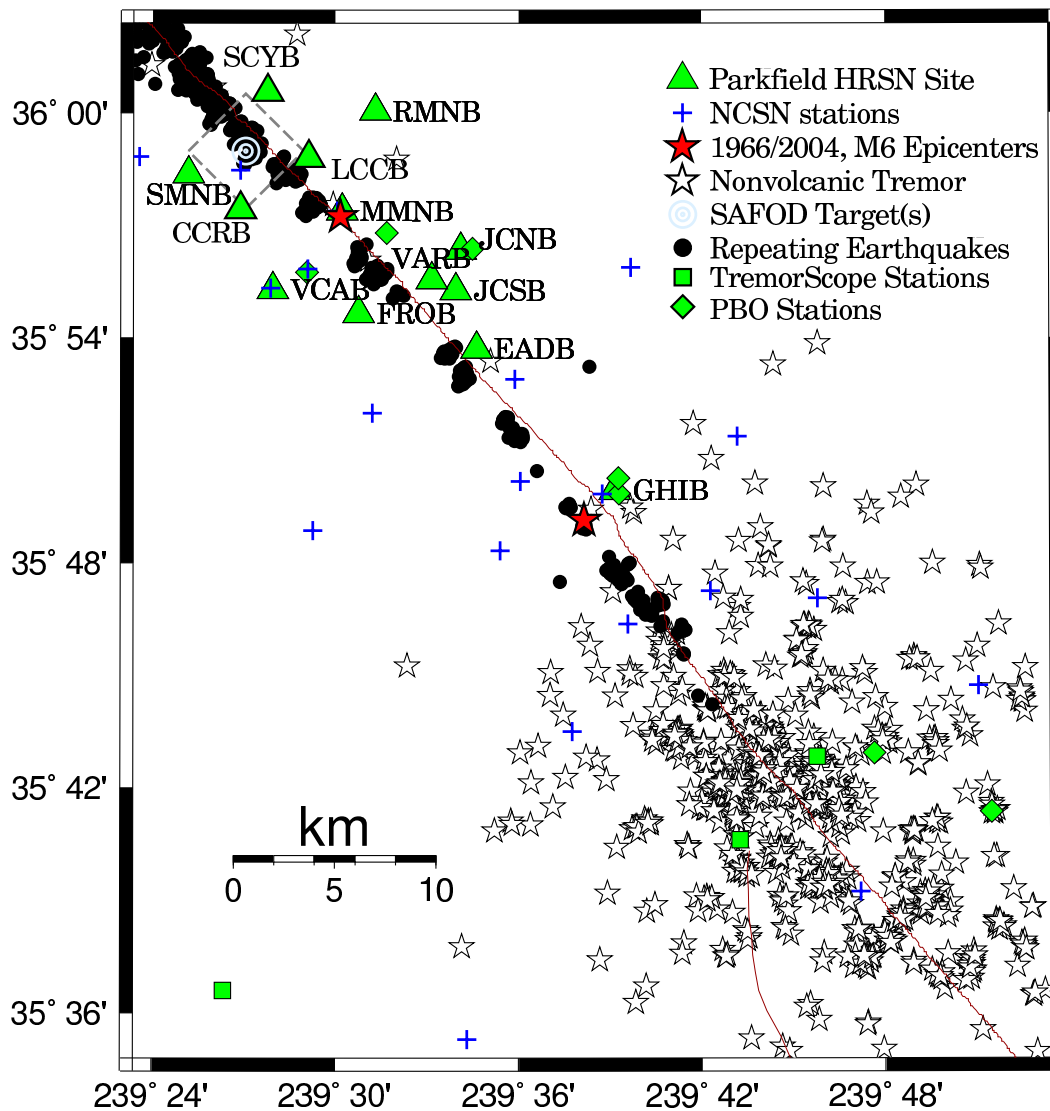


Figure 3.16: Map showing the San Andreas Fault trace and locations of the 13 Parkfield HRSN stations, the repeating M2 SAFOD targets (a 4 km by 4 km dashed box surrounds the SAFOD zone), and the epicenters of the 1966 and 2004 M6 Parkfield mainshocks. Also shown are locations (stars) of nonvolcanic tremors in the Cholame, CA area relocated using a joint hypocenter tomography station-pair double-difference method (*Zhang et al.*, in revision, 2012), and routine locations of clusters of repeating earthquakes processed by the integrated HRSN and NCSN networks. Recently installed or planned (Moore Foundation funded) TremorScope and borehole PBO stations (squares and diamonds, respectively) also complement the HRSN borehole coverage and are particularly useful for the study of the tremor. These stations are shown as squares and diamonds, respectively. There are an additional five TremorScope and one PBO station outside the map bounds.

Sensor	Channel	Rate (sps)	Mode	FIR
Geophone	DP?	250.0	C	Ca
Geophone	BP?	20.0	C	Ac

Table 3.10: Data streams currently being acquired at operational HRSN sites. Sensor type, channel name, sampling rate, sampling mode, and type of FIR filter are given. C indicates continuous; Ac acausal; Ca causal. “?” indicates orthogonal, vertical, and two horizontal components.

radic telemetry failures. Properties of the sensors are summarized in Table 3.9.

The three newest borehole stations (CCRB, LCCB, and SCYB) were added, with NSF support, at the northwest end of the network as part of the SAFOD project to improve resolution of the structure, kinematics, and monitoring capabilities in the SAFOD drill-path and target zones. Figure 3.16 illustrates the location of the drill site and the new borehole sites, as well as locations of earthquakes recorded by the initial and upgraded/expanded HRSN.

These three new stations have a similar configuration to the original upgraded 10 station network and include an additional channel for electrical signals. Station descriptions and instrument properties are summarized in Tables 3.8 and 3.9. All the HRSN data loggers employ FIR filters and extract data at 250 Hz (causal) and 20 Hz (acausal). [Table 3.10].

The remoteness of the SAFOD drill site and supporting HRSN stations required an installation of an intermediate data collection point at Gastro Peak, with a microwave link to our CDF facility. There was also one station, RMNB, that was located on Gastro Peak that transmitted directly to the CDF and served as a repeater for station LCCB. Prior to June 2008, eight of the HRSN sites transmitted either directly to or through repeaters directly to the CDF. This included stations RMNB and LCCB. The other five sites transmitted to a router at Gastro Peak, where the data was aggregated and transmitted to the CDF. However, due to disproportionately increasing landowner fees for access to the Gastro Peak site, we reduced our dependence on that site in the summer and fall of 2008 (in cooperation with the USGS) by re-routing telemetry of five of the sites previously telemetered through Gastro Peak through an alternative site at Hogs Canyon (HOGS). This eliminated the Gastro Peak microwave link, but left station RMNB and its repeater for LCCB at the mercy/good-graces of the Gastro Peak landowner. Subsequent negotiations with the landowner stalled and it was decided that RMNB was to be closed (a replacement repeater path for LCCB was also found this year).

Continuous 20 and 250 Hz data from all HRSN chan-

nels are recorded to disk at our central site data collection facility on the California Department of Forestry’s (CDF) property in Parkfield. The waveforms are automatically picked at the HRSN computer, and this information is radio telemetered to the USGS site at Carr Hill for inclusion into Northern California Seismic System (NCSS) processing. The waveform data are also telemetered over a dedicated T1 circuit to the USGS and the Northern California Earthquake Data Center (NCEDC) at UC Berkeley for archiving and online access by the community. The HRSN system also generates autonomous event trigger associations which are also archived at the NCEDC.

The HRSN’s telemetry system also provides remote access to the local site data acquisition systems for state of health monitoring and control, and the recent upgrade to BASALT acquisition systems allows for local storage and retrieval of the data during telemetry outages.

Another feature of the HRSN system that has been particularly useful both for routine maintenance and for pathology identification has been the Internet connectivity of the central site processing computer and the individual stations’ data acquisition systems. Through this connectivity, locally generated warning messages from the central site processor are sent directly to the BSL for evaluation by project personnel. If, upon these evaluations, more detailed information on the HRSN’s performance is required, additional information can also be remotely accessed from the central site processing computer and generally from the individual site data loggers as well. Analysis of this remotely acquired information has been useful for trouble shooting by allowing field personnel to schedule and plan the details of maintenance visits to Parkfield. The connectivity also allows for local site acquisition shut-downs and restarts and for remote implementation of data acquisition parameter changes when needed.

The network connectivity and seamless data flow to UC Berkeley also provide near-real-time monitoring capabilities that are useful for rapid evaluation of significant events as well as the network’s general state of health.

For example, shown in Figure 3.17 are surface wave seismograms of the distant region  $M_w$  7.4 earthquake in Oaxaca, Mexico (Lat.: 16.662N; Lon.: 98.188W; depth 20 km) occurring on March 20, 2012 18:02:48 (UTC) and recorded on the SP1 (vertical) channels of the 10 HRSN borehole stations in operation at the time. The seismic data from the quake was telemetered to Berkeley and available for analysis by the Northern California Seismic System (NCSS) real-time/automated processing stream within a few seconds of being recorded by the HRSN.

This is also a good signal source for examining the relative responses of the BP borehole network station/components to seismic ground motion. In this case, for the large amplitude surface waves, the vertical channels all appeared to be working well and with proper

Site	Net	Latitude	Longitude	Surf. (m)	Depth (m)	Date	Location
EADB	BP	35.89525	-120.42286	466	245	01/1987 -	Eade Ranch
FROB	BP	35.91078	-120.48722	509	284	01/1987 -	Froelich Ranch
GHIB	BP	35.83236	-120.34774	400	63	01/1987 -	Gold Hill
JCNB	BP	35.93911	-120.43083	527	224	01/1987 - 02/18/2008	Joaquin Canyon North
JCNB*	BP	35.93911	-120.43083	527	4	07/2011 -	Joaquin Canyon North
JCSB	BP	35.92120	-120.43408	455	155	01/1987 -	Joaquin Canyon South
MMNB	BP	35.95654	-120.49586	698	221	01/1987 -	Middle Mountain
RMNB*	BP	36.00086	-120.47772	1165	73	01/1987 - 07/20/2011	Gastro Peak
SMNB	BP	35.97292	-120.58009	699	282	01/1987 -	Stockdale Mountain
VARB	BP	35.92614	-120.44707	478	572	01/1987 - 08/19/2003	Varian Well
VARB*	BP	35.92614	-120.44707	478	298	08/25/2003 -	Varian Well
VCAB	BP	35.92177	-120.53424	758	200	01/1987 -	Vineyard Canyon
CCRB	BP	35.95718	-120.55158	595	251	05/2001 -	Cholame Creek
LCCB	BP	35.98005	-120.51424	640	252	08/2001 -	Little Cholame Creek
SCYB	BP	36.00938	-120.53660	945	252	08/2001 -	Stone Canyon

Table 3.8: Stations of the Parkfield HRSN. Each HRSN station is listed with its station code, network id, location, operation period, and site description. The latitude and longitude (in degrees) are given in the WGS84 reference frame. The surface elevation (in meters) is relative to mean sea level, and the depth to the sensor (in meters) below the surface is also given. Coordinates and station names for the three new SAFOD sites are given at the bottom. Notes, denoted with '\*': There are 2 entries for JCNB, which failed in February of 2008 and has been replaced with a post-hole installation with ARRA funds. There are 2 entries for VARB, whose recording from a deep failed sensor (failure in August, 2003) was changed to a shallower sensor. Recording of data from station RMNB ended in July of 2011, due to landowner issues.

Site	Sensor	Z	H1	H2	RefTek 24	Quanterra 730	BASALT
EADB	Mark Products L22	-90	170	260	01/1987 - 06/1998	03/2001 - 07/2011	07/2011 -
FROB	Mark Products L22	-90	338	248	01/1987 - 06/1998	03/2001 - 11/2010	11/2010 -
GHIB	Mark Products L22	90	failed	unk	01/1987 - 06/1998	03/2001 - 07/2011	07/2011 -
JCNB	Mark Products L22	-90	0	270	01/1987 - 06/1998	03/2001 - 02/2008	-
JCNB*	Oyo GeoSpace GS-20DX	90	0	90	-	-	09/2011 -
JCSB	Geospace HS1	90	300	210	01/1987 - 06/1998	03/2001 - 04/2011	04/2011 -
MMNB	Mark Products L22	-90	175	265	01/1987 - 06/1998	03/2001 - 12/2010	12/2010 -
RMNB*	Mark Products L22	-90	310	40	01/1987 - 06/1998	03/2001 - 07/2011	-
SMNB	Mark Products L22	-90	120	210	01/1987 - 06/1998	03/2001 - 04/2011	04/2011 -
VARB	Litton 1023	90	15	285	01/1987 - 06/1998	03/2001 - 04/2011	-
VARB*	Litton 1023	90	358	88	01/1987 - 06/1998	03/2001 - 04/2011	04/2011 -
VCAB	Mark Products L22	-90	200	290	01/1987 - 06/1998	03/2001 - 04/2011	04/2011 -
CCRB	Mark Products L22	-90	258	348	-	05/2001 - 08/2011	08/2011 -
LCCB	Mark Products L22	-90	50	140	-	08/2001 - 09/2011	09/2011 -
SCYB	Mark Products L22	-90	342	72	-	08/2001 - 08/2011	08/2011 -

Table 3.9: Instrumentation of the Parkfield HRSN. Most HRSN sites have L22 sensors and were originally digitized with a RefTek 24 system. The WESCOMP recording system failed in mid-1998, and after an approximate three year hiatus the network was upgraded and recording was replaced with a new 4-channel system. The new system, recording since July 27, 2001, uses a Quanterra 730 4-channel acquisition. Three new stations were also added during the network upgrade period (bottom) In 2010-2011, with ARRA funding, additional replacement/upgrade to 24-bit BASALT acquisition with station-local data storage took place. Notes, denoted with '\*': There are 2 entries for JCNB, which failed in February of 2008 and has been replaced with a post-hole installation with ARRA funds. There are 2 entries for VARB, whose recording from a deep failed sensor (failure in August, 2003) was changed to a shallower sensor. Recording of data from station RMNB ended in July of 2011, due to landowner issues.

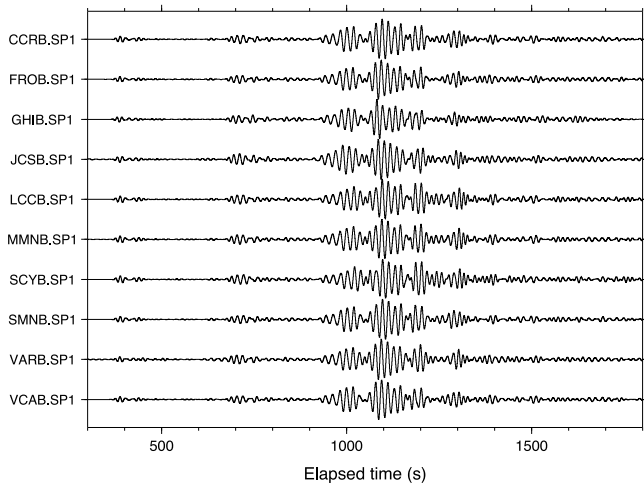


Figure 3.17: Plot of surface wave seismograms of the distant regional  $M_w$  7.4 earthquake in Oaxaca, Mexico (Lat.: 16.662N; Lon.: 98.188W; depth 20 km) occurring on March 20, 2012 at 18:02:48 (UTC) recorded on the SP1 (vertical) channels of the 10 HRSN borehole stations. Data from EADB and JCNB were not shown because of their lower signal-to-noise ratios, and station RMNB no longer records data due to landowner issues. Here, vertical component geophone (velocity) data have been 0.05-0.10 Hz bandpass filtered and normalized by the maximum amplitude for each trace.

polarities. Closer inspection of the unfiltered pre-event noise for these channels and for their corresponding horizontal (DP2 and DP3 channels) indicated that on a finer scale, the following channels were not entirely responding normally to seismic ground motions at the time of this event:

- FROB.BP.DP1 - strong 60 Hz noise
- LCCB.BP.DP2 - anomalously low signal level
- VARB.BP.DP2 - excessive ringing
- VARB.BP.DP3 - excessive ringing
- EADB.BP.DP1 - no response to earthquake
- EADB.BP.DP2 - no response to earthquake
- EADB.BP.DP3 - no response to earthquake
- JCNB.BP.DP1 - poor signal to noise, post-hole
- JCNB.BP.DP2 - poor signal to noise, post-hole
- JCNB.BP.DP3 - poor signal to noise, post-hole

By rapidly generating such plots following large teleseismic events, quick assessment of the HRSN seismometer responses to real events is easily done and corrective measures implemented with relatively little delay.

## Data Flow

*Initial Processing Scheme.* Continuous data streams on all HRSN components are recorded at 20 and 250 sps on disk on the local HRSN computer at the CDF facility.

These continuous data are transmitted in near-real-time to the Berkeley Seismological Laboratory (BSL) over a T1 link and then archived at the NCEDC. In addition, the near-real-time data are being transmitted over the T1 circuit to the USGS at Menlo Park, CA, where they are integrated into the Northern California Seismic System (NCSS) real-time/automated processing stream. This integration has also significantly increased the sensitivity of the NCSN catalog at lower magnitudes, effectively doubling the number of small earthquake detections in the critical SAFOD zone.

Shortly after being recorded to disk on the central site HRSN computer, event triggers for the individual stations are also determined, and a multi-station trigger association routine then processes the station triggers and generates a list of HRSN-specific potential earthquakes. For each potential earthquake that is detected, a unique event identification number (compatible with the NCEDC classification scheme) is also assigned. Prior to the San Simeon earthquake of December 22, 2003, 30 second waveform segments were then collected for all stations and components and saved to local disk as an event gather, and event gathers were then periodically telemetered to BSL and included directly into the NCEDC earthquake database (DBMS) for analysis and processing.

Because of its mandate to record very low amplitude seismic signals and microearthquakes in the Parkfield area, the HRSN was designed to operate at very high sensitivity levels. To some degree, this comes at the expense of dynamic range for the larger events (above  $\sim 3.5$ ), but high sensitivity is also achieved by recording in the low noise borehole environment (200-300m) and by exhaustive efforts at knocking down extraneous noise sources that arise in the electronics of the recording, power, and telemetry systems or from interference from cultural or scientific noise sources near the stations. As a consequence of the network's high sensitivity, the HRSN also records above its noise floor numerous signals from regional events and relatively distant and small amplitude nonvolcanic tremor events. For example, spot checks of aftershocks following the M 6.5 San Simeon earthquake of December 22, 2003 using continuous data and HRSN event detection listings revealed that the overwhelming majority of HRSN-generated detections following San Simeon resulted from seismic signals generated by San Simeon's aftershocks, despite the HRSN's  $\sim 50$  km distance from the events. Data from the California Integrated Seismic Network (CISN) show that there were  $\sim 1,150$  San Simeon aftershocks with magnitudes  $> 1.8$  in the week following San Simeon, and during this same period, the number of HRSN event detections was  $\sim 10,500$  (compared to an average weekly rate before San Simeon of 115 HRSN detections). This suggests that, despite the  $\sim 50$  km distance, the HRSN is detecting San Simeon

aftershocks well below magnitude 1.

*Current Processing.* Since the beginning of the network's data collection in 1987, and up until 2002, the local and regional events were discriminated based on analyst assessment of S-P times, and only local events with S-P times less than  $\sim 2.5$  s at the first arriving station were picked and located as part of the HRSN routine catalog. However, because of the network's extreme sensitivity to the large swarm of aftershocks from the 2003 San Simeon and 2004 Parkfield M6 earthquakes (e.g., in the first five months following the San Simeon mainshock, over 70,000 event detections were made by the HRSN system, compared to an average five month detection rate of 2500 prior to San Simeon) and because of ever declining funding levels, analyst review of individual microearthquakes had to be abandoned.

In addition, the dramatic increase in event detections following the San Simeon and Parkfield earthquakes vastly exceeded the HRSN's capacity to process and telemeter both continuous and triggered event waveform data. To prevent the loss of seismic waveform coverage, processing of the triggered waveform data was discontinued to allow the telemetry and archival of the 20 and 250 sps continuous data to continue uninterrupted. Subsequent funding limitations have since precluded reactivation of the triggered event processing. Cataloging of associated event triggers from the modified REDI real-time system algorithm continues, however, and both the continuous waveform data and trigger times are telemetered to and archived at the NCEDC, for access by the research community.

Because funding to generate catalogs of local micro-events from the tens of thousands of San Simeon and Parkfield aftershocks has not been forthcoming, major changes in our approach to cataloging events have had to be implemented. For example, HRSN data flow has now been integrated into NCSN automated event detection, picking, and catalog processing (with no analyst review). In addition, we have implemented a high resolution cross-correlation (pattern matching) based procedure to automatically detect, pick, locate, double-difference relocate, and determine magnitudes for select similar and repeating earthquake families down to very low magnitudes (i.e., below  $-1.0M_L$ ). These new schemes are discussed in more detail in the activities section below.

### 4.3 2011-2012 Activities

This year, routine operation and maintenance of the HRSN (California's first and longest operating borehole seismic network) have been additionally augmented by funding through the USGS from the American Recovery and Reinvestment Act (ARRA). This funding is directed toward upgrading the data loggers at all sites with government furnished equipment (GFE) data loggers, and with improving and upgrading telemetry and power in-

frastructure at the sites. Many of the routine maintenance activities described below were also carried out with ARRA support.

In addition to routine operations and maintenance, project activities this year include: a) processing of ongoing similar and repeating very low magnitude seismicity; b) implementing the ARRA upgrades and identifying needed corrections to the upgrades using repeating events; c) supporting SAFOD activities with the repeating and similar event seismicity catalogs; d) monitoring non-volcanic tremor activity in the Parkfield-Cholame area; and e) additional one time adaptations.

### Routine Operations and Maintenance

Routine maintenance tasks required this year to keep the HRSN in operation include cleaning and replacing corroded electrical connections; grounding adjustments; cleaning solar panels; testing and replacing failing batteries; ventilating battery and data logger housings to address problems with low power during hot weather, and repairing and realigning repeater sites and antennas.

Remote monitoring of the network's health using the Berkeley Seismological Laboratory's internally developed and SeisNetWatch software is also performed to identify both problems that can be resolved over the Internet (e.g. rebooting of data acquisition systems due to clock lockups) and more serious problems requiring field visits. Over the years, such efforts have paid off handsomely by providing exceptionally low noise recordings of very low amplitude seismic signals produced by microearthquakes (below  $0.0M_L$ ) and nonvolcanic tremors.

The network connectivity over the T1 circuit also allows remote monitoring of various measures of the state of health (SOH) of the network in near-real-time using waveforms directly. For example, background noise levels can be rapidly evaluated. Shown in Figure 3.18 are power spectral density (PSD) plots of background noise for the 12 vertical HRSN channels in operation at the time (beginning 01:00 AM local time on day 01/01/2012) over a 1000 second period.

By periodically generating such plots, we can rapidly evaluate, through comparison with previously generated plots, changes in the network's station response to seismic signals across the wide band high-frequency spectrum of the borehole HRSN sensors. Changes in the responses often indicate problems with the power, telemetry, or acquisition systems, or with changing conditions in the vicinity of station installations that are adversely affecting the quality of the recorded seismograms. Once state of health issues are identified with the PSD analyses, further remote tests can be made to more specifically determine possible causes for the problem, and corrective measures can then be planned in advance of field deployment within a relatively short period of time.

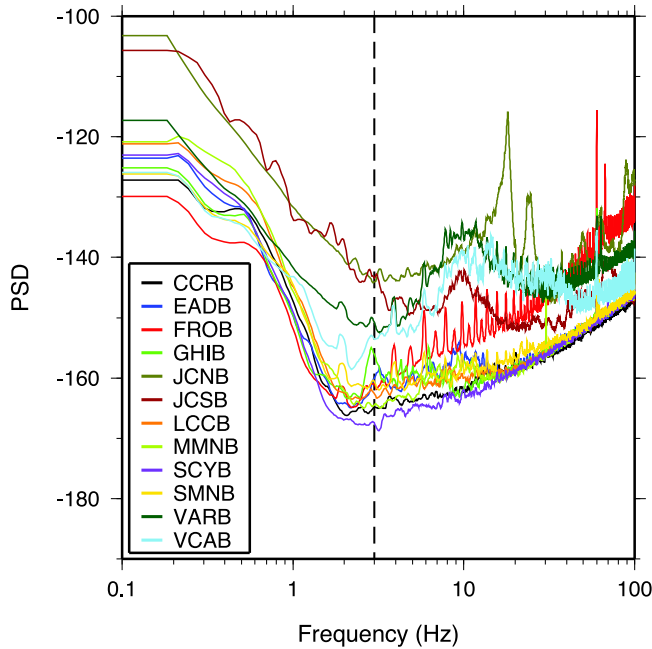


Figure 3.18: Background noise Power Spectral Density (PSD) levels as a function of frequency for the twelve 250 sps vertical component channels (DP1) of the HRSN borehole stations in operation during the 1000 second period analyzed, beginning 01:00 AM local time on day 01/01/2012. The approximate 2 Hz minimum of the PSD levels occurs because of the 2 Hz sensors used at these sites. Below 2 Hz, noise levels rise rapidly. The PSD (dB) ranking (lowest to highest) at 3 Hz (intersection with vertical line) for the vertical channels is:

SCYB.BP.DP1 -167.217  
MMNB.BP.DP1 -164.746  
CCRB.BP.DP1 -164.630  
LCCB.BP.DP1 -163.346  
FROB.BP.DP1 -161.281  
SMNB.BP.DP1 -160.395  
EADB.BP.DP1 -159.894  
GHIB.BP.DP1 -157.995  
VCAB.BP.DP1 -152.920  
VARB.BP.DP1 -150.796  
JCNB.BP.DP1 -145.028  
JCSB.BP.DP1 -144.259

Note that station RMNB is now closed due to landowner issues and failed station JCNB (failure in late 2007) has been reopened as a post-hole installation.

### Similar and Repeating Event Catalogs

The increased microseismicity (thousands of events) resulting from the San Simeon M6.5 (SS) and Parkfield M6 (PF) events, the lack of funds available to process and catalog the increased number of micro-earthquakes, and the increased interest in using the micro-quakes in repeat-

ing earthquake and SAFOD research have required new thinking on how to detect and catalog microearthquakes recorded by the HRSN.

One action taken to help address this problem has been to integrate HRSN data streams into the NCSN event detection and automated cataloging process. This approach has been successful at detecting and locating a significantly greater number of micro-earthquakes over the previous NCSN detection and location rate (essentially doubling the number of events processed by the NCSN). However, the HRSN-sensitized NCSN catalog is still only catching about half the number of local events previously cataloged by the HRSN using the old, HRSN-centric processing approach. Furthermore, triggered waveforms for the additional small NCSN-processed events are often not reviewed by an analyst, nor do these smaller events generally have NCSN magnitude determinations associated with them.

These limitations can severely hamper research efforts relying on the more numerous similar and characteristically repeating micro-events (e.g., earthquake scaling studies, SAFOD-related research, deep fault slip rate estimation, and the compilation of recurrence interval statistics for time-dependent earthquake forecast models). They also reduce the efficacy of using frequently recurring micro-events as a tool for monitoring the network state-of-health (SOH).

To help overcome these limitations, we continued this year to implement our semi-automated similar event cataloging scheme based on pattern matching (match filter) scans using cross-correlation of the continuous HRSN data. The method uses a library of reference event (pattern) waveforms, picks, locations, and magnitudes that have been accurately determined, to automatically detect, pick, locate, and determine magnitudes for events similar to the reference event with a level of accuracy and precision that only relative event analysis can bring.

The similar event detection is also remarkably insensitive to the magnitude of the reference event used, allowing similar micro-events ranging over about 3 magnitude units to be fully cataloged using a single reference event, and it does a remarkably good job at discriminating and fully processing multiple superposed events.

Once a cluster of similar events has been processed, an additional level of resolution can then be achieved through the identification and classification of characteristically repeating microearthquakes (i.e., near identical earthquakes) occurring within the similar event family (Figure 3.19). The pattern scanning approach also ensures optimal completeness of repeating sequences owing to scans of the matching pattern through “all” available continuous data (critical for applications relying on recurrence interval information). For example, only about half of the magnitude 0.26 events shown in Figure 3.19 were picked up by the NCSN-HRSN integrated network.

Figure 3.19 also shows how stable the performance of the borehole VCAB.BP.DP1 channel has remained over the  $\sim 4.5$  year period shown. Due to station malfunctions or human error during field maintenance, this would not necessarily be the case. Because repeating events can generally be identified using any combination of 4 of the HRSN's 35 channels, assessment of the channel responses for channels not in the 4 channel combination can be carried out. This can be carried out repeatedly through time as additional repeats are identified with time resolutions depending on the number of repeating sequences used and the frequency of their repeats. Repeating sequences of this magnitude typically repeat every 1 to 2 years, and we are in the process of expanding our similar event monitoring capability to 61 of these sequences. Hence, on average, evaluations of this type can be possible approximately every 10 days on an automated basis. However, there are on the order of 200 such sequences known in the Parkfield area, and if one is willing to include even more frequently occurring similar but non-identical events into the equation, near-daily automated SOH analyses are a possibility.

Armed with this type of information, technicians and field engineers can quickly identify and address major problems. In addition to a visual assessment, the high similarity of the events lends itself to the application of differencing techniques in the time and frequency domains to automatically identify even subtle SOH issues. For other networks recording continuously in the Parkfield area (e.g., NCSN, BDSN) it is also a relatively simple process to extend the SOH analysis using characteristic repeating event signals recorded at their stations (See BDSN station RAMR example in Figure 3.20) Furthermore, numerous repeating and similar event sequences are also known to exist in the San Francisco Bay, San Juan Bautista and Mendocino Triple Junction areas, where continuous recording takes place. Hence, application of the repeating event SOH technique to these zones should also be feasible.

This year we have worked at adapting our cataloging codes to take advantage of faster computing now available. We have expanded the library of reference event patterns and plan to retroactively scan these patterns through previously recorded and ongoing data to capture and catalog an ever growing body of similar and repeating earthquakes for research purposes, in support of SAFOD and for SOH monitoring (including the use of repeaters to identify and correct problems associated with the ARRA upgrade of the HRSN).

### Progress on ARRA upgrades

This year, funding through the USGS from the American Recovery and Reinvestment Act (ARRA) was used to complete upgrade of data loggers at all sites with government furnished equipment (GFE) data loggers, and

for improving and upgrading telemetry and power infrastructure at the sites. Because of increased use of pattern-match scanning techniques through continuous seismograms to detect and process repeating and Low Frequency Events (LFEs), care is being taken in our upgrade efforts to maintain the response characteristics of the HRSN's continuous data. At the time of this report, all 12 of the open HRSN stations have had new BASALT data loggers installed, with corresponding power and telemetry infrastructure upgrades. A station (JCNB), whose connection to its downhole sensor (cemented in place) was severed, has now had a new sensor emplaced at  $\sim 4$  m depth and is fully operational.

The repeating and similar event data we are compiling provide nearly ideal natural sources for ensuring the stability of the HRSN station's response characteristics across the transition to ARRA upgrade electronics. In comparing waveforms from repeating events before and after the the first two BASALT installations (i.e., at FROB and MMNB), it became immediately apparent that the nominal polarities of the BASALT data loggers were of the opposite sign to those of their predecessors (Q730s). In subsequent installations, this was taken into account. We were also immediately able to recognize in the repeating event waveforms that the horizontal channel assignments were switched in about half of the cases (i.e., DP2 mapped to DP3 and DP3 mapped to DP2). Whether this was due to incorrect cable preparation or to incorrect documentation is still not known, but subsequent site visits and analyses of ongoing repeat event waveforms are being used to correct and confirm appropriate channel assignments and polarities.

The repeating earthquake analyses have also shown that, absent the polarity flips, channel swaps and superposed signals, preservation of the the waveform and spectral shapes and spectral phasing relative the Q730 predecessors is very good. However, the analyses do reveal a significant ( $\sim 15$ - $20\%$ ) drop in the amplitude of the BASALT signals relative to the Q730s. At this time it appears this could involve an impedance matching issue at the interface of the BASALT with the other components of the HRSN stations. This is currently being investigated further, and corrective measures are being considered.

### Tremor Monitoring

The HRSN played an essential role in the initial discovery of nonvolcanic tremors (NVT) and associated Low Frequency Events (LFE) along the San Andreas Fault (SAF) below Cholame, CA (*Nadeau and Dolenc, 2005; Shelly et al., 2009*), and continues to play a vital role in ongoing NVT research. The Cholame tremors occupy a critical location between the smaller Parkfield ( $\sim M6$ ) and much larger Ft. Tejon ( $\sim M8$ ) rupture zones of the SAF (Figure 3.16). Because the time-varying nature of tremor

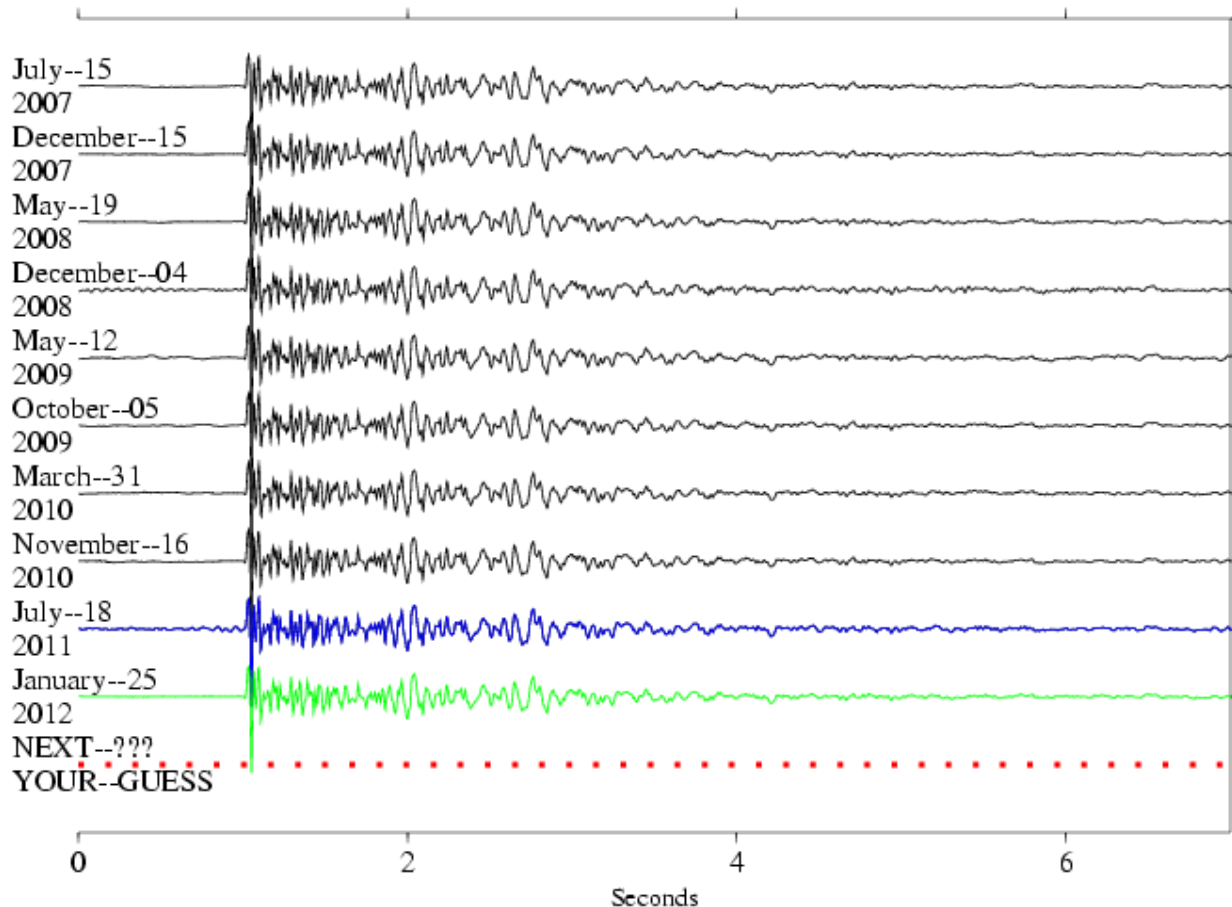


Figure 3.19: Ten most recent repeats of a characteristic sequence of repeating magnitude 0.26 ( $M_p$ , USGS preferred magnitude) microearthquakes recorded by vertical (DP1) channel of HRSN station VCAB. Characteristically repeating micro-events are extremely similar in waveform (typically 0.95 cross-correlation or better). High-precision location and magnitude estimates of these events show they are also nearly collocated (to within 5-10 m) and have essentially the same magnitude ( $\pm 0.13 M_p$  units, among all sequences studied).

In last year’s annual report we noted that the recurrence intervals for events in this sequence were on the order of 6 to 8 months, and we predicted that the next repeat of the sequence would take place sometime in May through July of 2011. The occurrence of the July 18, 2011 event (blue/dark-gray) confirmed our prediction, and a subsequent repeat on January 25, 2012 (green/light-gray) also followed the 6 to 8 month recurrence pattern. The dashed line labeled “NEXT” serves to illustrate our expectation that events in this sequences will continue the repeat pattern. Because the recent recurrence intervals continue to range between about six to eight months, we anticipate at least one and possibly two additional repeats within the next year, with the next repeat expected to occur sometime in July through September of 2012. For network operational purposes, the repeating behavior of this and other sequences in the Parkfield area allows us to use repeating sequences to monitor changes in channel response relative to past performance and to rapidly identify and correct state-of-health (SOH) issues with real, naturally occurring signals.

activity is believed to reflect time-varying deep deformation and presumably episodes of accelerated stressing of faults, because anomalous changes in Cholame area NVT activity preceded the 2004 Parkfield M6 earthquake, and because elevated tremor activity has continued since the

2004 Parkfield event, we are continuing to monitor the tremor activity observable by the HRSN to look for additional anomalous behavior that may signal an increased likelihood of another large SAF event in the region. To date, over 3087 NVT bursts have been identified and cat-

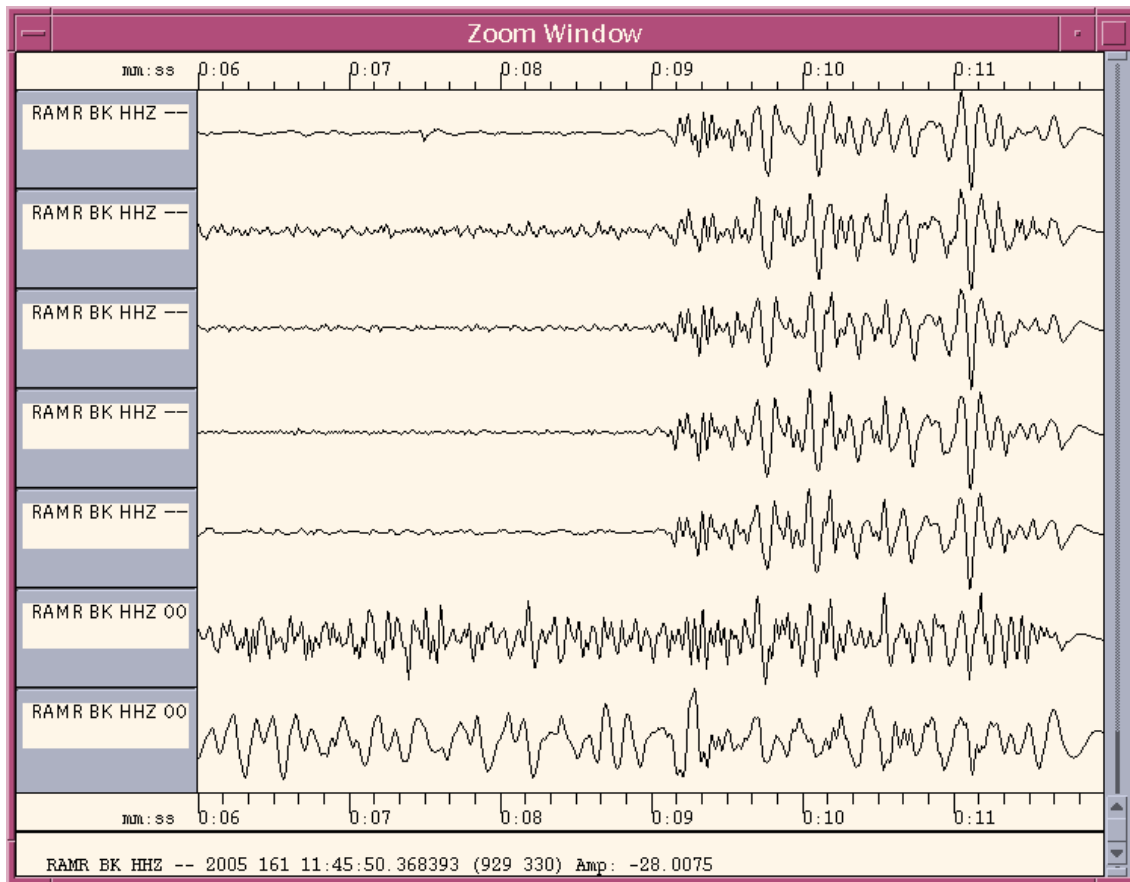


Figure 3.20: Figure of repeating earthquake data illustrating their utility for identifying problematic channel responses. Here a repeat of EarthScope’s SAFOD LA sequence ( $\sim$ M1.7) occurring on 21 March 2012 was identified using HRSN stations. The event was large enough, however, to use the repeating sequence waveforms to evaluate the performance of stations from other networks out to distances greater than 50 km from the HRSN. Shown are the last 7 LA sequence events recorded on the HH vertical channel of Berkeley’s Broadband station RAMR (formerly EarthScope TA station V04C) high-pass filtered at 3 Hz. RAMR is 55 km from the repeating events. From top to bottom, the events occurred on 01/23/2005, 06/10/2005, 01/28/2006, 05/30/2007, 12/19/2007, 10/21/2010, and 03/21/2012, respectively. Waveforms for the first 5 events are well recorded and consistent, indicating healthy station response. However, between the 2008 and 2010 events a significant degradation in response for frequencies above 3 Hz is seen to have taken place. Signal from the 2010 event is only just visible above the noise. For the 2012 repeat (bottom waveform), no signal is visible at all in the RAMR waveform. This affects all recorded broadband channels at RAMR. We are currently investigating the problem.

aloged, and regular updates of the NVT catalog continue on a biweekly basis.

### Efforts in Support of SAFOD

An intensive and ongoing effort by the EarthScope component called SAFOD (San Andreas Fault Observatory at Depth) is underway to drill through, sample, and monitor the active San Andreas Fault at seismogenic depths and in very close proximity (within a few tens of kilometers or less) to a repeating magnitude 2 earthquake site. The HRSN data plays a key role in these efforts by providing low noise and high sensitivity seismic waveforms from active and passive sources, and by providing a backbone of very small earthquake detections and con-

tinuous waveform data.

As of early September 2007, SAFOD drilling had penetrated the fault near the HI repeating target sequence and collected core samples in the fault region that presumably creeps and surrounds the repeatedly rupturing HI patch. Unfortunately, due to complications during drilling, penetration and sampling of the fault patch involved in repeating rupture was not possible, though core sampling and installation of seismic instrumentation in the region adjacent to the repeating patch was achieved. Current efforts are focused on long-term monitoring of the ongoing chemical, physical, seismological, and deformational properties in the zone (particularly any signals that might be associated with the next repeat of the SAFOD repeat-

ing sequences).

HRSN activities this year have contributed in three principal ways to these and longer-term SAFOD monitoring efforts:

1) Processing of integrated HRSN and USGS data streams in the Parkfield area continues, effectively doubling the number of small events available for monitoring seismicity in the SAFOD target zone and for constraining relative locations of the ongoing seismic activity.

2) Telemetry of all HRSN channels (both 20 and 250 sps data streams) continues to flow directly from Parkfield, through the USGS Parkfield T1 and the Northern California Earthquake Management Center (NCEMC) T1, to the USGS and the BSL for near real-time processing, catalog processing, and data archiving on the Web-based NCEDC. This also provides near-real-time access to the HRSN data for the SAFOD community, without the week- or month-long delay associated with the previous procedure of having to transport DLT tapes to Berkeley to upload and quality check the data.

3) Continued monitoring and expansion of our repeating (characteristic and similar event sequences) catalog has taken place this year, with particular focus on expansion and refinement of repeating event data within the 1.5 cubic km volume centered on the SAFOD target zone. Last year, we expanded the number of repeating sequence reference patterns in this zone from 3 to 18 and cataloged (detected, double-difference relocated, and determined magnitudes for) over 1200 earthquakes within this small volume. The pattern matching approach to detection is prone to identifying the same event from more than one reference earthquake, so a procedure was also developed this year to remove redundant events from the over-all catalog. A procedure was also developed to integrate arrival time information from the redundant pattern matches to improve connectivity of events from different similar event sequences in the double-difference relocations. This year, we have continued to monitor these sequences and have expanded the catalog of similar and repeating events in the immediate SAFOD zone by over 75 earthquakes. We also identified the only repeat of the 3 main SAFOD sequences. It occurred on 21 March of 2012 and was a member of the LA sequence.

### Additional One Time Adaptations

Owing to the break-down of negotiations with the landowner of Gastro Peak this year, we have closed station RMNB. Because RMNB also served as a repeater site for LCCB, we have also had to locate and implement an alternative telemetry path for LCCB through relay site PMM. Tests on the implementation show that despite a less than optimal path, the telemetry seems to be operating properly. Monitoring of the through-put continues to confirm robust year-round telemetry.

Telemetry through-put from the CDF to the USGS link at Carr Hill has degraded over time, and tests have revealed that the continued growth of tree branches within the telemetry path was most likely responsible. It was also recognized that the telemetry scheme between the CDF and Carr Hill was less than optimal and that the through-put problem could be largely compensated for with a streamlined scheme. In the past, CDF waveforms were sent to Carr Hill for phase picking by the NCSS processor at Carr Hill, requiring substantial band-width. In cooperation with our USGS partner, we have now transferred the phase picking task to the CDF computer and instead of sending waveforms, we now send just the picks to Carr Hill for NCSS processing, vastly reducing the bandwidth load on the CDF to Carr Hill telemetry link.

## 4.4 Acknowledgments

Under Robert Nadeau's and Doug Dreger's general supervision, Peggy Hellweg, Doug Neuhauser, Taka'aki Taira, and the engineering team (Bill Karavas, John Friday, Aaron Enright, and Joshua Miller) all contribute to the operation of the HRSN. Robert Nadeau prepared this section with help from Taka'aki Taira. During this reporting period, operation, maintenance, and data processing for the HRSN project was supported by the USGS, through grant G10AC00093. Additional improvements in the power and telemetry systems were funded under the USGS ARRA grant G09AC00487.

## 4.5 References

- Bakun, W. H., and A. G. Lindh, The Parkfield, California, prediction experiment, *Earthq. Predict. Res.*, *3*, 285-304, 1985.
- Hickman, S., M.D. Zoback and W. Ellsworth, Introduction to special section: Preparing for the San Andreas Fault Observatory at Depth, *Geophys. Res. Lett.*, *31*, L12S01, doi:10.1029/2004GL020688, 2004.
- Michelini, A. and T.V. McEvilly, Seismological studies at Parkfield: I. Simultaneous inversion for velocity structure and hypocenters using B-splines parameterization, *Bull. Seismol. Soc. Am.*, *81*, 524-552, 1991.
- Nadeau, R.M. and D. Dolenc, Nonvolcanic Tremors Deep Beneath the San Andreas Fault, *SCIENCE*, *307*, 389, 2005.
- Shelly, D.R., W.L. Ellsworth, T. Ryberg, C. Haberland, G.S. Fuis, J. Murphy, R.M. Nadeau and R. Bürgmann, Precise location of San Andreas Fault Tremors near Cholame, California using seismometer clusters: Slip on the deep extension of the fault?, *Geophys. Res. Lett.*, *36*, L01303, doi:10.1029/2008GL036367, 2009.
- Thurber, C., H. Zhang, F. Waldhauser, J. Hardebeck and A. Michael, Three-dimensional compressional wavespeed model, earthquake relocations, and focal mechanisms for the Parkfield, California region, *Bull. Seismol. Soc. Am.*, *96*, S38-S49, doi:10.1785/0120050825, 2006.
- Zhang, H., R.M. Nadeau, R.N. Toksoz, C.H. Thurber and M. Fehler, Nonvolcanic Tremors in Localized Low Shear Wave Velocity Zones Beneath the San Andreas Fault, *J. Geophys. Res.*, (in revision), 2012.

## 5 Bay Area Regional Deformation Network

### 5.1 Background

The Bay Area Regional Deformation (BARD) network is a collection of permanent, continuously operating GPS receivers that monitors crustal deformation in the San Francisco Bay Area and Northern California. Started in 1991 with two stations spanning the Hayward Fault, BARD has been a collaborative effort of the Berkeley Seismological Laboratory (BSL); the USGS at Menlo Park (USGS/MP); and several other academic, commercial, and governmental institutions. The BARD network is designed to study the distribution of deformation in Northern California across the Pacific-North America plate boundary and interseismic strain accumulation along the San Andreas fault system in the Bay Area for seismic hazard assessment, and to monitor hazardous faults and volcanoes for emergency response management. It also provides data in real time for use in Earthquake Early Warning (EEW) and rapid response applications. The BSL maintains and/or has direct continuous telemetry from 33 stations comprising the BARD Backbone (Table 3.11), while additional stations operated by the USGS, US Coast Guard and others fill out the extended BARD network.

Since the completion of major construction on the Plate Boundary Observatory (PBO) portion of EarthScope in 2004, the number of GPS stations in Northern California has expanded to over 250 (Figure 3.21). Together, PBO and BARD stations provide valuable information on the spatial complexity of deformation in the San Francisco Bay Area and Northern California, while the BARD network has the infrastructure and flexibility to additionally provide information on its temporal complexity over a wide range of time scales and in real time. All BARD Backbone stations collect data at 1 Hz sampling frequency (Table 3.11) and stream their data in real time to the BSL. Data in turn is provided in real time to the public. Furthermore, nineteen BARD Backbone sites are collocated with broadband seismic stations of the Berkeley Digital Seismic Network (BDSN), with which they share continuous telemetry to UC Berkeley (Table 3.11). As geodetic and seismic data become more closely integrated, these collocated stations are already available to provide combined data products.

This past year saw the completion of work performed under the American Reinvestment and Recovery Act (ARRA). Sixteen BARD sites were upgraded with more modern receivers (Topcon Net-3GA) that provide BINEX data streams with 1 Hz sampling over TCP/IP. The new receivers are also capable of recording L5 data in addition to L1 and L2; L5 is a third frequency that will be added to GPS satellites in the coming years. The BSL

also received ARRA funding to install seven new stations at existing BDSN stations (Table 3.11), thereby taking advantage of shared telemetry. Six of these stations (GASB, JRSC, MCCM, MNRC, PTRO, and WDCB) have been installed, while winter weather hampered construction of the seventh monument (HELL), which will be completed this summer.

### 5.2 BARD Overview

#### BARD station configuration

Following upgrades, the BARD network now includes just two models of receiver: Trimble NetRS and Topcon Net-G3A. The Topcon receivers replaced ones which were connected directly via serial connection and were thus susceptible to data loss during telemetry outages. The upgraded receivers should allow us to provide complete daily data. We were also able to finally upgrade the last two low-rate stations to high data collection rate (LUTZ, SODB), such that the entire BARD network now streams, collects and archives data at 1 Hz. All BARD stations use a radome-equipped, low-multipath choking antenna, designed to provide security and protection from weather and other natural phenomena, and to minimize differential radio propagation delays. A low-loss antenna cable is used to minimize signal degradation on the longer cable setups that normally would require signal amplification. Low-voltage cutoff devices are installed to improve receiver performance following power outages.

All BARD stations are continuously telemetered to the BSL. Many use frame relay technology, either alone or in combination with radio telemetry. Other methods include a direct radio link to Berkeley (TIBB) and satellite telemetry. At MODB, we are able to telemeter 1 Hz data using the USGS VSAT system that collects seismic broadband data as part of the National Seismic Network (NSN). We also changed our data strategy by allowing some data to be transferred by web-based telemetry (ADSL lines). This will reduce our communication operational costs and, we hope, will not affect our ability to react in the case of a large event.

BARD station monumentations broadly fall into three types. Most are anchored into bedrock, either directly or via a steel-reinforced concrete cylinder. The five “mini-PBO” stations that are still operated by the BSL are collocated with USGS strainmeters and the GPS antennas are bolted onto the borehole casing using an experimental mount developed at the BSL, which has since been adopted by PBO for their strainmeter sites. Four sites (UCD1, SRB1, UCSF, SBRB) are located on the roofs of buildings. Most of the last type have been installed in the past three years, and their stability over long periods

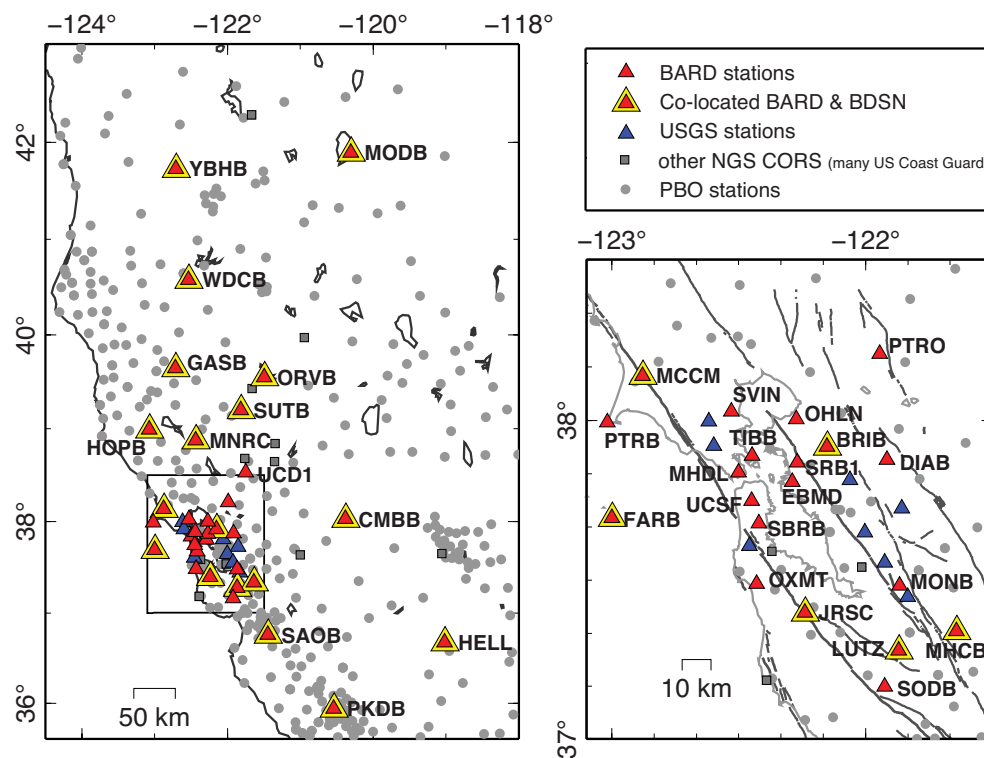


Figure 3.21: Map of the BARD Backbone network and surrounding PBO sites in Northern California. Box in left figure indicates the extent of the figure on right.

of time is yet to be evaluated.

### Data archival

Raw and RINEX data files from the 31 BARD Backbone stations and several other stations run by BARD collaborators, such as the USGS and LBNL, are archived at the Northern California Earthquake Data Center (NCEDC). The data are checked to verify their integrity, quality, completeness, and conformance to the RINEX standard, and are then made accessible, usually within 2 hours of the end of the UTC day, to all participants and other members of the GPS community through the Internet, both by anonymous FTP and through the World Wide Web (<http://ncedc.org/>). BARD data are also available to the community through the GPS Seamless Archive Centers (GSAC), such as that hosted by the Scripps Orbit and Permanent Array Center (SOPAC, <http://gsac.ucsd.edu>). High-rate raw data are also decimated to create 15 s RINEX data files. 1 Hz RINEX files are available for all BARD Backbone sites after May 2010.

As part of the activities funded by the USGS through the BARD network, the NCEDC has established an archive of the 10,000+ survey-mode occupations collected by the USGS since 1992. The NCEDC continues to archive non-continuous survey GPS data. The initial dataset archived is the survey GPS data collected by the

USGS Menlo Park for Northern California and other locations. The NCEDC is the principal archive for this dataset. Quality control efforts were implemented by the NCEDC to ensure that raw data, scanned site log sheets, and RINEX data are archived for each survey. All of the USGS/MP GPS data has been transferred to the NCEDC, and virtually all of the data from 1992 to the present has been archived and is available for distribution. These survey-mode data are used together with data from BARD and PBO stations to produce BAVU (Bay Area Velocity Unification), a united set of continuous and survey data from the wider San Francisco Bay Area, processed under identical conditions using GAMIT (*d'Alessio et al., 2005*).

Data from five of our sites (HOPB, MNCB, CMBB, OHLN, and YBHB) are sent to the National Geodetic Survey (NGS) in the framework of the CORS (Continuous Operating Reference Stations) project (<http://www.ngs.noaa.gov/CORS/>). The data from these five sites are also distributed to the public through the CORS FTP site.

### Real-time streaming

All BARD stations are currently available in real time with 1 Hz data sampling; a step toward our goal of integrating GPS with the Northern California Seismic System (NCSS) for use in hazard assessment and emergency

response and for Earthquake Early Warning applications. The streams are available in BINEX and RTCM formats from a Ntrip caster operated by the BSL (<http://earthquakes.berkeley.edu/bard/realtime>). The BSL also acts as a conduit for real-time streams for seven continuous GPS stations operated by the USGS, Menlo Park and five stations installed by the Lawrence Berkeley National Lab (LBNL), in order to make those data easily accessible to the GPS community.

### Data processing

Average station coordinates are estimated from 24 hours of observations for BARD stations and other nearby continuous GPS sites using the GAMIT/GLOBK software developed at MIT and SIO (King and Bock, 1999, Herring, 2005). GAMIT uses double-difference phase observations to determine baseline distances and orientations between ground-based GPS receivers. Ambiguities are fixed using the widelane combination followed by the narrowlane, with the final position based on the ionospheric free linear combination (LC or L3). Baseline solutions are loosely constrained until they are combined together. GAMIT produces solutions as H-files, which include the covariance parameters describing the geometry of the network for a given day and summarize information about the sites. We combine daily, ambiguity-fixed, loosely constrained H-files using the Kalman filter approach implemented by GLOBK (Herring, 2005). They are combined with solutions from the IGS global network and PBO and stabilized in an ITRF2005 reference frame. The estimated relative baseline determinations typically have 2-4 mm long-term scatter in the horizontal components and 10-20 mm scatter in the vertical.

BARD data are an important component of the Bay Area Velocity Unification (BAVU) project (dAlessio et al., 2005). BAVU contains all available campaign data in Northern California and processes them in a consistent manner to produce a comprehensive and high-density velocity map. It relies on a network of CGPS stations to provide a framework on which these data can be combined. With data going back to 1992, BARD stations can provide such a framework. An updated, though preliminary, version of the BAVU velocity model has been completed, which includes BARD stations (BAVU3 $\beta$ ). Average linear velocities for each station are estimated from monthly combinations of the campaign, BARD, PBO and IGS solutions and are shown in Figure 3.22. BAVU3 $\beta$  is still preliminary, but represents a substantial increase in data density over previous versions. A final BAVU3.0 will include even more campaign data collected recently and a closer integration with the BARD network.

### ARRA infrastructure improvements

A major activity of the last two years has been work performed under the ARRA program to upgrade BARD

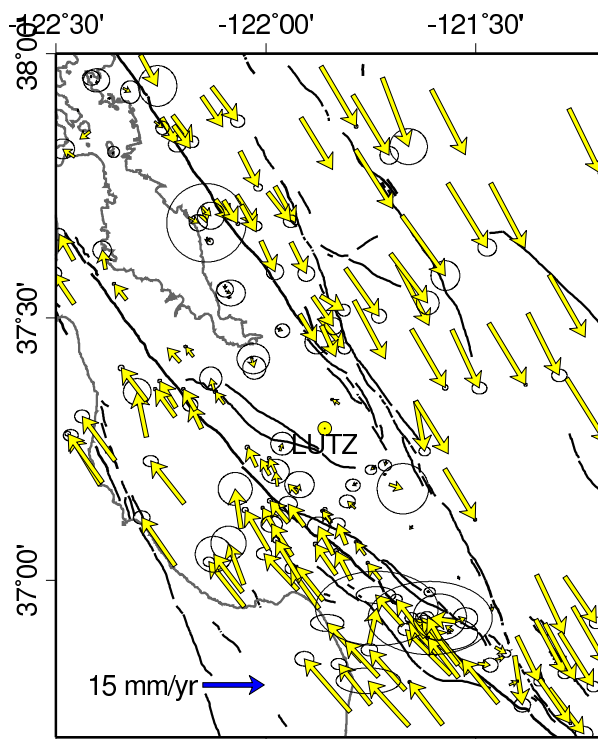


Figure 3.22: Velocities from BAVU3 $\beta$ , including BARD stations, as well as campaign and PBO stations. Yearly velocities are relative to station LUTZ, marked by a yellow circle.

infrastructure, including upgraded equipment at nearly half the BARD network stations and seven new stations. All receiver upgrades are now complete, though troubleshooting to ensure smooth operation of the new equipment is still on-going. During the course of the upgrades, site SBRN was decommissioned and has been officially replaced by site SBRB. SBRB was installed after vandalism at SBRN caused an extended data outage and has been running in tandem with SBRN for over a year. BSL engineers have also installed six new stations (GASB, JRSC, MCCM, MNRC, PTRO, and WDCB), all collocated with BDSN seismometers (or planned BDSN sites) and collecting and streaming data at 1 Hz.

Three types of monument design were used in the station installations. Stations JRSC and WDCB (and HELL) are short brace monuments, composed of four legs cemented into bedrock. A vault-mounted monument was used for three stations where there was adequate sky view directly above the seismic vault. The seismic vaults are large structures, framed by a shipping container and cemented to bedrock. The GPS antennas are mounted on pipe embedded in the vault wall, for this purpose, at the time of construction. These made them relatively cheap to install. Some work had previously been done to construct the monument at PTRO, so we continued the installation of a concrete post monument anchored to

	Sites	Lat. (deg.)	Lon. (deg)	Receiver	Telem.	Sampling rate	Collocated Network	Location
1	BRIB	37.91	-122.15	NETRS	FR	1 Hz	BDSN	Briones Reservation, Orinda
2	CMBB	38.03	-120.39	NET-G3A	FR	1 Hz	BDSN	Columbia College, Columbia
3	DIAB	37.87	-121.92	NETRS	FR	1 Hz		Mt. Diablo
4	FARB	37.69	-123.00	NETRS	R-FR	1 Hz	BDSN	Farallon Island
5	GASB	39.65	-122.72	NET-G3A	R-FR	1 Hz	BDSN	Alder Springs, CA
6	HOPB	38.99	-123.07	NET-G3A	R-FR	1 Hz	BDSN	Hopland Field Stat., Hopland
7	JRSC	37.4	-122.24	NET-G3A	Int	1 Hz	BDSN	Jasper Ridge Biol. Preserve
8	LUTZ	37.28	-121.87	NET-G3A	FR	1 Hz	BDSN	SCC Comm., Santa Clara
9	MCCM	38.14	-122.88	NET-G3A	VSAT	1 Hz	BDSN	Marconi Conference Center
10	MHCB	37.34	-121.64	NETRS	FR	1 Hz	BDSN	Lick Obs., Mt. Hamilton
11	MHDL	37.84	-122.49	NETRS	R-FR	1 Hz	mini-PBO	Marin Headlands
12	MNRC	38.88	-122.44	NET-G3A	VSAT	1 Hz	BDSN	McLaughlin Mine, CA
13	MODB	41.90	-120.30	NETRS	VSAT	1 Hz	BDSN	Modoc Plateau
14	MONB	37.48	-121.87	NET-G3A	FR	1 Hz		Monument Peak, Milpitas
15	OHLN	38.00	-122.27	NET-G3A	FR	1 Hz	mini-PBO	Ohlone Park, Hercules
16	ORVB	39.55	-121.50	NET-G3A	FR	1 Hz	BDSN	Oroville
17	OXMT	37.49	-122.42	NET-G3A	FR	1 Hz	mini-PBO	Ox Mountain
18	PKDB	35.94	-120.54	NETRS	R-T1	1 Hz	BDSN	Bear Valley Ranch, Parkfield
19	PTRB	37.99	-123.01	NETRS	R-FR	1 Hz		Point Reyes Lighthouse
20	PTRO	36.39	-121.55	NET-G3A	FR	1 Hz		Potrero Hills
21	SAOB	36.76	-121.45	NETRS	FR	1 Hz	BDSN	San Andreas Obs., Hollister
22	SBRB	37.69	-122.41	NET-G3A	FR	1 Hz	mini-PBO	San Bruno Replacement
23	SODB	37.17	-121.93	NET-G3A	R-FR	1 Hz		Soda Springs, Los Gatos
24	SRB1	37.87	-122.27	NET-G3A	Fiber	1 Hz		Seismic Replace. Bldg., Berkeley
25	SUTB	39.20	-121.82	NETRS	R-FR	1 Hz	BDSN	Sutter Buttes
26	SVIN	38.03	-122.53	NET-G3A	R-FR	1 Hz	mini-PBO	St. Vincents
27	TIBB	37.89	-122.45	NET-G3A	R-Int	1 Hz		Tiburon
28	UCD1	38.53	-121.75	NETRS	Int	1 Hz		UC Davis, Davis
29	UCSF	37.75	-122.46	NET-G3A	FR	1 Hz		UC San Francisco, San Francisco
30	WDC	40.58	-122.54	NET-G3A	FR	1 Hz	BDSN	Whiskeytown Dam, Whiskeytown
31	YBHB	41.73	-122.71	NETRS	FR	1 Hz	BDSN	Yreka Blue Horn Mine, Yreka
32	HELL	36.68	-119.02				BDSN	Rademacher Property, Miramonte

Table 3.11: List of BARD stations maintained by the BSL. Two models of receiver are in operation: Trimble NetRS, (NETRS), Topcon Net-G3A (NET-G3A). The telemetry types are listed in column 6: FR = Frame Relay, R = Radio, VSAT= Satellite, Int = Internet, T1=T1 line, Fiber=direct fiber connection. Some sites are transmitting data over several legs with different telemetry.

the underlying substrate with cemented reinforcing rods. This is a type of monument we have used for other BARD stations (e.g. MONB), which has been shown to be stable.

All of the new monuments have performed well in the short time they have been operational; the longer-term stability of the monuments will need to be evaluated after 2-3 years. The average daily uncertainty is calculated from the formal error estimated independently by GAMIT/GLOBK during each day of processing. This quantity will be large if there is poor sky view and/or large amounts of multi-path at the site and for GASB, MCCM and WDCB, this value is higher than typical for BARD stations (Table 3.12). The time series RMS is a measure of the scatter in the cleaned time series and thus represents the short-term stability of the monument. All the new stations have RMS values on a par with those of existing BARD stations. Furthermore the stations with slightly higher RMS (GASB, MCCM, WDCB) are also those with higher average uncertainty, suggesting that their scatter results from their environment, rather than from monument instability. Indeed, these sites all have challenging sky view environments, but we nonetheless believe they are adequate based on the RMS values. Better nearby sites were not available for any of these stations and we were constrained in our ability to choose locations by the necessity of sharing telemetry with the BDSN station. On this short time scale, there is therefore no indication that the vault-mounted monuments are less stable than the short brace monuments. A further analysis when 2-3 years of data are available will show whether these monuments are stable over longer time periods and correctly reflect tectonic motion.

In addition to the equipment upgrades, the ARRA program also funded the re-establishment of daily processing and time-series generation for BARD backbone stations and upgrades to the BARD website. Daily processing ensures that bad data is caught quickly and problems can be fixed in a timely manner. Each day of data is processed twice, first with IGS Rapid orbit files within 24 hours of collection and again after IGS Final orbit files are available, using within 2-3 weeks. BARD rapid solutions are used to generate a new data point in the station displacement series right away and IGS global solutions and PBO network solutions are combined in when they are available and provide improved constraints to the time series. Final time series displacements are held until BARD final solutions, IGS, and PBO final network solutions are all available. Time series can be viewed and downloaded from the BARD website (<http://earthquakes.berkeley.edu/bard>).

### Real-time data processing

A prototype system for processing BARD GPS data in real time had been established and will continue to be im-

	Time Series RMS			Avg Daily Uncert		
	N	E	U	N	E	U
New Monuments - Vault Mounted						
GASB	1.8	1.7	10	4.7	3.9	21.6
MCCM	1.8	2.3	10.9	5.3	6.5	29.3
MNRC	0.9	0.9	4.6	2.3	2.2	8.4
New Monuments - Short Brace						
JRSC	0.6	1	5.5	2.1	2	7.6
WDCB	1.7	1.7	7.5	6	4.9	22.4
New Monuments - Anchored Concrete Post						
PTRO	0.5	0.4	3	2.9	2.6	10.5
Existing Monuments						
BRIB	2.4	2.1	5.4	2.7	2.5	10.3
CMBB	0.8	1.4	5.4	3.6	3.7	13.9
DIAB	1.6	1.1	4.5	2.4	2.3	8.9
FARB	0.7	1.4	3.4	1.9	2	6.8
HOPB	1.5	1.3	10.1	3.2	3.1	13.6
LUTZ	2.4	1	3.8	2.3	2.3	8
MHCB	1.4	1.7	2.8	1.8	1.9	6.2
MHDL	1.8	2	9.5	3.3	3	12.5
MODB	1.4	1.6	7.1	3.3	3.2	12.4
MONB	0.8	1.3	3.3	2.1	2.1	7.2
OHLN	2.9	2.3	3.4	2.5	2.5	9.1
ORVB	0.9	1.3	7	2.4	2.3	8.5
OXMT	1.3	1.6	5.9	3	2.7	12.1
PKDB	1.7	1.1	4.4	2.9	2.9	11.3
PTRB	1.1	1.5	4	2.2	2.2	7.5
SAOB	1.2	1.2	3.3	2.3	2.4	8.3
SBRB	1.8	3.4	6.3	4.5	3.8	17.6
SODB	2.4	1.8	5.2	3.4	3.2	13.1
SRB1	3.8	1.2	4	2.7	2.5	9.9
SUTB	2.2	2.2	4.4	2.5	2.3	8.2
SVIN	0.9	1.3	4.3	2	1.9	7
TIBB	1.3	1.3	3.3	2.3	2.4	9
UCD1	1.4	1.8	12.6	2.3	2.3	8.2
UCSF	1.8	1.4	4.3	2.6	2.4	9.3
YBHB	2.8	3.9	7.7	2.9	2.6	10.6

Table 3.12: Table of results from short term site stability analysis. Time Series RMS is the RMS of the cleaned time series residuals after removing earthquake offsets and secular velocity and represents the repeatability of the station positions. Average daily uncertainty is the average formal error determined independently for each day by GAMIT/GLOBK.

proved upon. We are using TrackRT, together with predicted orbits from the International GPS service (IGS) to produce high sample rate displacement time series with 2-3 second latency. TrackRT was developed at MIT and is based on GAMIT/GLOBK, which we use for daily processing. TrackRT follows a network processing approach, with displacements generated with respect to a reference station. The benefits of this approach are that common noise sources, such as local atmosphere, are canceled out, leading to more precise relative displacements.

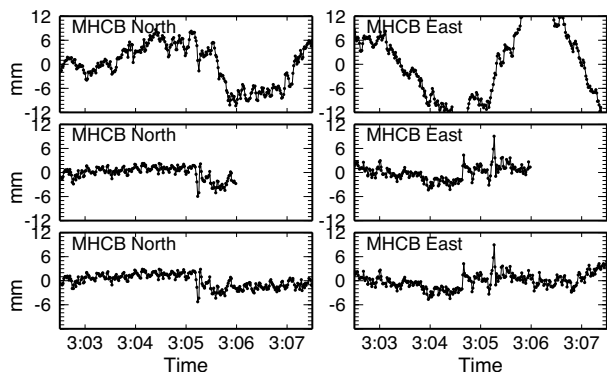


Figure 3.23: Time series of East and North motions for station MHCB during the M5.5 Alum Rock earthquake. The top row is simulated real-time data processing, the middle row is post-processing including up to a minute of data after the event origin time and the bottom row includes 10 minutes of post-earthquake data. Note that the plots are in GPS time, such that the earthquake origin time would plot as 3:05:09.

The scatter in the displacements time series for each baseline depends on distance and increases during days with changeable weather conditions. However, it is often within 2 cm over the course of 24 hours, which is considered a stable result. Nonetheless, the size of the scatter has implications for the size of earthquake for which GPS will be able to provide information in real time. Simulations of the moderately-sized 2007 M5.5 Alum Rock earthquake show that the time series produced in real time would have been very difficult to use to obtain static offsets (Figure 3.23). Post-processed time series, delayed by as little as 1 minute, produced cleaner time series and could have produced reasonable estimates of the static offsets (see Section 23). This implies that separate approaches should be taken for using GPS data for Earthquake Early Warning for large events and for using it for rapid response to moderate or large earthquakes.

### 5.3 Acknowledgements

The BARD program is overseen by Ingrid Johanson and Richard Allen. Bill Karavas, John Friday, Aaron Enright, Joshua Miller, Doug Neuhauser, Mario

Aranha and Jennifer Taggart contributed to the operation of the BARD network in 2011-12. Operation of the BARD network is partially supported by funding from the USGS/NEHRP program grant #G10AC00141 and infrastructure upgrades were made possible by funding from the ARRA grant #G10AC00079. Real-time data processing is supported by a grant from the Moore Foundation.

### 5.4 References

d'Alessio, M. A., I. A. Johanson, R. Bürgmann, D. A. Schmidt, and M. H. Murray, Slicing up the San Francisco Bay Area: Block kinematics from GPS-derived surface velocities, *J. Geophys. Res.*, *110*, B06403, doi:10.1029/2004JB003496, 2005.

Herring, T., GLOBK: Global Kalman Filter: VLBI and GPS Analysis Program, version 10.2, 2005.

Houlié, N. and Romanowicz, B., Asymmetric deformation across the San Francisco Bay Area faults from GPS observations in northern California, *Phys. Earth Planet. In.*, in press.

King, R., and Y. Bock, Documentation of the GAMIT software, MIT/SIO, 1999.

## 6 Northern California Earthquake Data Center

### 6.1 Introduction

The Northern California Earthquake Data Center (NCEDC) is a permanent archive and distribution center primarily for multiple types of digital data relating to earthquakes in central and northern California. The NCEDC is located at the Berkeley Seismological Laboratory, and has been accessible to users via the Internet since mid-1992. The NCEDC was formed as a joint project of the Berkeley Seismological Laboratory (BSL) and the U.S. Geological Survey (USGS) at Menlo Park in 1991, and current USGS funding is provided under a cooperative agreement for seismic network operations.

Time series data come from broadband, short period, and strong motion seismic sensors, and geophysical sensors such as electromagnetic sensors, strain meters, creep meters, pore pressure, water level, and wind speed sensors. Earthquake catalogs can include time, hypocenter, magnitude, moment tensor, mechanisms, phase arrivals, codas, and amplitude data. GPS data are available in both raw observables and RINEX formatted data.

The NCEDC also provides support for earthquake processing and archiving activities of the Northern California Earthquake Management Center (NCEMC), a component of the California Integrated Seismic Network (CISN). The CISN is the California regional organization of the Advanced National Seismic System (ANSS).

### 6.2 2011-2012 Activities

By its nature, data archiving is an ongoing activity. In 2011-2012, the NCEDC continued to expand its data holdings and enhance access to the data. Projects and activities of particular note include:

- Purchased SAN (Storage Area Network) storage and fibre channel switches to upgrade and expand the NCEDC data storage and archive systems.
- Developed and tested Web services for the distribution of station metadata using Station XML, waveform inventory, and MiniSEED data.
- Began receiving, archiving, and distributing event information (hypocenter, magnitude, phase, and amplitude data) and waveforms for the DOE Enhanced Geothermal Systems (EGS) monitoring project.
- Continued the process of reading and archiving continuous NCSN seismograms from tapes for 1993-1998.

- Continued to support the NCEMC earthquake analysis by providing real-time access to earthquake parameters and waveforms from the NCEDC for the CISN Jiggle earthquake review software.
- Completed work with the NCSN and USGS National Strong Motion Program (NSMP) to import the metadata and build dataless SEED volumes for all NSMP dialup stations.
- Began continuous data archiving from the LBNL Geysers Network, a dense network of 32 3-component stations acquiring data at 500 samples/second to monitor the California Geysers geothermal region.

### 6.3 Data Types and Contributors

Table 3.13 and Figure 3.24 provide a breakdown of the NCEDC data by data type. Figure 3.25 shows the total data volume by year as itemized in Table 3.13.

#### BDSN/NHFN/mPBO Seismic Data

The BDSN (Operational Section 1), NHFN (Operational Section 3), and Mini-PBO (Operational Section 3) stations (all network code BK) send real-time data from 50 seismic data loggers to the BSL. These data are written to disk files, used by the CISN AQMS software for real-time earthquake processing and by the prototype CISN ShakeAlert earthquake early warning (EEW) system, and delivered to the DART (Data Available in Real Time) system at the NCEDC, where they are immediately available to anyone on the Internet. Continuous high-rate data (200 - 500 samples/second) are now available for most of the NHFN borehole seismic data channels. All timeseries data from the Berkeley networks continue to be processed and archived by an NCEDC analyst using *calqc* quality control procedures in order to provide the highest quality and most complete data stream for the NCEDC archive. The recent upgrades to the BDSN stations increased the onsite storage at each site, which allows us to recover data from the station after telemetry outages and improve the completeness of the BDSN data archive.

#### NCSN Seismic Data

NCSN continuous waveform data are transmitted from USGS/Menlo Park in real time to the NCEDC via the Internet, converted to MiniSEED, and made available to users immediately through the NCEDC DART. NCSN event waveform data, as well as data from all other real-time BSL and collaborating networks, are automatically

Data Type	GBytes
BDSN/NHFN/mPBO (broadband, electric and magnetic field, strain) waveforms	8,203
NCSN seismograms	30,118
Parkfield HRSN seismograms	3,877
GPS (RINEX and raw data)	2,933
UNR Nevada seismograms	1,580
SCSN seismograms	2,791
Calpine/Unocal Geysers region seismograms	38
EarthScope SAFOD seismograms	2,119
EarthScope USArray seismograms	281
EarthScope PBO strain and seismic waveforms	2,949
PG&E seismograms	688
USGS low frequency geophysical waveforms	3
Misc data	3,245
Total size of archived data	58,825

Table 3.13: Volume of Data Archived at the NCEDC by network.

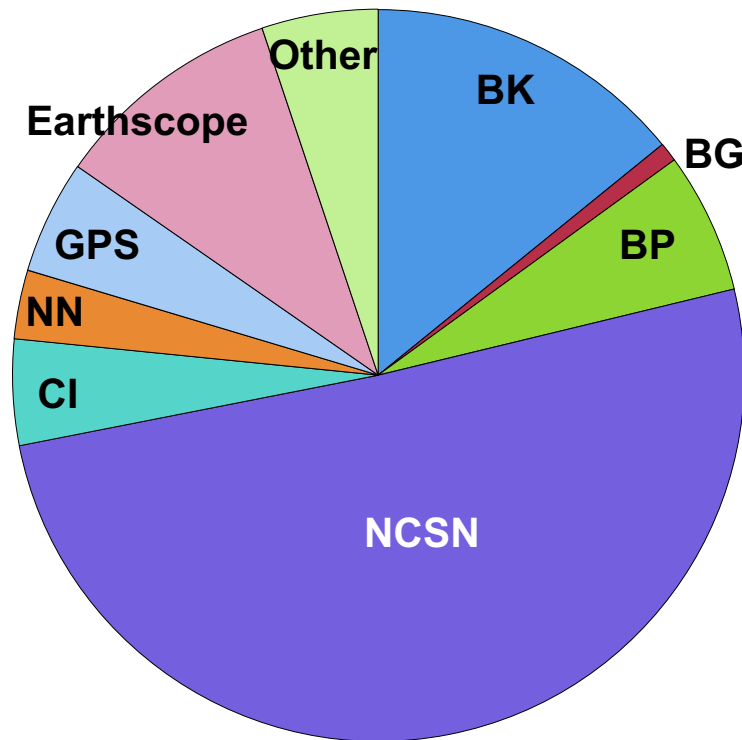


Figure 3.24: Chart showing the relative proportion of each data set at the NCEDC. BK - Berkeley Digital Seismic Network; BP - Berkeley High-resolution Seismic Network in Parkfield; NCSN - Northern California Seismic Network and collaborators; CI - Southern California Seismic Network; NN - University of Nevada, Reno Seismic Network; GPS - various GPS datasets, including BARD; EarthScope - data from various EarthScope activities; Other - various small data sets.

collected by the NCEMC waveform archiver and stored at the NCEDC for event review and analysis and for distribution to users. All NCSN and NCEMC data are archived in MiniSEED format.

Improvements in the acquisition of NCSN data, described in the 2005-2006 BSL Annual report, enabled the NCEDC to start archiving continuous NCSN waveforms in early 2006. We then started the process of reading and archiving continuous NCSN waveforms from previous years that had been saved on tapes. We finished the first phase of the NCSN tape continuous waveform archiving for the data from 1996 to early 2006, and have continued the project this year by processing and archiving NCSN tape data from 1993 through 1996.

### **Parkfield High Resolution Seismic Network Data**

The history of upgrades to the acquisition and archival of HRSN data can be found in the 2010-2011 BSL Annual Report. We continue to archive continuous 250 and 20 sample-per-second data from the HRSN stations. The most recent HRSN station upgrade added 16 GB of local storage at each site, which allows us to recover data from the station after telemetry outages, and greatly improves the completeness of the HRSN data archive.

### **EarthScope Plate Boundary Observatory (PBO) Strain Data**

The NCEDC is one of two funded archives for PBO EarthScope borehole and laser strain data. Strain data are collected from all of the PBO strain sites and are processed by UNAVCO. MiniSEED data are delivered to the NCEDC using SeedLink, and raw and XML processed data are delivered to the NCEDC using Unidata's Local Data Manager (LDM). The MiniSEED data are inserted into the NCEDC DART and are subsequently archived from the DART. UNAVCO provides EarthScope funding to the NCEDC to help cover the processing, archiving, and distribution costs for these data. In early 2010, the NCEDC began receiving and archiving all of the continuous seismic waveform data from the PBO network to complement the PBO strain data. The seismic data are received from an Antelope ORB server at UNAVCO and converted from their native format to MiniSEED on a data import computer. The data are then transferred via the SEEDLink protocol to the NCEDC, inserted into the NCEDC DART for immediate Internet access, and subsequently archived from the DART.

### **EarthScope SAFOD**

The NCEDC is an archive center for the SAFOD event data and has also processed the continuous SAFOD data. Starting with the initial data in July 2002 from the SAFOD Pilot Hole, and, later, data from the SAFOD

Main Hole, the NCEDC converted data from the original SEG-2 format data files to MiniSEED, and developed the SEED instrument responses for this data set. Continuous 4 KHz data from SAFOD written to tape at SAFOD were periodically sent to the BSL to be converted, archived, and forwarded to the IRIS DMC (IRIS Data Management Center). SAFOD EarthScope funding to the NCEDC is to cover the processing, archiving, and distribution costs for these data. A small subset of the continuous SAFOD data channels are also incorporated into the NCSN, are available in real-time from the NCEDC DART, are archived at the NCEDC, and are forwarded to the IRIS DMC. After the failure of the SAFOD permanent instrument in September 2008, the USGS deployed a temporary network in the Main Hole, and the NCEDC continued to process and archive these data. Both the permanent and temporary seismic instruments were removed in mid-2010 in order to analyze the failure of the permanent SAFOD instrument packet, but the temporary seismic instruments were reinstalled in late 2010 and continue to send data for distribution and archiving to the NCEDC.

### **UNR Broadband Data**

The University of Reno in Nevada (UNR) operates several broadband stations in western Nevada and eastern California that are important for Northern California earthquake processing and analysis. Starting in August 2000, the NCEDC has been receiving and archiving continuous broadband data from selected UNR stations. The data are transmitted in real time from UNR to UC Berkeley, where they are made available for CISN real-time earthquake processing and for archiving. Initially, some of the stations were sampled at 20 Hz, but all stations are now sampled and archived continuously at 100 Hz.

The NCEDC installed Simple Wave Server (SWS) software at UNR, which provides an interface to UNR's recent collection of waveforms. The SWS is used by the NCEDC to retrieve waveforms from UNR that were missing at the NCEDC due to real-time telemetry outages between UNR and UC Berkeley.

In early 2006, the NCEDC started to archive continuous data from the UNR short-period stations that are contributed to the NCSN. Both the broadband and short-period UNR stations contributed to the CISN are available in real-time through the NCEDC DART.

### **Electro-Magnetic Data**

The NCEDC continues to archive and process electric and magnetic field data acquired at several UC Berkeley sites. The BSL operates both magnetic and electric field sensors at SAO. However, most of these channels have been down for repair during the 2010-2011 year. Through a collaboration with Dr. Simon Klemperer at Stanford

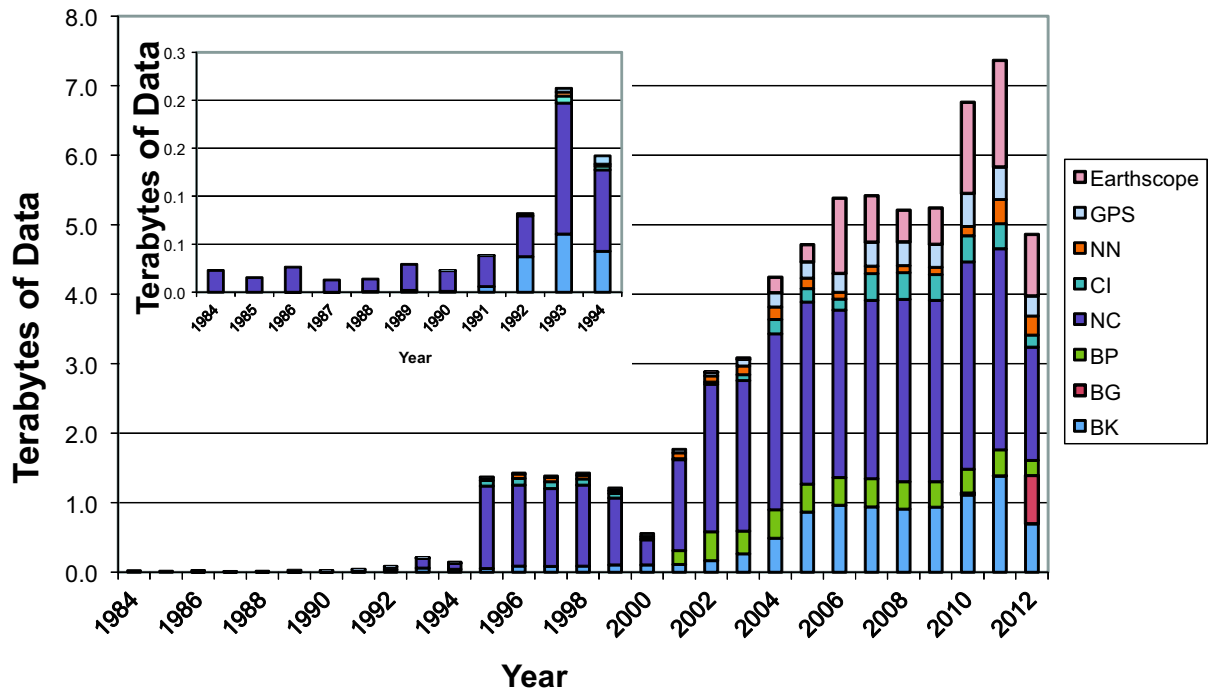


Figure 3.25: Figure showing the total volume of data archived at the NCEDC, broken down by data year.

University, we acquire magnetic and electric field channels at BSL sites JRSC and BRIB, and magnetic field channels at site MHDL. The three magnetic field channels and either two or four electric field channels are digitized at 40 Hz, 1 Hz, and 0.1 Hz, and are telemetered in real-time along with seismic data to the Berkeley Seismological Laboratory, where they are processed and archived at the NCEDC in a similar fashion to the seismic data.

### GPS Data

The NCEDC continues to archive GPS data through the BARD (Bay Area Regional Deformation) network of continuously monitored GPS receivers in Northern California (Operational Section 5). The NCEDC GPS daily archive now includes 80 continuous sites in Northern California. Of these, there are ~ 32 core BARD sites owned and operated by UC Berkeley, USGS (Menlo Park and Cascade Volcano Observatory), LLNL, UC Davis, UC Santa Cruz, Trimble Navigation, and Stanford. Data are also archived from sites operated by other agencies, including the East Bay Municipal Utilities District, the City of Modesto, the National Geodetic Survey, and the Jet Propulsion Laboratory (JPL).

In addition to the standard 15 second continuous GPS data files, the NCEDC is now archiving and distributing high-rate 1 Hz continuous GPS data from all of the BSL-operated BARD stations. In collaboration

with UC San Diego/Scripps Institution of Oceanography (UCSD/SIO), USGS/Pasadena and USGS/MP, the BSL is now streaming real-time 1 Hz continuous data from 42 sites, including all BSL sites and the 13 PBO stations in Parkfield, to the BSL, where it makes the data available to researchers in real time through an Ntripcaster.

The NCEDC also archives non-continuous survey GPS data. The initial dataset archived is the survey GPS data collected by the USGS Menlo Park for Northern California and other locations. The NCEDC is the principal archive for this dataset. Significant quality control efforts were implemented by the NCEDC to ensure that the raw data, scanned site log sheets, and RINEX data are archived for each survey.

### Geysers Seismic Data

The Calpine Corporation operated a micro-seismic monitoring network in the Geysers region of Northern California. Prior to 1999, this network was operated by Unocal. Through various agreements, both Unocal and Calpine have released triggered event waveform data from 1989 through 2000 along with preliminary event catalogs for the same time period for archiving and distribution through the NCEDC. This dataset represents over 296,000 events that were recorded by the Calpine/Unocal Geysers network and are available via research accounts at the NCEDC.

The Lawrence Berkeley National Laboratory (LBNL),

with funding from the California Energy Commission, currently operates a 32 station network in the Geysers region with an emphasis on monitoring seismicity related to well water injection. The earthquake locations and waveforms from this network are sent to the NCEDC, and the locations are forwarded to the NCSN so that they can be merged into the NCSN earthquake catalog. In August 2007, the NCSN installed an Earthworm system at the Geysers to receive continuous LBNL Geysers data, and this system provides event waveforms for events detected by the NCEMC real-time earthquake monitoring and processing system and the corresponding event data archive at the NCEDC. The event data from LBNL Geysers event waveforms collected from April 2004 to August 2007 will be associated with events from the NCSN catalog and will be included with the existing waveforms for these events. In March 2012, the NCEDC began to receive continuous data from the stations in near real-time, and began archiving these continuous data.

### **DOE Enhanced Geothermal Monitoring (EGS) Data**

Starting in 2010-2011, BSL was funded through LBNL to archive and disseminate seismic event parameters and corresponding waveform timeseries from monitoring networks operated under the auspices of the US Department of Energy Geothermal Monitoring Program. We have collected and verified the station metadata for these networks, and populated the data into the database. This year we began to receive and archive the event data and waveforms from these networks. The timeseries data are available via our suite of data delivery methods, and the event and parametric information are available via a new Web catalog search page.

### **USGS Low Frequency Data**

Since 1974, the USGS at Menlo Park, in collaboration with other principal investigators, has collected an extensive low-frequency geophysical data set that contains over 1300 channels of tilt, tensor strain, dilatational strain, creep, magnetic field, and water level as well as auxiliary channels such as temperature, pore pressure, rain and snow accumulation, and wind speed. In collaboration with the USGS, we assembled the requisite information for the hardware representation of the stations and the instrument responses for many channels of this diverse dataset, and developed the required programs to populate and update the hardware database and generate the instrument responses. We developed the programs and procedures to automate the process of importing the raw waveform data and converting it to MiniSEED format. Since these data are delivered to the NCEDC on a daily basis and immediately archived, these data are not inserted into the NCEDC DART.

We have currently archived timeseries data from 887 data channels from 167 sites, and have instrument response information for 542 channels at 139 sites. The waveform archive is updated on a daily basis with data from 350 currently operating data channels.

The USGS is reducing support for these stations, and the network is being slowly retired. The NCEDC continues to receive and archive the data channels that are being provided by the USGS.

### **SCSN/Statewide Seismic Data**

In 2004, the NCEDC started to archive broadband and strong motion data from 15 SCSN (network CI) stations that are telemetered to the Northern California Earthquake Management Center (NCEMC) of the California Integrated Seismic Network (CISN). These data are used in the prototype real-time state-wide earthquake processing system and also provide increased coverage for Northern California events. Since the data are telemetered directly from the stations in real time to both the SCSN and to the NCEMC, the NCEDC archives the NCEMC's copy of the data to ensure that at least one copy of the data will be preserved. Due to reduced state funding, the SCSN has gradually reduced the number of telemetered stations to 9.

In early 2006, the NCEDC started to continuously archive all of the selected SCSN short-period stations that are contributed to the NCSN. All of these data are also available in real time from the NCEDC DART. In 2009, the NCEMC started incorporating data from ~ 25 additional SCSN stations near the southern border of the NCEMC monitoring area in its event waveform collection to provide better azimuthal coverage of events in that area. In 2009-2010, the NCEMC also started retrieving event waveform data from the SCSN for other SCSN stations that are expected to receive signals from Northern California earthquakes. All of these event waveforms are also archived at the NCEDC.

### **Earthquake Catalogs**

The NCEDC hosts multiple earthquake catalogs.

**Northern California catalog:** The NCEDC provides searchable access to both the USGS and BSL earthquake catalogs for northern and central California. The "official" UC Berkeley earthquake catalog begins in 1910 and runs through 2003, and the "official" USGS catalog begins in 1966. Both of these catalogs are archived and available through the NCEDC, but the existence of two catalogs has caused confusion among both researchers and the public.

In late 2006, the NCEMC began archiving and distributing a single unified Northern California

earthquake catalog in real time to the NCEDC through database replication from the NCEMC's real-time systems. The NCEDC developed and tested the required programs used to enter all previous NCSN catalog data into the NCEDC database. In 2008, we migrated all of the historic NCSN catalog, phase, and amplitude data from 1967 through 2006 into the NCEMC catalog. In addition, we spent considerable effort addressing the mapping of phase data in the BSL catalog to SEED channel names. We plan to merge the BSL catalog with the NCEMC catalog to form a single unified Northern California catalog from 1910 to the present. The BSL and the USGS have spent considerable effort over the past years to define procedures for merging the data from the two catalogs into a single northern and central California earthquake catalog in order to present a unified view of Northern California seismicity. The differences in time period, variations in data availability, and mismatches in regions of coverage all complicate the task.

**Enhanced Geothermal Systems (EGS) catalog:**

US Department of Energy Geothermal Monitoring Program is operating a number of seismic networks that monitor earthquakes in the regions of enhanced geothermal systems. The event catalogs and parametric information are available via a new EGS catalog search page.

**Worldwide catalog:** The NCEDC, in conjunction with the Council of the National Seismic System (CNSS), produced and distributed a world-wide composite catalog of earthquakes based on the catalogs of the national and various U.S. regional networks for several years. Each network updates their earthquake catalog on a daily basis at the NCEDC, and the NCEDC constructs a composite world-wide earthquake catalog by combining the data, removing duplicate entries that may occur from multiple networks recording an event, and giving priority to the data from each network's *authoritative region*. The catalog, which includes data from 14 regional and national networks, is searchable using a Web interface at the NCEDC. The catalog is also freely available to anyone via FTP over the Internet.

With the demise of the CNSS and the development of the Advanced National Seismic System (ANSS), the NCEDC was asked to update its Web pages to present the composite catalog as a product of the ANSS. This conversion was completed in the fall of 2002. We continue to create, house, distribute, and provide a searchable Web interface to the ANSS composite catalog, and to aid the regional networks in submitting data to the catalog.

## 6.4 NCEDC Operations

The current NCEDC facilities consist of a mass storage environment hosted by a 8-core Sun X4150 computer, a 100 slot LTO3 tape library with two tape drives and a 20 TByte capacity, and 180+ TBytes of RAID storage, all managed with the SAM-FS hierarchical storage management (HSM) software. Four additional 8-core Sun computers host the DART data import, data archiving, computing Probability Density Function (PDF) plots for the bulk of the NCEMC waveforms, data quality control procedures, and Internet distribution. Two 64-bit Linux systems host redundant Oracle databases.

In 2005, the NCEDC relocated its archive and distribution system from McCone Hall to a new state-of-the-art computer facility in a new seismically braced building on the Berkeley campus. The facility provides seismically braced equipment racks, gigabit Ethernet network, air conditioning, and power conditioning. The entire facility is powered by a UPS with generator backup.

In 2008-2009, the tape library was upgraded from LTO2 to LTO3 drives, and all online tape data was re-archived on LTO3 tapes. DLT tape libraries are used to read NCSN continuous data tapes.

In 2011-2012, the NCEDC data archive grew to exceed the NCEDC online disk capacity. We acquired a new SAN disk storage system that provides the NCEDC with 90 TB of primary online storage and 90 TB of SAMFS cache to improve filesystem performance. We migrated all of the waveform and GPS archive data to the new SAN storage. In addition, we upgraded the fibre channel switches to support the 8 Gbit/second interfaces of the new SAN disk system and computer interfaces.

The SAMFS hierarchical storage management (HSM) software used by the NCEDC is configured to automatically create multiple copies of each data file in the archive. The NCEDC creates one copy of each file on an online RAID, a second copy on LTO3 tape (of which the most recent data are stored online in the tape library), and a third copy on LTO2 tape which is stored offline and off-site. In addition, all SAMFS data are stored in an online disk cache which provides instant access to these data. In 2011-2012 we renewed our SAMFS license, which now allows us to manage an unlimited amount of storage.

The NCEDC operates two instances of its Oracle database, one for internal operations and one for external use for user data queries and data distribution programs, and communicates with a third identical database operated offsite by the USGS in Menlo Park. These three databases are synchronized using multi-master replication.

**DART (Data Available in Real Time)**

The DART (Data Available in Real Time) provides a network-accessible structured filesystem to support real-time access to current and recent timeseries data from

all networks, stations, and channels. All real-time time-series data streams delivered to the NCEDC are placed in MiniSEED files in a Web-accessible directory structure. The DART currently contains the most recent 40 days of data. The DART waveforms can be accessed by users from Web browsers or command-line programs such as *wget*, or through NCEDC data services described in the data distribution section of this document.

We use the IRIS ringserver software as the primary method for delivering real-time data to the DART. The ringserver packages implement an object ring buffer (ORB) and server which provides a reliable storage ring buffer and an interface for client programs to read, write, and query the orbserver. Clients running at the NCEDC computer connect to remote servers at the BSL, USGS/Menlo Park, and UNAVCO, retrieve the MiniSEED timeseries data records, and write them to daily channel files in the NCEDC DART. Strain data from the EarthScope PBO network are delivered to the NCEDC using SeedLink and are inserted into the DART using a similar SeedLink client program.

The NCEDC developed an automated data archiving system to archive data from the DART on a daily basis. It allows us to specify which stations should be automatically archived, and which stations should be handled by the NCEDC's Quality Control program *calqc*. The majority of non-BSL data channels are currently archived automatically from the DART.

### Data Quality Control

The NCEDC developed a GUI-based state-driven system *calqc* to facilitate the quality control processing that is applied to the BSL stations continuously archived data sets at the NCEDC.

The quality control procedures for these datasets include the following tasks:

- data extraction of a full day of data,
- quickcheck program to summarize the quality and stability of the stations' clocks,
- determination if there is missing data for any data channel,
- provided procedures to retrieve missing data from the stations and incorporate it into the day's data,
- optional creation of multi-day timeseries plots for state-of-health data channels,
- optional timing corrections for data,
- optional extraction of event-based waveforms from continuous data channels,
- optional repacking of MiniSEED data,

- creating waveform inventory entries in the NCEDC database,
- publishing the data for remote access on the NCEDC.

*Calqc* is used to process all data from the BDSN and HRSN network, and all continuous broadband data from the NCSN, UNR, and SCSN networks that are archived by the NCEDC. The remainder of the continuously archived data are automatically archived without any analyst interaction.

### Database Activity

The NCEDC continues to support the Northern California Earthquake Management Center (NCEMC) by providing information and resources vital to the NCEMC's role of rapid earthquake analysis and data dissemination. The NCEDC receives earthquake parametric data in real time from the NCEMC real-time systems and provides real-time access to the NCEDC database for *jiggle*, the CISEN event analysis tool. The NCEMC continues to support the maintenance and distribution of the hardware configurations and instrument responses of the UCB, USGS/MP NCSN, and other seismic stations used by the NCEMC. BSL staff currently chairs the CISEN Schema Change working group, which coordinates all database schema changes and enhancements within the CISEN.

The NCEDC instrument response schema represents full multi-stage instrument responses (including filter coefficients) for the broadband data loggers. The hardware tracking schema represents the interconnection of instruments, amplifiers, filters, and data loggers over time, and is used to describe all of the UC Berkeley and USGS stations and channels archived at the NCEDC.

Database developments in the 2011-2012 year include new sets for associating strong ground motion observations with events, merging of channel table tables for real-time and post-processing applications, and adding additional event types to describe a wider range of earth motions.

Full details on the database schema used at the NCEDC may be found at <http://www.ncedc.org/db>

### PSD and PDF

Changes in the seismic noise recorded at a site in the absence of earthquakes may be an indication of instrumental or other problems. Thus, the regular review of the noise is a useful tool for evaluating station performance and quality. Programs developed by Dan McNamara and Ray Buland at the USGS use a probability density function (PDF) to compute the distribution of seismic power spectral density (PSD) on a daily basis. The results are

aggregated into weekly and yearly plots for each data channel.

The NCEDC computes daily PDFs for all high-rate seismic and strain channels from the Berkeley networks, and for many of the data channels of the NCSN network and other networks that contribute to the operation of the NCEMC. The NCEDC noise analysis plots are available at <http://www.ncedc.org/ncedc.PDF/>

## 6.5 Data Distribution

The NCEDC continues to use the Internet as the interface for users to request, search for, and receive data from the NCEDC. In fall 2005, the NCEDC acquired the domain name *ncedc.org*. The NCEDC's Web address is <http://www.ncedc.org/>

### Earthquake Catalogs

The NCEDC provides users with searchable access to Northern California earthquake catalogs, the DOE EGS catalogs, and the ANSS world-wide catalog via the Web. Users can search the catalogs by time, magnitude, and geographic region, and can retrieve either hypocenter and magnitude information or a full set of earthquake parameters including phase readings, amplitudes, and codas. Moment tensor and first motion mechanisms have been added to the NCEMC California earthquake catalog and are searchable from the NCEDC Web catalog search page.

### Station Metadata

In addition to the metadata returned through the various data request methods, the NCEDC provides dataless SEED volumes and SEED RESP files for all data channels archived at the NCEDC. The NCEDC currently has full SEED instrument responses for 20,891 data channels from 2,315 stations in 23 networks. This includes stations from the California Geological Survey (CGS) strong motion network that will contribute seismic waveform data for significant earthquakes to the NCEDC and SCEDC. In collaboration with the USGS NCSN and the NSMP (National Strong Motion Program), the NCEDC is building the metadata and dataless SEED volumes for over 700 stations and 4700 data channels of the NSMP dialup stations. Station metadata can be acquired by downloading pre-assembled dataless SEED files, using NetDC to request metadata by station, channel and time, or by new NCEDC Web services.

### Web Services

The NCEDC developed and deployed five Web services for distributing both timeseries and related channel metadata. Web services use standard web HTTP protocol for sending requests and receiving data. Web services can be used interactively from a web browser, or can be easily

called from scripts and user programs. These Web services are compatible with the corresponding IRIS DMC Web services. These new data services are:

**ws-station** - provides station and channel metadata in StationXML format.

**ws-resp** - provides channel instrument response in RESP format.

**ws-availability** - returns information about what time series data is available at the NCEDC archive.

**ws-dataselect** - returns a single channel of time series data in miniSEED format from the NCEDC archive.

**ws-bulkdataselect** - returns multiple channels of time series data in miniSEED format for specified time ranges.

StationXML is an XML (Extensible Markup Language) schema designed for sharing station metadata. StationXML was originally designed at the SCEDC and is now maintained in collaboration with NCEDC, IRIS, and NEIC. RESP format is the ascii channel response format created by the IRIS rdseed program, and supported by programs such as evalresp. Documentation on Station XML is available at <http://www.data.scec.org/xml/station/>

### SeismiQuery

The NCEDC ported and installed the IRIS *SeismiQuery* program at the NCEDC, which provides a web interface to query network, station, and channel attributes and query the availability of archived timeseries data.

### NetDC

In a collaborative project with the IRIS DMC and other worldwide datacenters, the NCEDC helped develop and implement *NetDC*, a protocol which will provide a seamless user interface to multiple datacenters for geophysical network and station inventory, instrument responses, and data retrieval requests. *NetDC* builds upon the foundation and concepts of the IRIS *BREQ\_FAST* data request system. The *NetDC* system was put into production in January 2000 and is currently operational at several datacenters worldwide, including NCEDC, IRIS DMC, ORFEUS, Geoscope, and SCEDC. The *NetDC* system receives user requests via email, automatically routes the appropriate portion of the requests to the appropriate datacenter, optionally aggregates the responses from the various datacenters, and delivers the data (or FTP pointers to the data) to the users via email.

## STP

In 2002, the NCEDC wrote a collaborative proposal with the SCEDC to the Southern California Earthquake Center, with the goal of unifying data access between the two data centers. As part of this project, the NCEDC and SCEDC are working to support a common set of 3 tools for accessing waveform and parametric data: *Seis-miQuery*, *NetDC*, and *STP*.

The *Seismogram Transfer Program* or *STP* is a simple client-server program, developed at the SCEDC. Access to *STP* is either through a simple direct interface that is available for Sun or Linux platforms, or through a GUI Web interface. With the direct interface, the data are placed directly on a user's computer in several possible formats, with the byte-swap conversion performed automatically. With the Web interface, the selected and converted data are retrieved with a single FTP command. The *STP* interface also allows rapid access to parametric data such as hypocenters and phases.

The NCEDC has continued work on *STP*, working with the SCEDC on extensions and needed additions. We added support for the full SEED channel name (Station, Network, Channel, and Location), and are now able to return event-associated waveforms from the NCSN waveform archive.

## EVT\_FAST

In order to provide Web access to the NCSN waveforms before the SEED conversion and instrument response for the NCSN has been completed, the NCEDC implemented *EVT\_FAST*, an interim email-based waveform request system similar to the *BREQ\_FAST* email request system. Users email *EVT\_FAST* requests to the NCEDC and request NCSN waveform data based on the NCSN event ID. *EVT\_FAST* event waveforms can be delivered in either MiniSEED or SAC format, and are now named with their SEED channel names.

## FISSURES

The *FISSURES* project developed from an initiative by IRIS to improve earth scientists' efficiency by developing a unified environment that can provide interactive or programmatic access to waveform data and the corresponding metadata for instrument response, as well as station and channel inventory information. *FISSURES* was developed using CORBA (Common Object Request Broker Architecture) as the architecture to implement a system-independent method for the exchange of this binary data. The IRIS DMC developed a series of services, referred to as the *Data Handling Interface (DHI)*, using the *FISSURES* architecture to provide waveform and metadata from the IRIS DMC.

The NCEDC has implemented the *FISSURES Data Handling Interface (DHI)* services at the NCEDC, which

involves interfacing the DHI servers with the NCEDC database schema. These services interact with the NCEDC database and data storage system and can deliver NCEDC channel metadata as well as waveforms using the *FISSURES* interfaces. We have separate *FISSURES DHI* waveform servers to serve archived and DART data streams. Our *FISSURES* servers are registered with the IRIS *FISSURES naming services*, which ensures that all *FISSURES* users have transparent access to data from the NCEDC.

## SWC and SWS

UC Berkeley developed the Simple Wave Server *swc* and Simple Wave Client *sws* programs to provide access to its MiniSEED data from the DART and the NCEDC archive. It currently operates a separate server for each of the above services. The *swc* program is a command-line client program written in perl that runs under Linux, Unix, and MacOS and allows users to easily retrieve waveform data in MiniSEED format by channel and time window or by NCEMC event gathers. The program is packaged for easy user installation and can be downloaded from the NCEDC web site.

The NCEDC operates two distinct SWS services. The *ncedc.archive* service provides access to data that has been formally archived at the NCEDC, and the *dart* service provides access to real-time data from the DART.

## GPS

GPS data (raw data, RINEX data at 15 second interval, and high-rate 1 Hz RINEX data) are all available via HTTP or FTP over the Internet in a well-defined directory structure organized by data type, year, and day-of-year.

## 6.6 Metrics for 2011-2012

- Distributed over 7,075 GB of waveform, GPS, and earthquake catalog data to external users.
- NCEDC uptime for data delivery was over 99.5% for the year.
- Tables 3.14 and 3.15 show the percentage of data archived as a percentage of the station operational time for BSL stations based on the highest rate vertical data channel for each station. If channels were renamed during the year due to equipment upgrades, or we operated multiple data loggers at the site, there may be multiple entries for that site.

Net	Sta	Cha	Loc	%Archived
BP	CCRB	DP1	–	24.12%
BP	CCRB	DP1	40	99.80%
BP	EADB	DP1	–	99.70%
BP	EADB	DP1	40	99.98%
BP	FROB	DP1	40	99.91%
BP	GHIB	DP1	–	97.64%
BP	GHIB	DP1	40	99.90%
BP	JCNB	DP1	–	0.00%
BP	JCNB	DP1	40	99.95%
BP	JCSB	DP1	40	99.97%
BP	LCCB	DP1	–	26.50%
BP	LCCB	DP1	40	99.93%
BP	MMNB	DP1	40	100.00%
BP	RMNB	DP1	–	100.00%
BP	SCYB	DP1	–	97.96%
BP	SCYB	DP1	40	100.00%
BP	SMNB	DP1	40	99.93%
BP	VARB	DP1	40	99.98%
BP	VCAB	DP1	40	99.89%

Table 3.14: Percentage of Continuous Data Archived for BP stations based on station operation time for the year.

## 6.7 Acknowledgements

The NCEDC is a joint project of the BSL and the USGS Menlo Park and is funded primarily by BSL and USGS Cooperative Agreements G10AC00141 and G10AC00093. Additional funding for the processing and archiving of the EarthScope PBO and SAFOD data were provided by EarthScope subawards EAR0732947-07 through UNAVCO. Archival of geothermal monitoring data are provided through LBNL project number 6948613.

Douglas Neuhauser is the manager of the NCEDC. Stephane Zuzlewski, Mario Aranha, Ingrid Johanson, Taka’aki Taira, Jennifer Taggart, Clay Miller, and Peggy Hellweg of the BSL and David Oppenheimer, Hal Macbeth, Lynn Dietz, and Fred Klein of the USGS Menlo Park contribute to the operation of the NCEDC. Doug Neuhauser and Peggy Hellweg contributed to the preparation of this section.

Net	Sta	Cha	Loc	%Archived
BK	BDM	HHZ	00	100.00%
BK	BKS	HHZ	00	100.00%
BK	BL67	HHZ	00	52.17%
BK	BL88	HNZ	00	99.69%
BK	BRIB	DP1	40	99.99%
BK	BRIB	HHZ	00	100.00%
BK	BRK	HHZ	00	100.00%
BK	CMAB	DP1	–	97.98%
BK	CMAB	DP1	40	99.99%
BK	CMB	HHZ	00	100.00%
BK	CVS	HHZ	00	100.00%
BK	FARB	HHZ	00	99.99%
BK	GASB	HHZ	00	84.58%
BK	HAST	HHZ	00	100.00%
BK	HATC	HHZ	00	100.00%
BK	HELL	HHZ	00	100.00%
BK	HERB	DP1	–	100.00%
BK	HOPS	HHZ	00	99.84%
BK	HUMO	HHZ	00	100.00%
BK	JCC	HHZ	00	100.00%
BK	JRSC	HHZ	00	100.00%
BK	KCC	HHZ	00	99.93%
BK	MCCM	HHZ	00	99.91%
BK	MHC	HHZ	00	100.00%
BK	MHDL	EP1	40	100.00%
BK	MNRC	HHZ	00	100.00%
BK	MOBB	BHZ	00	98.71%
BK	MOD	HHZ	00	100.00%
BK	OHLN	EP1	40	99.95%
BK	ORV	HHZ	00	100.00%
BK	OXMT	LP1	40	99.98%
BK	PACP	HHZ	00	99.66%
BK	PETB	EP1	40	99.71%
BK	PKD	HHZ	00	99.98%
BK	RAMR	HHZ	00	100.00%
BK	RB2B	DP1	–	99.67%
BK	RFSB	CN1	40	99.36%
BK	RFSB	HNZ	00	100.00%
BK	SAO	HHZ	00	100.00%
BK	SBRN	EP1	40	99.73%
BK	SCCB	HNZ	00	100.00%
BK	SM2B	DP1	40	100.00%
BK	SUTB	HHZ	00	93.92%
BK	SVIN	EP1	40	99.81%
BK	THIS	HHZ	00	96.44%
BK	TSCN	HHZ	00	99.20%
BK	VAK	HHZ	00	100.00%
BK	VALB	EP1	–	100.00%
BK	WDC	HHZ	00	100.00%
BK	WENL	HHZ	00	99.98%
BK	YBH	HHZ	00	99.31%
BK	YBH	HHZ	50	100.00%

Table 3.15: Percentage of continuous data archived for BK stations based on station operation time for the year.

## 7 Data Acquisition and Quality Control

### 7.1 Introduction

Stations from the networks operated by the BSL transmit data continuously to the BSL facilities on the UC Berkeley campus for analysis and archival. In this section, we describe activities and facilities which pertain to the individual networks described in Operational Sections 1, 3, and 4, including procedures for data acquisition and quality control, and sensor testing capabilities and procedures. Some of these activities are continuous from year to year and have been described in prior BSL annual reports. In this section, we describe changes or activities which are specific to 2011-2012.

### 7.2 Data Acquisition Facilities

The computers and the associated telemetry equipment are located in the campus computer facility in Warren Hall at 2195 Hearst Avenue. This building was constructed to current “emergency grade” seismic codes and is expected to be operational even after a M 7 earthquake on the nearby Hayward Fault. The hardened campus computer facility within was designed with special attention for post-earthquake operations. The computer center contains state-of-the art seismic bracing, UPS power and air conditioning with generator backup, and extensive security and equipment monitoring.

### 7.3 Data Acquisition

Central-site data acquisition for data from the BDSN/HRSN/NHFN/mPBO networks is performed by two computer systems in the Warren Hall data center (Figure 3.26). These acquisition systems also collect data from the Parkfield-Hollister electromagnetic array and the BARD network. A third system is used primarily for data exchange. It transmits data to the U.S. National Seismograph Network (USNSN) from HOPS, CMB, SAO, WDC, HUMO, JCC, MOD, MCCM, ORV and YBH. Data from various subsets of stations also go to the Pacific and Alaska Tsunami Warning Centers, to the University of Washington and to the University of Reno, Nevada. In addition, the Southern California Earthquake Management Center has access to our wavepools for retrieving waveform data to include in its event gathers. Data for all channels of the HRSN are now telemetered continuously from Parkfield to the BSL over the USGS T1 from Parkfield to Menlo Park, and over the NCEMC T1 from Menlo Park to Warren Hall.

The BSL uses the programs `comserv` and `qmaserv` developed by Quanterra for central data acquisition. These programs receive data from remote Quanterra data loggers and redistribute it to one or more client programs.

The clients include `datalog`, which writes the data to disk files for archival purposes, `wdafill`, which writes the data to the shared memory region for processing with the network services routines, and other programs such as the seismic alarm process, the DAC480 system, and the feed for the Memento Mori Web page. Data from the TremorScope stations are acquired using the program `scream`. We are currently developing procedures to feed them into realtime analysis and to archive them.

The two computers performing data acquisition are also “network services” computers that reduce waveforms for processing with the AQMS software (Figure 3.27). To facilitate processing, each system maintains a shared memory region containing the most recent 30 minutes of data for each channel.

In the past, BDSN data loggers which use frame relay telemetry were configured to enable data transmission simultaneously to two different computers over two different frame relay T1 circuits to UCB. Normally, only one of these circuits was enabled. Unfortunately, we had to discontinue the second T1 circuit to which we had subscribed, because of decreases in funding from the State. The `comserv/qmaserv` client program `cs2m` receives data and multicasts it over a private ethernet. The program `mcast`, a modified version of Quanterra’s `comserv` program, receives the multicast data from `cs2m`, and provides a `comserv`-like interface to local `comserv` clients. Thus, each network services computer has a `comserv/qmaserv` server for all stations, and each of the two systems has a complete copy of all waveform data.

We have extended the multicasting approach to handle data received from other networks such as the NCSN and UNR (University of Nevada, Reno). These data are received by Earthworm data exchange programs and are then converted to MiniSEED and multicast in the same manner as the BSL data. We use `mserv` on both network services computers to receive the multicast data and handle it in the same way as the BSL MiniSEED data.

In 2006, the BSL established a real-time data feed of all BSL waveforms between the BSL acquisition systems and the NCEDC computers using the open source Freeorb software. This allows the NCEDC to provide near-real-time access to all BSL waveform data through the NCEDC DART (Data Available in Real Time) system.

We monitor seismic stations and telemetry using the program `seisnetwatch`. This program extracts current information such as time quality, mass positions, and battery voltage and allows it to be displayed. If the parameter departs from the nominal range, the station is marked with yellow or red to indicate a possible problem.

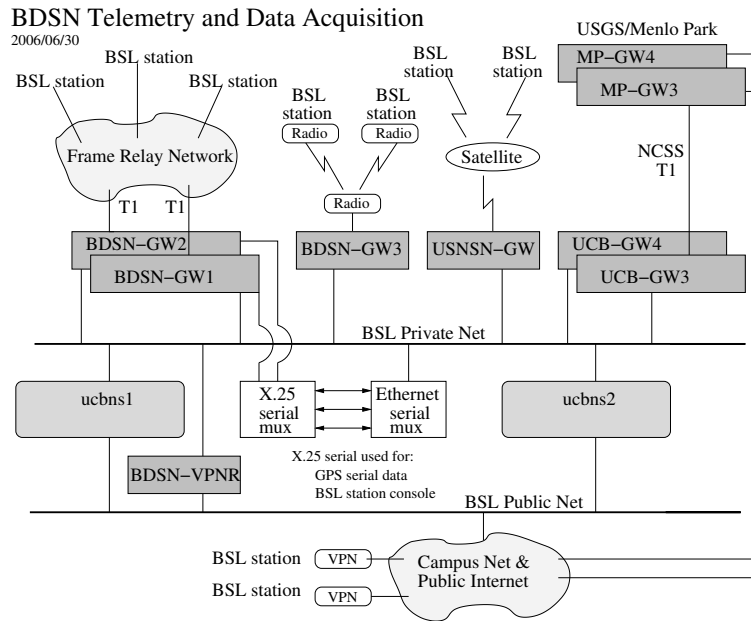


Figure 3.26: Data flow from the BDSN, NHFN, mPBO, HRSN, and BARD networks into the BSL central processing facility.

## 7.4 Seismic Noise Analysis

BSL seismic data are routinely monitored for state of health. An automated analysis is computed regularly to characterize the seismic noise level recorded by each broadband seismometer. In addition, this year we took advantage of the April 11, 2012, M 8.6 earthquake off the coast of northern Sumatra to check noise levels at our STS1 stations in the frequency band from 0.2 mHz to 2 mHz, by looking at the normal mode spectra (see Operational Section 1).

### PSD Noise Analysis

The estimation of the Power Spectral Density (PSD) of the ground motion recorded at a seismic station, as documented in the 2000-2001 BSL annual report ([http://earthquakes.berkeley.edu/annual\\_report/](http://earthquakes.berkeley.edu/annual_report/)) provides an objective measure of background seismic noise characteristics over a wide range of frequencies. It also provides an objective measure of seasonal variation in noise characteristics and supports early diagnoses of instrumental problems. In the early 1990s, a PSD estimation algorithm was developed at the BSL for characterizing the background seismic noise and as a tool for quality control. The algorithm generates a bar graph output in which all the BDSN broadband stations can be compared by component. We also use the weekly PSD results to monitor trends in the noise level at each station. Cumulative PSD plots are generated for each station and show the noise level in 5 frequency bands for the broadband channels. The plots make it easier to spot certain problems, such as failure of a sensor. In addition to the station-based plots, a summary plot is produced

for each channel. The figures are presented as part of a noise analysis of the BDSN on the web at <http://www.earthquakes.berkeley.edu/seismo/bdsn/psd/>.

### PDF PSD Noise Analysis

In addition to the PSD analysis developed by Bob Uhrhammer, the BSL has implemented the Ambient Noise Probability Density Function (PDF) analysis system developed by *McNamara and Buland (2004)*. This system performs its noise analysis over all the data of a given time period (week or year). The data processed includes earthquakes, calibration pulses, and cultural noise.

This is in contrast to Bob Uhrhammer's PSD analysis, which looks at only the quietest portion of data within a day or week. Pete Lombard of the BSL extended the McNamara code to cover a larger frequency range and support the many different types of sensors employed by the BSL. Besides the originally supported broadband sensors, our PDF analysis now includes surface and borehole geophones and accelerometers, strain meters, and electric and magnetic field sensors. These enhancements to the PDF code, plus a number of bug fixes, were provided back to the McNamara team for incorporation in their work. The results of the PDF analysis are presented on our newly upgraded webpage at <http://www.ncedc.org/ncedc/PDF/>. In addition to accessing the PDF plots for each component at a station, the entry page now provides summary figures of the noise at each station, so they can be reviewed quickly. To provide an overview, we have developed summary figures for all components in two spectral bands, 32 - 128 s and 0.125 - 0.25 s for broadband sensors, and

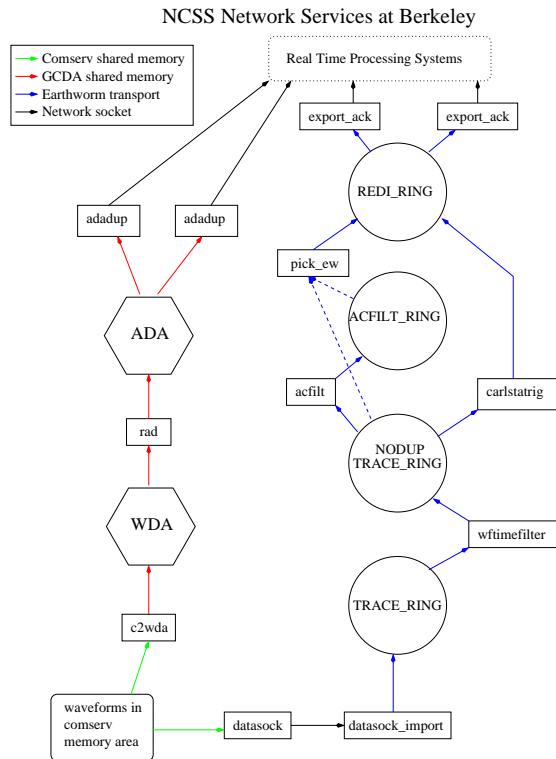


Figure 3.27: Flow of data from `comserv/qmaserv` areas through network services processing. One stream of the network services provides picks (and currently still provides codas) determined using the programs shown in the right flow path. Every 5 seconds, ground motion parameters are also determined, including PGA, PGV, PGD, and ML100 (left flow column). Parameters from the network services are available to the AQMS software for event detection and characterization. Data are also logged to disk (via `dataalog`), distributed to other computers (`mserv`), and spooled into a trace ring for export.

only in the short period band for other short period sensors. The figures are also available on the web at <http://www.ncedc.org/ncedc/PDF/>.

## 7.5 Sensor Testing and Calibration

The BSL has an Instrumentation Test Facility in the Byerly Seismographic Vault where the characteristics of up to eight sensors can be systematically determined and compared. The test equipment consists of an eight-channel Quanterra Q4120 high-resolution data logger and a custom interconnect panel. The panel provides isolated power and preamplification, when required, to facilitate the connection and routing of signals from the sensors to the data logger with shielded signal lines. The vault also has a GPS rebroadcaster, so that all data loggers in the Byerly vault operate on the same time base. Upon acquisition of data at up to 200 sps from the instruments under

test, PSD analysis, coherence analysis, and other analysis algorithms are used to characterize and compare the sensor performance. Tilt tests and seismic signals with a sufficient signal level above the background seismic noise are also used to verify the absolute calibration of the sensors. A simple vertical shake table is used to assess the linearity of a seismic sensor. The sensor testing facility of the BSL is described in detail in the 2001-2002 Annual Report (<http://www.earthquakes.berkeley.edu/>).

## Borehole Geophone Calibration Analysis

Borehole geophones can be calibrated as described in last year's annual report. If there are several sensors at a site, calibration can also proceed by comparing data from two sensors with similar orientation. The NHFN borehole station CMAB, for example, is equipped with OYO Geospace GS-11 geophones and Wilcoxon 731A accelerometers. Data from co-sited geophone and strong-motion sensors allow us to verify the instrument response of the sensors. Assuming the accelerometer response is flat in a frequency band analyzed (e.g., 1-10 Hz), we determine and verify the instrument response of the geophones.

We compared the ground motion observed from the geophones with the corresponding ground motions inferred from the co-sited accelerometers for the 5 March 2012 Mw 4.0 El Cerrito local earthquake (Figure 3.28). Using the instrument response from the factory calibration sheet (the sensor sensitivity of 50 V/m/s, the natural period of 0.2222 sec or 4.5 Hz, and the fraction of critical damping of 0.62), we observed the amplitude and phase discrepancies in a 1-10 Hz band between the geophone and strong-motion data (gray lines in Figures 3.28d and 3.28e). These observed discrepancies indicate that the sensor sensitivities of the accelerometers and geophones, and the natural periods and fractions of critical damping of the geophones need to be updated. Assuming that the sensor sensitivities of the accelerometers in the factory calibration sheet are correct, we determine the geophone sensor sensitivities, natural periods, and fraction of critical dampings by using a grid search approach that finds the solution minimizing the variance between the inferred ground motions from the geophones and the accelerometers in each component. For example, we find the sensitivity vertical geophone component at CMAB to be 42.805 V/m/s, its natural period 0.2288 sec and its fraction of critical damping 0.67. Using the instrument responses determined in our analysis, the inferred ground motions from the geophones in individual components agree with those from the accelerometers (solid lines in Figures 1d and 1e).

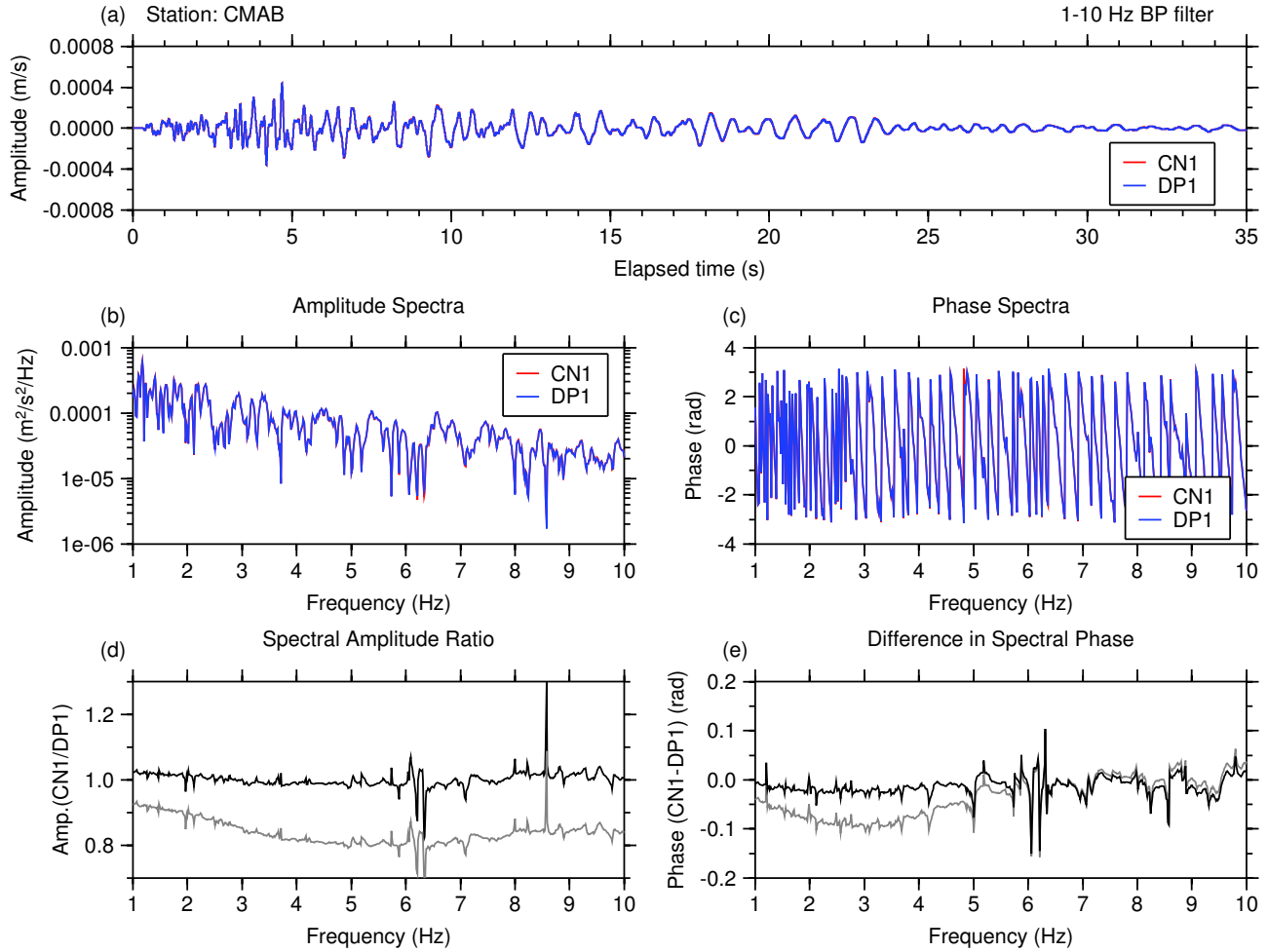


Figure 3.28: Example of the CMAB geophone data with the instrument response determined through our analysis. (a) Observed ground velocity from the CMAB geophone (blue) and accelerometer (red) in the vertical component with a 1-10 Hz bandpass filter. (b) Amplitude and (c) phase spectra of the data shown in (a). (d) Spectral amplitude ratio and (e) difference in spectral phase for the geophone and strong-motion data. Solid lines are the results with the instrument response determined by our analysis while gray lines are results with the instrument responses based on the factory calibration sheet.

## 7.6 STS-1/E300 Calibration Analysis

### Introduction

E300 electronics packages have now been installed as replacement electronics for the STS-1s at BDSN stations CMB, BKS, HOPS, KCC and YBH. The Metrozet STS-1/E300 is an advanced electronics package that is a direct replacement for the original Streckeisen feedback electronics boxes. It matches the analog performance of the original electronics and provides enhancements to facilitate the installation and operation of the STS-1 seismometers in a modern seismic network. In particular, it provides digital control of all seismometer parameters, recentering, and state of health parameters, and it has auxiliary analog and digital input lines. All the control

and diagnostic functions can be controlled either locally or remotely via ethernet. For a detailed description of the determination of the response of the STS-1/E300 seismometer system, see the Annual Report of 2010-2011.

### Monitoring and Evaluating Instrument Response of the STS-1/E300 Systems in the BDSN

After the data logger for the CTBT STS-2 was reinstalled at YBH, we noticed that the response of the STS-1/E300 at that site had changed. As a result, we decided to regularly calibrate the STS-1/E300 combinations installed in the BDSN. At KCC, the E300 does not respond to remote commands, likely due to moisture that entered the cables at splices. We plan to replace those cables with a factory prepared set. In the meantime, we

calibrated the other STS-1/E300 systems shortly after their original installations, and again in February 2012. Results are shown in Table 3.16.

## 7.7 Acknowledgements

Doug Neuhauser, Bob Uhrhammer, Taka Taira, Peggy Hellweg, Pete Lombard, Jennifer Taggart, Tom Weldon and Clay Miller are involved in the data acquisition and quality control of BDSN/HRSN/NHFN/mBPO data. Development of the sensor test facility and analysis system was a collaborative effort of Bob Uhrhammer, Tom McEvelly, John Friday, and Bill Karavas. IRIS (Incorporated Research Institutions for Seismology) and DTRA (Defense Threat Reduction Agency) provided, in part, funding for and/or incentive to set up and operate the facility, and we thank them for their support. Bob Uhrhammer, Taka Taira, Peggy Hellweg, Pete Lombard, Doug Neuhauser and John Friday contributed to the preparation of this section.

## 7.8 References

McNamara, D. and R. Buland, Ambient Noise Levels in the Continental United States *Bull. Seism. Soc. Am.*, 94, 4, 2004.

Rodgers, P.W., A.J. Martin, M.C. Robertson, M.M. Hsu and D.B. Harris, Signal-coil calibration of electromagnetic seismometers, *Bull. Seism. Soc. Am.*, 85, 845-850, 1995.

Calibration Date	Stn	Cmp	Ts	hs	fg	hg	Calibration Date	Stn	Cmp	Ts	hs	fg	hg
2011.235	BKS	Z	359.8	0.715	12.38	0.437	2010.117	HOPS	Z	391.6	0.732	14.98	0.350
			-3.8%	-3.6%	0.5%	4.6%				-0.6%	0%	6.1%	3.1%
2012.040	BKS	Z	346.2	0.689	12.44	0.457	2012.039	HOPS	Z	389.1	0.732	15.89	0.361
			0.6%	0.3%	0%	0.9%				-0.4%	-0.7%	-0.1%	0%
2012.122	BKS	Z	348.2	0.691	12.44	0.461	2012.128	HOPS	Z	387.5	0.727	15.88	0.361
			0.1%	0.1%	-2.8%	-1.3%				0.8%	0.8%	-0.3%	-1.1%
2012.256	BKS	Z	348.4	0.692	12.09	0.455	2012.254	HOPS	Z	390.6	0.733	15.83	0.357
2011.235	BKS	N	360.7	0.716	17.10	0.336	2010.117	HOPS	N	391.9	0.740	16.17	0.326
			-3.8%	-2.5%	-0.8%	0%				1.2%	3.5%	3.9%	7.1%
2012.040	BKS	N	347.1	0.698	16.96	0.336	2012.039	HOPS	N	396.5	0.766	16.80	0.349
			0.7%	0.9%	0.9%	0%				-0.4%	-0.4%	1.8%	-4.3%
2012.122	BKS	N	349.4	0.704	17.11	0.336	2012.128	HOPS	N	394.8	0.763	17.11	0.334
			0%	-1.0%	-0.4%	0.3%				0.9%	1.3%	-0.4%	0%
2012.256	BKS	N	349.3	0.697	17.05	0.337	2012.254	HOPS	N	398.4	0.773	17.05	0.334
2011.235	BKS	E	360.5	0.722	13.19	0.400	2010.117	HOPS	E	392.4	0.731	15.85	0.339
			-4%	-4.3%	0.8%	5.2%				-1.4%	-1.6%	6%	2.9%
2012.040	BKS	E	346.1	0.691	13.30	0.421	2012.039	HOPS	E	387.1	0.719	16.80	0.349
			0.5%	-0.3%	-0.1%	0.2%				-0.5%	-0.7%	-0.1%	-1.7%
2012.122	BKS	E	347.9	0.689	13.29	0.422	2012.128	HOPS	E	385.3	0.714	16.79	0.343
			0.2%	1.0%	0%	-1.9%				0.6%	0.8%	-0.5%	1.2%
2012.256	BKS	E	348.5	0.696	13.29	0.414	2012.254	HOPS	E	387.7	0.720	16.70	0.347
2011.012	CMB	Z	365.7	0.731	12.91	0.461	2011.160	YBH	Z	371.5	0.731	11.94	0.465
			-0.1%	1.6%	2%	1.1%				-2%	-3.6%	1.9%	1.7%
2012.041	CMB	Z	365.4	0.743	13.17	0.466	2012.038	YBH	Z	364.0	0.705	12.17	0.473
			-0.3%	-0.3%	0.3%	0.2%				0%	-0.1%	-0.1%	-0.2%
2012.123	CMB	Z	364.4	0.741	13.21	0.467	2012.124	YBH	Z	364.1	0.704	12.16	0.472
			0.1%	-3.9%	0.7%	-1.9%				0.2%	0.1%	0%	-0.2%
2012.255	CMB	Z	364.9	0.712	13.12	0.458	2012.255	YBH	Z	365.0	0.705	12.16	0.471
2011.012	CMB	N	365.4	0.714	17.11	0.335	2011.160	YBH	N	370.2	0.736	13.12	0.418
			-0.3%	-1%	1.9%	-7.8%				-1.5%	-1.5%	-0.8%	5.7%
2012.041	CMB	N	364.3	0.707	17.43	0.309	2012.038	YBH	N	364.6	0.725	13.01	0.442
			0.2%	0.4%	-0.1%	4.2%				0.1%	-0.1%	-0.5%	-3.6%
2012.123	CMB	N	365.1	0.710	17.42	0.322	2012.124	YBH	N	365.0	0.724	12.95	0.426
			0.2%	3.2%	-5%	1.2%				0.1%	1.1%	0.3%	2.6%
2012.255	CMB	N	366.0	0.733	17.33	0.326	2012.255	YBH	N	365.2	0.732	12.99	0.437
2011.012	CMB	E	365.0	0.718	13.31	0.425	2011.160	YBH	E	389.0	1.019	12.76	0.430
			-0.4%	-2.8%	1.7%	9.4%				11.7%	28.9%	4.8%	-4.4%
2012.041	CMB	E	363.5	0.698	13.53	0.465	2012.038	YBH	E	434.6	1.313	13.37	0.411
			0.4%	1.4%	-1.3%	-29%				1.8%	5.6%	0%	1.9%
2012.123	CMB	E	365.1	0.708	13.35	0.330	2012.124	YBH	E	442.3	1.386	13.37	0.419
			0.4%	0.1%	2.9%	33.3%				10.9%	0.2%	-0.1%	-9.1%
2012.255	CMB	E	366.4	0.709	13.74	0.440	2012.255	YBH	E	490.7	1.389	13.36	0.381

Table 3.16: Initial calibration, February 2012 calibration, May 2012 calibration, and September 2012 calibration for STS-1/E300 units at BKS, CMB, HOPS and YBH. Percentages indicate change in response between the two dates.

## 8 Northern California Earthquake Monitoring

### 8.1 Introduction

Earthquake information production and routine analysis in Northern California have been improving over the past two decades. Since June 2009, the BSL and the USGS in Menlo Park have been operating mirrored software systems (see 2010 Annual Report). For this system, processing begins as the waveforms arrive at the computers operating the real-time, or AQMS, software, and ranges from automatic preparation of earthquake information for response to analyst review of earthquakes for catalogs and quality control.

This is the most recent step in a development at the BSL that began in the mid-1990s with the automated earthquake notification system called Rapid Earthquake Data Integration (REDI, *Gee et al.*, 1996; 2003a). This system determined earthquake parameters rapidly, producing near real-time locations and magnitudes of Northern and Central California earthquakes, estimates of the rupture characteristics and the distribution of ground shaking following significant earthquakes, and tools for the rapid assessment of damage and estimation of loss.

A short time later, in 1996, the BSL and the USGS began a collaboration for reporting on Northern and Central California earthquakes. Software operating in Menlo Park and Berkeley were merged to form a single, improved earthquake notification system using data from both the NCSN and the BDSN (see past annual reports). The USGS and the BSL are now joined as the Northern California Earthquake Management Center (NCEMC) of the California Integrated Seismic Network (Operational Section 2).

With partial support from the USGS, the BSL is currently also participating in the development and assessment of a statewide demonstration system for warning of imminent ground shaking in the seconds after an earthquake has initiated but before strong motion begins at sites that may be damaged (See Research Studies 20, 21, 22, 23, and 24.)

### 8.2 Northern California Earthquake Management Center

In this section, we describe how the Northern California Earthquake Management Center fits within the CISN system. Figure 3.11 in Operational Section 2 illustrates the NCEMC as part of the the CISN communications ring. The NCEMC is a distributed center, with elements in Berkeley and in Menlo Park. The 35 mile separation between these two centers is in sharp contrast to the Southern California Earthquake Management Center, where the USGS Pasadena is located across the street from the Caltech Seismological Laboratory.

As described in Operational Section 2, the CISN partners are now connected by an Internet-based communications link. The BSL has maintained two T1 communication links with the USGS Menlo Park, to have robust and reliable links for shipping waveform data and other information between the two processing systems.

Figure 3.29 provides more detail on the system operating at the NCEMC since mid-June, 2009. Now, complete earthquake information processing systems operate in parallel in Menlo Park and Berkeley. Incoming data from each network are processed locally at each of the two data centers in network services computers. The continuously reduced data, which include picks, codas, ground motion amplitudes, and ML100, are exchanged between the data centers and fed into both processing streams. Real time analysis is coordinated using up-to-date information from the local real-time database, which is replicated to the local data center database. Event review and automatic downstream processes such as computation of fault plane solutions access the internal data center databases. To maintain redundancy, robustness, and completeness, these two databases replicate with each other across the San Francisco Bay. They also replicate with the public database from which information is made available to the public. The system includes the production of location and origin time as well as estimates of  $M_d$ ,  $M_L$ , and  $M_w$ . For events with  $M > 3.5$ , ShakeMaps are also calculated on two systems, one in Menlo Park and one in Berkeley. Finite fault calculation is not yet integrated into the new processing system. It is only calculated at the BSL at this time.

This new system combines the advantages of the NCSN with those of the BDSN. The dense network of the NCSN contributes to rapid and accurate earthquake locations, low magnitude detection thresholds, and first-motion mechanisms. The high dynamic range data loggers, digital telemetry, and broadband and strong-motion sensors of the BDSN provide reliable magnitude determination, moment tensor estimation, calculation of peak ground motions, and estimation of source rupture characteristics. Robust preliminary hypocenters, or “Quick Looks” are published within about 25 seconds of the origin time. Event information is updated when preliminary coda magnitudes are available, within 2-4 minutes of the origin time. Estimates of local magnitude are generally available less than 30 seconds later, and other parameters, such as the peak ground acceleration and moment magnitude, follow within 1-4 minutes (Figure 3.30).

Earthquake information is now distributed to the web through EIDS and is available through the USGS Earthquake Notification Service (<http://ssl.earthquake>).

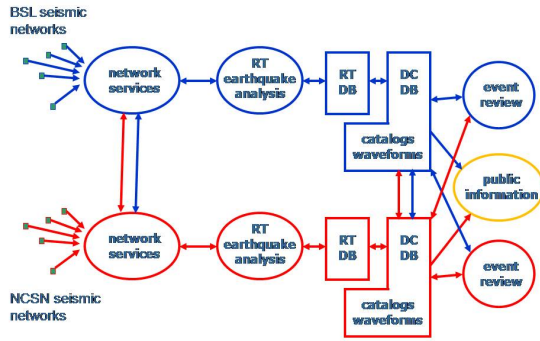


Figure 3.29: Details of the new Northern California processing system, which has been operational since mid-June, 2009. Network services processing, that is, production of picks, ground motion amplitudes, and other reduced information, occurs at both datacenters, and the information is exchanged. Complete earthquake information processing systems exist on both sides of the San Francisco Bay, and up-to-date information is exchanged by database replication.

usgs.gov/ens). We are working with the USGS in Golden, CO to implement exchange of earthquake information using a new transport mechanism, PDL. PDL allows larger packages of more complete information to pass from our analysis systems to the USGS as the National Earthquake Information Center in Golden and to other users. We are also working to develop readers and writers for QuakeML. Organizations with the need for more rapid earthquake information should use CISN Display (<http://www.cisn.org/software/cisndisplay.htm>). The *recenteqs* site has enjoyed enormous popularity since its introduction and provides a valuable resource for information which is useful not only in the seconds immediately after an earthquake, but in the following hours and days as well.

### 8.3 2011-2012 Activities

In June 2009, we began operating the ANSS Quake Monitoring System (AQMS) software, formerly CISN Software, as the production system in the Northern California Seismic System (NCSS) for monitoring and reporting on Northern California earthquakes. This came as the result of a long effort to adapt and test software developed for the TriNet system operating in Southern California.

Data flow in the new Northern California system (Figure 3.31) has been modified to allow for local differences (such as very different forms of data acquisition and variability in network distribution). In addition, the BSL and

the USGS want to minimize use of proprietary software in the system. One exception is the database program, Oracle. The NCEDC Oracle database hosts all earthquake information and parameters associated with the real time monitoring system. It is the centerpoint of the new system, providing up-to-date information to all processing modules. Reliability and robustness are achieved by continuously replicating the databases. The public, read-only, database provides event and parametric information to catalog users and to the public.

During the last few years, BSL staff members, particularly Pete Lombard, have become extremely familiar with elements of the TriNet software. The software is now adapted for Northern California, with many adjustments and modifications completed along the way. For example, Pete Lombard adapted the TriNet magnitude module to Northern California. Pete made a number of suggestions on how to improve the performance of the magnitude module and has worked closely with Caltech and the USGS/Pasadena on modifications.

The BSL and the USGS Menlo Park are exchanging “reduced amplitude time series.” One of the important innovations of the TriNet software development is the concept of continuous processing (*Kanamori et al.*, 1999). Waveform data are constantly processed to produce Wood Anderson synthetic amplitudes and peak ground motions. A program called *rad* produces a reduced time series, sampled every 5 seconds, and stores it in a memory area called an “Amplitude Data Area” or ADA. Other modules can access the ADA to retrieve amplitudes to calculate magnitude and ShakeMaps as needed. The BSL and the USGS Menlo Park have collaborated to establish tools for ADA-based exchange. The next step in improving reliability and robustness is to implement ADA exchange with Southern California as well.

### Moment Tensor Solutions with *tmts* and Finite Fault Analysis

The BSL continues to focus on the unique contributions that can be made from the broadband network, including moment tensor solutions and finite fault analysis. *tmts* is a Java and web-based moment tensor processing system and review interface based on the complete waveform modeling technique of *Dreger and Romanowicz* (1994). The improved, web-based review interface has been operating in Northern California since July 2007. The automatically running version for real-time analysis was extensively tested and updated by Pete Lombard, and has been running since June 2009. Reporting rules now allow automatically produced solutions of high quality to be published to the web.

From July 2011 through June 2012, BSL analysts reviewed many earthquakes in Northern California and adjoining areas of magnitude 2.9 and higher. Reviewed mo-

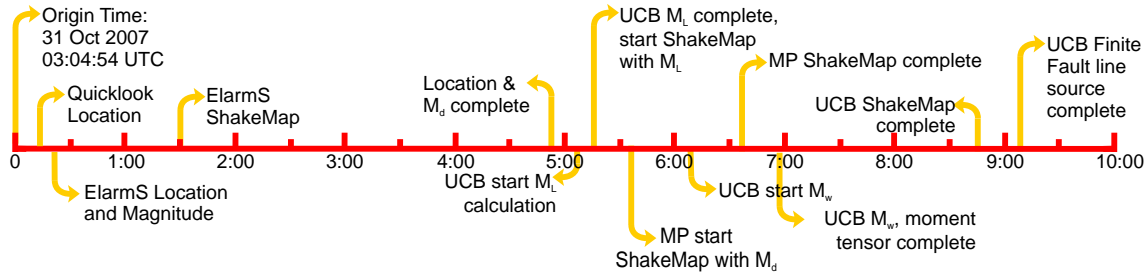


Figure 3.30: Illustration of the earthquake products timeline for the  $M_w$  5.4 Alum Rock earthquake of October 30, 2007. Note that all processing was complete within 10 minutes of the origin time.

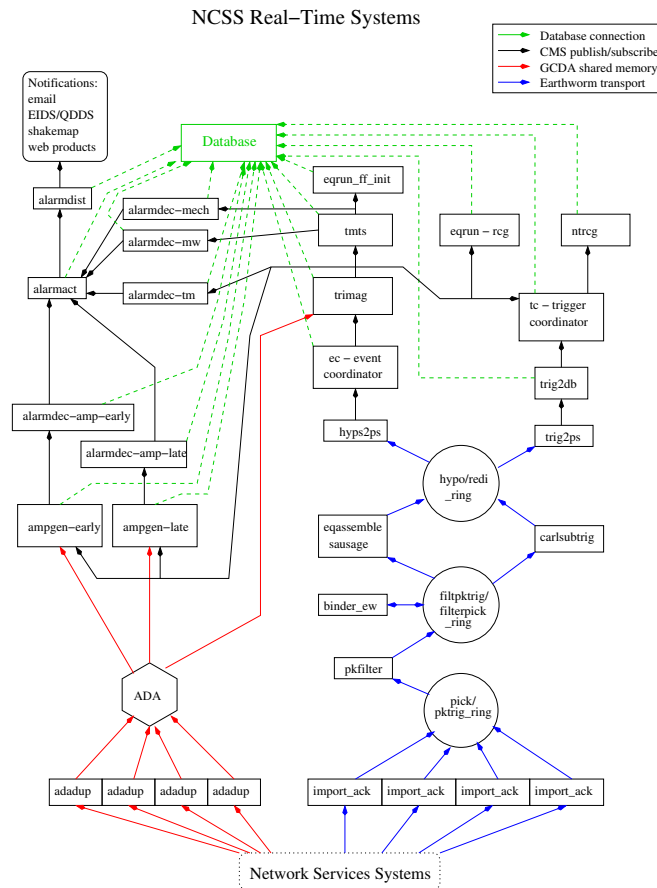


Figure 3.31: Schematic diagram of processing in the NCSS system. The design combines elements of the Earthworm, TriNet, and REDI systems

ment tensor solutions were obtained for 59 of these events (through 6/30/2012). Figure 3.32 and Table 3.17 display the locations of earthquakes in the BSL moment tensor catalog and their mechanisms. During this year, no finite fault inversions were produced for Northern California

earthquakes.

The version of `tmts` currently operating in Northern California allows full inversions that include an isotropic element of the source, i.e. explosions or collapses. With the advent of the new code, we reviewed “old” events in

the Geysers events from before 2007 with the new interface to produce and store deviatoric solutions for them in the database. In the next step, we will reanalyze events which exhibited anomalous radiation using the option for the full moment tensor (see Research Section 15). Some, but not all of these events will exhibit robust isotropic components.

We are currently developing a new version of the moment tensor system which will permit the use of records from strong motion sensors.

### Station Metadata, Reversals and `fpfit`

In a review of the fault plane solution for a recent event near the Geysers, we discovered that the orientation information for many of the seismic stations there was inconsistent. The fault plane solution program, `fpfit`, uses a file listing the stations with “reversed” polarity from the standard orientation. In the past, this file has been generated by hand and updated only occasionally. We reviewed the orientations of the borehole sensors contributing data to NCEMC operations, at Parkfield, in the San Francisco Bay Area and at the Geysers, using regional or teleseismic earthquakes. This information has been fed into the instrument response data. In a final step, we developed a procedure to compile the reversals file for `fpfit` from the database.

## 8.4 Routine Earthquake Analysis

In fiscal year 2010-2011, more than 27,000 earthquakes were detected and located by the automatic systems in Northern California. This compares with over 25,000 in 2009-2010, 21,500 in 2008-2009, 26,000 in 2007-2008, 23,000 in 2006-2007, 30,000 in 2005-2006, and 38,800 in 2004-2005. Many of the large number of events in 2004-2005 are aftershocks of the 2003 San Simeon and 2004 Parkfield earthquakes. Of the more than 27,000 events, about 126 had preliminary magnitudes of three or greater. Nine events had  $M_L$  or  $M_w$  greater than 4. The three largest events (on March 6, 2011, January 12, 2011 and March 1, 2011) had magnitudes close to 4.5. They were located offshore of Petrolia, CA, near San Juan Bautista, CA and near the Geysers, CA, respectively (see Table 3.17 for more details).

Although BSL staff no longer read BDSN records for local and regional earthquakes (see Annual Report of 2003-2004), they now participate in timing and reviewing earthquakes with `Jiggle`, mainly working on events from past sequences that have not yet been timed. This work contributes to improving the earthquake catalog for Northern California, but also ensures robust response capabilities, should the Menlo Park campus be disabled for some reason.

## 8.5 Acknowledgements

Peggy Hellweg oversees our earthquake monitoring system and directs the routine analysis. Peter Lombard and Doug Neuhauser contribute to the development of software. Taka’aki Taira, Ingrid Johanson, Doug Dreger, Sierra Boyd, Holly Brown, Sanne Cottaar, Andrea Chiang, Shan Dou, Scott French, Aurelie Guilhem, Mong-Han Huang, Rob Porritt, Jennifer Taggart, Amanda Thomas, Tom Weldon, Kelly Wiseman, and Zhou (Allen) Zheng contribute to the routine analysis of moment tensors. Peggy Hellweg, Doug Neuhauser, and Taka’aki Taira contributed to the writing of this section. Partial support for the development, implementation and maintenance of the AQMS software, as well as for the production of earthquake information, is provided by the USGS under Cooperative Agreement G10AC00093.

## 8.6 References

- Dreger, D., and B. Romanowicz, Source characteristics of events in the San Francisco Bay region, *USGS Open File Report 94-176*, 301-309, 1994.
- Gee, L., J. Polet, R. Uhrhammer, and K. Hutton, Earthquake Magnitudes in California, *Seism. Res. Lett.*, *75*(2), 272, 2004.
- Gee, L., D. Neuhauser, D. Dreger, M. Pasyanos, R. Uhrhammer, and B. Romanowicz, The Rapid Earthquake Data Integration Project, *Handbook of Earthquake and Engineering Seismology*, IASPEI, 1261-1273, 2003a.
- Gee, L., D. Dreger, G. Wurman, Y. Gung, B. Uhrhammer, and B. Romanowicz, A Decade of Regional Moment Tensor Analysis at UC Berkeley, *Eos Trans. AGU*, *84*(46), Fall Meet. Suppl., Abstract S52C-0148, 2003b.
- Gee, L., D. Neuhauser, D. Dreger, M. Pasyanos, B. Romanowicz, and R. Uhrhammer, The Rapid Earthquake Data Integration System, *Bull. Seis. Soc. Am.*, *86*, 936-945, 1996.
- Pasyanos, M., D. Dreger, and B. Romanowicz, Toward real-time estimation of regional moment tensors, *Bull. Seis. Soc. Am.*, *86*, 1255-1269, 1996.
- Romanowicz, B., D. Dreger, M. Pasyanos, and R. Uhrhammer, Monitoring of strain release in central and northern California using broadband data, *Geophys. Res. Lett.*, *20*, 1643-1646, 1993.

Location	Date	UTC Time	Lat.	Lon.	MT Depth	$M_L$	$M_w$	Mo	Str.	Dip	Rake
Tres Pinos, CA	7/6/2011	7:18:52	36.67	-121.29	8	3.73	3.8	6.20E+21	44	88	-14
Petrolia, CA	7/14/2011	13:18:44	40.32	-125.59	21	3.08	3.33	1.25E+21	97	82	162
Berkeley, CA	7/16/2011	10:51:26	37.86	-122.26	5	3.28	3.28	1.05E+21	145	87	-173
Tres Pinos, CA	7/18/2011	16:36:47	36.75	-121.34	8	3.12	3.17	7.12E+20	284	54	67
Petrolia, CA	8/5/2011	1:18:43	40.4	-124.96	8	3.09	3.55	2.59E+21	200	76	59
Alturas, CA	8/9/2011	16:28:08	41.52	-120.49	18	3.21	3.37	1.39E+21	313	83	-151
Trinidad, CA	8/14/2011	19:27:06	41.03	-125.17	18	3.7	4.1	1.79E+22	119	88	159
Anderson Springs, CA	8/17/2011	9:02:51	38.79	-122.75	5	3.43	3.67	4.03E+21	356	89	-179
San Leandro, CA	8/24/2011	6:36:54	37.74	-122.15	11	3.74	3.6	3.18E+21	69	89	-9
Mammoth Lakes, CA	8/24/2011	11:59:51	37.55	-118.87	8	4.34	4.23	2.71E+22	148	77	-133
San Leandro, CA	8/24/2011	16:57:44	37.75	-122.15	8	3.46	3.38	1.48E+21	140	80	-157
Pinnacles, CA	8/25/2011	18:17:35	36.58	-121.17	8	3.23	3.24	9.06E+20	41	85	-12
Pinnacles, CA	8/27/2011	7:18:21	36.58	-121.18	8	4.76	4.64	1.15E+23	135	82	-171
Pinnacles, CA	8/27/2011	7:22:00	36.6	-121.2	5	3.36	3.61	3.19E+21	38	76	-39
San Simeon, CA	9/13/2011	12:27:14	35.73	-121.11	5	3.69	3.56	2.71E+21	113	66	75
The Geysers, CA	9/17/2011	20:14:56	38.83	-122.8	3.5	3.02	3.38	1.47E+21	9	69	-131
San Leandro, CA	9/26/2011	3:08:10	37.75	-122.15	8	3.35	3.24	9.07E+20	54	89	-4
Angwin, CA	9/26/2011	9:01:23	38.6	-122.39	5	3.4	3.43	1.75E+21	147	66	153
Toms Place, CA	10/15/2011	11:42:30	37.91	-118.56	11	4.07	4.03	1.38E+22	203	51	-89
Berkeley, CA	10/20/2011	21:41:04	37.86	-122.25	8	4.1	3.95	1.01E+22	144	88	176
Berkeley, CA	10/21/2011	3:16:05	37.86	-122.26	8	4.13	3.84	7.20E+21	56	86	-9
Whitehawk, CA	10/27/2011	6:37:09	39.61	-120.47	14	5.18	4.73	1.55E+23	53	83	17
Berkeley, CA	10/27/2011	12:36:44	37.87	-122.26	11	3.8	3.62	3.39E+21	51	85	-9
Whitehawk, CA	10/30/2011	13:25:20	39.61	-120.48	14	4.05	3.8	6.32E+21	55	72	22
Kettleman City, CA	10/30/2011	13:26:44	35.94	-120.03	8	3.41	3.45	1.86E+21	322	65	111
Petrolia, CA	11/2/2011	7:21:06	40.41	-126.22	27	3.39	3.94	1.01E+22	182	89	14
Markleeville, CA	11/21/2011	9:39:04	38.54	-119.51	8	3.72	3.49	2.14E+21	203	50	-78
Petrolia, CA	12/8/2011	5:19:12	40.41	-125.59	14	3.52	4.02	1.35E+22	275	90	-168
Ferndale, CA	1/17/2012	9:55:01	40.53	-124.78	24	3.67	4.28	3.29E+22	124	83	-170
Clearlake, CA	1/24/2012	12:11:29	38.97	-122.69	11	3.39	3.8	6.20E+21	337	88	173
The Geysers, CA	1/30/2012	3:56:17	38.83	-122.8	5	2.9	3.31	1.14E+21	47	65	-60
Anderson Springs, CA	2/13/2012	4:47:13	38.79	-122.74	1.5	3.93	4.16	2.15E+22	67	89	-3
Weitchpec, CA	2/13/2012	21:07:03	41.14	-123.79	33	4.98	5.6	3.17E+24	215	48	-75
Crockett, CA	2/16/2012	2:09:14	38.08	-122.23	8	3.53	3.51	2.30E+21	144	90	-166
Crockett, CA	2/16/2012	17:13:21	38.08	-122.23	8	3.56	3.54	2.51E+21	55	82	-10
Petrolia, CA	2/25/2012	5:17:16	40.28	-124.31	30	3.6	4.28	3.24E+22	98	85	170
Weitchpec, CA	2/29/2012	5:00:33	41.14	-123.79	30	3.46	3.73	4.97E+21	345	75	-72
Pinnacles, CA	3/1/2012	16:31:09	36.64	-121.25	5	3.04	3.15	6.64E+20	45	89	-30
Pinnacles, CA	3/1/2012	17:15:34	36.64	-121.25	5	3.53	3.42	1.69E+21	139	83	156
El Cerrito, CA	3/5/2012	13:33:20	37.93	-122.31	8	4.24	3.99	1.19E+22	147	83	-170
Clearlake Oaks, CA	3/14/2012	6:30:21	39.02	-122.58	5	2.96	3.4	1.59E+21	68	76	-34
Cobb, CA	3/17/2012	23:21:23	38.83	-122.77	1.5	2.89	3.08	5.12E+20	166	52	-115
Petrolia, CA	3/19/2012	9:50:22	40.41	-124.59	21	3.24	3.61	3.19E+21	320	85	-168
Pinnacles, CA	4/6/2012	3:16:20	36.56	-121.12	5	3.82	3.69	4.21E+21	279	85	45
Aromas, CA	4/13/2012	22:18:54	36.89	-121.63	8	3.22	3.48	2.10E+21	314	78	-152
Trinidad, CA	4/17/2012	20:31:35	40.97	-124.42	21	3.51	4.15	2.10E+22	246	83	10
San Juan Bautista, CA	4/21/2012	15:19:10	36.78	-121.5	8	3.2	3.08	5.22E+20	44	87	-22
Petrolia, CA	4/27/2012	8:38:38	40.38	-124.99	8	3.5	3.83	6.82E+21	108	88	-172
The Geysers, CA	5/5/2012	9:23:23	38.8	-122.76	3.5	4.04	4.25	2.99E+22	143	87	-167
The Geysers, CA	5/5/2012	9:24:34	38.8	-122.78	1.5	0	3.34	1.29E+21	8	77	-161
The Geysers, CA	5/13/2012	12:38:52	38.79	-122.78	8	3.47	3.9	8.86E+21	169	82	164
Petrolia, CA	5/15/2012	10:19:33	40.39	-125.42	24	3.47	4.08	1.64E+22	93	81	168
Morgan Hill, CA	6/3/2012	17:31:37	37.26	-121.64	11	3.53	3.52	2.39E+21	235	84	-9
Trinidad, CA	6/10/2012	6:55:50	40.99	-124.83	24	3.4	3.55	2.65E+21	36	89	-7
Lee Vining, CA	6/11/2012	4:20:27	38.09	-119.14	8	3.36	3.16	6.92E+20	328	88	-164
Willow Creek, CA	6/13/2012	13:25:03	40.87	-123.47	18	3.26	3.4	1.55E+21	49	74	-64
Morgan Hill, CA	6/25/2012	8:13:41	37.26	-121.64	8	3.34	3.28	1.03E+21	326	89	-164
Willits, CA	6/25/2012	13:24:33	39.46	-123.32	8	3.24	3.47	1.99E+21	80	76	38
Ferndale, CA	6/30/2012	1:53:56	40.74	-125.15	14	3.67	3.97	1.14E+22	49	82	20

Table 3.17: Moment tensor solutions for significant events from July 1, 2011 through June 30, 2012 using a complete waveform fitting inversion. Epicentral information is from the UC Berkeley/USGS Northern California Earthquake Management Center. Moment is in dyne-cm and depth is in km.

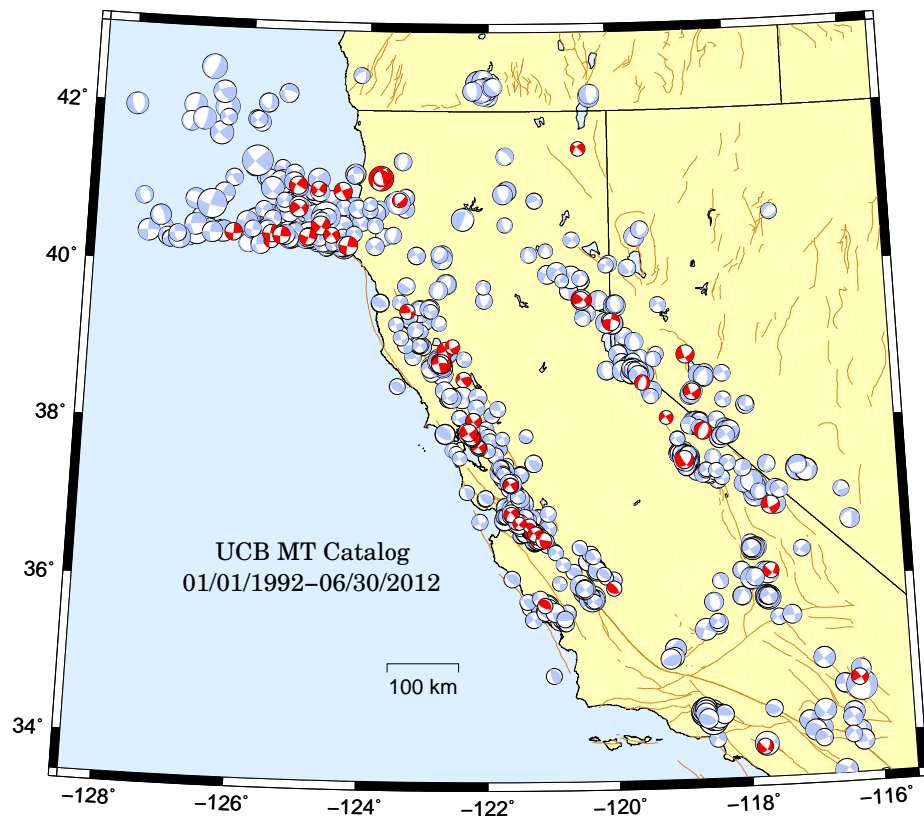


Figure 3.32: Map comparing reviewed moment tensor solutions determined by the BSL from past years (gray) with those from the fiscal year 2011-2012 (red/dark).

## 9 Outreach and Educational Activities

### 9.1 Introduction

BSL faculty, staff, and graduate students are involved in a wide variety of outreach activities, ranging from public lectures to tours of Hayward Fault geomorphology on campus. This year, of note was the BSL's response to the flood of media enquiries generated by the August 23 DC-area earthquake and by several mild to moderate earthquakes in the greater Berkeley area.

### 9.2 Highlights of 2011-2012

#### Responding to Media Enquiries

This year, the BSL's most far-reaching outreach activities were our interviews with local and national media. National news outlets contacted the BSL in response to the M 5.8 Mineral, VA earthquake that shook the Washington-DC area. Local earthquakes ranging in magnitude from 3.5 to 4.0 also generated a flurry of media requests. Faculty and researchers gave more than 30 interviews in 2011-2012, responding to over a dozen media enquiries for the DC-area quake alone.

In 2011-2012, Dr. Peggy Hellweg worked with KRON4 News to set up the USGS SWARM program for viewing seismic data. SWARM provides an alternative to the aging drum recorders currently filmed by news stations during an earthquake. (KRON and KPIX also continue to receive data feeds for their drum recorders from BSL station BKS via dedicated phone lines.)

#### Public Lectures

The Lawson Lecture is a free, public lecture hosted by the BSL every year in April. In this year's Lawson Lecture, Dr. Bill Ellsworth, from the US Geological Survey, gave a talk titled: "Earthquakes from the Top to the Bottom of the Magnitude Scale: Insights into Earthquake Physics from EarthScope." The Lawson Lectures are viewable as Flash video at [http://earthquakes.berkeley.edu/news/lawson\\_lecture](http://earthquakes.berkeley.edu/news/lawson_lecture).

In October, 2011, Dr. Hellweg gave the monthly public Science@Cal lecture, entitled "Tectonic Timebombs: Earthquakes Near and Far." Also in conjunction with Science@Cal, as well as the San Francisco Arts Commission, Dr. Hellweg was featured on a panel of scientists and artists: "Vast and Undetectable: Artists and Scientists in Dialogue."

### 9.3 Ongoing Activities

During 2011-2012, many groups, ranging from elementary-school students to international guests, visited the BSL for talks, tours, and hands-on science experiences. BSL Director Richard Allen met with a Chinese

delegation and spoke on Earthquake Early Warning and BSL operations, while Dr. Hellweg met with a delegation of Austrian provincial disaster management officials. Staff and graduate students conducted several talks and tours for school field trip groups and others. In addition, Drs. Johanson and Wiseman gave talks at the Lake Merritt Breakfast Club and a Bay Area middle school, respectively.

Recorded information on current earthquake activity is updated regularly on our information tape (510-642-2160).

#### Earthquake Research Affiliates Program

The UC Berkeley Earthquake Research Affiliates (ERA) Program links BSL researchers and their developments to those industry and public sector groups with an interest in BSL research. The purpose is to promote the use of new research and technology, and provide a forum for inviting optimal and essential users to participate in the development and testing of new technologies. The ERA program is designed to serve groups with an interest and need for rapid, robust and reliable earthquake information. This includes industrial groups with high-value equipment and products sensitive to earthquake ground shaking, public groups responsible for the safety of large cross-sections of society, and groups actively working to reduce the impacts of future earthquakes. More information on this public-private, industrial-academic community can be found on the ERA web pages (<http://earthquakes.berkeley.edu/ERA/>).

#### Cal Day - BSL Open House

The BSL once again opened its doors to visitors on UC Berkeley's *Cal Day*, the UC Berkeley open house for prospective students and community members. Visitors could jump up and down in front of a seismometer to make their own "earthquake," view current seismic data from our station BKS on a flatscreen monitor with the SWARM program, or learn about inertia and seismometers with a helium balloon tied to a radio-controlled car. Younger guests were offered their very own seismograms, while adults could pick up earthquake preparedness information provided by the BSL and the USGS. The BSL also participated in the Passport to Science@Cal program, helping children to fill up their "passports" with stamps and stickers from the *Cal Day* science exhibits they visited. Graduate student volunteers were on hand throughout the day to explain our exhibits and talk with visitors about UC Berkeley's role in earthquake monitoring.

## Displays

A large flatscreen monitor featuring the USGS SWARM program is now mounted in the McCone Hall first floor lobby display case. Streaming real-time data from station BKS, the SWARM display allows students and visitors the opportunity to view up to 96 hours of seismic data.

The BSL provides local waveform feeds for helicorders at visitor centers associated with BDSN stations (CMB and MHC). Organizations such as LHS, KRON, and KPIX receive feeds from BKS via dedicated phone lines for display, while the USGS Menlo Park uses data from CMB for display in the lobby of the lecture hall.

## BSL Web Pages

The BSL's main web pages describe our mission, introduce our research groups, provide information on our seminars and other special events (such as the Lawson Lecture), and point the public to sources of frequently sought-after earthquake-related information such as Alquist Priolo Zoning Act maps. The "seismic networks" web pages provide detailed information on each of our seismic stations, of interest to the research community. Our education and outreach web site (<http://earthquakes.berkeley.edu/outreach>) teaches the public about earthquakes and about Bay Area seismicity and hazards through Flash videos and FAQs while acting as a resource clearinghouse for teachers and those who wish to dig deeper. In addition, since September, 2008, the BSL has hosted its own blog, written by Horst Rademacher (<http://earthquakes.berkeley.edu/seismo.blog>).

## 9.4 Acknowledgements

Peggy Hellweg oversees the outreach activities at the BSL. Richard Allen, Bob Uhrhammer, Jennifer Taggart, Clayton Miller, and many other faculty, staff, and students at the BSL contribute to the outreach activities. Jennifer Taggart, Peggy Hellweg, and Richard Allen contributed to the preparation of this section.

# Glossary of Common Acronyms

Table 3.18: Standard abbreviations used in this report.

Acronym	Definition
ADA	Amplitude Data Area
ANSS	Advanced National Seismic System
ANSS NIC	ANSS National Implementation Committee
AQMS	ANSS Quake Monitoring System
ARRA	American Recovery and Reinvestment Act
BARD	Bay Area Regional Deformation
BAVU	Bay Area Velocity Unification
BDSN	Berkeley Digital Seismic Network
BSL	Berkeley Seismological Laboratory
CalEMA	California Emergency Management Agency
Caltrans	California Department of Transportation
CDF	California Department of Forestry
CGS	California Geological Survey
CISN	California Integrated Seismic Network
DART	Data Available in Real Time
EEW	Earthquake Early Warning
ElarmS	Earthquake Alarm Systems
EM	Electromagnetic
FACES	FlexArray along Cascadia Experiment for Segmentation
FEMA	Federal Emergency Management Agency
HFN	Hayward Fault Network
HRSN	High Resolution Seismic Network
InSAR	Interferometric Synthetic Aperture Radar
IRIS	Incorporated Research Institutions in Seismology
IRIS DMC	IRIS Data Management Center
LBL	Lawrence Berkeley National Laboratory
LFE	Low Frequency Event
LLNL	Lawrence Livermore National Laboratory
MARS	Monterey Accelerated Research System
MBARI	Monterey Bay Aquarium Research Institute
MOBB	Monterey Ocean Bottom Broadband Observatory
mPBO	Mini-Plate Boundary Observatory
MT	Magnetotelluric
MT	Moment Tensor
MTJ	Mendocino Triple Junction
NCEDC	Northern California Earthquake Data Center
NCEMC	Northern California Earthquake Management Center
NCSN	Northern California Seismic Network
NCSS	Northern California Seismic System
NHFN	Northern Hayward Fault Network

*continued on next page*

Table 3.18: *continued*

Acronym	Definition
NVT	Non-volcanic Tremor
PBO	Plate Boundary Observatory
PDF	Probability Density Function
PGV	Peak Ground Velocity
PSD	Power Spectral Density
QDDS/EIDS	Quake Data Distribution System/Earthquake Information Distribution System
REDI	Rapid Earthquake Data Integration
RES	Repeating Earthquake Sequence
SAF	San Andreas Fault
SAFOD	San Andreas Fault Observatory at Depth
SCSN	Southern California Seismic Network
SEED	Standard for Exchange of Earthquake Data
SEM	Spectral Element Method
SHFN	Southern Hayward Fault Network
SOH	State of Health
SSE	Slow Slip Event
UNAVCO	University NAVSTAR Consortium
USGS/MP	United States Geological Survey/ Menlo Park
USNSN	United States National Seismic Network

# Appendix I: Publications, Presentations, Awards, and Panels 2011-2012

## Publications

- Allen, R.M., Transforming Earthquake Detection? *Science*, *335*, 297-298, doi: 10.1126/science.1214650, 2012.
- Bodin, T., Sambridge, M., Rawlinson, N., & Arroucau, P., Transdimensional tomography with unknown data noise, *Geophys. J. Int.*, *189*(3), 1536-1556, 2012.
- Brossy, C.C., K.I. Kelson, C.B. Amos, J.N. Baldwin, B. Kozłowicz, D. Simpson, M.G. Ticci, A.T. Lutz, O. Kozaci, A. Streig, R. Turner, and R. Rose, Map of the late Quaternary active Kern Canyon and Breckenridge faults, Southern Sierra Nevada, California, *Geosphere*, *8*, doi:10.1130/GES00663.1, 2012.
- Cottaar S. and Buffett, B.A., Convection in the Earth's inner core, *Phys. Earth Planet. Int.*, *198-199*, 67-78, 2012.
- Durand, S., J.P. Montagner, P. Roux, F. Brenguier and R.M. Nadeau, Passive monitoring of anisotropy change for the Parkfield 2004 earthquake, *Geophys. Res. Lett.*, *38*, L13303, doi:10.1029/2011GL047875, 2011.
- Fisher, G.B., Amos, C.B., Bookhagen, B., Burbank, D.W., and Godard, V., Channel widths, landslides, faults, and beyond: The new world order of high spatial resolution Google Earth imagery in the study of earth surface processes, in Whitmeyer, S.J., Bailey, J.E., De Paor, D.G., and Ornduff, T., eds., Google Earth and Virtual Visualizations in Geoscience Education and Research: Geological Society of America Special Paper 492, doi:10.1130/2012.2492(01), 2012.
- Ford., S. R., W. R. Walter and D. S. Dreger, Event discrimination using regional moment tensors with teleseismic-P constraints, *Bull. Seism. Soc Am.*, *102*, 867-872, doi:10.1785/0120110227, 2012.
- Guilhem, A., and D. S. Dreger, Rapid detection and characterization of large earthquakes using quasi-finite-source Green's functions in continuous seismic moment tensor inversion, *Geophys. Res. Lett.*, *38*, L13318, doi:10.1029/2011GL047550, 2011.
- Kuyuk, H.S., E. Yildirim, E. Dogan, G. Horasan, An Unsupervised Learning Methodology: Application to discrimination of Seismic Event and Quarry Blasts in the Vicinity of Istanbul, *Natural Hazards and Earth Science*, *11*, 93100, 2011.
- Kuyuk, H.S., R.T. Kuyuk, E. Yildirim, Y. Sumer, Assessment of Near- And Far- Field Earthquake Ground Motion with Wavelet Transform, *Engineering Sciences*, *6*(1), 209-215, 2011.
- H.S. Kuyuk, E. Yildirim, E. Dogan, G. Horasan, Application of k-means and Gaussian mixture model for classification of seismic activities in Istanbul, *Nonlinear Processes in Geophysics*, *19*(4), 401-419, 2012.
- Lekic, V., French, S.W., and Fischer, K., Lithospheric Thinning Beneath Rifted Regions of Southern California, *Science*, *334*(6057), 783-787, DOI:10.1126/science.1208898, 2011.
- Liu, K., Levander, A., Zhai, Y., Porritt, R. W., Allen, R. M., Asthenospheric flow and lithospheric evolution near the Mendocino Triple Junction, *Earth Planet. Sci. Lett.*, *323-324*(1), 60-71, doi: 10.1016/j.epsl.2012.01.020, 2012.

- Lutz, A., K.I. Kelson, C. Amos, D. Simpson, A. Jayko, and B. Kozlowicz, Seismic hazard, tectonics, and geomorphology of the southern Sierra Nevada range and southern Walker Lane belt, California, Friends of the Pleistocene Pacific Cell Annual Fieldtrip Guidebook, September 15 - 18, 2011, 158 p., 2011.
- Malagnini, L., A. Akinci, K. Mayeda, I. Munafo, R.B. Herrmann, A. Mercuri, Characterization of earthquake-induced ground motion from the L'Aquila seismic sequence of 2009, Italy, *Geophys. J. Int.*, *184*, 325-337, 2011.
- Obrebski, O., R.M. Allen, F. Zhang, J. Pan, Q. Wu, S.-H. Hung, Shear wave tomography of China using joint inversion of body and surface wave constraints, *J. Geophys. Res.*, *117*, B01311, doi:10.1029/2011JB008349, 2012.
- Panning, M., A. Cao, A. Kim and B. Romanowicz, Non-linear 3D Born shear waveform tomography in southeast Asia, *Geophys. J. Int.*, in press.
- Pollitz, F., R. Bürgmann, and P. Banerjee, Geodetic Slip Model of the 2011 M9.0 Tohoku Earthquake, *Geophys. Res. Lett.*, *38(L00G08)*, doi:10.1029/2011GL048632, 2011.
- Reddy, C. D., P. S. Sunil, R. Bürgmann, D. V. Chandrasekhar, and T. Kato, Postseismic relaxation due to Bhuj earthquake on January 26, 2001: possible mechanisms and processes, *Natural Hazards*, *62*, doi: 10.1007/s11069-11012-10184-11067, 2012.
- Romanowicz, B., and H. Yuan, On the interpretation of SKS splitting measurements in the presence of several layers of anisotropy, *Geophys. J. Int.*, *188*, 1129-1140, doi: 10.1111/j.1365-246X.2011.05301.x, 2012.
- Ryder, I., R. Bürgmann, and F. Pollitz, Lower crustal relaxation beneath the Tibetan Plateau and Qaidam Basin following the 2001 Kokoxili earthquake, *Geophys. J. Int.*, *187(2)*, doi: 10.1111/j.1365-1246X.2011.05179.x, 2012.
- Ryder, I., A. Rietbrock, K. Kelson, R. Bürgmann, M. Floyd, A. Socquet, C. Vigny, and D. Carrizo, Large extensional aftershocks in the continental forearc triggered by the 2010 Maule earthquake, Chile, *Geophys. J. Int.*, DOI: 10.1111/j.1365-1246X.2011.05321.x, 2012.
- Shirzaei, M., A wavelet based multitemporal DInSAR algorithm for monitoring ground surface motion, *GRSL*, doi: 10.1109/LGRS.2012.2208935, 2012.
- Shirzaei, M., R. Bürgmann, O. Oncken, T. R. Walter, P. Victor, and O. Ewiak (2012), Response of forearc crustal faults to the megathrust earthquake cycle: InSAR evidence from Mejillones Peninsula, Northern Chile, *Earth Planet. Sci. Lett.*, *333-334*, doi:10.1016/j.epsl.2012.1004.1001.
- Shirzaei, M., and R. Bürgmann, Topography correlated atmospheric delay correction in radar interferometry using wavelet transforms, *Geophys. Res. Lett.*, *39(L01305)*, doi:10.1029/2011GL049971, 2012.
- Stehly, L., P. Cupillard and B. Romanowicz, Towards improving ambient noise tomography using simultaneously curvelet denoising filters and SEM simulation of ambient noise, *C.R. Geoscience*, *343*, 591-599, 2011.
- Thomas, A. M., R. Bürgmann, D. R. Shelly, N. M. Beeler, and M. L. Rudolph, Tidal triggering of low frequency earthquakes near Parkfield, CA: Implications for fault mechanics within the brittle-ductile transition, *J. Geophys. Res.*, *117(B05301)*, doi:10.1029/2011JB009036, 2012.
- Uhrhammer, R.A., M. Hellweg, K. Hutton, P. Lombard, A.W. Walters, E. Hauksson and D. Oppenheimer: California Integrated Seismic Network (CISN) Local Magnitude Determination in California and Vicinity, *Bull. Seismol. Soc. Am.*, *101*, 2685-2693; doi:10.1785/0120100106, 2011.
- Yoo, S-H, J. Rhie, H. Choi, K. Mayeda, Coda-derived source parameters of earthquakes and their scaling relationships in the Korean Peninsula, *Bull. Seism. Soc. Am.*, *101*, 2388-2398, 2011.
- Zechar, J.D. and R.M. Nadeau, Predictability of repeating earthquakes near Parkfield, California, *Geophys. J. Int.*, *190*, 457-462, doi:10.1111/j.1365-246X.2012.05481.x, 2012.
- Zhao, L., R.M. Allen, T. Zheng, R. Zhu, High-resolution body wave tomography models of the upper mantle beneath eastern China and the adjacent areas *Geochem. Geophys. GeoSys.*, *13*, Q06007, doi:10.1029/2012GC004119, 2012.

## **Presentations**

### **Asia Oceania Geosciences Society, 2011, Taipei, Taiwan, August 8-12, 2011**

Mong-Han Huang, Douglas Dreger, Seung Hoon Yoo, Roland Bürgmann, and Manabu Hashimoto, Joint Inversion of Seismic and Geodetic Data for the Source of the 4th March 2010 Mw 6.3 Jia-Shian, SW Taiwan, Earthquake.

### **Southern California Earthquake Center (SCEC) 2011 Annual Meeting, Palm Springs, CA, September 11-14, 2011**

Nadeau, R.M., R.C. Turner, and R. Bürgmann, Slip Deficits, Release and Transients Along the Central SAF from Repeating Microearthquakes, Poster A-102.

### **EarthScope Institute on the Lithosphere-Asthenosphere Boundary, Portland, OR, September 19-21, 2011**

Yuan, H., B. Romanowicz, D. Abt, H. Ford and K. Fischer, LAB and MLD in the NA Craton.

### **Association of Environmental and Engineering Geologists, 2011 Annual Meeting, Anchorage, AK, September 17-25, 2011**

Cohen-Waeber, J., Bürgmann, R., Sitar, N., Landslide Risk Assessment (LSRA): GPS Instrumentation and Remote Sensing Study of Slope Movement In the Berkeley Hills, CA.

### **Seismological Society of Japan, Fall Meeting, Shizuoka, Japan, October 12-15, 2011**

Taira, T., Detecting Stress-Induced Temporal Changes in Structures at Depth near Fault Zones from High-Frequency Seismic Coda Waves (invited).

### **Geothermal Resources Council Annual Meeting , San Diego, CA, October 23-26 2011**

Dreger, D.S. Boyd, O.S., and Gritto, R., Deviatoric and full moment tensor analysis at The Geysers Geothermal Field.

### **Geoengineering Seminar, UC Berkeley, Berkeley, CA, November 30, 2011**

Dreger, D. S., Seismic source-type identification and moment tensors of exotic events.

### **American Geophysical Union, 2011 Fall Meeting, San Francisco, CA, December 5-9, 2011**

Allen, R.M., M. Boese, H. Brown, M. Caprio, G.B. Cua, M. Fischer, D.D. Given, E. Hauksson, T.H. Heaton, M. Hellweg, I. Henson, M. Luikis, P.J. Maechling, M.A. Meier, D.S. Neuhauser, D.H. Oppenheimer and K. Solanki, CISM ShakeAlert: Delivering test warnings for California earthquake, Abstract S52A-01.

Allen, R.M., A. Ziv. Application of real-time GPS to earthquake early warning, Abstract G33C-05.

Amos, C.B., J.R. Unruh, A. Lutz, G.B. Fisher, K.I. Kelson, D.H. Rood, and A.S. Jayko, Lithospheric control on spatial patterns of active faulting in the southeastern Sierra Nevada, California, Abstract T31B-2342.

Boyd, O.S., Dreger, D.S., Hellweg, M., Lombard, P., Ford, S.R., Taira, T., Taggart, J., and Weldon, T.J., Full moment tensor analysis at The Geysers Geothermal Field, Abstract S33A-2301.

Brown, H., Allen, R.M., Neuhauser, D., Henson, I., Hellweg, M., Lim, I., and the CISM-EEW project team, CISM ShakeAlert: ElarmS, Abstract S53A-2253.

Bürgmann, R., Thomas, R., Freed, A., Shelly, D., Strong Rocks and Weak Faults in the Lower Crust of California (invited), Abstract T21C-05.

Chiang, A., D.S. Dreger, S.R. Ford, and W.R. Walter, Free-Surface Vanishing Traction Effects on Shallow Sources, Abstract S43B-2233.

- Chong, J., Yuan, H., French, S.W., Romanowicz, B.A., and Ni, S., Imaging 3D anisotropic upper mantle shear velocity structure of Southeast Asia using seismic waveform inversion, Abstract T33B-2409.
- Cottaar S., and Romanowicz, B.A., Anisotropy across superplume boundaries, Abstract DI144A-02.
- Cottaar S., and Romanowicz, B.A., Observations on the northern boundary of the Pacific Superplume and neighbouring ULVZ, Abstract DI132A-08.
- Dziewonski, A.M., Lekic, V., Cottaar, S., Romanowicz, B.A., Topology of the mantle abyssal layer; superplumes big and small, Abstract DI132A-06.
- French, S.W., Lekic, V., and Romanowicz, B.A., Toward global waveform tomography with the SEM: Improving upper-mantle images, Abstract S13C-02.
- Guilhem, A., and Dreger, D. S., Rapid detection of great earthquakes using moment tensors: the example of the 2011 Tohoku-Oki earthquake, Abstract U51B-0005.
- Hellweg, M, M. Vinci, The CISN-EEW project team, CISN ShakeAlert: Using early warnings for earthquakes in California, Abstract S53A-2254.
- Johanson, I. R. Bürgmann, Characterizing Slow Slip Events on the Hayward Fault from Two Decades of SBAS-InSAR Data, Abstract S23B-2284.
- Kelly, C.M., A. Rietbrock, D.R. Faulkner and R.M. Nadeau, Temporal Changes in Seismic Attenuation associated with the 2004 M6.0 Parkfield Event, Abstract S24A-01.
- Kuyuk, H.S., R.M. Allen, M. Aktas, Earthquake Early Warning Systems; how many seconds do we really have?, Abstract S53A-2257.
- Levander, A.; K. Liu; R.W. Porritt; R.M. Allen. The Seismic Structure of the Mantle Wedge under Cascade Volcanoes, T53A-2494.
- Maceira, M., C.S. Larmat, C.A. Rowe, R.M. Allen, M.J. Obrebski, Validating Seismic Imaging Methods and 3D Seismic Velocity Models, Abstract S41A-2182.
- Mayeda, K.M., Malagnini, L., Yoo, S., Apparent Stress of the M5.8 Mineral, Virginia Sequence and Comparison with Other Crustal Sequences using the Coda Ratio Methodology, Abstract S11B-2238.
- Mayeda, K.M., Oth, A., Malagnini, L., Yoo, S., Walter, W.R., A Source Scaling Comparison for Selected Japanese Earthquake Sequences, Abstract S43C-2268.
- Masson, Y., Romanowicz, B.A., and French, S.W., Superposition principle and waveform tomography. How well can we do?, Abstract S51D-03.
- Mong-Han Huang, Roland Bürgmann, Manoochehr Shirzaei, Probing the Deep Rheology of Tibet: Constraints from the 2008 Mw 7.9 Wenchuan, China Earthquake, Abstract T23C-2411.
- Neuhauser, D.S., I. Henson, R.M. Allen, CISN ShakeAlert: Decision Module Enhancements for Earthquake Alerts, Abstract S53A-2249.
- Obrebski, M.J., R.M. Allen, F. Zhang, J. Pan, Q. Wu, F.F. Pollitz, S. Hung. Seismic tomography of the US and China using joint- inversion of body- and surface-wave constraints, Abstract S43D-03.
- Porritt, R. W., Allen, R. M., Pollitz, F. F., Hung, S-H., Obrebski, M. J Lithosphere-asthenosphere structure beneath the United States from joint inversion of body waves, surface waves, and receiver functions, Abstract DI51A-2118.
- Romanowicz, B.A., Lekic, V., Cottaar, S., Dziewonski, A.M., Seismological constraints on deep mantle processes, Abstract U44A-02.
- Shirzaei, M.; Bürgmann, R., Spatiotemporal model of aseismic slip on the Hayward fault inferred from joint inversion of geodetic and seismic data time series, Abstract G22A-04.
- Taira, T., Time-Lapse Monitoring for Detection of Transient Stress Changes in Geysers Geothermal Field, Abstract V53C-2630.
- Thomas, A.M., N. M. Beeler, R. Bürgmann, and D. R. Shelly, The frequency dependence of friction in experiment, theory, and observations of low frequency earthquakes, Abstract S23B-2249.

- Toomey, D.R.; R.M. Allen; J.A. Collins; R.P. Dziak; E.E. Hooft; D. Livelybrooks; J.J. McGuire; S.Y. Schwartz; M. Tolstoy; A.M. Trehu; W.S. Wilcock. Status of the Ocean Bottom Seismology Component of the Cascadia Initiative, Abstract T11C-08.
- Turner R.C., Nadeau R.M., Bürgmann R., Aseismic Slip, Repeating Earthquakes and Fault Interaction in the Loma Prieta Aftershock Zone, Abstract S23B-2269 (OSPA Honorable Mention).
- Wiseman, K., P. Banerjee, R. Bürgmann, K. E. Sieh, and D. Dreger, Joint Seismic and Geodetic Analysis of the 2009 Padang, Sumatra Intraslab Earthquake (invited), Abstract T54B-04.
- Zhao, L., T. Zheng, R.M. Allen, Spatially varying upper mantle of eastern China caused by Pacific Plate subduction: constraints from body-wave tomography and SKS wave splitting measurements, Abstract S24B-08.
- Zheng, Z. and Romanowicz, B., Small-scale Lateral Variations of S670S Characteristics at Okhotsk Sea Observed on the US Transportable Array, Abstract DI31B-2177.
- Yoo, S., Dreger, D.S., Mayeda, K.M., Walter, W.R., Source Scaling and Ground Motion of the 2008 Wells, Nevada, earthquake sequence, Abstract S51B-2219.
- Yuan, H., P. Cupillard, and B. A. Romanowicz, Refining upper mantle structure in the North American continent using Spectral Element method, Abstract S44A-05.
- Yuan, H., French, S.W., Lekic, V., and Romanowicz, B., Global azimuthal anisotropy structure of the upper mantle, Abstract DI51C-03.

### **8th Annual Northern California Earthquake Hazards Workshop, USGS, Menlo Park, CA, January 24-25, 2012**

- Allen, R.M., H. M. Brown, M. Hellweg, D. Neuhauser, I. Henson, H.S. Kuyuk, CISN Earthquake Early Warning.
- Johanson, I., R. Bürgmann, The BARD Continuous GPS Network: Monitoring Earthquake Hazards in Northern California and the San Francisco Bay Area.
- Johanson, I., R. Bürgmann, BAVU3βετα The BARD Continuous GPS Network: Monitoring Earthquake Hazards in Northern California and the San Francisco Bay Area.
- Shirzaei, M., T. Taira, I. Johanson, R. Bürgmann, Transient Slip on the Hayward Fault from SBAS-InSAR, GPS and Seismicity Data.
- Turner R.C., Nadeau R.M., Bürgmann R., Aseismic Slip, Repeating Earthquakes and Fault Interaction in the Loma Prieta Aftershock Zone.

### **Big Data at Berkeley, Berkeley EECS Annual Research Symposium, Berkeley, CA, February 23, 2012**

- Kong, Q., Allen, R.M., Bray, J., Bayen, A., droidShake: Using smartphones to provide earthquake warnings.

### **2012 UNAVCO Science Workshop, Boulder, CO, February 28- March 1, 2012**

- Johanson, I., Real-time Data Processing for Retrieving Earthquake Parameters from the BARD Network.
- T. Taira, K. Hodgkinson, O. Fox, and D. Mencin, Measurements of PBO Borehole Seismometer Orientations.

### **International Symposium on Statistical modeling and Real-time Probability Forecasting for Earthquakes, Institute of Statistical Mathematics, Tokyo, Japan, March 11-14, 2012**

- Nomura, S., Y. Ogata and R.M. Nadeau, Space-Time Models of Repeating Earthquakes in Parkfield Segment.

## **European Geophysical Union, Vienna, Austria, April 22-27, 2012.**

Levander, A., K. Liu, R.W. Porritt, R.M. Allen, The Seismic Structure of the Mantle Wedge under Cascade Volcanoes.

## **2012 Seismological Society of America Annual Meeting, San Diego, CA, April 17-19, 2012**

Allen, R.M., I. Johanson, S. Colombelli, A. Ziv, Applications of real-time GPS to earthquake early warning.

Beeler, N.M., A. M. Thomas, R. Bürgmann, and D. R. Shelly, Modulation of tectonic tremor by the tides: physical models descended from Leon Knopoff with application to the deep San Andreas.

Dreger, D. S., A. Guilhem, O. S. Boyd, A. Chiang, and M Hellweg, Seismic source studies at the Berkeley Seismological Laboratory, *Seism. Res. Lett.*, 83(2), 383, 2012.

Guilhem, A., and Nadeau, R. M., Episodic Tremor as Slow-slip events (SSE) at Parkfield, CA, *Seism. Res. Lett.*, 83(2), 2012.

Hellweg, M., R.M. Allen, H. M. Brown, I. Henson, Q. Kong, H.S. Kuyuk, D. Neuhauser, Developments in Earthquake Early Warning at UCB: CISN ShakeAlert.

Maceira, M., Larmat, C., Allen, R. M., Porritt, R., Rowe, C., Obrebski, M., 3D Seismic models and Finite-Frequency vs. Ray Theoretical approaches.

Porritt, R. W., Allen, R. M., Poolitz, F. F., Hung S-H., Obrebski, M. J., Lithosphere-Asthenosphere structure beneath the United States from joint inversion of body waves and surface waves.

Taira T., Investigating Interactions of Creeping Segments with Adjacent Earthquake Rupture Zones in the Mendocino Triple Junction Region.

## **GSA Rocky Mountain Section 64th Annual Meeting, Albuquerque, NM, May 9-11, 2012**

Porritt, R. W., Allen, R. M., Pollitz, F. F., The Rocky Mountains in the context of the North American continent from jointly inverted body and surface wave tomography.

## **3rd QUEST workshop, Tatranska Lomnica, Slovakia, May 20-26, 2012**

Cottaar S., and Romanowicz, B.A., A large ULVZ beneath Hawaii from S diffracted waveform modeling.

Romanowicz, B.A., Full waveform modeling of the earth's mantle at the global scale: from normal modes to SEM (invited).

## **Global challenges for seismological data analysis, 38th Workshop of the International School of Geophysics, Erice, Sicily, 25-30 May, 2012**

Kong, Q., Allen, R.M., Bray, J., Bayen, A., myShake: Using smartphones to detect earthquakes.

## **Annual IRIS workshop, Boise, ID, June 13-15, 2012**

Allen, R.M., When N is not enough: Engaging citizen scientists to expand geophysical networks (invited).

Guilhem, A., and Nadeau, R. M., Nonvolcanic Tremors and Deep Slow Slip Events in Central California.

## **Asia Oceania Geosciences Society - American Geophysical Union Western Pacific Geophysics Meeting (AOGS - AGU (WPGM)) Joint Assembly, Resorts World Convention Centre, Singapore, August 13-17, 2012**

Chen K.H., R. Bürgmann and R.M. Nadeau, Do Earthquakes Talk to Each Other? Triggering and Interaction of Repeating Sequences at Parkfield, Abstract SE76-A001.

## Speaking Engagements

- Allen, R.M., Using Real Time GPS to Deliver Earthquake Early Warning in California, Civil GPS Service Interface Committee, Sacramento, CA, August 2011.
- Allen, R.M., NSF's Amphibious Array, GeoPrisms Alaska Implementation Planning Meeting, Portland, Oregon, September 2011.
- Allen, R.M., Delivering earthquake warnings to California, UC Berkeley Science Talks, San Francisco, California, September 2011.
- Allen, R.M., Delivering Earthquake Early Warning to California, University of California Town and Gown Meeting, Berkeley, California, October 2011.
- Allen, R.M., NSF's Amphibious Array, Earthscope Steering Committee Meeting, Phoenix, Arizona, October 2011.
- Allen, R.M., Delivering Earthquake Early Warning to California, Northern California Geological Society, Orinda, California, October 2011.
- Allen, R.M., M.J. Obrebski, R. Porritt, C. Eakin, F. Pollitz, S. Hung, Mantle upwelling and lithospheric destruction beneath western North America, Dept. Earth and Planetary Sciences, Washington University in St Louis, Missouri, November 2011.
- Allen, R.M., Scientific briefing for Jacob Appelsmith, Senior Advisor to Governor Jerry Brown, State of California, December 2011.
- Allen, R.M., Scientific briefing for Federal Executive Board (with representatives for all federal agencies with a presence in the San Francisco Bay Area), March 2012.
- Allen, R.M., Scientific briefing for City of San Francisco, San Francisco, CA, April 2012.
- Allen, R.M. Reaching beyond the Ivory Tower: Reducing earthquake hazard while driving scientific discovery. Princeton University, New Jersey, April 2012.
- Allen, R.M., Scientific briefing for Advisors for Senators Barbara Boxer and Dian Feinstein, and Representatives John Garamendi, Jerry McNerney and Jackie Speier, Washington DC, May 2012.
- Allen, R.M., Scientific briefing for California Emergency Management Agency, May 2012.
- Allen, R.M., When N is not enough: Beyond traditional seismic networks. Global challenges for seismological data analysis, Fondazione Ettore Majorana, Erice, Italy, May 2012.
- Allen, R.M., California's dual-use geophysical networks: Increased science, reduced risk. Global challenges for seismological data analysis, Fondazione Ettore Majorana, Erice, Italy, May 2012.
- Allen, R.M., Scientific briefing for California Council on Science and Technology, June 2012
- Amos, C.B., Active faulting and regional deformation of the southern Sierra Nevada block, San Jose State University, San Jose, CA, November 7, 2011.
- Amos, C.B., Spatial and temporal patterns of faulting and active deformation of the Sierra Nevada, CA, California State University Bakersfield, Bakersfield, CA, February 8, 2012.
- Amos, C.B., What can ancient rivers tell us about active faults?, Western Washington University, Bellingham, WA, April 5, 2012.
- Amos, C.B., Spatial and temporal patterns of faulting and active deformation of the Sierra Nevada, CA, Berkeley Seismological Laboratory, Berkeley, CA, April 24, 2012.
- Bürgmann, R., Lithosphere and Asthenosphere Rheology from Post-loading Deformation, EarthScope Institute on Lithosphere-Asthenosphere Boundary, Portland, OR, September 19, 2011.
- Bürgmann, R., The Role of Fluids in the Rheology of Rocks and Fault Zones in the Lower Crust and Upper Mantle, Geofluids Symposium: Dynamics and Evolution of the Earth's Interior, Misasa, Japan, March 18, 2012.
- Cottaar S., Earthquakes and Seismology, for the Stamford School, UK, at UC Berkeley, Berkeley Seismological Laboratory, July 18, 2011.

- Cottaar S., Seismic anisotropy and superplume boundaries in the D" region, Bullard Laboratories Wednesday Colloquia, Cambridge, UK, September 2011.
- Dreger, D. S., Seismic source-type identification and moment tensors of exotic events, Earth Science Seminar, Scripps, University of California, San Diego, CA, April 16, 2012.
- Guilhem, A., The power of near (almost) realtime moment tensors, Exit Seminar, Berkeley Seismological Laboratory, UC Berkeley, November 20, 2011.
- Guilhem, A., Analysis of unusual earthquake and tremor seismicity at the Mendocino Triple Junction and Parkfield, California, PhD Defense, Institut de Physique du Globe, Paris, March 28, 2012.
- Hellweg, M., Tectonic Timebombs: Earthquakes Near and Far, Science@Cal Lecture Series, UC Berkeley, Berkeley, CA, October 15, 2011.
- Hellweg, M., Vast and Undetectable Panel Discussion: Visual Languages of Art and Science, San Francisco Arts Commission Gallery, San Francisco, CA, March 21, 2012.
- Johanson, I., Transient Slip on the Hayward Fault from SBAS-InSAR, FRINGE 2011, Frascati, Italy, September 19-23, 2011.
- Johanson, I., Earthquakes on the Hayward Fault, Lake Merritt Breakfast Club, Oakland, CA, January 12, 2012.
- Johanson, I., Earthquake Early Warning and Cascadia, GeoPRISMS/EarthScope Planning Workshop for the Cascadia Primary Site, Portland, OR, April 5-6, 2012.
- Nadeau R.M., Repeating Earthquake Recurrence Intervals: Magnitude and Time-Dependence, International Symposium on Statistical Modeling and Real-time Probability Forecasting for Earthquakes, The Institute of Statistical Mathematics, Tokyo, Japan, March 11-14, 2012.
- Nadeau R.M., Repeating Earthquakes: Some Physical Considerations, National Research Institute for Earth Science and Disaster Prevention (NIED), Tsukuba, Japan, March 16, 2012.
- Romanowicz, B., Lateral variations in seismic structure and anisotropy in the lowermost mantle, UCL-IPGP Workshop on high pressure Physics, Paris, September 2011.
- Romanowicz, B., Stratification in the lithosphere in archaic cratons: evidence from seismic waveform tomography, University College London, London, UK, November 1, 2011.
- Romanowicz, B., Stratification in the lithosphere in archaic cratons: evidence from seismic waveform tomography, Institut de Physique du Globe, Paris, France, November 10, 2011.
- Romanowicz, B., Global seismic tomography in the age of numerical wavefield computations, Department of Statistics, UC Berkeley, February 22, 2012
- Romanowicz, B., Global seismic tomography in the age of numerical wavefield computations, USGS Menlo Park, Menlo Park, CA, May 9, 2012.
- Taira, T., Seismic Constraints on Fault-Zone Strength and Rheology at Seismogenic Depth on the San Andreas Fault, Parkfield, National Research Institute for Earth Science and Disaster Prevention, Tsukuba, Japan, October 17, 2011.
- Taira, T., Seismic Constraints on Fault-Zone Rheology at Depth from Characteristically Repeating Earthquakes at Parkfield, California, Kyoto University, Kyoto, Japan, October 18, 2011.
- Taira, T., Seismic Constraints on Fault-Zone Rheology at Depth from Characteristically Repeating Earthquakes at Parkfield, California, California State University Northridge, Department of Geological Sciences Colloquia, Northridge, CA, November 1, 2011.
- Taira, T., Seismic Constraints on Fault-Zone Rheology at Depth from Characteristically Repeating Earthquakes at Parkfield, California, Caltech Dix Seismological Laboratory seminar, Pasadena, CA, November 4, 2011.
- Wiseman K., The far reach of megathrust earthquakes: evolution of stress, deformation, and seismicity following the 2004 Sumatra-Andaman earthquake, UC Berkeley, Berkeley Seismological Laboratory Seminar, May 1, 2011.

- Wiseman, K., My life as a geophysicist, Raymond J. Fisher Middle School, Los Gatos, CA, June 1, 2011.
- Wiseman K., The far reach of megathrust earthquakes: evolution of stress, deformation, and seismicity following the 2004 Sumatra-Andaman earthquake, USGS Earthquake Science Center, Menlo Park, CA, June 13, 2011.
- Yuan, H., and B. A. Romanowicz, Exploring the North American Upper Mantle Using EarthScope Data, EarthScope Transportable Array Working Group Webinar, January 11, 2012.
- Yuan, H. and B. A. Romanowicz, Probing the North American Continent Using Seismic Anisotropy, Shell Colloquium Series, Spring 2012, ConocoPhillips School of Geology & Geophysics, The University of Oklahoma, Norman, OK, January 26, 2012.

## **Awards**

### **Barbara Romanowicz**

2012 Harry F. Reid Medal, Seismological Society of America

## **Panels and Professional Service**

### **Richard M. Allen**

Member, Cascadia Initiative Expedition Team Chair, International Earthquake Early Warning Advisory Committee, Geological Institute of Israel

Member, Scientific Advisory Board, European Union Framework 6 Project: Strategies and tools for Real Time Earthquake Risk Reduction (REAKT)

Chair, Amphibious Array Steering Committee (for the NSF Cascadia Initiative)

Chair, IRIS PASSCAL Standing Committee

Convener, Special sessions: "The origin of intraplate volcanism: hotspots, non-hotspots, and large igneous provinces" and "Earthquake Early Warning Capabilities and Delivery Around the World". AGU December 2011.

### **Roland Bürgmann**

Associate Editor, Bulletin of the Seismological Society of America

Editorial Advisory Board, Eos

Editorial Board, Earth and Planetary Science Letters

Member, EarthScope PBO Advisory Committee

Co-chair, EarthScope Thematic Working Group on Crustal Strain and Deformation

Member, National Earthquake Prediction Evaluation Council (NEPEC)

### **Douglas S. Dreger**

Cosmos Board of Directors

Four day short course on Moment Tensors in Quito, Ecuador (Pan-American Advanced Studies Institute on New Frontiers in Seismological Research: Sustainable Networks, Earthquake Source Parameters, and Earth Structure, July 11-24, 2011)

### **Margaret Hellweg**

Commissioner, Alfred E. Alquist Seismic Safety Commission

Member, CISN Program Management Committee

Member, CISN Standards Committee

Member, CISN Steering Committee

Member, CISN Outreach Committee

Member, ANSS Performance Standards Committee

Member, ANSS Comprehensive Catalog Advisory Committee

Chair, ANSS Class C Instrumentation Evaluation Committee

Member, Bay Area Earthquake Alliance Committee

Member, Bay Area Earthquake Alliance Executive Committee

Member, Editorial Board of Journal of Volcanology and Geothermal Research  
Member, New Media Committee, Seismological Society of America

### **Douglas S. Neuhauser**

Chair, Standards Group, California Integrated Seismic Network (CISN)  
Acting Member, CISN Program Management Committee

### **Barbara Romanowicz**

Member, International Evaluation Committee, School of Earth Sciences, ETH Zurich  
Member, International Review Committee, Earth Observatory of Singapore  
GEOSCOPE Scientific Adv. Committee, Paris  
Recruitment committee, Geophysics faculty position, École Normale Supérieure, Paris  
Scientific Advisory Committee, Dept of Geology, École Normale Supérieure, Paris  
Member, COMPRES advisory committee

### **Taka'aki Taira**

Member, California Integrated Seismic Network, Standards Committee  
Member, California Integrated Seismic Network, ShakeMap Working Group  
Member, Plate Boundary Observatory, Data Working Group

Appendix II

Seminar Speakers 2011-2012

WALTER MOONEY

USGS

*“Field assessments and Seismology of the M=8.8 Chile and M=9.0 Japan earthquakes”*

Tuesday, August 30, 2011

ISABELLE RYDER

University of Liverpool

*“Stressful times following the 2010 Maule earthquake, Chile”*

Tuesday, September 6, 2011

No seminar

Tuesday, September 13, 2011

No seminar

Tuesday, September 20, 2011

MANOOCHEHR SHIRZAEI

UC Berkeley

*“Spatiotemporal deformation field monitoring and modeling using advanced InSAR time series and time-dependent modeling”*

Tuesday, September 27, 2011

No seminar

Tuesday, October 4, 2011

MARGARET SEGOU

USGS Menlo Park

*“Post seismic stress evolution in strike slip faults along plate boundaries Comparing Northern California with Western Greece”*

Tuesday, October 11, 2011

CHRISTINA MORENCY

Lawrence Livermore National Laboratory

*“Seismic imaging based on spectral-element and adjoint methods: application to geothermal reservoir management”*

Tuesday, October 18, 2011

SEUNG HOON YOO

UC Berkeley

*“Earthquake Source Scaling and Ground Motion: Comparison for selected Japanese and west US earthquake sequences”*

Tuesday, October 25, 2011

ERIC FIELDING

JPL

*“Complex Fault Rupture of the 2010 El Mayor-Cucupah Earthquake in Baja California”*

Tuesday, November 1, 2011

KEITH KNUDSEN

USGS Menlo Park

*“Geomorphic and Geologic Evaluation of Liquefaction Case Histories: Toward Rapid Hazard Mapping”*

Tuesday, November 8, 2011

ROSS STEIN

USGS Menlo Park

*“What triggers most earthquakes? (The answer's in the shadows)”*

Tuesday, November 15, 2011

AURELIE GUILHEM

UC Berkeley

*“The power of near-realtime moment tensors: application for small to tsunamigenic earthquakes”*

Tuesday, November 22, 2011

GILEAD WURMAN

Seismic Warning Systems

*“Benefits and Challenges of Designing an Earthquake Warning System from the Ground Up”*

Tuesday, November 29, 2011

CHIN-WU CHEN

Carnegie Institution of Washington

*“Upper mantle structure beneath the High Lava Plains, eastern Oregon, imaged by scattered wavefield”*

Tuesday, December 13, 2011

SERDAR KUYUK

UC Berkeley

*“Forward Forecasting of Ground Motion for Earthquake Early Warning Using Artificial Neural Network and Its Advanced Engineering Applications”*

Tuesday, January 17, 2012

No seminar

Tuesday, January 24, 2012

EMILY MONTGOMERY-BROWN  
University of Wisconsin  
*"Kilauea Slow Slip Events and the Hunt for  
Tectonic Tremor"*  
Tuesday, January 31, 2012

MAURIZIO BATTAGLIA  
University of Rome I "La Sapienza"  
*"Modeling Unrest at Mount St Helens"*  
Tuesday, February 7, 2012

VICTOR TSAI  
Caltech  
*"Quantifying the Seismic Signature of Rivers  
and Sea Ice"*  
Tuesday, February 14, 2012

BRAD AAGAARD  
U.S. Geological Survey  
*"Probabilistic Estimates of Surface Coseismic  
Slip and Afterslip for Hayward Fault  
Earthquakes"*  
Tuesday, February 21, 2012

ARMEN DER KIUREGHIAN  
Department of Civil & Environmental  
Engineering, UC Berkeley  
*"Bayesian Network for Post-Earthquake Risk  
Assessment and Decision"*  
Tuesday, February 28, 2012

RONNI GRAPENTHIN  
University of Alaska Fairbanks  
*"Volcano Geodesy on Gliding Timescales:  
Sources, Plumes, and Precursory Signals"*  
Tuesday, March 6, 2012

ANDY FREED  
Purdue University  
*"Using earthquakes as large rock squeezing  
experiments"*  
Tuesday, March 13, 2012

LINGSEN MENG  
Caltech  
*"The Broad Spectrum of Earthquake Ruptures  
Inferred from High Resolution Array Back-  
Projections"*  
Tuesday, March 20, 2012

No seminar  
Tuesday, March 27, 2012

SARAH MINSON  
U.S. Geological Survey  
*"Bayesian Earthquake Source Modeling"*  
Tuesday, April 3, 2012

JONATHAN AJO-FRANKLIN  
Lawrence Berkeley National Laboratory  
*"Using Continuous Active Source Seismic  
Monitoring (CASSM) for Mapping Injected CO2  
and Evolving Hydraulic Fractures"*  
Tuesday, April 10, 2012

No seminar  
Tuesday, April 17, 2012

COLIN AMOS  
UC Berkeley  
*"Spatial and Temporal Patterns of Active  
Faulting and Deformation of the Southeastern  
Sierra Nevada, CA"*  
Tuesday, April 24, 2012

BILL ELLSWORTH  
USGS  
*"Earthquakes from the Top to the Bottom of the  
Magnitude Scale: Insights into Earthquake  
Physics from EarthScope"*  
2012 Lawson Lecture  
Wednesday, April 25, 2012

KELLY WISEMAN  
Berkeley Seismological Lab.  
*"The Far Reach of Megathrust Earthquakes:  
Evolution of Stress, Deformation and Seismicity  
following the 2004 Sumatra Earthquake"*  
Tuesday, May 1, 2012



